Program and Book of Abstracts

The 9th International Conference on

TWO-PHASE SYSTEMS FOR GROUND AND SPACE APPLICATIONS

September 22-26, 2014

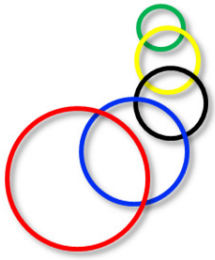

ITTW 2014

Grand Historic Venue, Embassy Suites Hotel
225 N. Charles Street, Baltimore, MD USA

ittw2014.umd.edu

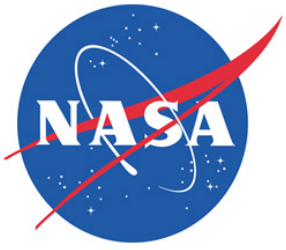

DOWNTOWN BALTIMORE

ITTW 2014

SEPTEMBER 22-26, 2014
BALTIMORE, MD

The 9th International Conference on
TWO-PHASE SYSTEMS FOR GROUND AND SPACE APPLICATIONS

Welcome

The organizing committee welcomes you to the 9th International Conference on Two-Phase Systems for Ground and Space Applications (ITTW2014) held in Baltimore, MD. We hope this meeting will continue the rich traditions of the previous ITTW conferences, and hope this conference will serve as a venue to make productive contacts and exchanges between researchers all over the world.

Chair

- Prof. Jungho Kim, University of Maryland (USA)

Co-Chairs

- Prof. Oleg A. Kabov, Institute of Thermophysics, Russian Academy of Sciences (Russia)
- Prof. Haruhiko Ohta, Kyushu University (Japan)
- Prof. Peter Stephan, Darmstadt Technical University (Germany)
- Prof. Jian-Fu Zhao, Chinese Academy of Sciences (China)

Scientific Committee

- Yoshiyuki Abe, AIST, Japan
- Vladimir Ajaev, SMU, USA
- Sergey V. Alekseenko, IT, Russia
- Alidad Amirfazli, UA, Canada
- Avram Bar-Cohen, UM, USA
- Dieter Bothe, TU Darmstadt, Germany
- Gian Piero Celata, ENEA, Italy
- Catherine Colin, IMFT, France
- Oleg A. Kabov, KIT, Russia
- Yoshiyuki Abe, AIST, Japan
- Vladimir Ajaev, SMU, USA
- Sergey V. Alekseenko, IT, Russia
- Alidad Amirfazli, UA, Canada
- Avram Bar-Cohen, UMD, USA
- Dieter Bothe, TU Darmstadt, Germany
- Gian Piero Celata, ENEA, Italy
- Catherine Colin, IMFT, France
- Oleg A. Kabov, KIT, Russia
- Paolo Di Marco, UNIPI , Italy
- Michael Dreyer, ZARM, Germany
- Olga N. Goncharova, ASU, Russia
- Jungho Kim, UM, USA
- Qiu-Sheng Liu, IM, China
- Dmitriy Markovich, IT, Russia
- Olivier Minster, ESA
- Haruhiko Ohta, KU, Japan
- Eduard E. Son, JIHT, Russia
- Peter Stephan, TUD, Germany
- Lounes Tadrist, IUSTI, France
- John R. Thome, EPFL, Switzerland

Conference History

Previous ITTW conferences along with the chief organizers:

2006	Brussels	Oleg Kabov and Jean-Claude Legros
2007	Kyoto	Haruhiko Ohta and Oleg Kabov
2008	Brussels	Oleg Kabov and Jean-Claude Legros
2009	Novosibirsk	Oleg Kabov
2010	Kyoto	Haruhiko Ohta and Oleg Kabov
2011	Cava de' Tirreni	Oleg Kabov and Raffaele Savino
2012	Beijing	Qiu-Sheng Liu and Oleg Kabov
2013	Bremen	Michael Dreyer

Sponsors

The organizers gratefully acknowledge support for this conference by NASA and the Department of Mechanical Engineering at the U. of Maryland.

Conference Organization

Lisa Press, Assistant Director, Conferences and Visitor Services, U. of Maryland
Kelly Hedgepeth, Meeting Services Manager, Conferences and Visitor Services, U. of Maryland

Conference Secretary and Website Designer

Mr. Alex Scammell, Dept. of Mechanical Engineering, U. of Maryland

Special Session: NASA fluidsLAB Workshop

The low-gravity environment of the NASA International Space Station (ISS) offers a unique opportunity for the study of fluid physics and transport phenomena. Experiments conducted in space have yielded rich results. Some were unexpected and most could not be observed in Earth-based labs. These results have provided valuable insights into fundamental fluid behavior that apply to both terrestrial and space environments. As an example, recent capillary flow research results have discovered both an unexpected sensitivity to symmetric geometries associated with fluid container shape, and identified key regime maps for design of corner or “wedge-shaped” passive gas/liquid phase separators. Results from research on fluid management and heat transfer, for both propulsion and life-support systems, have contributed greatly to U.S. leadership in space exploration.

In order to capture recommendations for future themes and areas of microgravity research, NASA is planning to provide a forum for presentation and discussion of these recommendations at the International Conference on Two-Phase Systems for Space and Ground Applications to be held on September 22-26, in Baltimore, MD. This forum will be referred to in the conference program as a “fluidsLAB workshop” and will consist of three theme areas: (1) Adiabatic Two-Phase Flow, (2) Boiling and Condensation, and (3) Capillary Flow and Interfacial Phenomena.

If you are not able to attend this conference to participate in this fluidsLAB workshop, you are invited to provide input in the form of a Request for Information (RFI) that is presently available on the NASA NSPIRES web site (see web link below). You can contribute to this RFI by describing a mission, observation, theory, or modeling activity that, making use of the ISS environment, promises to advance an existing or new scientific objective, contributes to fundamental understanding of fluid physics, and facilitates the connection between science and societal needs. All responses will be considered non-proprietary public information for distribution with attribution.

The recommendations from the fluidsLAB workshop and RFI opportunity will form the basis for future ISS fluid physics experiment designs. Facilitating the future research directions is a new Physical Science (PS) Informatics System that will provide global access to all past, present and future ISS PS experimental data. This will promote an open source approach to scientific data analysis and become a gateway to hundreds of new ISS-based scientific investigations that will define the next generation of ISS experiments. The subsequent multiplication of investigators with data access will greatly enhance discovery and innovation.

To respond to the RFI mentioned above, answers to a series of specific questions must be submitted electronically using the NASA Solicitation and Proposal Integrated Review and Evaluation System (NSPIRES) website by opening the NASA Research Opportunities homepage at http://nspires.nasaprs.com, then clicking the links through the menu listings "Solicitations" to "Open Solicitations" and selecting this RFI. The full RFI and submission instructions can be found at http://tinyurl.com/cfLAB-RFI.

NASA Primary Point of Contact (POC):
Dr. Francis Chiaramonte, Program Executive-ISS Research Project
NASA Headquarters
E-mail: francis.p.chiaramonte@nasa.gov
Phone: 202-358-0693

Interfacial Phenomena and Heat Transfer

Editor-in-Chief Oleg Kabov

Begell House is pleased to provide attendees to the ITTW2014 Conference *full access* to the articles published in this journal. All published articles (Volume 1 Issues 1-4, 2013 and Volume 2 Issue 1, 2014) and forthcoming articles can be accessed through the journal website

http://www.dl.begellhouse.com/journals/728e68e739b67efe.html

Table of Contents for Volume 2, 2014 Issue 1

MODELLING THE FLOW OF DROPLETS OF BIO-PESTICIDE ON FOLIAGE
Sergii Veremieiev, A. Brown, P. H. Gaskell, C. R. Glass, N. Kapur, H. M. Thompson, pages 1-14

REVIEW AND MODELING OF TWO-PHASE FRICTIONAL PRESSURE GRADIENT AT MICROGRAVITY CONDITIONS
M. M. Awad, Yuri S. Muzychka, pages 15-40

REBOUND OF LIQUID DROPLETS CAUSED BY SUDDEN DECREASE OF GRAVITY
Liang Zhang, Zhen-Dong Li, Jian-Fu Zhao, pages 41-54

NONLINEAR INSTABILITY OF A THIN FILM FLOWING DOWN A SMOOTHLY DEFORMED THICK WALL OF FINITE THERMAL CONDUCTIVITY
Luis Antonio Davalos-Orozco, pages 55-74

APPLICATION OF THE NONLINEAR POISSON-BOLTZMANN MODEL TO THE STABILITY OF AN ELECTROLYTE FILM
Christiaan Ketelaar , Vladimir S. Ajaev, pages 75-84

GRAVITY EFFECT ON EVAPORATION AND INTERFACIAL DEFORMATIONS IN NONISOTHERMAL LIQUID FILM MOVED BY A GAS FLOWIN A MICROGAP
Yulia Kabova, Vladimir Kuznetsov, Oleg A. Kabov, pages 85-102

Forthcoming Articles:

INVESTIGATION OF WETTING BEHAVIOR ON PATTERNED SURFACES WITH DIFFERENT MICROGEOMETRIES
Alidad Amirfazli, Guoping Fang

IMPINGEMENT COOLING OF HOT METAL STRIPS IN RUNOUT TABLE- A REVIEW
PURNA CHANDRA MISHRA, Santosh Kumar Nayak, Premananda Pradhan, Durga Prasad Ghosh

PROGRAM

MONDAY, SEPTEMBER 22

12:00-1:00	**REGISTRATION (5th Floor, Edinburgh Room)**
1:00-1:20	Opening remarks and welcome, *Jungho Kim*
	SESSION: SPACE EXPERIMENTS AND HARDWARE (pg. 1-10) **Chairs: I. Mudawar and Y. Abe**
1:20-2:00	**Keynote:** "Achievements and Perspectives of Space Experiment on Marangoni Convection Onboard the ISS", *Satoshi Matsumoto*
2:00-2:20	ESA Activities Overview, *Olivier Minster*
2:20-2:40	NASA Activities Overview, *Francis Chiaramonte*
2:40-3:00	"Gravity Dependent Two-Phase Research at NASA Glenn Research Center", *Brian Motil*
3:00-3:30	**Coffee**
3:30-3:50	"Physical Science Informatics: Providing Open Source Access to MABE Data", *John McQuillen, Robert D. Green, Ben Henrie, Teresa Miller, and Francis Chiaramonte*
3:50-4:10	"Pressurization & Pressure Control in The Zero Boil-Off Tank (ZBOT) Experiment", *Mohammad Kassemi, Sonya Hylton, and Olga Kartuzova*
4:10-4:30	"The Static Bubble Point Pressure Model for Porous LAD Screens Operating in Cryogenic Propulsion Systems", *Jason Hartwig, John McQuillen, and David Chato*
	SESSION: LIQUID FILMS/THERMOCAPILLARY FLOW 1 (pg. 11-16) **Chair: M. McCarthy**
4:30-4:50	"Thermocapillary instability of a thin film falling down a thick and deformed cooled wall", *Luis Antonio Davalos-Orozco*
4:50-5:10	"Three Dimensional Direct Numerical Simulations of Non-isothermal Pools and Sessile Droplets with Phase Change: Hydrothermal Waves and Convective Rolls", *P. Sáenz, P. Valluri, O. K. Matar, K. Sefiane, and G. Karapetsas*
5:10-5:30	"Oscillatory Thermocapillary Convection of High Prandtl Number Fluid", *Ruquan Liang, and Shuo Yang*

6:00-7:00	**CONFERENCE RECEPTION (2nd Floor, Roman Strada)**

7:00-9:00	**Special Session: NASA fluidsLAB Feedback (5th Floor, Edinburgh Room)**

TUESDAY, SEPTEMBER 23

8:00-8:20	**REGISTRATION (5th Floor, Edinburgh Room)**
	SESSION: POOL AND FLOW BOILING (pg. 17-32) **Chairs: V. Narayanan and D. Brutin**
8:20-9:00	**Keynote:** "Criteria for Negating Influence of Gravity on Flow Boiling Critical Heat Flux in Space Systems", *Issam Mudawar*
9:00-9:20	"Transition to Microbubble Emission Boiling on Horizontal Circular Heated Surface in Subcooled Pool", *Jun Ando, Takahito Saiki, Toshihiro Kaneko, and Ichiro Ueno*
9:20-9:40	"Wettability Influence on the Solid Superheat at the Onset of Pool Boiling on Nanometrically Smooth Surfaces", *B. Bourdon, R. Rioboo, P. Di Marco, R. Sevkan, M. Marengo, and J. De Coninck*
9:40-10:00	"The Effect of Wickability on Pool Boiling Critical Heat Flux on Micro/Nanostructured Surfaces", *Md Mahamudur Rahman and Matthew McCarthy*
10:00-10:20	"Computation of Bubble Growth on a Hot Substrate: Asymptotic Scheme for Small Contact Angles", *Alexey Rednikov, Nicolas Hollander, Marta Hernando and Pierre Colinet*
10:20-11:00	**Coffee**
11:00-11:20	"A Study of Flow Structure's Effect on Forced Convective Boiling Heat Transfer", *Alex Scammell and Jungho Kim*
11:20-11:40	"Flow boiling in tube in normal and microgravity conditions", *Marine Narcy and Catherine Colin*
11:40-12:00	"Enhanced Boiling Heat Transfer of FC-72 over Micro-Pin-Finned Surfaces with Jet Impingement", *Yonghai Zhang, Jinjia Wei, Xin Kong, and Ling Guo*
12:00-1:20	**LUNCH**
	SESSION: BUBBLES 1 (pg. 33-40) **Chairs: P. Valluri and F. Ye**
1:20-2:00	**Keynote:** "Air Entrainment and Cavity Generation in Solid-liquid Impact", *H. Ding, B.Q. Cheng, and C.Y. Zhang*
2:00-2:20	"Electric Field Effects on Bubbles in Microgravity", *Ezinwa Elele, Dana Qasem, John Tang, and Boris Khusid*
2:20-2:40	"Bubble Injection to Increase the Thrust of a Nozzle", *Xiongjun Wu, Jin-Keun Choi, and Georges L. Chahine*
2:40-3:00	"Bubble Growth Behavior in a Direct Methanol Fuel Cell Under Different Gravity Level", *Fang Ye, Ziguang Yang, Hang Guo, Longyun Xu, and Chongfang Ma*
3:00-3:40	**Coffee**

3:40-5:30	**POSTER SESSION 1 (5 min presentations)** **Chair: J. Kim**

Space Experiments **(pg. 41-46)**

- "Future ESA experiments in Two-phase Heat and Mass Transfer Research on-board the International Space Station", *Balázs Tóth, Olivier Minster, and Hans Ranebo*
- "Introduction and Status of hardware and development for Boiling and Two-Phase Experiments onboard ISS/Kibo", *Takashi Kurimoto, Satoshi Matsumoto, Haruo Kawasaki, Kenichiro Sawada, Hitoshi Asano, Osamu Kawanami, Koichi Suzuki, Ryoji Imai, Yasuhisa Shinmoto, and Haruhiko Ohta*
- "High-speed imaging system for two-phase flow research on the ISS", *Jeffery R. Mackey*

Droplets and Bubbles **(pg. 47-52)**

- "Interfacial Deformation and Internal Flow during Rotational Breakup of Electrostatic Levitated Droplet", *Soma Watahiki, Satoshi Matsumoto, Akiko Kaneko, and Yutaka Abe*
- "The Interaction of a Rising Bubble and Particle in Oscillating Fluid as a Part of a Flotation Process", *Dmitriy Lyubimov, Tatyana Lyubimova, and Lyudmila Klimenko*
- "Finite Amplitude Propagation of Acoustic Waves in Bubbly Liquids Based on Nonlinear Evolution Equations", *Tetsuya Kanagawa*

Flow Boiling **(pg. 53-58)**

- "Phenomenological Model for Annular Two-phase Friction Pressure Drop under Microgravity Condition", *Jiajun Xia, Zhencheng Huang, Wan Wu, Xingbin Zhang, and Zhenhui He*
- "Two-Phase Heat Transfer Mechanisms within Plate Heat Exchangers: Experiments and Modeling", *Valentin Solotych and Jungho Kim*
- "Flow Boiling Critical Heat Flux Measurements in Reduced Gravity", *Henry Nahra*

7:00	**SCIENTIFIC COMMITTEE MEETING (Invitation Only)**

WEDNESDAY, SEPTEMBER 24

8:00-8:20	**REGISTRATION (5th Floor, Edinburgh Room)**
	SESSION: DROPS AND SPRAYS **(pg. 59-76)** **Chairs: I. Ueno and C. Buffone**
8:20-9:00	**Keynote:** "Floating on Air*", Detlef Lohse*
9:00-9:20	"Alcohols and Alkanes Sessile Droplets Evaporation into Air: an Empirical Model for Convective Evaporation", *Florian Carle and David Brutin*
9:20-9:40	"Comparing the Measured Vapour Concentration Field Surrounding an Evaporating Pendant Deposited Droplet with Numerical Simulations", *S. Dehaeck, A. Rednikov and P. Colinet*
9:40-10:00	"On the Effect of Ambeint Gas, Heat Transfer, and Thermal Patterns During Evaporation of Small Droplets", *Yuki Fukatani, Takaaki Wakui, Suhaila Hussain, Masamichi Kohno, Yasuyuki Takata, Khellil Sefiane and Jungho Kim*
10:00-10:30	**Coffee**
10:30-10:50	"Influence of Interfacial Transport Phenomena on Internal and External Flow Behavior around an Acoustically Levitated Droplet", *Atsushi Goda, Koji Hasegawa, Akiko Kaneko, and Yutaka Abe*
10:50-11:10	"Levitation stability and restoring force of an acoustically levitated droplet", *Koji Hasegawa, Taku Furukawa, Hiroyasu Ohtake, and Yutaka Abe*
11:10-11:30	"A New Concept for Investigating Heat Transfer Mechanisms during Spray Cooling", *Matthias Winter, Tatiana Gambaryan-Roisman, and Peter Stephan*
11:30-11:50	"Temperature Evolution during the Evaporation of a Sessile Droplet", *Aziz Maatar, Salah Chikh, Mebrouk Ait-Saada, and Lounès Tadrist*
11:50-12:10	"Role of Surface Charges in Drop-Evaporation-Triggered 'Coffee Stain' Formation" *Siddhartha Das*
12:10-1:10	**LUNCH**
1:10-1:50	**Keynote:** "Multiphase Systems Under Vibrations in Different Gravity Conditions", *Tatiana Lyubimova* **(pg. 77)**
	SESSION: LIQUID FILMS/THERMOCAPILLARY FLOW 2 **(pg. 79-90)** **Chairs: S. Dehaek and P. Geshev**
1:50-2:10	"Convective Fluid Flows with Evaporation: Analytical, Numerical, and Experimental Investigations", *Olga Goncharova, Yuriy Lyulin, Ekaterine Rezanova, and Oleg Kabov*
2:10-2:30	"Experimental Investigation of Heat Transfer Characteristics Due to Evaporation of Shear-driven Liquid Film Flow", *Tomoki Hirokawa, Masahiko Murozono, Oleg Kabov, Yasuhisa Shinmoto, and Haruhiko Ohta*
2:30-2:50	"The Formation of Disturbance Waves in Downward Annular Flow", *S.V. Alekseenko, A.V. Cherdantsev, M.V. Cherdantsev, S.V. Isaenkov, and D.M. Markovich*

2:50-3:10	"Simple Model for Calculation of Film Thickness and Heat Transfer in a Turbulent Liquid Film", *P.I. Geshev*
3:10-3:40	**Coffee**
3:40-4:00	"Two-phase Flows in Channels with Chemically Patterned Walls", *Elizaveta Gatapova, Vladimir Ajaev, and Oleg Kabov*
4:00-4:20	"Annular Flow Instability in Microgap Channels", *Caleb Holloway, Ahmed Kaffel, Avram Bar-Cohen, and Amir Riaz*
4:20-5:50	**POSTER SESSION 2 (5 min presentations)** **Chair: J. Kim**
	Space Systems **(pg. 91-96)**
	• "Numerical Modeling of Bubbly Two-Phase Flow in Vortex Separator", *Jingsen Ma, Chao-Tsung Hsiao, and Georges L. Chahine* • "Gravitational Effect on Performance of a Direct Methanol Fuel Cell", *Fang Ye, Cuiping Lv, Hang Guo, Feng Wu, Jianfu Zhao, and Chongfang Ma* • "Qualification of a Degassing Method for FC-72/PF-5060", *Sebastian Fischer and Peter Stephan*
	Droplets, Bubbles and Particles **(pg. 97-104)**
	• "Numerical Simulations of Thermo-convective Instabilities in a Sessile Drop of Ethanol Under Evaporation in Microgravity Conditions", *Sergey Semenov, Florian Carle, Marc Medale, and David Brutin* • "Bubble Generation and Sizing in Fresh and Salt Water", *A. Leaman Nye, X. Wu, and G.L. Chahine* • "Effect of High-frequency Normal Vibrations on Critical Heat Flux of Subcooled Film Boiling", *V.V. Konovalov, T.P. Lyubimova, and O.A. Kabov* • "Diffusive Growth of Carbon Dioxide Bubbles", *Devaraj van der Meer, Oscar Enríquez, Chao Sun, Detlef Lohse and Andrea Prosperetti*
	Miscellaneous **(pg. 105-108)**
	• "Void Fraction Measurement of Two Phase Flows Inside Microchannels Using a Capacitance probe", *F. Creatini, P. Di Marco, S. Filippeschi, and M. Mameli* • "Development of A Long-Distance Loop Heat Pipe for Ground Application", *Hosei Nagano and Masataka Mitomi*

6:30	**CONFERENCE BANQUET (Spirit of Baltimore, Inner Harbor)** ***Boarding starts at 6:30 and the boat departs at 7:00.** ***If you wish to take the Charm City Circulator from the hotel (stop #317), get off at stop #320 for the harbor.**

THURSDAY, SEPTEMBER 25

8:00-8:20	**REGISTRATION (5th Floor, Edinburgh Room)**
8:20-9:00	**Keynote:** "Electrohydrodynamically Driven Two-Phase Heat Transport Devices for Space and Ground Applications", *Jamal S. Yagoobi* **(pg. 109)**
	SESSION: CONDENSATION (pg. 111-116) **Chair: J. McQuillen**
9:00-9:20	"Condensation Heat Transfer and Pressure Drop of R32/R1234ze Mixture Inside a Single Circular Microchannel", *Marco Azzolin, Stefano Bortolin, and Davide Del Col*
9:20-9:40	"Condensation on Asymmetric Microstructures- Effect of Orientation, Microstructure Size and Gravity", *Shashank Natesh, Vinod Narayanan, and Sushil Bhavnani*
9:40-10:00	"Effect of Heterogeneous Wettability on Droplet Dynamic and Condensation Process", *Felipe Mancio Reis, Pascal Lavieille, and Marc Miscevic*
10:00-10:40	**Coffee**
	SESSION: HEAT PIPES (pg. 117-128) **Chair: H. Nagano**
10:40-11:00	"Experimental Investigation of a Transparent Sintered Heat Pipe", *Cosimo Buffone*
11:00-11:20	"Ground Results with Self-rewetting Fluids in SELENE Space Experiment", *W. Tzevelecos and S. Van Vaerenbergh*
11:20-11:40	"The Constrained Vapor Bubble Heat Pipe Experiment: A Model to Predict the Thickness of the Flat Film in the Marangoni Flow Dominated Region", *Akshay Kundan, Joel L. Plawsky, and Peter C. Wayner, Jr.*
11:40-12:00	"Closed Loop Pulsating Heat Pipe: Ground and Microgravity Experiments", *M. Mameli, L. Marelli, M. Manzoni, L. Araneo, S. Filippeschi, and M. Marengo*
12:00-1:20	**LUNCH**
1:20-1:40	"Two Phase Titanium Water Heat Pipe for Space Rated Stirling Power Conversion", *Marc Gibson, Jim Sanzi, and Max Briggs*
1:40-2:00	"Study on Internal Flow Characteristics of Multiple Evaporators Loop Heat Pipe", *Yuta Matsuda, Hosei Nagano, Shun Okazaki, Hiroyuki Ogawa, and Hiroki Nagai*
	SESSION: MICROCHANNELS (pg. 129-132) **Chair: H. Guo**
2:00-2:20	"2.5-D Modeling of Manifold-Microchannels in Thin Film Evaporation", *Raphael Mandel, Serguei Dessiatoun, and Michael Ohadi*
2:20-2:40	"Heater Size Influence on Evaporation and Deformations of Liquid Film Sheared by Gas in a Microchannel", *Yu. O. Kabova, V.V. Kuznetsov, O. A. Kabov*
2:40-3:20	**Coffee**

	SESSION: BUBBLES 2 **(pg. 133-140)** **Chair: A. Rednikov**
3:20-3:40	"Modeling Shock Wave Propagation in Bubbly Media", *Anil Kapahi, Chao-Tsung Hsiao, and Georges L. Chahine*
3:40-4:00	"A Microgravity Two-Phase Flow Separator Experiment in Development for Flight on ISS", *Lauren M. Sharp, Enrique Ramé, Kelly M. Gilkey, Jay Owens, Nang T. Pham, and Philip A. Stehno*
4:00-4:20	"Void Fraction Characteristics and Flow Patterns of One Component Gas-Liquid Two-Phase Flow", *Taisaku Gomyo, Hithoshi Asano, Osamu Kawanami, Koichi Suzuki, Ryoji Imai, Takashi Kurimoto, Satoshi Matsumoto, Yasuhisa Shinmoto, Tomoki Hirokawa, and Haruhiko Ohta*
4:20-4:40	"Experimental Study on Bubble Dynamics of Gas-Liquid Two-Phase Flow in Capillary Vertical Tubes", *Bo Xu, Wenguang Nan, Yueshe Wang, Gang Huang, and Zhiqiang Wu*
4:40-5:00	**Summary and Wrap Up**

Ninth International Conference on
TWO-PHASE SYSTEMS FOR GROUND AND SPACE APPLICATIONS
Baltimore, Maryland, USA, September 22-26, 2014

Achievements and Perspectives of Space Experiment on Marangoni Convection onboard the ISS

Satoshi Matsumoto

Institute of Space and Astronautical Science, Japan Aerospace Exploration Agency
2-1-1, Sengen, Tsukuba, Ibaraki 305-8505, Japan
matsumoto.satoshi@jaxa.jp

Very interesting phenomenon is happening in two phases across the interface. In general, surface tension becomes strong with decreasing temperature. When a temperature difference exists along surface, the surface is pulled towards the low temperature region. Eventually, Marangoni convection (thermocapillary convection) would be induced. The surface tension difference is also produced under existing concentration distribution [1]. Marangoni flow is categorized in the natural convection same as buoyancy convection caused by density difference. A trait of Marangoni convection is a surface-tension-driven flow which driving force is localized at the only surface.

Marangoni convection affects the quality of grown crystal such as semiconductors, optical materials, or bio materials. Cröll *et al*. performed a crystal growth of semiconductor by a floating zone method under microgravity [2]. They pointed out that striation was introduced by time-dependent Marangoni convection. Therefore, it is important to understand an underlying principal and nature of Marangoni convection. The finding and knowledge obtained through this experiment can be applied to industrial methods, as well as advance of fluid dynamics.

A liquid bridge configuration is often employed to investigate Marangoni convection, because it is simulated a floating-zone method which is one of many crystal growth techniques. A liquid bridge (cylindrical liquid column) of silicone oil is formed into a pair of supporting solid disks. Convection is induced by imposing a temperature difference between disks, one end heating and other end cooling. Due to the convective instability, flow transits from laminar to oscillatory, chaos, and turbulence flows one by one as the driving force increases. Marangoni convection is characterized a non-dimensional index of Marangoni number which is the product of Reynolds number, *Re*, and Prandtl number, *Pr*, as defined below,

$$Ma \equiv Re \cdot Pr = \frac{|\sigma_T| \Delta T L}{\mu \alpha} \qquad (1)$$

where, σ_T is temperature coefficient of surface tension, ΔT temperature difference, L length of liquid bridge, μ dynamic viscosity, α thermal diffusivity. When Marangoni number exceeds the certain value (called as critical Marangoni number), convection transits from steady to time-dependent oscillatory flow due to instability. To determine the critical Marangoni number and effect of the control parameter such as geometry, thermopysical properties and heat exchange at the interface.

Final goal of out study is to syatematically understand the convective instability on Marangoni convection in liquid bridge configuration and to compare with other flow such as Rayleigh-Bénard convection [3], Taylor-Couette flow [4].

Fundamental questions regarding to Marangoni Convection are as follows;

- What are the conditions that determine the onset of unsteady (or oscillatory) convection in liquid bridge?
- What are the characteristics of unsteady, three-dimensional flow and temperature fields?
- What are the mechanisms that are responsible for the formation of dynamic particle accumulation structures?

Answering these questions should contribute to the better understanding of the instability mechanisms of Marangoni convection. Now, why do we need to conduct Marangoni experiment on board the International Space Station (ISS)? On the ground, we can see the only several millimeters liquid bridge because surface tension cannot support its tare weight due to gravity. On the other hand, microgravity conditions provide strong advantages as follows;

- Large and long liquid bridges can be formed (Fig. 1).
- Therefore, high Marangoni numbers can be realized.
- No density-driven convection exists.
- No gravity-induced deformation of liquid bridge exists.
- Very long period for experiment can be allotted utilizing the ISS.
- Very precise data with a wide range of parameters can be obtained by utilizing these merits in space.

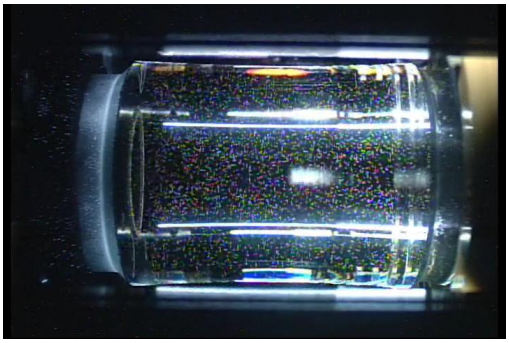

Figure 1: Side view of liquid bridge with 50 mm diameter and 60 mm length. Right side is heating and left is cooling.

The Fluid Physics Experiment Facility (FPEF) is used, and mounted in the Ryutai Rack inside KIBO Pressurized Module. Experiment is conducted in combining FPEF, and experiment unique hardware which is exchangeable according to the purpose of investigation, and is called the "Experiment Cell". FPEF is equipped with several cameras,

and an Infrared Imager for flow and temperature visualizations. Three units of black and white CCD cameras are mounted near the heating disk to observe three dimensional flow patterns through the transparent sapphire disk. This system allows for constructing 3-dimensional visualizations of the flow field using a 3D Particle Tracking Velocimetry (3D-PTV) technique. A color CCD camera takes side views of the liquid bridge to check the flow pattern, and the liquid bridge shape. The infrared imager is used to observe dynamic temperature distribution on the liquid bridge surface. Two Ultrasonic Velocity Profilers (UVPs) are embedded in the cooling disk. UVP is a method to measure an instantaneous velocity profile in a liquid flow by echography. This technique is expected to reveal spatio-temporal flow structure. The Marangoni experiment also uses the Image Processing Unit (IPU) and Microgravity Measurement Apparatus (MMA) with accelerometer to measure the microgravity environment near the FPEF.

Design for space experiment is shown in Fig. 2 schematically [5].

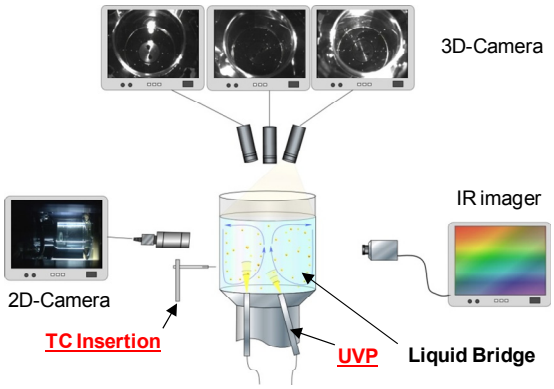

Figure 2: Schematic diagram of space experiment of Marangoni convection in half-zone liquid bridge. Several video images are taken to observe velocity and temperature fields. Temperature sensors are detects the temperature fluctuations in and near the liquid bridge when oscillatory, chaotic and turbulent flows

Silicone oil with the viscosity of 5, 10 and 20 mm^2/s, which Prandtl number are 68, 113 and 207 respectively, is employed as a working fluid, and is suspended between a pair of solid disks (10, 30 and 50 mm in diameter). A small amount of fine particles are mixed into the liquid bridge for flow visualization purposes. One of the disks is heated, and another cooled, to impose a temperature difference on both end of the liquid bridge. The temperature difference is gradually enlarged in order to increase the driving force of a thermocapillary flow (Marangoni flow). The flow transits from steady to oscillatory flow at the certain critical temperature differences. With increasing temperature difference, the convection becomes more complicated toward turbulent via chaotic flows. These transition processes are observed in detail.

Four Marangoni experiments on the ISS have been implemented and started in August 2008. The first and second experiments are for understanding of transition process. Third one is to make clear the mechanism of onset of oscillatory flow. Final one is to control Marangoni instability. Total series of experiments are twelve. At present, Two thirds of them have been completed successfully. Typical results are listed as follows.

(1) ΔT_c and Ma_c for large liquid bridges are determined.
(2) Azimuthal mode numbers and oscillation frequencies are determined.
(3) 3-D flow structures are measured.
(4) Chaotic and turbulent flows are detected and characterized.
(5) Hydrothermal waves and their propagation are captured.
(6) PAS with mode number of 2 and 3 could be observed.

Recently, importance of heat exchange through the surface is recognized for the onset of oscillatory flow. Especially in high Prandtl number fluid, temperature distribution along the interface is greatly distorted by thermocapillary flow, radiation and convective heat transfer with ambient gas. By using this susceptibility, it might be control the convective instability. For instance, oscillatory flow changes to steady flow when a forced flow introduces near the surface. This would be result in affecting the surface temperature distribution which could be changed the driving force.

Japan Aerospace Exploration Agency (JAXA) plans to carry out experiments on board the ISS over a period of eight years. Through these experiments, a deeper understanding of Marangoni convection is expected to proceed. It will be useful as a basis of knowledge to various fields.

Acknowledgement

Author acknowledges the scientists and their students joining space experiment of Marangoni convection on board the ISS. He also appreciates the operation team, planning team, international partner, crew members for their cooperation.

References

[1] Kuhlamnn, H.C., Themocapillary Convection in Models of Crystal Growth, Springer, (1998)

[2] Cröll, A., Kaiser, Th., Schweizer, M., Danilewsky, A.N., Lauer, S., Tegetmeier, A., Benz, K.W., Floating-zone and floating-solution-zone growth of GaSb under microgravity, J. Crystal Growth, Vol.191, pp.365-376 (1998)

[3] Krishnaumurti, R., On the transition to turbulent convection. Part 2 The transition to time dependent flow, J. Fluid Mech., Vol. 42, pp.309-320 (1970).

[4] Andereck, C., Liu, S.S. and Swinney, H.L., Flow regimes in a circular Couette system with independently rotating cylinders, J. Fluid Mech., Vol. 164, pp.155-183 (1986).

[5] Kawamura, H., Nishino, K., Matsumoto, S. and Ueno, I., Report on Microgravity Experiments of Marangoni Convection Aboard International Space Station, Transactions of ASME, Journal of Heat Transfer, Vol. 134, pp. 031005-031018 (2012).

Gravity Dependent Two-Phase Research at the NASA Glenn Research Center

Dr. Brian Motil[1*] and Dr. Francis Chiaramonte[2]

[1]NASA Glenn Research Center, 21000 Brookpark Road, Cleveland, Ohio, USA
[2]NASA Headquarters, 300 E St. SW, Washington D.C., USA
*Brian.J.Motil@nasa.gov

Two-phase systems in spacecraft face significant challenges in the low-gravity environment experienced in space. From the very beginning of the US space program, the NASA John H. Glenn Research Center (GRC) has been at the forefront of gravity dependent two-phase research starting with the first in-flight microgravity fluids experiment flown in 1962 by Scott Carpenter on the Mercury-Atlas 7 (MA-7) flight. Since the MA-7 flight, GRC has continued to lead by the development of several facilities including drop towers, zero-g aircraft, and most importantly, space-based facilities in order to advance microgravity research. The microgravity environment has allowed the study of textbook fluids problems without the complication of buoyancy-induced convection advancing areas of technological and ecological importance such as global atmospheric change, groundwater pollution, oil production, and advanced materials manufacturing that often rely on advances in fluid physics.

This presentation will discuss the recent advances resulting from NASA's Fluid Physics discipline. The discussion will include recent experiments flown on the International Space Station (ISS) as well as a preview of a number of experiments planned on the ISS. The presentation is divided into two-phase systems with and without heat transfer. The experiments without heat transfer include capillary flows, gas-liquid separation, and gas-liquid flow through porous media. The experiments with heat transfer include wickless heat pipes, pool and flow boiling, condensation, and temperature and pressure control for cryogenic systems.

Recent advances have been made in two-phase systems without heat transfer and there are a number of new experiments planned for the ISS in the next decade. Reviews of the following ISS experiments will be presented:

The Capillary Flow Experiment (CFE) includes a suite of fluid test vessels to investigate capillary flows in low gravity. The first series of experiments (CFE-1) was completed in 2007 and included experiments in interior corner flows, vane gaps, and contact lines. The second series (CFE-2) continues through this year extending the vessels to more complex containers. [1], [2], [3] In addition, NASA has collaborated with DLR and ZARM on the Capillary Channel Flow (CCF) experiment.

In 2015, the Packed Bed Reactor Experiment (PBRE) will launch the first ISS experiment to study two-phase flow through porous media. Aircraft studies have already demonstrated that steady state pulse flow occurs at much lower flow rates than seen on earth. A flow regime map for bubble to pulse flow has been developed as well as a new pressure drop model. The PBRE will validate the pressure drop model at lower flow rates that take several minutes to develop but represent realistic flows seen in reactor bed systems. In addition, the PBRE will examine startup and transient flows as well as viscous fingering of the gas phase into a continuous liquid phase. [4]

Two types of cyclonic passive two-phase separators will be demonstrated in 2019 as part of the Two-phase Flow Separator Experiment (TPFSE). One concept will characterize an annular injection of the two-phase stream and the other will characterize a conical injection as shown in figure 1. The goal will be to establish the range of flow rates for acceptable performance along with the effect of fluid properties and separator geometry. Start up and shutdown cases will also be evaluated. [5]

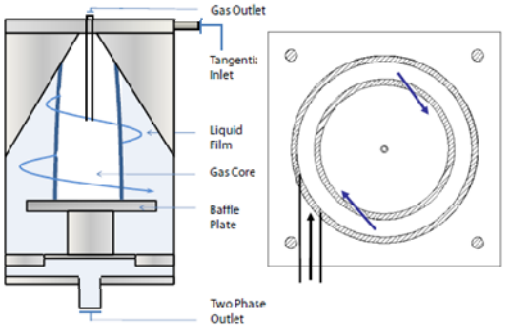

Figure 1: Concepts for cyclonic separators for TPFSE.

Research in multiphase flows with heat transfer in low gravity is critical to thermal control systems, cryogenic storage, and life support systems. Summaries of the following ISS experiments will be reviewed:

The Constrained Vapor Bubble (CVB) experiment which flew successfully in 2010 established the prototype for a miniature wickless heat pipe using a rectangular-shaped quartz glass tube filled with pentane. CVB studied the fundamental physics and interfacial phenomena underlying the heat pipe operation and performance. This research will also help improve the design of terrestrial heat pipes for use in laptops, servers, and high-power LED luminaires. CVB-2 recently concluded a series of tests to extend the studies to a pentane/iso-hexane mixture. [6], [7]

The Boiling Experiment Facility (BXF) recently flew on the ISS in 2010 to accommodate two investigations, the Microheater Array Boiling Experiment (MABE) and the Nucleate Pool Boiling Experiment (NPBX). Both examined fundamental boiling phenomena in microgravity. MABE focused on determining the local boiling heat transfer mechanisms in microgravity for nucleate and transition boiling by using a microheater array with all heaters operated at a constant temperature while carefully monitoring the power into each microheater.[8] NPBX selectively activated nucleation sites in order to understand bubble growth, detachment, and the subsequent motion of

single and merged bubbles. [9]

The next logical step in developing an understanding of boiling heat transfer will be the Flow Boiling and Condensation Experiment (FBCE) scheduled to fly in 2017. This experiment will develop an integrated two-phase flow boiling/condensation facility for the ISS to serve as a platform for obtaining two-phase flow and heat transfer data in microgravity. The FBCE will provide detailed and comprehensive measurements on flow regime, pressure gradients, heat transfer coefficients, critical heat flux, and vapor volume fraction under microgravity conditions.

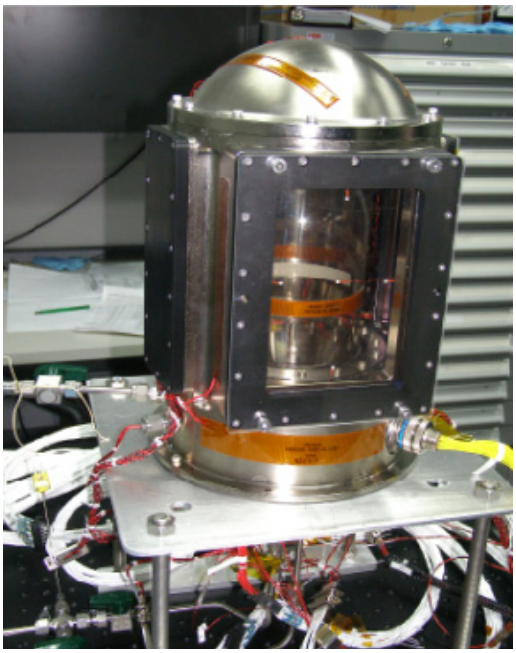

Figure 2: Zero-Boil-Off Tank Experiment (ZBOT)

The ability to store and transfer cryogenic liquids efficiently and economically over long periods of time in space is a critical technology for nearly all future human missions beyond low earth orbit. The Zero-Boil-Off Tank (ZBOT) experiments planned in 2015 and 2019 will investigate the complex interaction of two-phase transport mechanisms and the phase change phenomena that control propellant storage tank pressurization and its active pressure control in microgravity. The experiments will be based on high-fidelity measurements using a transparent simulant volatile fluid in a small scale transparent Dewar (figure 2) with very precise boundary condition control. [10], [11]

The goal of the NASA GRC Fluids Physics discipline is to gain a deeper fundamental knowledge of various aspects of fluid phenomena which will permit the design and development of systems which enable safe, long-term manned exploration of space and planetary environments as well as to enhance our ability to impact Earth-based industrial, environmental and health-related issues through the isolation and study of phenomena in the weightless environment of space. The fluids experiments discussed here are designed to provide the underpinning for thermal management, propellant storage, life support systems, energy transport and power generation.

References

[1] Chen, Y., Tavan, N., Weislogel, M.M., A mean curvature model for compound capillary flows in asymmetric containers and conduits, Physics of Fluids, Vol. 24, 082111, pp. 1-16 (2012).

[2] Weislogel, M.M. Compound Capillary Rise, J. Fluid Mech., Vol. 709, pp. 622-647, (2012).

[3] Weislogel, M. M., J. A. Baker, R. M. Jenson, “Quasi-steady capillary-driven flows in slender containers with interior edges,” J. Fluid Mechanics, vol. 685, pp. 271-305, 2011.

[4] Motil, B. J., Balakotaiah, V., and Kamotani, Y., “Gas-Liquid Two-Phase Flows Through Packed Beds in Microgravity,” AIChE J., vol 49, no. 3, pp. 557-565 (2003).

[5] Hoyt, N.; Kang, M.F.; Kharraz, A.; Kadambi, J.; Kamotani, Y., "Cyclonic two-phase flow separator experimentation and simulation for use in a microgravity environment", J. of Physics: Conference Series, Volume 327, Number 1, 2011 , pp. 12056-12069(14)

[6] Chatterjee, Arya, Joel L. Plawsky and Peter C. Wayner, Jr., David F Chao, Ronald J Sicker, Tibor Lorik, Louis Chestney, John Eustace, Raymond Margie, John Zoldak “The Constrained Vapor Bubble Experiment Fin Heat Pipe in Microgravity,” Industrial & Engineering Chemistry Research, February 25, 2011.

[7] Joel L. Plawsky, Peter C. Wayner Jr., " Explosive nucleation in microgravity: The Constrained Vapor Bubble experiment," Int. J. Heat and Mass Transfer, 55, 6473–6484 (2012).

[8] Raj, R., Kim, J., and McQuillen, J., “Pool Boiling Heat Transfer on the International Space Station: Experimental Results and Model,” Journal of Heat Transfer, Vol. 134, No. 10, 101504 (October 2012).

[9] Dhir, V. K., et al. (2012). “Nucleate Pool Boiling Experiments (NPBX) on the International Space Station.” J. Heat Transfer, 2012.

[10] Panzarella, C. H., Kassemi, M., “One-dimensional model of evaporation and condensation in the presence of a noncondensable gas with applications to cryogenic fluid storage”, International J. of Heat and Mass Transfer, vol. 52, no 15, pp. 3767-3777, 2009.

[11] Panzarella, C. H., Kassemi, M., “On the validity of purely thermodynamic descriptions of two-phase cryogenic fluid storage,’ J. Fluid Mechanics, vol. 484, pp. 41-68, 2003.

Physical Science Informatics: Providing Open Source Access to Microheater Array Boiling Experiment Data

John McQuillen[1*], Robert D. Green[1], Ben Henrie[2], Teresa Miller[2], Francis Chiaramonte[3]

[1]NASA Glenn Research Center
21000 Brookpark Road, Cleveland, OH 44135 USA

[2]NASA Marshall Space Flight Center
Huntsville, AL 44135 USA

[3]NASA Headquarters
Washington DC 20546-0001

*Corresponding Author's email address: John.B.McQuillen@nasa.gov

The President of the United States has directed government agencies to make more data and information freely available on-line for researchers and the general public[1,2]. NASA is pursuing development of an open source informatics system for the physical science flight experiments to allow full access to the trove of data collected over the life of ISS, along with the on-going , open source experiments.

Previously, a team at MSFC has developed series of informatics systems for several other applications, beginning with the Materials and Processes Technical Information System (MAPTIS), an informatics systems that provided detailed properties on a large database of materials used for spacecraft systems. This informatics system is being developed within the Athena platform, a software environment developed in-house by the EM60 Informatics team to incorporate large databases of science data and allows access in an open, organized manner.

The Physical Science Informatics (PSI) system is the next step in this an effort to make NASA sponsored flight data available to the scientific and engineering community, along with the general public. The experimental data, from six overall disciplines, Combustion Science, Fluid Physics, Complex Fluids, Fundamental Physics, and Materials Science, will present some unique challenges. Besides data in textual or numerical format, large portions of both the raw and analyzed data for many of these experiments are digital images and video, requiring large data storage requirements. In addition, the accessible data will include experiment design and engineering data (including applicable drawings), any analytical or numerical models, publications, reports, and patents, and any commercial products developed as a result of the research.

One of the first experiments to be included within this database will be the Microheater Array Boiling Experiment (MABE). MABE and the Nucleate Pool Boiling Experiment (NBPX) were two separate investigations that were conducted within the Boiling Experiment Facility (BXF)[3]. BXF conducted operations within the the Microgravity Science Glovebox (MSG) located in the U.S. Laboratory on the International Space Station (ISS) from March until May 2011.

The BXF uses normal-perfluorohexane as the test fluid and will operate between pressures of 60 to 244 kPa and temperatures of 35 to 60 °C.

The BXF consisted of a boiling chamber mounted within a containment vessel. The boiling chamber has three science heaters (one for NPBX and two heater arrays for MABE), pressure and temperature measurement instrumentation, a bellows assembly for pressure control, and pumps for liquid conditioning. The containment vessel provides the second and third levels of containment for the test fluid in the event of a leak from the boiling chamber of the test fluid. Standard rate video cameras are mounted inside the chamber to provide two orthogonal side-view images of the vapor bubble during tests with the NPBX heater and a single side view of the vapor bubble during MABE testing. The high-speed video camera is mounted on the exterior of the containment vessel wall and acquires 4 seconds of images through the bottom of the MABE heater at 500 images per second.

An avionics box contains the data acquisition and control unit, removable hard drives, indicator panel, and the control unit for the high-speed video camera. The avionics box interfaces with the MSG mobile launch computer, the high-speed video camera, and the BXF-embedded controller boards within the containment vessel.

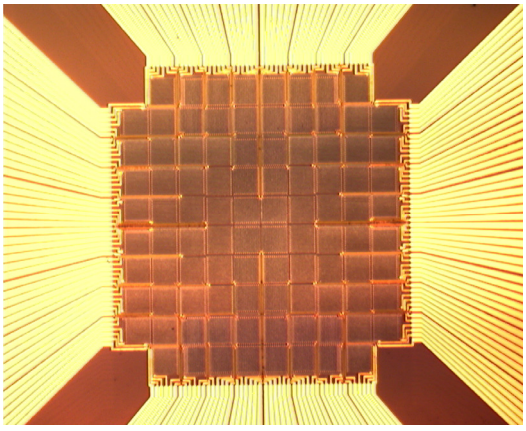

Figure 1: Microscopic image of 2.7 mm x 2.7 mm microheater array.

The objective of MABE was to determine the boiling heat transfer mechanisms in microgravity and correlate local heat transfer coefficients versus the vapor and liquid positions for nucleate and transition boiling regimes and at critical heat

flux conditions. While most boiling studies have focused on providing a constant power or heat flux at the heater surface, MABE uses a constant temperature approach for controlling heater power.

There are several advantages with this approach:

• The risk of heater burnout is minimized, especially at critical heat flux and heater dryout conditions. As vapor engulfs the heater surface, less power is required to maintain the heater temperature. As cold liquid contacts the heater surface, more power is required. Burnout occurs when the heater surface is dry and its temperature becomes elevated.

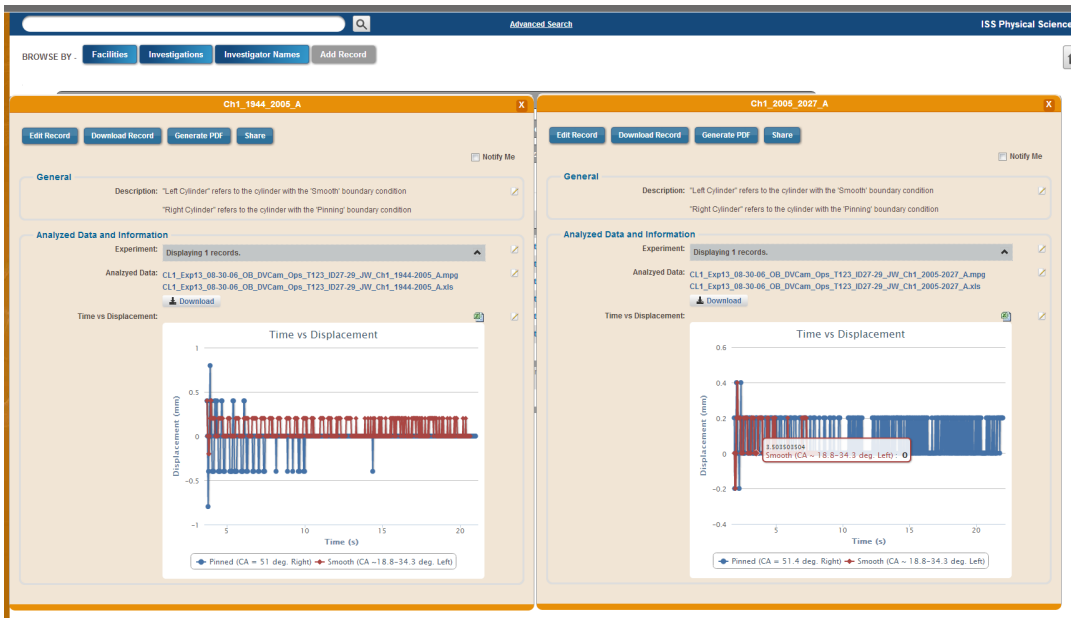

Figure 2: Sample data record within PSI Database

• Lateral substrate conduction is minimized. Since adjacent microheaters are maintained at or nearly at the same temperature, there is very little thermal conduction among microheaters. Only the outer rows of active microheaters conduct significant amounts of heat laterally outward on the quartz substrate. These microheaters actually serve as "guard heaters."

As such, these local surface heat flux and temperature measurements are provided by an array of ninety-six platinum resistance heaters deposited on a quartz wafer. Two of these arrays are used in the BXF: An array of 2.7 mm x 2.7 mm (Figure 1) and an array of 7.0 mm x 7.0 mm.

Operations for the two experiments supported by BXF, Microheater Array Boiling Experiment (MABE) and Nucleate Pool Boiling Experiment (NPBX), were planned to be interspersed during a nine week period of 24 hour days three to four days a week.

During MABE science operations, anomalous pressure readings tripped the BXF safety circuit, halting operations. Attempts to restart/reset/recycle BXF did not correct these readings and BXF was shut down. By this point MABE completed 260 of 540 tests, all using the 7.0 x 7.0 mm array. Subsequent retrieval and investigation revealed that one of the bulk fluid heaters that were used to condition the fluid to an appropriate temperature had shorted[4]. Due to the design of the electrical system, only tests for NPBX were able to be conducted but at temperatures well below normal perfluorohexane's normal boiling point of 56°C. While there has been publication of the scientific results[5], there remains an enormous amount of data that still can be analyzed.

This objective of paper includes the following:

- present the preliminary layout (Figure 2) of MABE data within the PSI database.
- Obtain feedback on the layout.
- Present the procedure to obtain access to this database.

References

[1] Burwell, S. M., VanRoekel, S., Park, T. and Mancini, D. J. "Open Data Policy – Managing Information as an Asset," OMB Memorandum M-13-13, May 9, 2013.

[2]J. Holdron, "Increasing Access to the Results of Federally Funded Scientific Research", Office of Science and Technology Policy (OSTP) memorandum, Feb. 22, 2013. http://www.whitehouse.gov/sites/default/files/microsites/ostp/ostp_public_access_memo_2013.pdf

[3] R. DeLombard, R., McQuillen, J. and Chao, D., "Boiling Experiment Facility for Heat Transfer Studies in Microgravity," *AIAA-2008-814,* 2008.

[4] Booth, W. H., "Boiling Experiment Facility (BXF): Post Flight Assessment Anomaly Investigation Report," NASA/CR-2012-216036, 2012.

[5] Raj, R., Kim, J., and John McQuillen, "Pool Boiling Heat Transfer on the International Space Station: Experimental Results and Model," Journal of Heat Transfer, Vol. 134, (2012).

Ninth International Conference on
TWO-PHASE SYSTEMS FOR GROUND AND SPACE APPLICATIONS
Baltimore, Maryland, USA, September 22-26, 2014

Pressurization & Pressure Control in The Zero Boil-Off Tank (ZBOT) Experiment

Mohammad Kassemi*, Sonya Hylton, and Olga Kartuzova

National Center for Space Exploration Research (NCSER)
NASA Glenn Research Center
21000 Brookpark Rd, MS110-3
Cleveland Ohio 44135
*Mohammad.Kassemi@nasa.gov

Integral to all phases of NASA's projected space and planetary expeditions is *affordable* and *reliable* cryogenic fluid storage for use in propellant or life support systems. Without safe, efficient, and flexible cryogen storage, economically justified human missions may not be possible. Cryogen vaporization caused by various heat leaks into the tank from its surroundings is the main cause of storage tank self-pressurization. This has led to the development of innovative pressure control designs based on mixing of the bulk liquid with or without active cooling. Unfortunately, both tank pressurization and pressure control are governed by intricate and complicated dynamic interactions among the forced mixing, the various gravity dependent transport mechanisms in the vapor and liquid phases, and the condensation/evaporation process at the interface. Consequently, effective implementation and optimization of a dynamic pressure control system for space applications cannot be accomplished solely by empiricism, especially, since there is a serious scarcity of relevant microgravity data.

The Zero-Boil-Off Tank (ZBOT) Experiment is a small scale tank pressurization and pressure control experiment that uses a transparent vent-less Dewar and a transparent simulant phase change fluid. It is scheduled for flight aboard the International Space Station (ISS) in the April 2015 timeframe. In this paper, we will present the results of ZBOT's ground based research that includes measurement of both pressurization and pressure reduction trends in the Zero-Boil-Off Dewar. Tank pressurization is accomplished through heating of the test cell wall in the wetted and un-wetted regions simultaneously or separately and investigating the effect of wall heat flux (power and distribution) and tank fill level. Pressure control is established through mixing and cooling of the bulk liquid using a temperature controlled sub-cooled jet flow. Here, the effect of jet temperature, flow rate and fill level are studied.

In order to delineate the intricate transport and phase change phenomena underlying tank pressurization and pressure control, we have also developed two classes of two-phase CFD models. The first model assumes a stationary sharp interface between the ullage and the liquid and solves the momentum and energy equations in both phases. The species equation is also solved in the ullage region to account for the transport of residual noncondensables gas that coexists in the vapor region. The interfacial energy and force balances and the Stefan wind relationship for evaporation/condensation process are rigorously formulated and applied at the sharp interface boundary. The kinetically based Schrage equation is used to compute the evaporating/condensing mass flux at the interface and the dependence of surface tension on temperature is also included to account for Marangoni convection for those situations that the interfacial temperature varies spatially with the vapor partial pressure or when it departs from its saturation value. In the second model, the interface is allowed to move according to the forces imposed upon it. Here, a VOF scheme is used to capture the movement of the interface based on an evolution equation for the gas-liquid volume fraction Essentially, the same set of equations as in the previous model are solved in the two phases except for the fact that in the VOF implementation, the interfacial balances are satisfied on a volumetric basis using source terms in the interfacial region as marked/captured by the volume fraction. Again, the Schrage equation is used to evaluate the evaporation/condensation mass flux and the Brackbill continuum source force model is used to account for the surface tension forces driving the Marangoni convection.

Numerical prediction of both models are compared to the 1g ground-based experimental pressurization and pressure control results to validate the models and shed light on the intricate interactions between natural, Marangoni, and forced convection that takes place in the liquid and its effect on the thermal stratifications in the liquid, on the flow and thermal structures that evolve in the ullage, and on the mass transfer at the interface. Special attention is also focused on the effect of residual noncondensable in the ullage and its impact on the pressurization and pressure control process.

Comparison between the numerical predictions and the ground-based experimental results indicate that the in 1g the impact of residual noncondensible on both pressurization (during heating) and pressure reduction (during the jet mixing-cooling operation) is rather minimal. Nevertheless, it seems that the residual noncondensable has a considerable impact on the evolution of thermal and solutal, flow structures that develop in the ullage region.

Microgravity numerical simulation seem to indicate that although the impact of the noncondensable gas and Marangoni convection on the evolution of tank pressure during the heating (pressurization) interval is at best marginal, its effect on pressure reduction during the jet mixing cooling operation is quite prominent. Here, as shown in Fig.1, it is seen that the noncondensable gas can form an effective barrier in the ullage, decreasing the condensation mass transfer considerably and, thereby, reducing the rate of pressure reduction in the tank with a dangerous possibility of loss of tank pressure control. In addition, it is also numerically shown that in microgravity, the effect of Marangoni convection, in both presence and/or absence of noncondensable gas, on the thermal destratification of the liquid and on the rate of tank pressure reduction can be considerable. The need for microgravity data to check the validity of these predictions is emphasized.

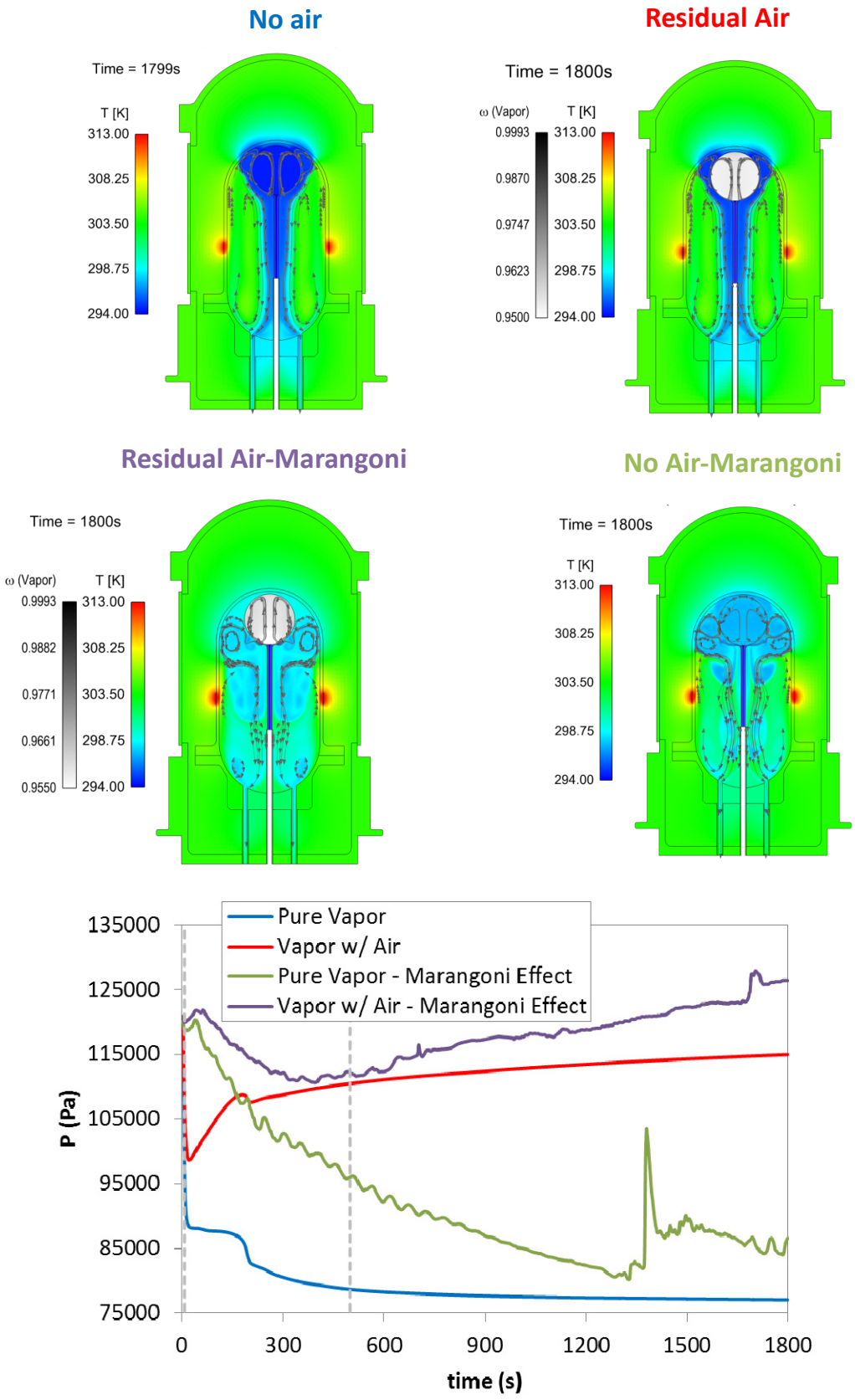

Figure 1: Numerical prediction of the effects of noncondensable gas and Marangoni convection on tank pressure reduction and thermal destratification during jet mixing-cooling pressure control operations in microgravity

The Static Bubble Point Pressure Model for Porous LAD Screens Operating in Cryogenic Propulsion Systems

Jason Hartwig, John McQuillen, and David Chato

NASA Glenn Research Center
Cleveland, OH, 44135
Jason.W.Hartwig@nasa.gov

In the low Bond number conditions of Low Earth Orbit (LEO), surface tension forces control the location of the liquid and vapor phases within a propellant tank. Any one of a number of propellant management devices (PMDs) may be required to ensure that the tank outlet is sufficiently covered with liquid during all phases of a mission. One such PMD, a porous screen channel liquid acquisition device (LAD), relies on surface tension forces to maintain communication between liquid and tank outlet by admitting liquid into the channel, separating and controlling phases through the use of micron sized pores within the fine mesh screen, and to also wick liquid to areas of the screen that dry out due to evaporation. As shown in Figure 1a, LAD channels are composed of three solid walls and one porous wall, with the porous side facing the tank walls where liquid tends to reside in microgravity. The channels connect to a common manifold over the tank outlet. The specific weave pattern, number of wires per area, and metal characterize the screen. Figure 1b shows a popular Dutch Twill mesh where each smaller shute wire passes over two larger warp wires before going over the next warp wire. Fine meshes create small pores which counter the ultra-low surface tension of cryogenic propellants to block vapor ingestion, but finer screens yield higher flow losses and may become clogged easier. Screen channel LADs have flight heritage in storable propulsion systems like the Agena Upper Stage[1], Apollo Reaction Control System (RCS)[2], and most notably the Shuttle RCS[3,4] and Orbital Maneuvering System, but have no flight heritage in cryogenic propulsion systems.

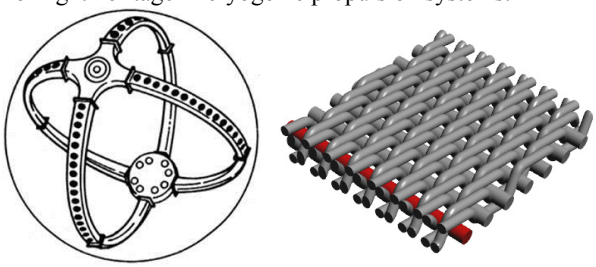

Figure 1: a) Total communication screen channel LAD mounted inside a propellant tank b) Dutch Twill LAD screen

The primary performance parameter characterizing LAD performance is the maximum bubble point pressure based on Adamson and Gast[5], or point at which pressurant gas overcomes liquid surface tension forces within the screen pore and vapor is admitted into the channel. The bubble point sets the upper limit on either the highest adverse acceleration level against which liquid must be delivered into the channel or the maximum allowable flow rate through the channel. A simplified room temperature bubble point model was developed from the Young-LaPlace equation for the pressure jump across a liquid/vapor interface for storable propellants[6]:

$$\Delta P_{BP} = \frac{4\gamma_{LV}\cos\theta_C}{D_P} \quad (1)$$

where γ_{LV} is the surface tension, θ_C is the contact angle between liquid and screen pore, and D_p is the effective pore diameter, which is determined through room temperature bubble point tests using a reference liquid with known surface tension and contact angle. The simplified model fails to match bubble point data taken in cryogenic liquids by failing to account for additional effects:

1. The temperature dependence of the screen pore diameter.
2. The effect of pressurant gas type.
3. The effect of subcooling the liquid.
4. The effect of elevating the temperature of the pressurant gas above the liquid temperature.

Therefore the purpose of this presentation is to update the room temperature bubble point model for cryogenic liquids by deriving and validating a model which accounts for the seven parameters that affect cryogenic bubble point pressure, including surface tension (liquid type), contact angle, screen mesh, liquid temperature, degree of subcooling, and pressurant gas type and temperature.

The empirical model presented here is based off 45 years of historical bubble point data as well as recent tests in cryogenic hydrogen, nitrogen, oxygen, and methane conducted over the past 5 years. In all, over 5000 bubble points taken in 20 different liquids using 26 different LAD mesh types are accounted for in the new model.

Liquid surface tension is modeled using a modification of the original two parameter fit from Ferguson and Kennedy to account for water, superfluid helium, and all other cryogenic liquids[7]:

$$\gamma_{LV} = \gamma_0\left(1-\frac{T}{T_C}\right)^{a_0+a_1\frac{T}{T_C}+a_2\frac{T^2}{T_C}} \quad (2)$$

where γ_0, a_0, a_1, a_2 are parameters fit to the data, T_C is the critical temperature, and T is the temperature of the liquid at the screen. Meanwhile, contact angle is zero for all cryogenic liquids in contact with the stainless steel LAD screen because the surface tension for all cryogenic liquids is less than the measured critical Zisman value of $\gamma_{CZ} = 23.2 \pm 2\ mN/m$[8].

Equation 1 can be used to solve for effective pore diameter at any temperature with a liquid with known surface tension and contact angle. Figure 2 plots the effective pore diameter as a function of liquid temperature for a 450x2750 screen for cryogenic liquid in a normally saturated state. As shown, for gaseous helium (GHe) pressurization, effective pore diameter decreases as

temperature decreases due to metal pore shrinkage and gain in bubble point due to evaporation at the interface. Meanwhile, effective pore diameter is approximately constant for autogenous pressurization with the liquid's own vapor due to gain in bubble point due to screen pore shrinkage and loss in bubble point due to condensation at the screen. The following function can be fit to each screen and pressurant gas type to determine the temperature dependent effective pore diameter:

$$D_P(T) = D_{P,295K}\left(1 + b_0 \xi(T)\right) \quad (3)$$

where $D_{P,295K}$ is the room temperature pore, b_0 is a fitting parameter and $\xi(T)$ is the volumetric coefficient of thermal contraction.

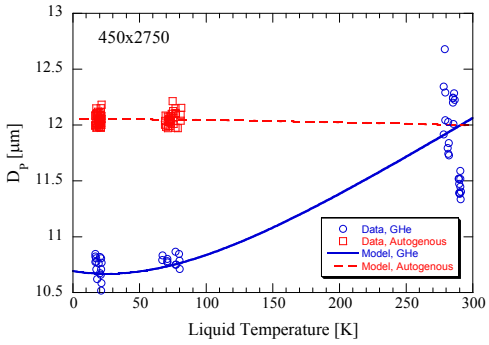

Figure 2: Temperature dependent screen pore diameter

Finer mesh screens at colder liquid temperatures always yield higher bubble points due to reduced effective pore diameter. Decreasing the temperature of the liquid always increases bubble point pressure due to increased surface tension. Additional gain or loss from room temperature is dependent on the type of pressurant gas in contact with the screen.

Figure 3 plots 325x2300 LN_2 data using helium pressurant as a function of the temperature and pressure of the liquid at the LAD screen. As shown, pressurizing and subcooling the interface adds margin in bubble point proportional to the distance away from the black saturation line. The rate of gain in bubble point is dependent on the pressurant gas in contact with the screen. Higher bubbles points are obtained when pressurizing and subcooling the liquid with the noncondensible gas, due to enhanced evaporation, and thus more interfacial cooling at the screen.

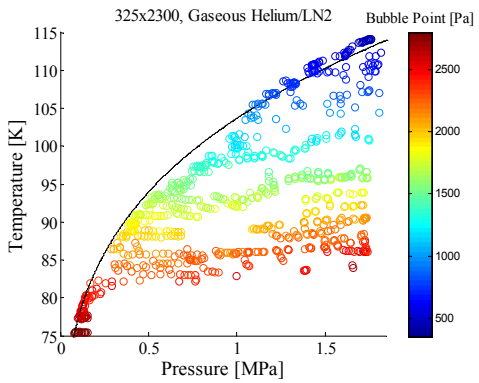

Figure 3: 325x2300 Subcooled Bubble Point Data

Figure 4 plots the ratio of LH_2 heated pressurant gas bubble point data divided by the bubble point when the gas and liquid temepratures are equal as a function of the temperature difference between liquid and gas for three LAD screens. As shown, elevating the temperature of the pressurant gas always acts as a degradation factor on the static bubble point. Higher degradation occurs when pressurizing with condensable vapor using coarser meshes.

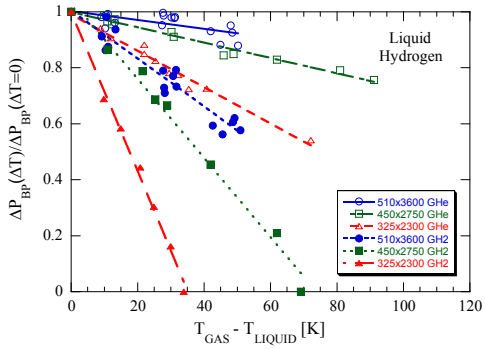

Figure 4: Heated Pressurant Gas LH_2 Bubble Point Data

The final bubble point equation takes the following form:

$$\Delta P_{BP} = \frac{4\gamma_{LV}\cos\theta_C}{D_P(T)}\left(1 + n_{Sub}\left(\frac{P - P_{Sat}}{P_{critical}} + \frac{T_{Sat} - T}{T_{critical}}\right)\right)\left(1 - n_{Hot}(T_{Gas} - T)\right) \quad (4)$$

where n_{Sub} and n_{Hot} are parameters fit to subcooled and heated pressurant gas data, respectively. The new model is shown to be accurate to within 3% of the experimental data where data is available for fluids that exist as liquids below room temperature.

References

[1] DiFrancesco, A., and Boorady, F. "The Agena Rocket Engine Story" *AIAA 89-2390*, 25th Joint Propulsion Conference, Monterey, CA, July 10-12, 1989.

[2] De Brock, S.C., Grove, R.K., Sloma, R.O., Balzer, D.L., Brill, Y., and Yankura, G.A. "A Survey of Current Developments in Surface Tension Devices for Propellant Acquisition" *Journal of Spacecraft*, 8: 83 – 98. 1971.

[3] Fester, D.A., Eberhardt, R.N., and Tegart, J.R. "Space Shuttle Reaction Control Subsystem Propellant Acquisition" *AIAA-74-1106*, 10th AIAA/SAE Joint Propulsion Conference, San Diego, CA, October 21 – 23, 1974.

[4] Anglim, D.D. "Low-g Testing of the Space Shuttle OMS Propellant Tank" *AIAA-79-1258* 15th Joint Propulsion Conference, Las Vegas, NV, June 18 – 20, 1979.

[5] Adamson, A.W. and Gast, A.P. "Physical Chemistry of Surfaces" New York: John Wiley and Sons, Inc. 1997.

[6] Hartwig, J.W. and Mann, J.A. A Predictive Bubble Point Pressure Model for Porous Liquid Acquisition Device Screens. *Journal of Porous Media* (accepted for publication). Vol. 7, No. 2, February, 2014.

[7] Ferguson, M.A. and Kennedy, S.J. Free and Total Surface Energies and Related Quantities. *Transactions of the Faraday Society*. 1936; 32: 1474.

[8] Hartwig, J.W. and Mann, J.A. "Liquid Transport in Microgravity II: Bubble Point Pressures of Binary Methanol/Water Mixtures in Fine-Mesh Screens" *AIChE Journal* 60, 730 – 739. 2014.

Thermocapillary instability of a thin film falling down a thick and deformed cooled wall

Luis Antonio Dávalos-Orozco

Instituto de Investigaciones en Materiales, Departamento de Polímeros
Circuito Exterior S/N, Ciudad Universitaria, Delegacion Coyoacán, 04510 México D. F. México
e-amil: ldavalos@unam.mx

The problem of thin films falling down walls has been investigated since many years ago and has been reviewed in a number of papers for different applications, as by Fulford [1] for chemical engineering and Ruschak [2] and Weinstein and Ruschak [3] for coating. Other surveys have been published for the isothermal problem Chang [4] and the non-isothermal case Oron et al. [5]. Craster and Matar [6] review the problem of dewetting with the action of heat and surfactants. Kabov [7] presents the problem of the non-uniform heating of films in practical applications. A complete and very recent review of isothermal and non isothermal phenomena in thin films is presented in Dávalos-Orozco [8].

When the heating of the film is from below it is usual to assume that the wall is a very good conductor. This assumption neglects extra parameters from the problem which add to the number of parameters that already complicate the theoretical understanding of the phenomena. It is clear that the effective conductivity depends on the physical properties and geometry of the bounding wall. The thickness of the wall has been taken into account by Oron et al. [9] who use it to eliminate some singularities in the calculation of thermal evaporative instabilities. Also, Kabova et. al. [10] used the thickness of the wall in a thermocapillary problem in order to compare with experiments when the wall is deformed in the side of the fluid. Besides, Gambaryan-Roisman [11] includes the thickness of the wall in order to understand the thin film behavior when the thermal conductivity is non-uniform. Gambaryan-Roisman and Stephan [12] include the thickness of the wall but their main interest is to investigate a rivulet flow subjected to wall deformation. Recently, the effect of the thickness and thermal conductivity of the wall on the thin film flow stability has been investigated systematically by Dávalos-Orozco [13].

The effect of wall deformation on the stability has been investigated for the isothermal case by Dávalos-Orozco [14,15] and for a viscoelastic fluid by Dávalos-Orozco [16] in the lubrication approximation. It is found that a resonant effect of the free surface response to the wall deformation stabilizes the flow in space and time (see Ref. [8]).

Here, the effect of the heat conductivity and variation of the thickness of the wall on the thin film instability is investigated. The wall deformation is sinusoidal in the side of the fluid film and it is flat in the other side, where it may be heated or cooled. Due to the thickness variation of the wall the film is heated or cooled non uniformly (see Ref. [8]). It is well known that when a thin film is falling down a wall heated from below, the free surface perturbations destabilize for certain magnitude of the parameters and when it is cooled from below those perturbations stabilize.

In the case of a film falling down an isothermal sinusoidal deformed wall [14,15] two kinds of perturbations exist: spatial and temporal. As explained above, the spatial instability occurs as a response of the free surface to the wall deformations. The temporal instability is due to the time dependent perturbations imposed at the origin.

Here, it is shown that when cooling from below the thick and sinusoidally deformed wall, the time dependent perturbations in fact stabilize in space and time. However, the spatial response to the wall deformation of the free surface destabilizes (the amplitude increases) when cooling from below for some values of the wall parameters. Moreover, it is shown that the stabilizing effect of spatial resonance [14,15] is still present and that it works even more effectively to stabilize the time dependent perturbations in comparison to the negative Marangoni numbers used in this investigation.

Physically, the film is cooled and the time dependent perturbations are stabilized in space and time. However, the response of the free surface is different above the thicker part of the wall than above the thinnest one. In the thicker part the effective thermal conductivity of the wall is smaller than in the thinner part [13]. Therefore, in the thinnest part the effect of the negative Marangoni number is more important than in other places. This produces a depression of the free surface near the thinnest region. As a consequence, the free surface response shows a growth in amplitude. The growth increases with an increase of the magnitude of the negative Marangoni number. The wall variations in space appear in the denominator of the thermocapillary term of the evolution equation of the Benney type. It is operated by space derivatives which make it to appear in the numerator of a nonlinear term. This affects in an important way the nonlinear response of the free surface.

Two related examples are presented in Figs. 1 and 2. Notice that β is the angle of inclination of the wall, Pr is the Prandtl number, Bi is the Biot number, Q_C is the ratio of the wall over the fluid thermal conductivities, d is the ratio of wall over the fluid thicknesses. The time dependent perturbations are applied at x = 0 with a frequency ω, Reynolds number R and a running time T. The parameter L is ratio of the wavelength of the wall over that of the time dependent perturbations. Ma is the Marangoni number.

As can be seen in both examples the amplitude of the response is larger when Ma is more negative. This effect is enhanced when the free surface is in spatial resonance [14,15] at L = 5 (see the different scales of the vertical axes). Notice that spatial resonance works more effectively to stabilize the free surface perturbations than the negative Ma. The pure response of the free surface is clearly seen to the left of x = 0, the origin of the x-axis.

Conclusions

Here it is shown that taking into account the thickness (geometry) and thermal conductivity of the wall new

phenomena appears when cooling the liquid film flowing down the wall. Two examples are given which show the stabilizing effect of Ma < 0 on the time dependent perturbations. However, it is also shown that the free surface response increases in amplitude when the magnitude of the negative Marangoni number increases. It is important to point out that the amplitude of the response is larger than that of the isothermal problem [14]. These are general results under the wall conditions assumed here, as shown by numerical calculations.

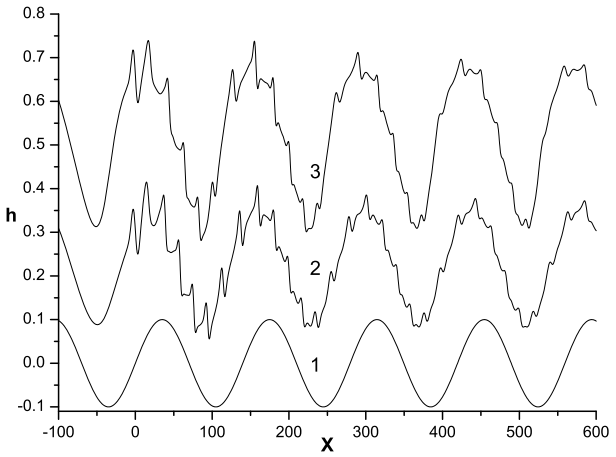

Fig. 1 β=90º, Pr = 7, Bi = 0.1, Q_C = 0.01, d = .11. Perturbations at x = 0 with ω = 0.5, R = 1.391, time T = 1000, and L = 8. 1) Wall deformation, flat at d = -0.11, 2) Ma = - 10, 3) Ma = - 50.

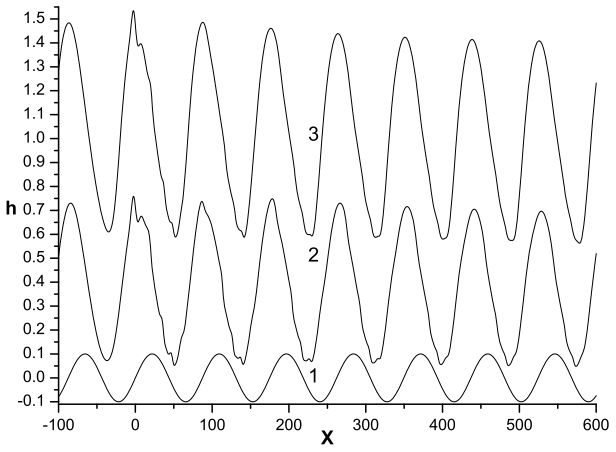

Fig. 2 β=90º, Pr = 7, Bi = 0.1, Q_C = 0.01, d = .11. Perturbations at x = 0 with ω = 0.5, R = 1.391, time T = 1000, and L = 5. 1) Wall deformation, flat at d = -0.11, 2) Ma = - 10, 3) Ma = - 50.

References

[1] Fulford, D. E., The flow of liquids in thin films, *Adv. Chem. Eng.*, **5**, 151 - 236 (1964).

[2] Ruschak, K. J., Coating flows, *Ann. Rev. Fluid Mech.,* **17**, 65 - 89 (1985).

[3] Weinstein, S. J. and Ruschak, K. J., Coating flows, *Ann. Rev. Fluid Mech.,* **36**, 29 - 53 (2004).

[4] Chang, H. C., Wave evolution on a falling film, *Ann. Rev. Fluid Mech.,* **26**, 103 - 136 (1994).

[5] Oron, A., Davis, S. H. and Bankoff, S. G., Long-scale evolution of thin liquid films, *Rev. Mod. Phys.*, **69**, 931 - 980 (1997).

[6] Craster, R. V. and Matar, O. K., Dynamics and stability of thin films, *Rev. Mod. Phys.*, **81**, 1131 – 1198 (2009).

[7] Kabov, O. A., Interfacial thermal fluid phenomena in thin liquid films, *Int. J. Emerging Multidisc. Fluid Sci.*, **2**, 87 – 121 (2010).

[8] Dávalos-Orozco, L. A., Stability of thin liquid films falling down isothermal and nonisothermal walls, *Interfacial Phenomena and Heat Transfer*, **1**, 93 – 138 (2013).

[9] Oron, A., Bankoff, S. G. and Davis, S. H., Thermal singularities in film rupture, *Phys. Fluids*, **8**, 3433 – 3435 (1996).

[10] Kabova, Yu. O., Alexeev, A., Gambarian-Roisman, T. and Stephan, P.,, Marangoni-induced deformation and rupture of a liquid film on a heated microstructured wall, *Phys. Fluids*, **18**, 012104 (2006).

[11] Gambaryan-Roisman, T., Marangoni convection, evaporation and interface deformation in liquid films on heated substrates with non-uniform thermal conductivity, *Int. J. Heat Mass Transfer*, **53**, 390 – 402 (2010).

[12] Gambaryan-Roisman, T. and P. Stephan, P., Flow and stability of rivulets on heated surfaces with topography, *J. Heat Transfer*, **131**, 033101 (2009).

[13] Dávalos-Orozco, L. A., The effect of the thermal conductivity and thickness of the wall on the nonlinear instability of a thin film flowing down an incline, *Int. J. Non-Linear Mech.*, **47**, 1 – 7 (2012).

[14] Dávalos-Orozco, L. A., Nonlinear instability of a thin film flowing down a smoothly deformed surface, *Phys. Fluids*, **19**, 074103, 1 - 8 (2007).

[15] Dávalos-Orozco, L. A., Instabilities of thin films flowing down flat and smoothly deformed walls, *Microgravity Sci. Technol.*, **20**, 225 – 229 (2008).

[16] Dávalos-Orozco, L. A., Stability of thin viscoelastic films falling down wavy walls, *Interfacial Phenomena and Heat Transfer*, **1**, 301 – 315 (2013).

Three dimensional direct numerical simulations of non-isothermal pools and sessile droplets with phase change: hydrothermal waves and convective rolls

P. Sáenz*, P. Valluri*, O. K. Matar‡, K. Sefiane*, and G. Karapetsas†

* School of Engineering, The University of Edinburgh, The Kings Buildings, Edinburgh EH9 3JL, United Kingdom
‡ Department of Chemical Engineering, Imperial College London, South Kensington, London SW7 2AZ, United Kingdom
† Department of Mechanical Engineering, University of Thessaly, Volos GR-38334, Greece
Prashant.Valluri@ed.ac.uk

Thermocapillary instabilities in Marangoni-driven flows is a fundamental phenomenon encountered in a vast variety of situations, ranging from the biomedical or the industrial to the geophysical or the domestic. The intriguing behaviour exhibited by these travelling perturbations has received considerable attention in the literature (Davis [1], Schatz & Neitzel [2]). Smith & Davis [3] first showed that the Marangoni flow in laterally-heated planar layers is naturally vulnerable to the formation of an oscillatory regime characterized by a myriad of thermal wave-like patterns propagating along the gas-liquid interface. i.e. hydrothermal waves (HTWs) (Fig. 1b). Using stability theory, these authors observed that, for sufficiently large horizontal temperature gradients, the preferred mode in the "return-flow" configuration is always a HTW propagating upstream at angles, $\pm\psi$, with respect to the axis opposite to the direction of the surface flow. The angle of propagation for oblique HTWs is solely a function of Prandtl number, *Pr*. To date, other than Sáenz et al. [8], investigations on HTWs have always ignored the effects of phase change. This is a simplification seldom encountered in experiments or real-life applications wherein liquid layers are frequently open to unsaturated atmospheres and, are therefore, subject to evaporation. Assumptions common to previous investigations addressing evaporation in other contexts have always included the use of the so-called "one-sided" or "1.5-sided" approaches. In these approaches, rather that attempting full DNS of both phases, the authors employ the arguments of negligible gas viscosity and/or thermal conductivity to decouple both phases and to justify concentrating in the liquid only.

The work presented here avoids these and similar simplifications by developing two-phase models grounded in general advection-diffusion transport equations and accounting for interfacial deformations. This distinctive capability permits us not only to capture advection-related phenomena in the gas (obviated in the past) but also to solve the interface energy, mass and momentum balances according to more realistic local conditions. To conclude, we present preliminary results of a similar investigation currently being performed on evaporating sessile drops on heated substrates.

1. Problem Statement and Mathematical Modelling

A sketch of the problem is provided in Fig. 1a. A rectangular pool of length $\hat{l}_x$, width $\hat{l}_y$ and height $\hat{l}_z$ is filled with a liquid layer of depth $\hat{d}$, bounded from above by an unsaturated gas. The carets identify dimensional quantities. The liquid is a pure substance while the gas is a

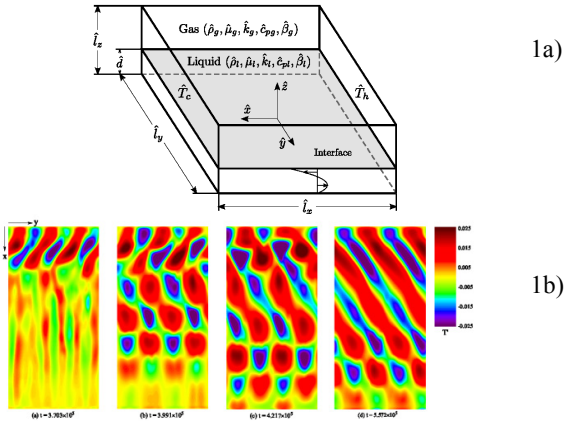

1a)

1b)

Figure 1: (a) Schematic of the planar layer; (b) Contour plots showing the spatio-temporal growth of the HTWs. Fully developed propagating towards the upper-right corner at $\psi = 55°$ with respect to the negative *x* axis. (reproduced from Sáenz et al. [7])

mixture of two component, inert gas and vapour, of variable composition. The density, dynamic viscosity, thermal conductivity, specific heat capacity and coefficient of thermal expansion are $\hat{\rho}_l$, $\hat{\mu}_l$, $\hat{k}_l$, $\hat{c}_{pl}$, $\hat{\beta}_l$ for the liquid and $\hat{\rho}_g$, $\hat{\mu}_g$, $\hat{k}_g$, $\hat{c}_{pg}$, $\hat{\beta}_g$ for the gas phase, respectively. The liquid-gas interface tension $\hat{\sigma}$ varies linearly with the temperature $\hat{T}$ as per $\hat{\sigma} = \hat{\sigma}_r - \hat{\gamma}(\hat{T} - \hat{T}_a)$, where $\hat{\gamma} = -\partial\hat{\sigma}/\partial\hat{T}$. The Marangoni effect induced by an externally – imposed thermal gradient in the *x* – direction, $(\hat{T}_h - \hat{T}_c)/\hat{l}_x$, gives rise to a capillary flow in the liquid equivalent to that referred to as *return-flow solution* in Smith and Davis [3]. The gas right next to the interface is assumed to be quasi-saturated, which is consistent with processes of relatively slow evaporation as the one under consideration. The Volume-of-Fluid (VOF) method [4] is used to compute the dynamics of the two-phase system under consideration. Regarding the interface as a deformable diffuse region of finite thickness, its spatio-temporal evolution is captured via the conservation equation,

$$\frac{\partial c}{\partial t} + \nabla \cdot (c\boldsymbol{u}) = -S \qquad (1)$$

where c is the liquid volume fraction acting as order parameter; t denotes the time, $\boldsymbol{u} = (u, v, w)$ is the velocity vector and $S = (1 - c)\rho_g[\omega_s - \omega]/t_s$ is the volumetric phase change rate accounting for the interface mass transfer ($S > 0$ corresponds to evaporation and $S < 0$ to condensation). The two-phase conservation of mass, momentum and energy is addressed with the one-fluid form of the continuity, Navier-Stokes and energy equations, respectively, i.e.,

$$\nabla \cdot \boldsymbol{u} = -S(1-\Omega_\rho) \quad (2)$$

$$\frac{\partial(\rho \boldsymbol{u})}{\partial t} + \nabla \cdot (\rho \boldsymbol{u}\boldsymbol{u}) = -\nabla p + \frac{1}{Re}\nabla \cdot [\mu(\nabla \boldsymbol{u} + \nabla \boldsymbol{u}^T)] + \boldsymbol{f}_\sigma + \boldsymbol{f}_g \quad (3)$$

$$\frac{\partial(\rho c_p T)}{\partial t} + \nabla \cdot (\rho c_p T \boldsymbol{u}) = \frac{1}{Re\, Pr}\nabla \cdot [k \nabla T] - \frac{1}{Ja} S \quad (4)$$

Here, p and T are the dimensionless pressure and temperature, respectively; Ω_ρ is the ratio of liquid to vapour density; ρ, μ, k and c_p are the one-fluid density, viscosity, thermal conductivity and specific heat capacity, respectively; $\boldsymbol{f}_\sigma = \left(\frac{\sigma \kappa \mathbf{n}}{\mathrm{We}} - \frac{\nabla_s \mathrm{T}}{\mathrm{Re}}\right)\delta$ accounts for the normal and tangential (Marangoni effect) stress additions due to surface tension; and $\boldsymbol{f}_g = -\rho\left(\frac{1}{Fr} - Bo_d \beta \frac{T}{Re}\right)\mathbf{e}_z$ incorporates the effects of gravity and buoyancy. The model is completed implementing a general advection-diffusion equation to solve the transient vapour distribution in the gas phase, i.e.,

$$\frac{\partial(\rho_g(1-c)\omega)}{\partial t} + \nabla \cdot (\rho_g(1-c)\omega \boldsymbol{u}) = \frac{1}{Re\, Sc}\nabla \cdot [\rho_g(1-c)\nabla \omega] + S \quad (5)$$

where ω represents the vapour mass fraction, and ρ_g is the gas-mixture density. The rectangular domain is bounded below by a adiabatic wall and in the x direction by vertical walls at fixed temperatures. These solid boundaries are all impermeable and the no-slip condition is applied for the momentum equation. Periodic boundary conditions are employed at the sidewalls. The upper surface is assumed to be a constant-pressure open boundary which allows flow into and/or out of the domain.

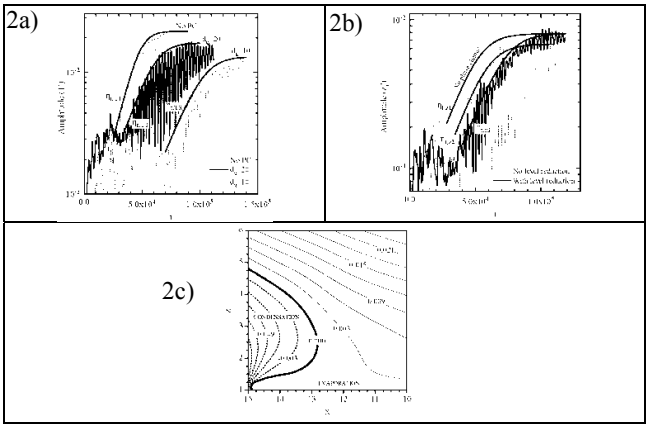

Figure 2: (a-b) Instantaneous FFT analysis showing effects of evaporation in the amplitude of the fundamental mode. (a) Stabilizing effect on the HTWs, (b) Destabilizing effect on the physical waves; (c) Self-inducing of condensation near the cold wall. (Sáenz et al. [8])

2. Results and Discussion

To ensure that the numerical model provides physically meaningful results, thorough validation work has been undertaken against the experiments by Riley and Neitzel [5] and Zhu and Liu [6] and against the theory by Smith & Davis [3]. Previously [7], we addressed the deformable-interface problem to investigate the linear and nonlinear spatio-temporal growth of the HTWs (Fig. 1b). This revealed previously-unknown interfacial waves coupled with the HTWs. Here, we analyse the onset and growth of the oscillatory regime reporting a stabilizing-destabilizing e ect associated with the interface mass transfer. The latent-heat consumption due to evaporation mitigates the inception of the thermal fluctuations (see Fig. 2a). Simultaneously, the associated liquid consumption promotes the interfacial waves by minimizing the role of gravity (see Fig. 2b). The dynamics of the gas phase are also extensively examined noticing the significance of instability-induced convective mechanisms on the local vapour distribution. Interestingly, high (low) concentration regions of vapour appear at a certain small distance above cold (hot) spots, even though the vapour concentration right at the interface follows exactly the opposite tendency as expected. Our results also show that the advection in the gas associated with the Marangoni effect plays a major role in the bulk vapour distribution as well as in the local evaporation flux along the interface and can lead to self-induced condensation in an otherwise evaporating liquid layer (see Fig. 2c). These results illustrate the importance of some of the physical mechanisms obviated by the previously-mentioned simplified models.

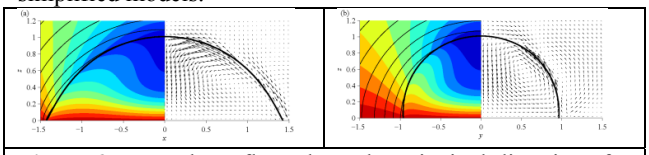

Figure 3: Two-phase flow along the principal directions for a drop with non-circular contact area Left: Temperature (colour contours) and vapour concentration (solid lines); Right: Velocity field.

3. Evaporating Sessile Droplets

We also present results from a parallel investigation devoted to elucidating the underlying transient dynamics of sessile drops evaporating on heated substrates. To that end, a more advanced model based on the diffuse-interface method is developed to solve complexities pertaining to contact-line dynamics in this configuration. The method offers a significant opportunity towards resolving non-spherical drops in 3D (see Fig. 3) as well as self-excited HTWs in evaporating drops, recently discovered by Sefiane et al. [9]. Karapetsas et al. [10] showed that the thermal fluctuations in the drops share the same mechanisms as the HTWs in planar layers.

References

1. Davis SH. Thermocapillary instabilities. Annu Rev Fluid Mech 1987; **19**: 403-435.
2. Schatz MF, Neitzel GP. Experiments on thermocapillary instabilities. Annu Rev Fluid Mech 2001; **33**: 93-127.
3. Smith MK, Davis SH. Instabilities of Dynamic Thermocapillary Liquid Layers. Part 1. Convective Instabilities. J Fluid Mech 1983; **132**: 119-144.
4. Hirt CW, Nichols BD. Volume of Fluid (VOF) Method for the Dynamics of Free Boundaries. J Comput Phys 1981; **39**: 201-225.
5. Riley RJ, Neitzel GP. Instability of thermocapillary-buoyancy convection in shallow layers. Part 1. Characterization of steady and oscillatory instabilities. J Fluid Mech 1998; **359**: 143-164.
6. Zhu ZQ, Liu QS. Coupling of thermocapillary convection and evaporation effect in a liquid layer when the evaporating interface is open to air. Chinese Science Bulletin 2010;55:233-238.
7. Sáenz PJ et al. Linear and nonlinear stability of hydrothermal waves in planar liquid layers driven by thermocapillarity. Phys Fluids 2013; **25**: 094101.
8. Sáenz PJ et al. On phase change in Marangoni-driven flows and its effects on the hydrothermal-wave instabilities. Phys Fluids 2014; **26**: 024114.
9. Sefiane K et al. Self-excited hydrothermal waves in evaporating sessile drops. Appl Phys Lett 2008; **93**: 74103.
10. Karapetsas G et al. Convective rolls and hydrothermal waves in evaporating sessile drops. Langmuir 2012; **28**: 11433-11439

Oscillatory Thermocapillary Convection of High Prandtl Number Fluid

Ruquan Liang and Shuo Yang

Key Laboratory of National Education Ministry for Electromagnetic Processes of Materials,
Northeastern University, No.3-11, Wenhua Road, Shenyang, 110819, China
liang@epm.neu.edu.cn, ys_yang_shuo@163.com

The convective motion along free surface caused by changed surface tension is called as Marangoni convection. Marangoni convection in liquid bridges has been studied intensively both numerically and experimentally under different gravity conditions. Due to the practical needs of material production and development of basic research in fluid physics, the mechanism of thermocapillary convection oscillations has become one of the hot subjects in microgravity fluid researches [1-2]. Experimental and numerical results show that when the temperature difference between the top and bottom disks exceeds a certain critical value, thermocapillary convection becomes oscillatory. When the oscillation appears, the critical temperature difference (ΔT_{cr}) corresponds with a critical Marangoni number $(Ma)_{cr}$. Since the 1980's, the several mechanisms of oscillations for thermocapillary convection have been proposed.

Smith and Davis presented two mechanisms of instability in their stability analysis for thermocapillary convection in a thin liquid layer. One kind of oscillation is the physical mechanism of hydrothermal wave instability [3]. This oscillation of thermocapillary convection is generated by the coupling effects of thermal diffusion and thermal convection. It is independent of free surface deformation. Another mechanism is surface wave instability [4]. The free surface deformation plays a vital role in the generation of thermocapillary convection. It is considered that the coupling effects of temperature field, velocity field and free surface deformation excite oscillatory thermocapillary flow. Xu and Davi [5] extended analysis results of the infinite thin liquid layer into the linear stability analysis of infinity axisymmetric cylindrical liquid bridge without surface deformation under zero gravity. The authors pointed out that the heat loss is intensified on the free surface of liquid bridge with increased Biot number which is conducive to stabilize thermocapillary convection. Their results were consistent with the qualitative analysis of Smith and Davis.

Ostrach and Kamotani pointed out that oscillatory thermocapillary flow is dependent on the temperature distribution on the free surface of liquid bridge [6]. Their experiments and numerical results showed that if the Marangoni number is enough high, the temperature changes very fast near top and bottom of free surface but temperature variation is uniform in the middle part. This temperature distribution is shaped like 'S' and defined necessary condition of inducing oscillations. They investigated time scales of the deformation and temperature variation of the free surface at the corner and got lag time of temperature variation relative to the free surface deformation. On the other, the radio of the time scale of temperature variation to that of velocity variation at the corner was presented by magnitude analysis. The author considered that the hysteresis of surface deformation and slow response of velocity to temperature can excite the oscillatory flow. The large deformation of the free surface is the important condition for inducing oscillatory thermocapillary flow.

Hu and Tang considered that buoyancy instability may arouse oscillatory thermocapillary flow [7]. The numerical analysis of ground and space experiment results about oscillatory thermalcapillary flow suggested that while the level of gravity is reduced greatly in low gravity environment, the effect of residual gravity still exists in space. If the imposed temperature difference is large enough in liquid bridge of half floating zone, buoyancy instability can be excited. The author summarized the critical Marangoni number $(Ma)_{cr}$ on the onset of oscillatory thermalcapillary flow and presented the relationship between the critical Marangoni number $(Ma)_{cr}$ and gravity in short-term microgravity experiments on ground and space experiments.

In the present paper, the coupling effects of the surface deformation and oscillatory flow on the velocity and thermal field in a 10cSt silicone oil bridge are investigated numerically, and the liquid bridge is suspended between two coaxial disks under gravity. The Navier-Stokes equations coupled with the energy conservation equation are solved on a staggered grid, and the mass conserving level set approach is used to capture the free surface deformation of the liquid bridge. The schematic of the thermocapillary convection model is shown in Fig. 1. The key parameters are $Re = \rho_l U_\infty \bar{L}/\mu_l$, Reynolds number, $We = \rho_l U_\infty^2 \bar{L}/\sigma$, Weber number, $Pr=\mu_l/\rho_l a$, Prandtl number, $Ca=\mu_l U_\infty/\sigma$, Capillary number, $Ma = \sigma_T \Delta T \bar{L}/\mu_l a = RePr$, Marangoni number, $\theta=(T-T_{low})/(T_{high}-T_{low})$, excess temperature, a is the thermal diffusivity, $\bar{L}$ is the characteristic length and we take $\bar{L} = 2R$. The relative importance of buoyancy and thermo-

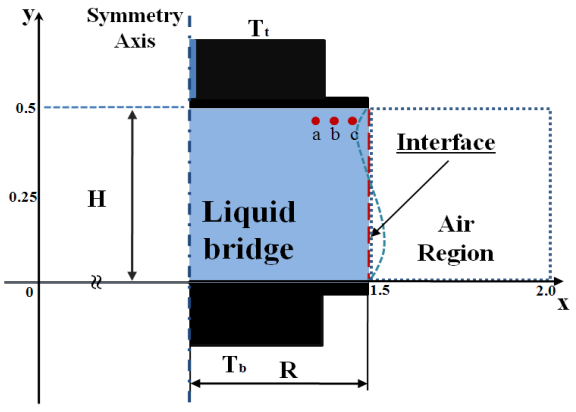

Figure 1: Schematic of a half-zone liquid bridge model.

capillary effects is determined by Bond number, $B = \rho g \beta \overline{L}^2 / \sigma_T$, β is the coefficient of thermal expansion. In this paper, a liquid bridge of 10 cSt silicone oil is used to investigate the oscillatory thermocapillary convection under gravity. The radius and height of the liquid bridge are R=2.5 mm and H=2.5 mm, respectively. The initial temperatures on the top and bottom disks are T_t=323 K and T_b=298 K, respectively, and the other initial computational conditions adopted are: Pr=105, Ma=33793, g=9.81 m/s^2.

Figure 2 shows the non-dimensional temperature distribution at the three monitoring points with the same height near the hot corner. The three monitoring points are a (1.425, 0.475), b (1.45, 0.475) and c (1.475, 0.475), respectively. The results show that when the temperature difference between the top and bottom disks exceeds $\Delta T_{cr} \approx 57$, temperature field begins to oscillate in hot corner. Meanwhile, the oscillatory pattern of temperature field is the periodic fluctuation by observing the shapes of the curves in Fig.2. The point "c" is on right side of the point "b" and near the free surface. The point "c" oscillates firstly. The onset of instability at the point "a" is late slightly comparing with that at the point "b". This phenomenon suggests that the oscillation originates from the free surface and the oscillation on free surface affects the oscillatory temperature field. The oscillatory frequencies at point "a" and "b" are similar. However, when the oscillatory curves of point "a" and "b" reach the troughs, the curve of point "c" reaches the crests. Furthermore, the amplitude at point "b" increases at the initial period and then keeps nearly constant, while the amplitudes at points "a" and "c" increase with time.

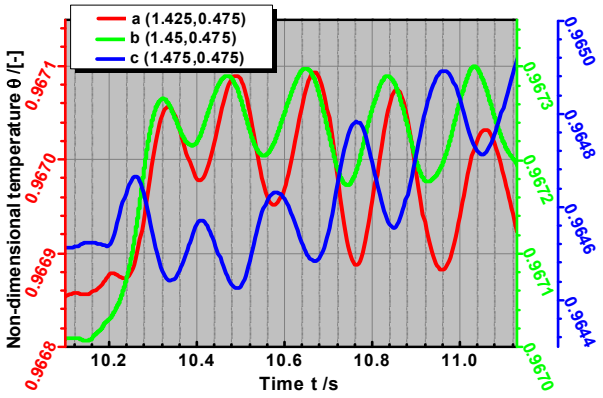

Figure 2: Time dependences of non-dimensional temperature θ at the three point ''**a**'', ''**b**'' and ''**c**'' ((x=1.425, y=0.475), (x=1.45, y=0.475), (x=1.475, y=0.475)), when Ma=77063, Re=733, g=9.81 m/s^2.

Figure 3 shows the time dependences of non-dimensional transverse velocity at the three monitoring points with the same height near the hot corner. The oscillatory characteristic of the transverse velocity is different with that of temperature distribution. As a whole, the three curves present pulsatory characteristics. The oscillatory frequencies at the three points are almost the same and the three oscillatory curves attain wave crests and troughs at the same time. The amplitudes at the three points decrease at the order of "a">"b">"c". Furthermore, the amplitudes slightly increase with time at the points of "a" and "b".

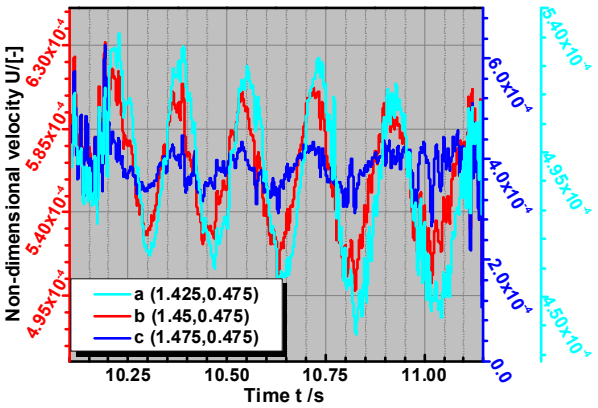

Figure 3: Time dependences of non-dimensional transverse velocity at the three point ''**a**'', ''**b**'' and ''**c**'' ((x=1.425, y=0.475), (x=1.45, y=0.475), (x=1.475, y=0.475)), when Ma=77063, Re=733, g=9.81 m/s^2.

Acknowledgements

The present work has been supported by the National Natural Science Foundation of China under the grants of 11072057 and 51376040.

References

[1] Shevtsova, V. M., Legros, J. C., Oscillatory convective motion in deformed liquid bridges, Physics of Fluids, 10, 1621 (1998).

[2] Shevtsova, V. M., Ermakov, M. K., Ryabitskii, E., Legros, J. C., Oscillations of a liquid bridge free surface due to the thermal convection, Acta. Astronautica, 41, 471-479 (1997).

[3] Smith, M. K., Davis, S. H., Instabilities of dynamic thermocapillary liquid layers, J. Fluid. Mech., 132(-1):119-144 (1983) .

[4] Smith, M. K., Davis, S. H., Instabilities of dynamic thermocapillary liquid layers, J. Fluid. Mech., 132(-1):145-162 (1983) .

[5] Xu, J. J., Davis, S. H., Convective thermocapillary instabilities in liquid bridges, Phys. Fluids., 27:1102 (1984).

[6] Ostrach, S., Kamotani, Y., Lai, C. L., Oscillatory thermocapillary flows, PCH Physic. Chemical. Hydrodynamics, 6:585-592 (1985).

[7] Hu W. R., Tang Z. M., Excitation mechanism of thermocapillary oscillatory convection, Sci. China. Ser. A, 33(8):934-943 (1990).

Criteria for Negating Influence of Gravity on Flow Boiling Critical Heat Flux in Space Systems

Issam Mudawar

Purdue University Boiling and Two-Phase Flow Laboratory (PU-BTPFL)
Mechanical Engineering Building, 585 Purdue Mall, West Lafayette, IN 47907, USA
mudawar@ecn.purdue.edu

An effective means to reducing the size and weight of future space vehicles is to replace present mostly single-phase thermal management systems with two-phase counterparts. By capitalizing upon both latent and sensible heat of the coolant rather than sensible heat alone, two-phase thermal management systems can yield orders of magnitude enhancement in flow boiling and condensation heat transfer coefficients.

Critical heat flux (CHF) is a primary concern when implementing flow boiling in reduced gravity, with microgravity potentially inducing vanishingly small CHF values at very low coolant flow rates. While high coolant flow rates can overcome the detrimental effects of reduced gravity, limited power budget places stringent limits on pumping power and therefore coolant flow rate in a space system. This creates a need to determine the minimum flow conditions that negate gravity effects. Exceeding this minimum enables the implementation of the vast body of published CHF data, correlations and models developed from terrestrial studies for design of thermal management systems for space applications.

Critical Heat Flux Mechanism

To determine the mechanism for flow boiling CHF, both CHF data and high-speed video records were obtained both in parabolic flight and ground experiments using FC-72 as working fluid; the latter experiments were performed at different orientation relative to Earth gravity. Figure 1 shows the parabolic flight apparatus and construction of the flow boiling module. Figure 2 shows the variation of CHF with inlet liquid velocity for slightly subcooled flow in a horizontal channel at one g_e and in microgravity. Overall, the effect of velocity is relatively mild at one g_e and very profound in microgravity, with CHF at the lowest velocity only 50% of that at one g_e. Notice also that data for the two gravitational environments converge around 1.5 m/s, proving the existence of a flow velocity above which gravitational effects are negated.

While different CHF mechanisms were captured in ground experiments, the parabolic flight microgravity experiments yielded only one unique mechanism. During intense boiling, discrete vapor bubbles began to coalesce into a fairly continuous wavy vapor layer that propagated along the heated wall as shown in Fig. 3. This layer effectively insulated the wall from liquid access save for wetting fronts corresponding to the wave troughs. CHF occurred when these wetting fronts began to lift away from the wall in accordance with the Interfacial Lift-off Model [1].

Predicting CHF according to the Interfacial Lift-off Model consists of determining the critical wavelength of instability of the wavy vapor layer. This wavelength is a function of the mean liquid and vapor velocities as well as mean thickness of the vapor layer. These parameters are determined with the aid of a separated flow model of the vapor and liquid layers. The CHF trigger event associated with wetting front separation is determined by equating the pressure force induced by curvature of liquid streamlines along the interface with the momentum of vapor production in the wetting front normal to the wall [2].

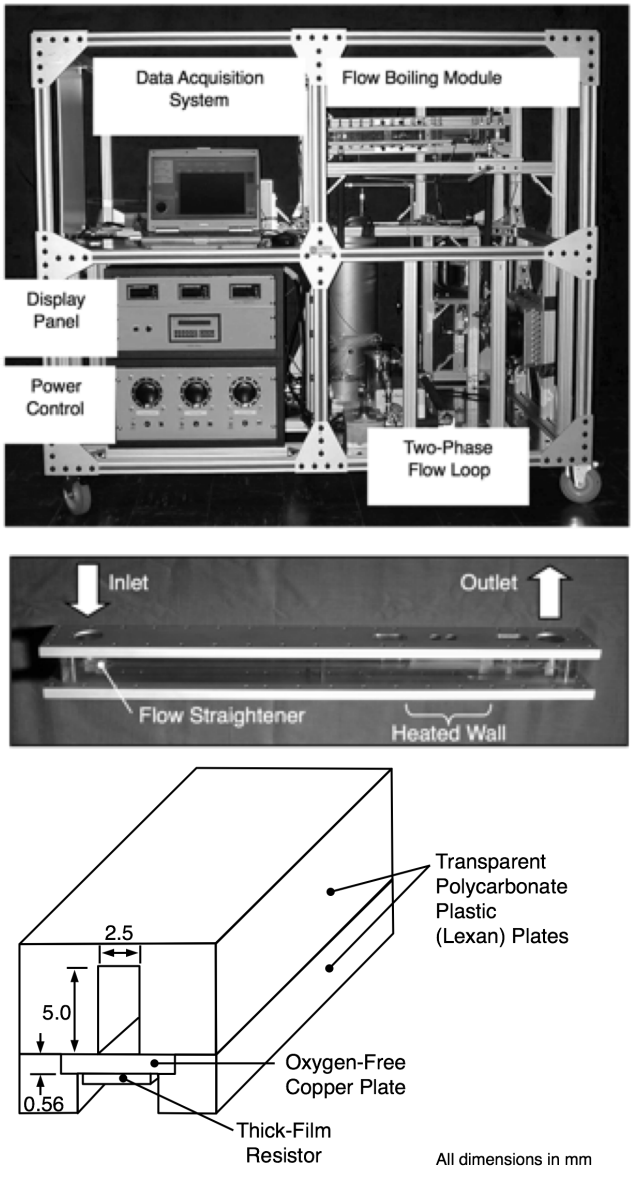

Figure 1: Microgravity flow boiling CHF apparatus and construction of flow boiling channel.

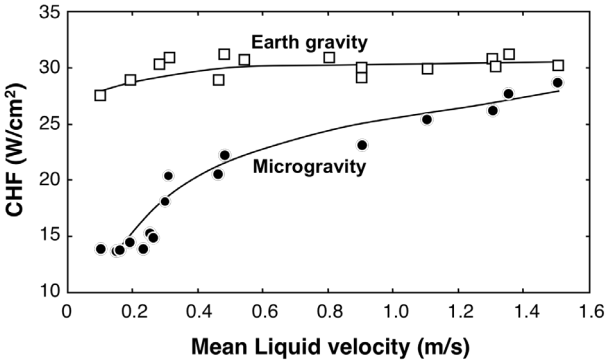

Figure 2: CHF data for FC-72 with outlet subcooling of 2-8°C measured in microgravity and in Earth gravity [2].

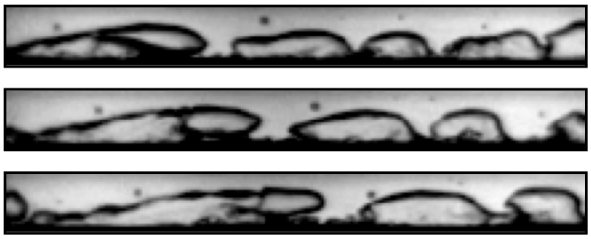

Figure 3: Wavy vapor layer observed at CHF in microgravity for inlet liquid velocity of 0.25 m/s and outlet subcooling of 4.1°C [2].

Criteria for Negating Gravity Effects

A systematic methodology for negating the influence of gravity has been developed, which consists of simultaneously satisfying three separate criteria: (1) overcoming the influence of gravity perpendicular to the heated wall using a relation based on Bond and Weber numbers, $Bo/We^2 = 0.9$, (2) overcoming the influence of gravity parallel to the heated wall using a Froude number relation, $1/Fr = 0.13$, and (3) ensuring that the heated wall is sufficiently long to ensure liquid contact, which is based on a Weber number relation based on the heated length, $We_L = 2\pi$. Figure 4 shows the minimum velocity required to satisfy the above criteria as a function of the ratio of prevailing gravity to Earth gravity, g/g_e. Each criterion predicts a particular value of liquid velocity that must be exceeded in order to overcome body force effects. Since these criteria must be satisfied simultaneously, exceeding the largest of the three values becomes the determining criterion.

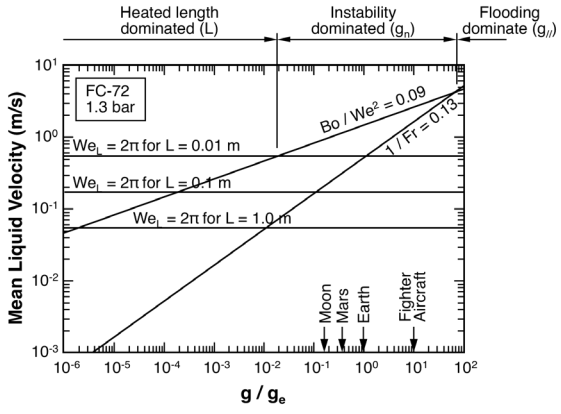

Figure 4: Determination of minimum liquid velocity required to negate body force effects [2].

Influence of Inlet Vapor Void

Recently, experiments were performed to determine the influence of saturated inlet conditions on the criteria for negating gravity effects [3]. These experiments were performed at different orientations at Earth gravity.

Figure 5 show CHF variations with orientation for inlet qualities of $x_{e,in} = 0.01$ and 0.19, respectively, for different values of mass velocities, G. They show two important trends: (1) CHF increases with increasing $x_{e,in}$, and (2) the influence of orientation is greatly reduced with increasing $x_{e,in}$. This trend can be explained by the higher inlet quality greatly increasing the velocities of the various fluid layers comprising the flow, thereby increasing the ratio of inertia to gravity effects.

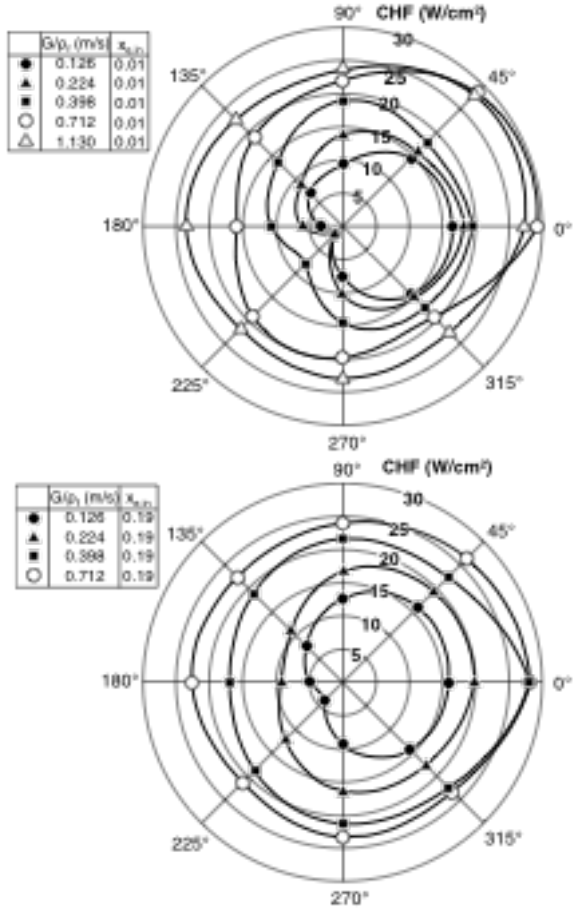

Figure 5: Variation of CHF with orientation for different mass velocities at $x_{e,in} = 0.01$ and 0.19 [3].

References

[1] Galloway, J.E., Mudawar, I., CHF Mechanism in Flow Boiling from a Short Heated Wall-Part 2. Theoretical CHF Model, International Journal of Heat and Mass Transfer, Vol. 36, pp. 2527-2540 (1993).

[2] Zhang, H., Mudawar, I., Hasan, M.M., A Method for Assessing the Importance of Body Force on Flow Boiling CHF, Journal of Heat Transfer, Vol. 126, pp. 161-168 (2004).

[3] Konishi, C., Mudawar, I., Hasan, M.M., 2013, Criteria for Negating the Influence of Gravity on Flow Boiling Critical Heat Flux with Two-Phase Inlet Conditions, International Journal of Heat and Mass Transfer, Vol. 65, pp. 203-218 (2013).

Transition to Microbubble Emission Boiling on Horizontal Circular Heated Surface in Subcooled Pool

Jun Ando[1*], Takahito Saiki[1], Toshihiro Kaneko[1,2], Ichiro Ueno[1,2+]

[1] Dept. Mechanical Engineering, Fac. Science & Technology, Tokyo University of Science
[2] Research Institute for Science & Technology, Tokyo University of Science
2641 Yamazaki, Noda, Chiba 278-8510, Japan
[*]a7510006@rs.tus.ac.jp, [+]ich@rs.tus.ac.jp

Generation of vigorous amount of heat by equipments for such as power generation systems and information/ communication technologies for huge data traffic has been serious issue to be overcome. We need to develop higher-performance cooling devices to realize stable and efficient operations of such systems. Boiling heat transfer with a liquid-vapor phase change accompanying with a latent heat is a key phenomenon to realize high heat dissipation capacity in the near future. We have an upper limit of the heat flux in the boiling phenomenon to remove the heat, known as the critical heat flux (CHF). Inada et al. [1] found a unique phenomenon, named as the microbubble emission boiling (MEB), which realize the heat flux higher than the CHF under highly subcooled conditions in the pool boiling over the heated plate. The MEB accompanies with radial emissions of small bubbles of the order of 10^{-6} m from the heated surface. Since then, a number of researches [e.g., 2,3] have been conducted to indicate the occurring conditions and the heat transfer characteristics of the MEB. In the present study, we carry out a series of experiments of the boiling on horizontal circular heated surface immersed in a subcooled pool with a special attention to a correlation between the behaviors of vapor bubbles and the transition processes from the nucleate boiling to the MEB for two heated surfaces of different sizes.

Figure 1 shows a schematic diagram of the experimental apparatus. The copper block with a cylindrical rod is heated using cartridge heaters, and the top surface of the rod exposed to the subcooled pool is the test area concerned. The diameter of the heated surface is of 5 mm and of 10 mm. Distilled water is the test fluid, and is pooled in a stainless-steel vessel. The temperature of the water is controlled to realize a designated degree of subcooling by placing the cooling channel made of copper around the test area. The test surface is finished by polishing with the emery papers of #1000, and then washed with acetone. Three

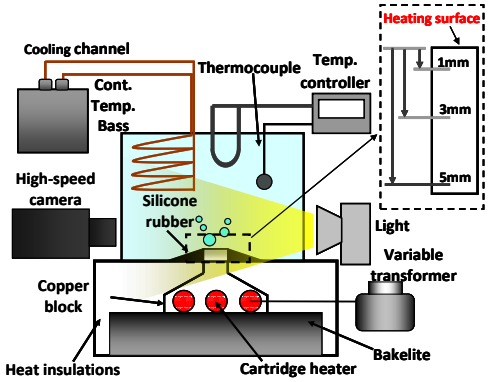

Figure 1: Experimental apparatus

thermocouples are inserted in the rod at different positions of 1 mm, 3 mm and 5 mm from the test surface to evaluate the temperature of the heated surface and the heat flux. The behaviors of the vapor bubbles are captured by a high-speed video camera at a frame rate of up to 50,000 fps with a back-lighting system.

Typical examples of the boiling curves are shown in Figure 2. The arrow indicates the CHF point. The figure consists of the curves under the degree of subcooling ΔT_{sub} = 0, 20 and 40 K. The CHF becomes higher for the test area of 5 mm in diameter. Bubble departure from the heated surface occurs much more frequently in the case of the smaller test area. In the case of ΔT_{sub} = 0 K, the boiling exhibits a transition from the nucleate boiling to the film boiling for both of the surface sizes. In the subcooled case, we have a significant 'jump' of the wall superheat, and have a further increase of the heat flux in the transition to the MEB. Such a 'jump' of the wall superheat is not seen in the case of the boiling on the heated thin wire [4,5].

Figure 3 indicates the temporal variation of the heat flux. The arrow and the accompanying number indicate the instance when the output of the heater is varied and the evaluated wall superheat. It is noted that we recognize the temporal resolution of the thermocouples is not good enough, and dare to evaluate the heat flux from the temporal variations of the temperature in the rod. Thus one must notice that the value itself of the evaluated 'heat flux' is not

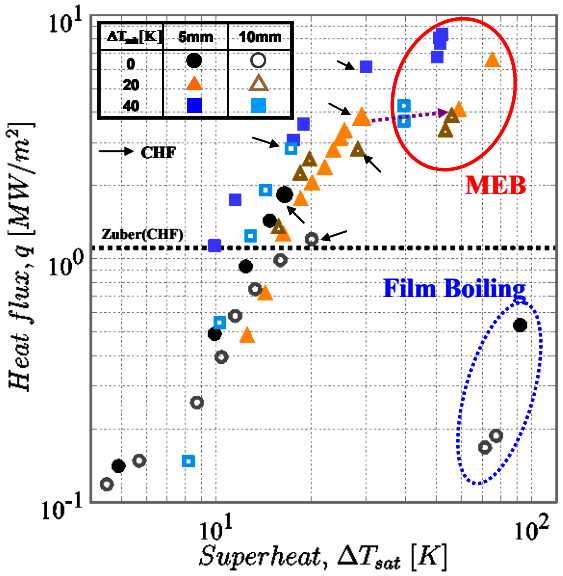

Figure 2: Boiling curve under ΔT_{sub} = 0, 20 and 40 [K]. Solid ones indicate the results for the boiling on the heated surface of 5 mm in diameter, null ones for the boiling on the heated surface of 10 mm in diameter.

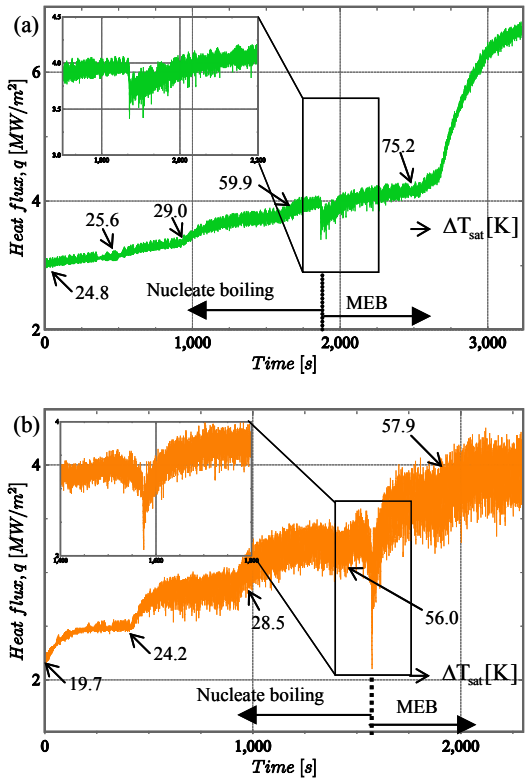

Figure 3: Typical examples of the heat flux as a function of time at ΔT_{sub} = 20 K; the diameter of heated surface is of (a) 5mm and (b) 10mm.

accurate. The temporal variation of the heat flux is categorized to three different regimes depending on the stages of the boiling. In the first regime, a general nucleate boiling takes place over the entire heated surface. The bubbles condense and collapse repetitively after the generation right above the heated surface. In the second regime, that is, the nucleate boiling at higher heat flux, there form coalesced bubbles covering almost of the whole area of the heated surface. After a while of growing stage, a significant shrink of the neck of the vapor bubble takes place, then the bubble detaches from the heated surface to drastically decrease its volume and to collapse. In this regime, the heat flux start oscillating with time due to the violent growth and departure of the vapor bubbles. These two regimes range in the 'nucleate boiling' in the figure. The third regime corresponds to the MEB; this regime occurs beyond the CHF accompanying with boiling song, and the heat flux oscillates more violently. We emphasize that a significant decrease of heat flux occurs right before the transition to the third regime. Such an abrupt drop of the heat flux does not emerge without the onset of the MEB. The heat flux rises again after the sudden drop. In the case of the smaller test area, the heat flux increases gradually with an intensive oscillation of its amplitude.

Figure 4 illustrates the behaviors of the vapor bubbles in the transition to the third regime on the heated surface under ΔT_{sub} = 20 K. Just prior to the occurrence of the MEB, the heated surface is thoroughly covered with the vapor bubbles like the film boiling for only a moment (frame (1) for both cases). That is the reason why the heat flux abruptly decreases at that period. It is found that the behavior of the vapor bubbles on the verge of the MEB is different

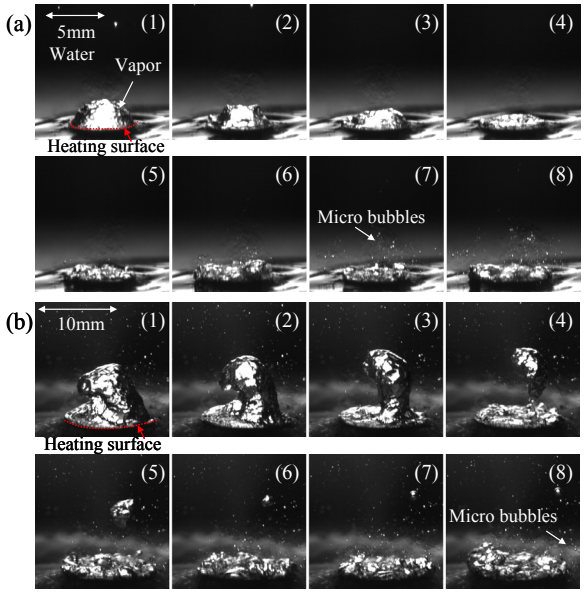

Figure 4: Successive images of condensing and collapsing vapor bubbles in the transition to MEB under ΔT_{sub} = 20 K; time averaged wall superheat (a) ΔT_{sat} = 59.9 K, (b) ΔT_{sat} = 56.0 K, The diameter of heated surface is of (a) 5 mm and (b) 10 mm. Frame interval Δt = 4.0 ms and the shutter speed is of 1/10000 s

depending on the size of the test area. In the case of smaller test area as shown in (a), the bubbles covering the test area condense on the heated surface without departing, which is similar to the film boiling. In the case of the larger test area as shown in (b), on the other hand, the coalesced bubbles iteratively grow and detach from the surface until the MEB occurs. These behaviors of the vapor bubbles cause significant differences in the way of the 'heat flux' re-rise as shown in Fig. 3. In the presentation, we will discuss a potential scenario toward the MEB over the heated surface.

References

[1] Inada, S., Miyasaka, Y., Sakamoto, S., Chandratilleke, G. R., Liquid-solid contact state in subcooled pool transition boiling system, Trans. ASME J. Heat Trans., 108, 219-221(1986)

[2] Suzuki, K., Saitoh, H., Matsumoto, K., High heat flux cooling by microbubble emission boiling, Ann. N. Y. Acad. Sci. 974, 364-377 (2002)

[3] Kumagai, S, Kubo, R, Kawasaki, T, Micro-bubble emission boiling from horizontal and vertical surfaces to subcooled parallel flow water, Heat Transfer—Asian Research 32, 2, 130-139 (2003)

[4] Tange, M., Yuasa, M., Takagi, S., Shoji, M., Microbubbles emission flow boiling in a microchannel and minichannel, Proc. Microchannels and Minichannels 2004, CD-ROM (2004)

[5] Saiki, T., Osawa, T., Ueno, I., Hong, C., Correlation between behaviors of the vapor bubbles and the characteristics of the heat transfer over the heated surface on MEB, InterPACK2013 (2013)

Wettability influence on the solid superheat at the onset of pool boiling on nanometrically smooth surfaces

Bourdon B.[1], Rioboo R.[1], Di Marco P.[2], Sevkan R.[1] , Marengo M.[3,4] and De Coninck J.[1]

[1]*Laboratoire de Physique des Surfaces et des Interfaces, Université de Mons, Av. Maistriau, 19, B-7000 Mons (Belgium)*

[2]*Università di Pisa - DESTEC , largo L. Lazzarino, 1, 56122, Pisa (Italy)*

[3]*Department of Engineering, University of Bergamo, Viale Marconi 5, 24044 Dalmine (Italy)*

[4]*School of Computing, Engineering and Mathematics, University of Brighton, Brighton BN2 4GJ, United Kingdom*

benoit.bourdon@umons.ac.be

Abstract

Pool boiling experiments of water on glass in stationary conditions is here performed. The wettability of the glass surface is triggered from hydrophilic to hydrophobic by grafting different silane molecules. The glass is chosen for its really low roughness (subnanometric) allowing us to separate the roughness effects from the wettabillity ones on the boiling. To quantify the boiling, we record the wall temperature at the onset of boiling and represent the graph of this temperature versus the static contact angle of water on this surface. The influence of the wettability is clear: increasing the wettability of very smooth non-conductive surface results in an increase of the necessary superheat to get the apparition of the first bubble. The relationship is not linear. We also visualize the boiling with a high-speed camera to determine the nucleation site density and the vapor volume flux for all different wettability cases. Once more, the trend is completely different passing from a hydrophilic surface to a hydrophobic one.

1. Experimental set-up and boiling procedure

We characterize the boiling behavior of the various substrates by standardly measuring the boiling curve and visualizing the appearance of bubbles on the surface using a high-speed camera (HCC-1000, VossKühler GmbH, Germany). The details of the experimental set-up can be found in a previous paper [1] and are just summarized here.

Figure 1 presents a schematic of the chamber where boiling on the surface is activated. The surface to be tested, a glass square plate of 45mm side and 1mm thick, is encapsulated in a chamber in which vacuum has been performed before filling with boiled water. Pressure is adjusted with a controller and experiments are performed at atmospheric pressure. A heater (ceramic cartridge, Acim Jouanin, 175Watts) is put in contact with the center part (20 mm diameter) of the back side of the glass plate using a spring. Between the heater and the plate a heat-flux meter (Captec, France) enables measuring directly the heat flux. The heating cartridge is insulated using Teflon. To compensate possible thermal leakage, additional heaters are placed inside the chamber and on the alumina walls of the chamber. The water in the chamber is maintained as close as possible to the saturation temperature using these heaters, K-thermocouples in the chamber and a PID controller.

2. Results and discussion

The Table 1 presents the various wettabilities obtained with the different surface treatments (cleaning alone and cleaning followed by self-assembling of various silanes monolayers). The low difference between values before and after boiling shows that grafting is of good quality. Moreover, the hysteresis of contact angles on glass surface is compatible with literature data [2,3]. The duration of the boiling process, while performing the acquisition of the Nukiyama curve, is of several hours.

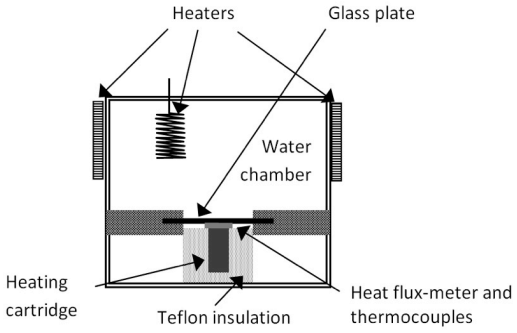

Figure 1: Schematic of the chamber. The glass plate, grafted with various silanes, is our studied surface.

For the not grafted case, before the experiment, it is impossible to measure neither the advancing nor the receding contact angle since the water completely wets the glass surface forming a thin film of water.

	Before boiling experiments			After boiling experiments		
Surface treatment	θr (°)	θa (°)	θa - θr (°)	θr (°)	θa (°)	θa - θr (°)
Not grafted	0	0	0	8 ± 1.5	36.5 ± 1.9	28.5 ± 3.4
MPEGPTMS	33.5 ± 1.7	37.1 ± 0.3	3.6 ± 2	26.1 ± 1.9	37.1 ± 0.1	11 ± 2
AcOUTES	66.4 ± 1.2	88.3 ± 4.4	21.9 ± 5.6	46.8 ± 2.1	81.2 ± 4.1	34.4 ± 6.2
OTS	94.6 ± 0.8	113.9 ± 2.9	19.3 ± 3.7	90.2 ± 5.4	107.8 ± 1.2	17.6 ± 6.6

Table 1: Different treated glass surfaces' wettability and the contact angle hysteresis before and after boiling experiments.

Figure 2 shows the surface superheat at which the first bubbles are appearing versus the wettability of the solid surface. In this figure the wettability presented (angle θ_0) is calculated using the mean value of the four measured values of the advancing and receding static contact angles before and after boiling for each surface. In the same way, the error bars are estimated using the maximum of the hysteresis of

the static contact angles (between the one before and the one after boiling) for each surface. The influence of the wettability is clear: increasing the wettability of very smooth non-conductive surface results in an increase of the necessary superheat to get the appearance of the first bubble. The relationship is clearly not linear. If one considers the theoretical case of perfect wetting (null static contact angles) and homogeneous nucleation an additional point would be at $\Delta T \approx 200°C$ [4].

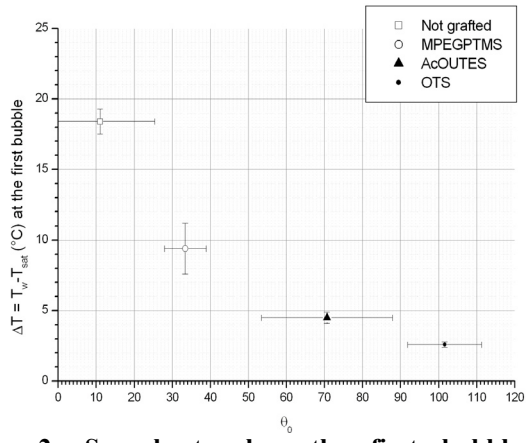

Figure 2: Superheat when the first bubbles are appearing in function of the wettability of the surface.

The upper part of Figure 3 shows the different boiling behavior between the AcOUTES (left) and the OTS (right) treatments at the same heat flux (12 kW/m2). One can remark that for the OTS case, nearly the whole heated surface is covered by bubbles, however, in the AcOUTES case, only few bubbles are present. This means that there is a big jump in the number of nucleation sites passing from a surface nearly hydrophobic ($\theta_0 \approx 75°$) to a hydrophobic one ($\theta_0 \approx 105°$).

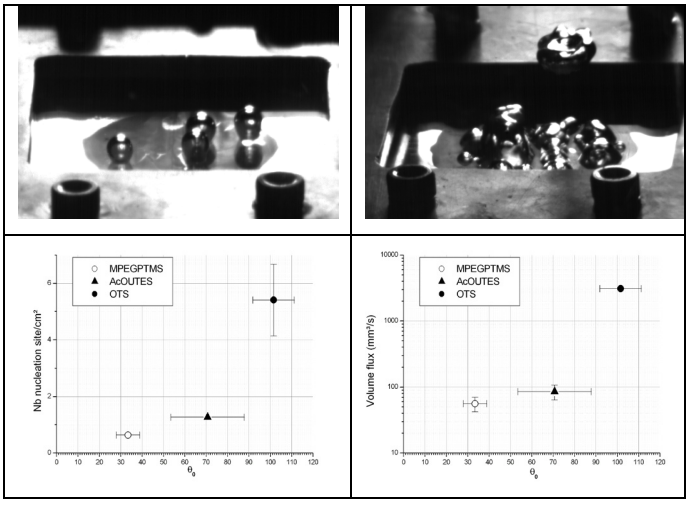

Figure 3: Comparison between surfaces boiling at the same heat flux (12kW/m²) on the smooth surfaces. Top: images from a tilted angle presenting the difference of boiling intensity on the surface (left: AcOUTES; right: OTS). Bottom: quantification in terms of nucleation site density (left) and vapor volume flux (right) of the boiling process in function of the wettability.

The bottom part of this figure represents the quantification in terms of the number of nucleation sites per unit area (left) and vapor volume flux (right) at this heat flux for the three grafted surfaces (OTS, AcOUTES and MPEGPTMS). The nucleation site density (bottom left) is in fact the mean number of bubbles present on the surface. The error bars are the standard deviations. The vapor volume flux is calculated by an estimation of the detached bubble volume per time unit. The error bars are calculated by estimating the error on the X and Y pixels on the images. The bubbles are considered to be spherical. The non-grafted case is not represented since at this level of heat flux, no bubbles were visualized.

These two graphs seem to have the same exponential growing trend in function of the contact angle. One can see that there is still a jump passing from a bit hydrophilic case to a hydrophobic one. This behavior, to the best of our knowledge, has never been studied in the literature and is not described by classical nucleation theories.

4. Conclusions

Pool boiling experiments of water on smooth glass surfaces in stationary conditions are performed. The wettability is changed grafting different monolayer on the surface. In this way, only the wettability is modify, without changing the roughness of the surface. Four different cases are studied: a “non-grafted” case, which have a 0° contact angles (CA) before boiling, a “MPEGPTMS” one, about 33° CA, a AcOUTES, about 70° CA and an OTS case, which is the most hydrophobic one, about 102° CA. The boiling curves have been measured for each case and the temperature of the surface at the onset of boiling has been recorded. We observe a non-linear decrease of the superheat temperature at the onset of boiling decreasing the wettability of the surface. We also quantify the nucleation site density and the vapor volume flux at a given heat flux for each case. Once more the trend is not linear with the wettability of the substrate, showing a big jump passing from a hydrophilic surface to a hydrophobic one.

References

[1] Bourdon, B., Di Marco, P.,Rioboo, R., Marengo, M., De Coninck, J., Enhancing the onset of pool boiling by wettability modification on nanometrically smooth surfaces, Int. Comm. In Heat and Mass Transfer, 45, 11-15 (2013).

[2] Fadeev, A. Y., McCarthy, T. J., Trialkylsilane Monolayers Covalently Attached to Silicon Surfaces: Wettability Studies Indicating that Molecular Topography Contributes to Contact Angle Hysteresis, Langmuir, 15(11), 3759–3766 (1999).

[3] Wei, M., Bowman, M. R. S., Wilson, J. L., Morrow, N. R., Wetting Properties and Stability of Silane-Treated Glass Exposed to Water, Air, and Oil, Journal of Colloid and Interface Science, 157(1), 154–159(1993).

[4] Carey, V.P., Liquid-Vapor Phase-Change Phenomena: An Introduction to the Thermophysics of Vaporization and Condensation Processes in Heat Transfer Equipment, Taylor & Francis Group, 2008.

The Effect of Wickability on Pool Boiling Critical Heat Flux on Micro/Nanostructured Surfaces

Md Mahamudur Rahman and Matthew McCarthy*

Department of Mechanical Engineering and Mechanics, Drexel University
3141 Chestnut Street, Philadelphia, PA 19104, USA
*mccarthy@coe.drexel.edu

This work presents the fabrication of novel micro/nanostructured surfaces based on biologically assisted fabrication techniques as well as the experimental characterization of both surface wickability and pool boiling heat transfer using water at atmospheric conditions. The role of wickability (the ability of the surface to wick liquids laterally) on critical heat flux is investigated and shown to be the dominant contributor for enhancement using micro/nanostructured surfaces.

While the enhancement of boiling heat transfer using macroscale structures has been in practice since the 1940's, scaling these structures down radically increases surface area and capillarity, leading to substantial heat transfer enhancements, which have been reported in a variety of publications. These works typically point to enhancement mechanisms, such as increased nucleation sites [1,2], liquid wicking [1,3,4], or contact line pinning [5,6], but they have not been used to explicitly characterize theses mechanism. This is in part to the complexity and variability of the structures and their fabrication processes, but also the coupled nature of critical phenomena inhibiting a systematic investigation into individual parameters.

This work leverages the simplicity and flexibility of biological templates to create nanostructured and hierarchically structured surfaces to elucidate the mechanisms of CHF enhancement. The *Tobacco mosaic virus* (TMV) is used here as a biological template for the creation of nanostructured coatings. The TMV nanofabrication process consists of exposing a surface to three room-temperature solutions in series. It requires no power whatsoever and is compatible with all metallic surfaces. First, the TMV naturally assembles from solution onto the surface in a "near-vertical" arrangement. The surface is then immersed in a palladium catalyst solution to activate the TMV, which is followed by electroless deposition of a thin nickel shell, conformally encasing the TMV. Figure 1a,b shows the resulting nickel nanostructures, where the TMV acts solely as a temporary scaffolding to support the nickel and plays no role in defining or maintaining the structure after fabrication is complete. This process has been demonstrated to enhanced pool boiling heat transfer onto a variety of metallic surfaces [4], and shown to be compatible with numerous materials and surface geometries [7]. Figure 1c-f shows microstructured and hierarchical surfaces fabricated for this work, comprised of silicon posts that are conformally coated with TMV nanostructures. Additionally, Figure 1g,h shows two types of copper oxide nanostructures fabricated using an alkaline process at two different solution temperatures.

Each of these micro, nano, and hierarchically structured surfaces are superhydrophilic displaying not only an apparent contact angle approaching zero degrees, but also the ability to draw liquid into their surface structures through capillary wicking. This wicking phenomenon has been cited as an underlying mechanism for boiling enhancement in numerous report works. "Wickability" is a loosely used phenomenological term without any formal definition. In this work we have quantified the wickability of various surfaces using a simple custom-built test apparatus, where a surface is slowly raised using a micrometer to touch a tube with a pendant droplet attached. When droplet touches the

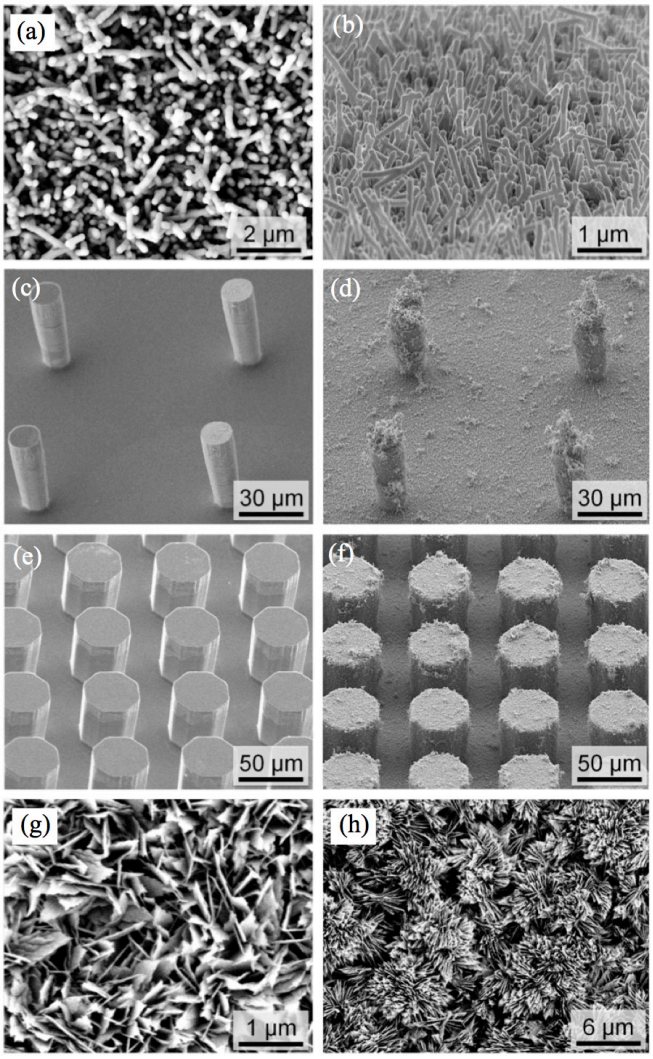

Figure 1: Super-wetting micro/nanostructured surfaces. (a,b) Nickel nanostructures based on biotemplating of the *Tobacco mosaic virus* (TMV), (c-f) microstructured silicon posts with and without TMV nanostructured coatings, and (g,h) copper-oxide nanostructures.

sample it is immediately wicked into the surface and high-speed imaging captures the descending meniscus in the capillary tube, yielding direct calculation of the wicked volume and wicked volume rate. The advantage of this technique is that it measures volume flow and not velocity of a hemi-wicking front; no information about the surface structure (height, porosity) is necessary to find volume flow rate. The wicking volume flux is then defined as the volume flow rate relative to the wetted area underneath the capillary. This method was first reported by Ahn *et al.* [8] to measure volume flow rate (rather than volume flux as presented here). The wicked volume flux for each of the surfaces was determined, followed by pool boiling test. Each of the surfaces was heated to it's CHF value in water at atmospheric conditions using a custom built pool boiling set-up, where cartridge heaters deliver heat through an insulated copper bar instrumented with thermocouples to a 1cm x 1cm test surface submerged in saturated water. Figure 2 shows the pool boiling curves for the various structured surfaces, with notable enhancements seen for several designs.

Figure 3 shows the relationship between CHF and wickability (characterized using the measured wicked volume flux) for each of the surfaces fabricated and tested in this work. An obvious linear trend relating CHF and wickability can be seen with excellent consistency for various samples. The data includes nanostructured and hierarchical TMV samples, etched silicon posts, and copper oxide nanostructures Additionally, data extracted from Ahn *et al.* using micro, nano, and hierarchical zirconium alloys matches the plotted trend line identically [8]. As wickability approaches zero the linear trend approaches the predictions of Zuber [9] and Lienhard and Dhir [10] for non-structured surfaces not capable of wicking liquids. These results, encompassing various materials, length scales, and levels of hierarchy, show that wicked volume flux is a key factor in dictating CHF enhancement using micro/nano-structured super-wetting surfaces.

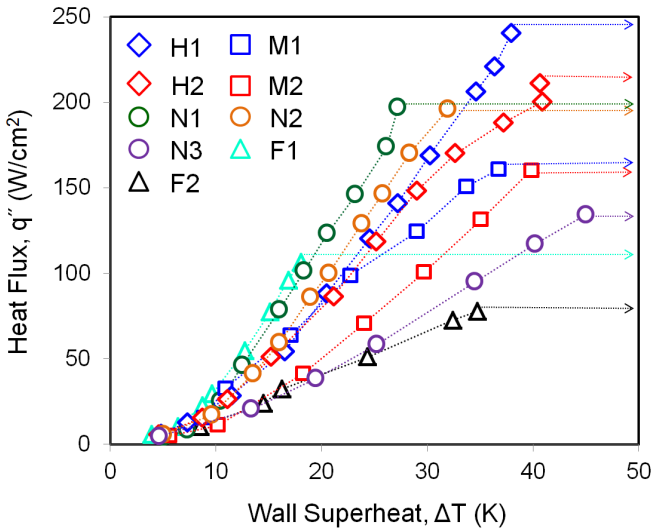

Figure 2: Pool Boiling curves showing heat flux as a function of wall superheat for water at atmospheric pressure, showing flat copper (F1), flat silicon (F2), microstructured silicon (M1-M2), TMV-templated nanostructures (N1), hierarchical silicon posts with TMV nanostructures (H1-H2), and two types of copper oxide nanostructures (N2-N3).

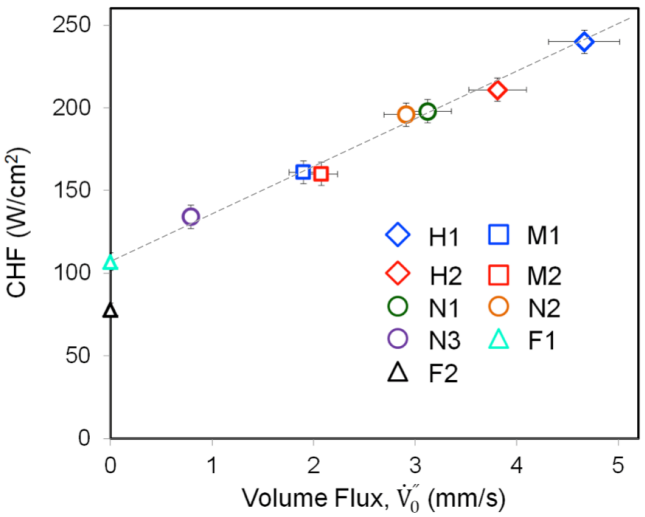

Figure 3: The role of wickability on pool boiling CHF enhancement, showing CHF as a function of wicked volume flux for each of the surfaces tested.

References

[1] Chen, R., Lu, M., Srinivasan, V., Wang, Z., Cho, H., and Majumdar, A., "Nanowires for Enhanced Boiling Heat Transfer," *Nano Letters,* vol. 9, pp. 548-553, Feb 2009.

[2] Li, C., Wang, Z., Wang, P., Peles, Y., Koratkar, N., and Peterson, G., "Nanostructured copper interfaces for enhanced boiling," *Small,* vol. 4, pp. 1084-1088, 2008.

[3] Bon, B., McKenna, E., and Klausner, J., "The Hoodoo: A New Surface Structure for Enhanced Boiling Heat Transfer," *Journal of Thermal Science and Engineering Applications,* vol. 5, 2013.

[4] Rahman, M., Olceroglu, E., and McCarthy, M., "Scalable Nanomanufacturing of Virus-templated Coatings for Enhanced Boiling," *Advanced Materials Interfaces,* vol. 1, 2014.

[5] Chu, K.-H., Enright, R., and Wang, E. N., "Structured surfaces for enhanced pool boiling heat transfer," *Applied Physics Letters,* vol. 100, pp. 241603-4, 2012.

[6] Chu, K.-H., Joung, Y. S., Enright, R., Buie, C. R., and Wang, E. N., "Hierarchically structured surfaces for boiling critical heat flux enhancement," *Applied Physics Letters,* vol. 102, pp. 151602-4, 2013.

[7] McCarthy, M., Gerasopoulos, K., Enright, R., Culver, J. N., Ghodssi, R., and Wang, E. N., "Biotemplated hierarchical surfaces and the role of dual length scales on the repellency of impacting droplets," *Applied Physics Letters,* vol. 100, Jun 2012.

[8] Ahn, H. S., Park, G., Kim, J. M., Kim, J., and Kim, M. H., "The effect of water absorption on critical heat flux enhancement during pool boiling," *Experimental Thermal and Fluid Sci.,* vol. 42, pp. 187-195, 2012.

[9] Zuber, N., "Hydrodynamic Aspects of Boiling Heat Transfer," University of California, Los Angeles, California, 1959.

[10] Lienhard, J.H., and Dhir, V.K., "Hydrodynamic prediction of peak pool-boiling he at fluxes from finite bodies," *J. Heat Transfer Transfer - ASME,* vol. 95, pp. 152– 158., 1973.

Computation of Bubble Growth on a Hot Substrate: Asymptotic Scheme for Small Contact Angles

Alexey Rednikov, Nicolas Hollander, Marta Hernando and Pierre Colinet

Université Libre de Bruxelles, Transfers, Interfaces and Processes (TIPs)
Av. F.D. Roosevelt 50, CP 165/67, Brussels, B-1050, Belgium
aredniko@ulb.ac.be

The present work deals with a model of nucleate pool boiling. Namely, we study the growth of a single bubble on a superheated horizontal solid substrate in a large volume of stagnant liquid (see Figure 1). We do not consider the nucleation stage. Rather, we assume that a bubble of a certain (small) size is already created on a flat substrate surface and analyze its growth dynamics.

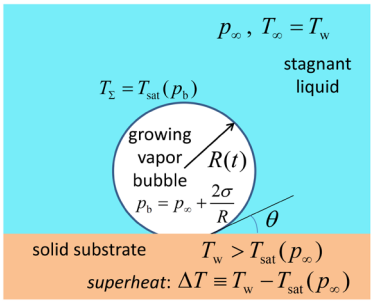

Figure 1: Sketch of the problem.

The modeling is significantly complicated by the presence of a vapor—liquid—solid triple line (hereafter simply referred to as the contact line), inherently amenable to a singular behavior. In contrast, the problem of bubble growth in the bulk of the liquid ("free bubble"), where no contact line is involved, is a significantly simpler one. Among the contact-line singularities, the most pertinent one here is a non-integrable divergence of the heat/evaporation flux occurring within a standard thermo-hydrodynamic approach (viz. if the temperature of the bubble surface is the saturation one, T_{sat}, whereas the superheated substrate temperature is $T_w > T_{sat}$, this amounts to a temperature discontinuity and an infinite heat flux at the contact line). This and other possible singularities are resolved by accounting for various microscopic effects, typically negligible on the macroscopic scale, such as the kinetic resistance to evaporation, the disjoining pressure and precursor films, or the Navier slip. Quite notably, the Kelvin effect (the saturation-condition dependence on the interface curvature), the only one in this list still belonging to standard thermo-hydrodynamics, is alone capable of taking care of all the singularities [1]. Obviously, even if the singularities are resolved on a microscale (in what is referred to as the *microregion* of the contact line), the local heat flux must still attain high values there and may therefore be important within the global flux.

Another, related reason for the need of incorporating the microregion consideration into an overall bubble-growth model is associated with the fact that the contact angle θ is generally not just the Young's one but may also contain a significant evaporation-induced contribution, which is established precisely in the microregion. In particular, in the perfect-wetting case (to which we shall limit ourselves in the present study), this angle is nonetheless finite, and evaporation-induced in its entirety. Note also that the contact angle θ as apparent on the macroscopic scale may in general also be modified due to contact-line motion if the velocity of the latter is sufficiently high (the effect being here modeled by means of the Cox-Voinov law). Given the disparity of the length scales involved (microscales versus macroscales), the microregion is typically treated as a submodel in the framework of an otherwise macroscopic modeling of bubble growth [2-5].

In the present study too, we stick to such a multiscale approach. However, a distinctive feature here is that we push it even further, by formally and consistently considering the asymptotic limit of small contact angles, $\theta \ll 1$ (θ being measured in radians). The thing is that the existing microregion analyses are all realized, to the best of our knowledge, in the framework of the lubrication approximation, and thus formally for $\theta \ll 1$. In practical terms, the lubrication approximation is deemed to work reasonably well up to θ as large as 30÷40°. On the other hand, the evaporation-induced contact angles in the case of perfectly wetting liquids are roughly expected to fall just within the same range (implying superheats $\Delta T \equiv T_w - T_{sat} \sim 1 \div 10°$), hence a practical consistency. As for a theoretical consistency, given that the microregion analysis formally belongs to $\theta \ll 1$ anyway, it may be reasonable to apply an asymptotic scheme based upon $\theta \ll 1$ to the macroscopic domain too, which we do here. Apart from the genuine conceptual benefits one expects of an asymptotic analysis, in more practical terms, this also brings to more accessible computation procedures.

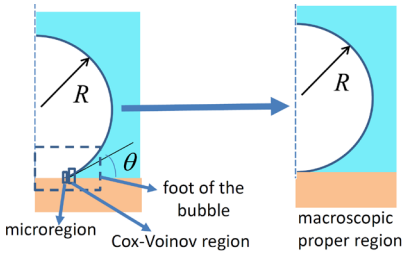

Figure 2: Asymptotic regions in the limit $\theta \ll 1$.

The present approach is most effective for bubbles not deviating too much from a spherical cap shape (small capillary, Weber and Bond numbers, the latter being valid either for sufficiently small bubbles or for microgravity experiments such as ESA RUBI). One of its key features is the splitting-off in its own right of the foot-of-the-bubble region from the macroscopic domain, the remainder of the latter being now referred to as the macroscopic proper

region (see Figure 2). In the latter region, the leading-order geometry is particularly simple: a sphere touching a planar surface just in one point, and no change of geometry is incurred should even θ vary with time, which may bring about appreciable computational benefits. In the foot-of-the-bubble region, on the other hand, a significant progress in the computations is attainable analytically.

Now we turn to some further details of the analysis. The increase of the mass of the bubble is due to the evaporation mass flux into its interior. Thus,

$$4\pi\rho_v R^2\dot{R} = J_{micro} + J_{CV} + J_{foot} + J_{macro} \qquad (1)$$

with $R = R(t)$ being the bubble radius as a function of time t, $\dot{R} \equiv dR/dt$, $\rho_v \approx p_\infty M/(R_g T_\infty)$ the vapor density (assumed constant on account of $\Delta T \ll T_\infty$ and the pressure change in the bubble being much smaller than p_∞), M the molar mass, and R_g the universal gas constant. The deviation of the bubble volume from that of a sphere with the same radius is negligible to leading order within our asymptotic scheme, which is taken into account on the left-hand side of (1). J is the mass flux given by

$$J = \frac{\lambda_l}{L}\int \frac{\partial T}{\partial n}\, dS$$

where λ_l is the liquid thermal conductivity, L [J/kg] the latent heat of evaporation, $\partial T/\partial n$ the (external) normal temperature gradient, S is the area, while the integration is performed over the appropriate, indicated by the subscripts on the right-hand side of (1), parts of the bubble surface. These subscripts refer to the microregion, the Cox-Voinov region, the foot of the bubble and the macroscopic proper region, respectively (cf. Figure 2). Note that, as the problem is here treated by means of asymptotic matching, the right-hand side of (1) naturally does not depend on a concrete choice of the boundaries between the regions involved, even if each term taken apart does.

For the time being, concrete computations are realized by us within the following scope: a bubble in the form of an exactly spherical cap, a uniform substrate temperature T_w, and the microregion model developed in [1]. In this case, the fluxes J_{micro}, J_{CV} and J_{foot} in (1) are given by analytical expressions, just with certain coefficients determined numerically from the microregion study. On the contrary, J_{macro} is determined by numerically solving the Navier-Stokes and heat transfer equations in the macroscopic proper region, for the geometry represented in Figure 2 (right), which has been realized in [6] using COMSOL Multiphysics™ software. An analytical expression for J_{macro} is only possible assuming a purely conductive heat transfer in the liquid.

Some selected results are shown in Figure 3. Additional key assumptions used in this modeling are the following. The liquid far away from the bubble is preheated to the substrate temperature, $T_\infty = T_w$ (cf. Figure 1). The material properties of the liquid are constant. The bubble radius is much greater than its critical (unstable-equilibrium) value. The effect of the contact-line velocity on the apparent contact angle θ is negligible (hence no Cox-Voinov region). The Reynolds number is small, so that the Stokes (creeping-flow) equations are used instead of the Navier-Stokes ones (the main reason why the results of Figure 3 are limited to relatively small superheats). Note though that the Peclet number is *not* assumed small (consistent with the small-Reynolds-number case in view of typically large Prandtl numbers), and the convective heat transfer is modeled in full.

Currently, work is underway on certain generalizations and extensions. In particular, the sensitivity of the global bubble growth results to the microregion model is studied, here including first of all a possible influence of the kinetic resistance to evaporation and the (unknown) accommodation coefficient upon which it depends. The modeling is being extended to bubble radiuses comparable with the critical one, finite Reynolds numbers, larger superheat values, and contact-line velocities at which the effect upon θ may already be appreciable. These results will also be presented at the conference.

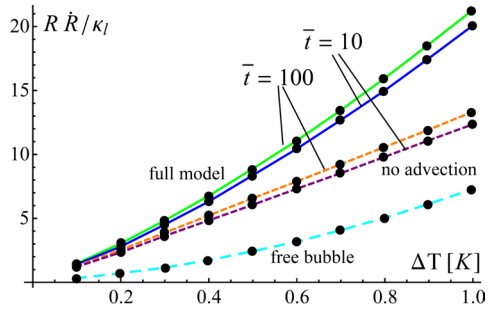

Figure 3: Computation results [6] for HFE-7100 at the atmospheric pressure. The instantaneous Peclet number of a growing bubble (κ_l being the thermal diffusivity of the liquid) versus the superheat at various dimensionless times $\bar{t} \equiv t\,\lambda_l\Delta T/(R_0^2 L\rho_v)$ (with an initial bubble radius $R_0 = 100\,\mu m$ at $t = 0$) and for various arrangements for comparison. For a free bubble in the bulk of the liquid (but not for our bubble sitting on a substrate, represented here by the full model and by the "no advection" one for which just the Laplace equation is solved for heat transfer in the liquid), a permanent regime $R \sim \sqrt{t}$ is established, hence eventually no dependence on $\bar{t}$.

References

[1] Rednikov, A., Colinet, P., Singularity-free description of moving contact lines for volatile liquids, Phys. Rev. E, 87, 010401 (2013).

[2] Stephan, P., Hammer, J., A new model for nucleate boiling transfer, Wärme- und Stoffübertragung, 30, 119-125 (1994).

[3] Kunkelmann, C., Stephan, P., CFD simulation of boiling flows using the Volume-of-Fluid method within OpenFOAM, Numer. Heat Transfer A 56, 631-646 (2009).

[4] Kunkelmann, C., Stephan, P., Numerical simulation of the transient heat transfer during nucleate boiling of refrigerant HFE-7100, Int. J. Refrigeration **33**, 1221–1228 (2010).

[5] Aktinal, E., Dhir, V.K., Numerical simulation of nucleate boiling phenomenon coupled with thermal response of the solid, Microgravity Sci. Technol. 24, 255-265 (2012).

[6] Hollander, N., Contribution à la modélisation de la croissance d'une bulle de vapeur sur une plaque surchauffée : acte élémentaire d'ébullition, Master Thesis, Université Libre de Bruxelles (2013).

A Study of Flow Structure's Effect on Forced Convective Boiling Heat Transfer

Alex Scammell* and Jungho Kim

Department of Mechanical Engineering, University of Maryland – College Park
2181 Glenn Martin Hall, University of Maryland, College Park, 20742 USA
ascammel@umd.edu

As a popular means to remove thermal energy from high heat flux devices in reduced gravity environments, flow boiling has been studied by numerous authors over the last three decades. Of great interest is the prediction of the heat transfer coefficient variation between terrestrial gravity (1g) and microgravity (µg), so that designers can efficiently construct space-based heat exchanger systems with the large 1g database available. Several researchers have commented on the effect of flow structure and dynamics on the heat transfer coefficient [1-3], but the local observation of these effects have not been discussed. It is the purpose of the presented work to describe the heat transfer characteristics of common flow regimes experienced in 1g and µg conditions so that the variation in heat transfer with gravity can be better predicted.

Experimental data for this study were collected using a flow boiling apparatus that utilizes infrared (IR) thermometry observe local heat transfer in the flow. The test section is constructed with a silicon tube to which a thermally insulating Kapton tape is applied. The tape is coated with a black, emmisive paint to allow for measurement of the inner and outer wall temperature of the tube. Figure 1 illustrates a cross-section of the silicon tube with six gold-plated mirrors to simultaneously measure heat transfer and visualize the flow.

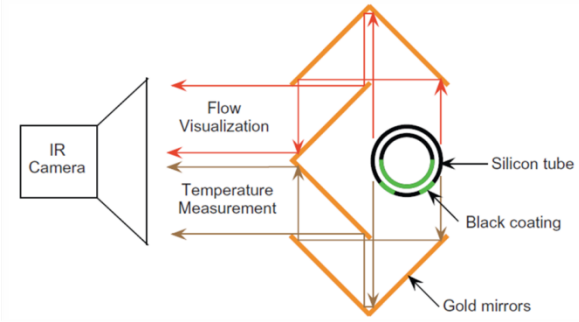

Figure 1: Schematic of silicon tube cross-section with gold mirrors.

In addition to the IR camera, a high-speed visual camera was used to collect detailed flow regime video in an adiabatic Teflon tube located directly after the main test section. The remaining components of the experimental rig are typical of a flow boiling loop, with specifics available in previous literature [4]. The flow direction tested was vertical-upward (with Novec HFE-7100) which provides a reasonable approximation of axisymmetric flow and allows for straightforward comparison of variable gravity data.

The parameters of interest for this work focus primarily on low mass fluxes (G = 50-200 kg/m^{2}s) for the purpose of studying gravity dependent flow regimes. One such pattern is churn flow, which is characterized as a primarily vapor-cored regime with oscillatory backflow of the liquid film due to lack of sufficient shear force from the vapor to overcome the body forces on the liquid. The heat flux and heat transfer coefficient also experience fluctuations with the flow as can be seen in Figure 2, which is a time trace of the heat transfer coefficient for one pixel.

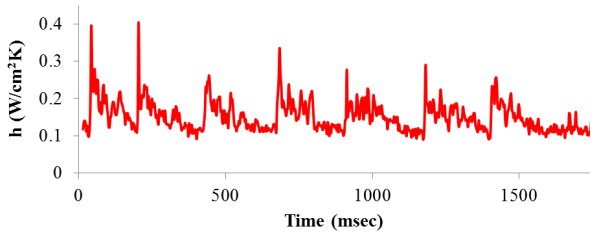

Figure 2: Oscillating heat transfer coefficient in churn flow for conditions of: G = 51 kg/m^{2}s, q" = 1.03 W/cm^2, x = 0.13.

It can be observed in the time trace that there are three main events that transpire during each churning cycle. First, as the main wave pulses upward in the tube, a large spike in the heat transfer coefficient results from violent mixing and disruption of the thermal boundary layer present in the liquid film. The liquid pulse is followed by a thinning of the film along the tube wall and a decrease in velocity until the liquid appears stagnant. This coincides with a drop and gradual decrease in heat transfer from the peak as the thermal boundary layer is re-established and thickens. As the flow begins to move downward in the tube, turbulence is minimal in the film allowing for further thickening of the boundary layer and decrease in heat transfer coefficient to a "base" value.

These three phases are represented in Figure 3, where the flow is moving left to right (upwards). To the right of the liquid pulse, the film is falling and the "base" heat transfer coefficient is seen with a steady, lower value. A spike in heat transfer is observed when the wave passes and then a slight decrease and smoothing afterwards.

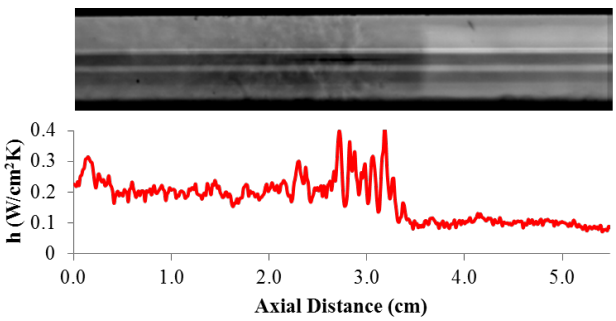

Figure 3: Experimental observation of heat transfer coefficient during three phases of churn flow.

A statistical analysis of the churn flow oscillations with respect to the heat transfer coefficient reveals that at low to

moderate qualities (x = 0.1-0.3), the first two phases represent 60% of the total heat transfer while the falling film contributes the remaining 40%. These calculations are completed by first visually identifying the time periods over which the phases are occurring, and then averaging the heat transfer coefficient over those times. The percentage contribution of the pulsing phases and the falling phase can then be calculated by,

$$\%_{pulse} = \frac{h_{pulse} t_{pulse}}{h_{pulse} t_{pulse} + h_{fall} t_{fall}}$$

$$\%_{fall} = \frac{h_{fall} t_{fall}}{h_{pulse} t_{pulse} + h_{fall} t_{fall}}$$

where h_{pulse}, h_{fall}, t_{pulse}, t_{fall} are the heat transfer coefficients and times for the pulsing phases (phases 1 and 2) and falling phase (phase 3).

When testing was completed at higher vapor qualities, the vapor core was strengthened and maintained a consistent liquid film on the tube wall, representative of annular flow. Similar to the churn flow, however, slight oscillations occurred in the heat transfer coefficient due to passing interfacial waves such as one shown in Figure 4.

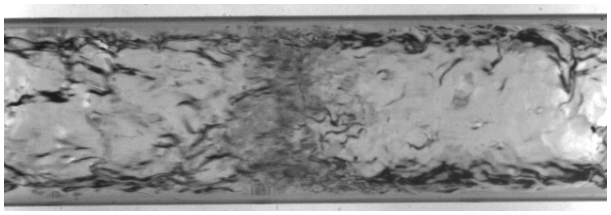

Figure 4: Visual image of passing interfacial wave in annular flow.

The heat transfer variations observed during this wavy annular regime were less cyclic than those seen previously in churn flow. In addition, between the large liquid waves, smaller Helmholtz disturbances and impacts from dispersed droplets also occurred causing smaller, random jumps in heat transfer coefficient. The result is a somewhat chaotic time-trace signal with no clear "base" value (see Figure 5), making a statistical analysis difficult. However, if the heat transfer coefficient is observed as the large waves move through the tube, a comparison can be made to heat transfer profiles present in falling films.

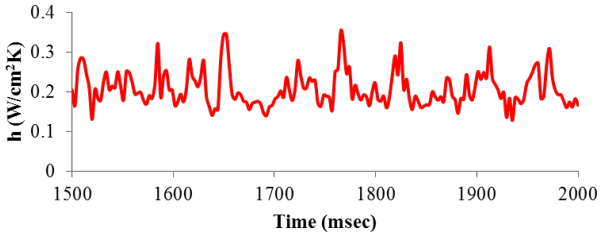

Figure 5: Irregular heat transfer coefficient variations in wavy annular flow for conditions: G = 100 kg/m2s, q" = 1 W/cm2, x = 0.42.

Figure 6 illustrates the heat transfer profile along the tube as a liquid wave passes with thinner annular flow on the upstream (right) side. The increase in heat transfer with the passing of the wave can be attributed to thinning of the thermal boundary layer by flow patterns within the liquid itself. As mentioned, this trend in wave heat transfer has been seen in falling films in previous literature [5]. It is explained that hot fluid from the thin film upstream is accelerated into the colder wave which decreases the bulk temperature due to mixing. Furthermore, the fluid temperature drop is coupled with a decrease in thermal boundary layer thickness resulting from rotational flow within the wave. These trends appear similar to those experienced in Figure 6, where the heat transfer coefficient rises when the wave passes and then falls again when a thinner annular film is re-established.

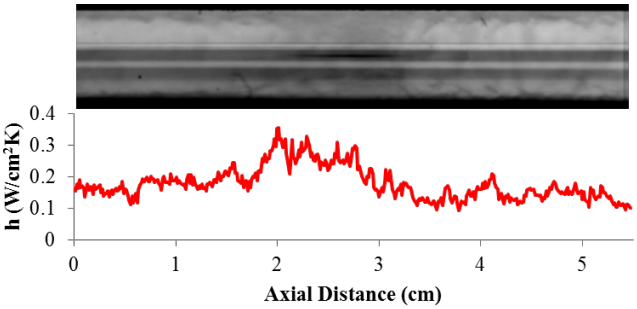

Figure 6: Experimental observation of heat transfer coefficient for passing wave in wavy annular flow.

Acknowledgements

The current work is funded through NASA grants NNX11AN49H and NNX09AK39A.

References

[1] Ohta, H., Experiments on microgravity boiling heat transfer by using transparent heaters, Nuclear Engineering and Design, 175, 167-180 (1997).

[2] Baltis, C., Celata, G.P., Cumo, M., Saraceno, L., Zummo, G., Gravity Influence on Heat Transfer Rate in Flow Boiling, Microgravity Science and Technology, 24, 203-213 (2012).

[3] Ohta, H., Baba, S., Boiling Experiments Under Microgravity Conditions, Experimental Heat Transfer, 26, 266-295 (2013).

[4] Narcy, M., Scammell, A., Colin, C., Kim, J., Flow Boiling Under Microgravity Conditions: Comparative Study of Two Experimental Data Sets, 15th International Heat Transfer Conference. Kyoto, Japan, August 10-15 (2014).

[5] Lyu, T.H., Mudawar, I., Statistical investigation of the relationship between interfacial waviness and sensible heat transfer to a falling liquid film, Int. J. Heat Mass Transfer, 34(6),1451-1464 (1991).

Flow boiling in tube in normal and microgravity conditions

Marine Narcy, Catherine Colin

Institut de Mécanique des Fluides de Toulouse, University of Toulouse, CNRS, INP
Allée du Professeur Camille Soula
Toulouse, 31400, FRANCE
E-mail: colin@imft.fr

Flow boiling is common in many industrial applications, in power plants (energy production or conversion), transport of cryogenic liquids and other chemical or petrochemical processes. These systems take advantage of latent heat transportation, which generally enables a good efficiency in heat exchanges. For that reason, two-phase thermal management systems are considered as extremely beneficial for space applications. But boiling is a complex phenomenon, which combines heat and mass transfers, hydrodynamics and interfacial phenomena. Furthermore, gravity affects the fluid dynamics and may lead to unpredictable performances of thermal management systems. It is thus necessary to perform experiments directly in (near) weightless environments. Therefore, several two-phase flow (gas-liquid flow and boiling flow) experiments have been conducted in the past forty years and enabled to gather data about flow patterns, pressure drops, and heat transfers including critical heat flux and void fraction in thermohydraulic systems. Previous state of the art and data can be found in the papers of Colin et al. [1], Ohta [2], and Celata and Zummo [3]. However, there is still a lack of reliable data on heat transfer in flow boiling in microgravity. Therefore, the purpose of our study is to clarify gravity effects on hydrodynamics and boiling heat transfer for space applications.

A two-phase flow loop for the study of flow boiling has been built at *IMFT* in order to perform experiments in both normal gravity (vertical upflow) and microgravity during parabolic flights aboard an aircraft. The working fluid is the refrigerant 1-methoxyheptafluoropropane (C3F7OCH3), commonly referred to as HFE-7000. It is first pumped at liquid state by a gear pump while the liquid flow rate is measured by a Coriolis flowmeter. Then the fluid is preheated or partly vaporised through preheaters. It enters a 22 cm long vertical stainless steel tube just upstream the test section. Downstream the test section it is condensed before entering the pump again. The test section is a sapphire tube of 6 mm ID and 8 mm OD. It is coated on its outer wall by a ITO deposite heated by Joule effect. The external wall temperature is measured in four locations by Pt100 sensors.
Liquid temperature is measured at the inlet and outlet of the test section by thermocouples. The pressure drop is measured just after the test section on an adiabatic part with two differential pressure transducers Valydine P305D. The mean void fraction upstream and downstream the test section are measured by capacitance probes. High-speed movies of the flow are taken with a *PCO* 1200HS camera working at 1000 or 1500 fps. The loop pressure is set from 1 to 2 bars and the fluid circulates with mass fluxes G between 50 and 500 kg/m^2/s. A wide range of flow boiling regimes is studied, from subcooled flow boiling to saturated flow boiling, by adjusting the power input of the preheaters (vapour mass qualities up to 0.8) and the power through the ITO coating (wall heat flux up to 4.5 W/cm^2). In subcooled boiling, bubbly flow and slug flows are mainly observed. For saturated conditions, the flow patterns are slug and annular flows depending on the quality value x (Figure 1).

(a) (b) (c)

Figure 1: Flow visualisations
(a) Bubbly Flow : G = 61 kg/s/m^2, ΔT_{sub} = 11°C, q = 1.1 W/cm^2
(b) Slug Flow: G = 202 kg/s/m^2, ΔT_{sub} = 4°C, q = 1.1 W/cm^2
(c) Annular Flow : G = 88 kg/s/m^2, x = 0.20, q = 2.2 W/cm^2

The local quality along the test section x is measured from an energy balance on the preheaters and the test section. The void fraction is measured at the inlet and outlet of the test section by the capacitance probes.
The wall shear stress τ_w is measured on the adiabatic section just downstream the test section. It is deduced from the pressure gradient measured along the section by substracting the hydrostatic contribution (2nd term of the RHS of Eq.(1)) :

$$\frac{dP}{dz} = \frac{4\tau_w}{D} - g\left(\rho_V \alpha + \rho_L (1-\alpha)\right) \qquad (1)$$

The ratio of the frictional pressure gradient in two-phase flow $\frac{4\tau_w}{D}$ and in single-phase liquid flow is given by the two-phase multiplier ϕ_L^2 according to Lockhart and Martinelli [4]. In Figure 2, Φ_L is plotted versus Martinelli's parameter X, the root mean square of the ratio of liquid and vapour frictional pressure gradient, according to [4]:

$$\phi_L^2 = 1 + \frac{C}{X} + \frac{1}{X^2} \quad \text{with} \quad X = \sqrt{\frac{(dP/dz)_L}{(dP/dz)_V}} \qquad (2)$$

The constant C depends on the Reynolds number of the liquid/vapour flows. In microgravity, the results are in good agreement with Lockhart and Martinelli's correlation and also with Awad's correlation [5] adapted to microgravity flows. Similar results are also obtained for 1-g experiments. The wall friction does not seem to be sensitive to gravity in the range of investigated parameters.

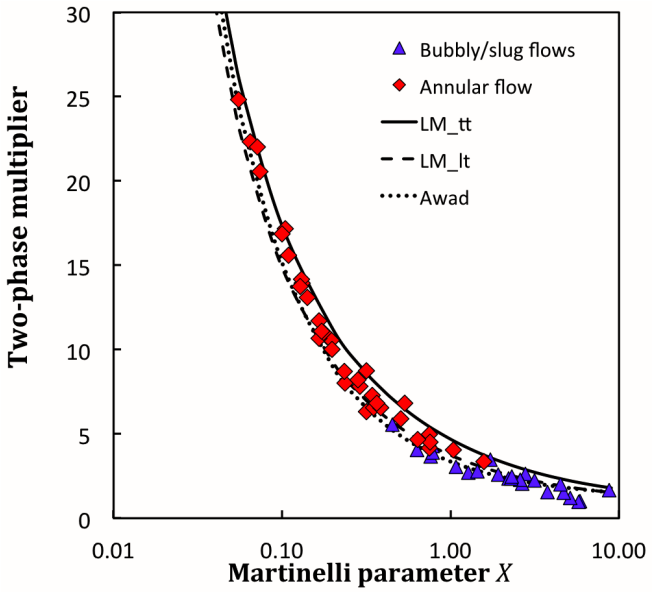

Figure 2: Frictional pressure drop in microgravity

The heat transfer coefficient is obtained from the measurement of wall heat flux q applied by Joule effect through the ITO coating and the measurement of the outer wall temperature measured with Pt100 probes. The inner temperature of the tube T_{Wi} is deduced from the outside temperature with a conduction calculation through the sapphire tube. Then, the heat transfer coefficient h is calculated versus q, T_{Wi} and T_L, the fluid temperature:

$$h = \frac{q}{T_{Wi} - T_L} \qquad (3)$$

In annular flow, the measured heat transfer coefficients are compared to the prediction of Cioncolini et Thome [6]:

$$h = \frac{k_L}{\delta} 0.0776 . \delta^+ \, Pr_L^{0.52} \quad \text{with} \quad \delta^+ = \frac{\delta u_*}{\nu_L} \qquad (4)$$

where k_L is the thermal conductivity, δ^+ is the liquid film thickness scaled by the viscous length scale. The friction velocity is determined from the pressure drop measurements and the liquid film thickness is deduced from the void fraction measurement neglecting liquid droplet entrainment:

$$\delta = \frac{D}{2}\left(1 - \sqrt{\alpha}\right) \qquad (5)$$

The experimental data are in very good agreement with the model of Cioncolini and Thome developed for dominant heat transfer convection. This good agreement can be explained by the weak effect of nucleate boiling heat transfer in the sapphire tube, which is very smooth. Despite the different film thicknesses measured in 1-g and 0-g, heat transfer coefficients are not sensitive to gravity for mass fluxes greater than 100 kg/m^2/s. Additional results can be found in [7].

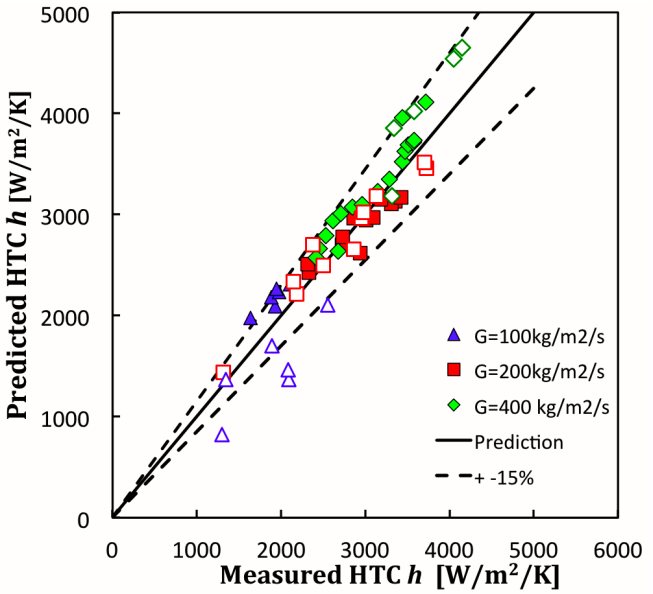

Figure 3: Heat transfer coefficients for 1-g (closed symbols) and microgravity (open symbols)

References

[1] Colin, C., Fabre, J., Mc Quillen, J., Bubble and slug flow at microgravity conditions: state of knowledge and open questions, Chem. Engng. Com., 141-142, 155-173 (1996).

[2] Ohta, H., Microgravity heat transfer in flow boiling, Advances in heat transfer, Vol 37, 1-76 (2003).

[3] Celata, G.P., Zummo, G., Flow Boiling Heat Transfer in Microgravity: Recent Progress, Multiphase Science and Technology, Vol. 21, No. 3, pp. 187–212, (2009).

[4] Lockhart, R.W., Martinelli, R.C., Proposed correlation of data for isothermal two-phase, two-component flow in pipes. Chem. Eng. Prog. Symp. Ser. 45, 39–48, (1949).

[5] Awad M.M., Muzychka Y.S., Review and modeling of two-phase frictional pressure gradient at microgravity conditions, Fluid Enginnering Division Summer Meeting ASME, Montreal, August 2010 (2010).

[6] Cioncolini, A., Thome, J.R., Algebraic turbulence modeling in adiabatic and evaporation annular two-phase flow. Int. J. Heat Fluid Flow 32, 805–817, (2011).

[7] Narcy M. De Malmazet E., Colin C., Flow boiling in tube under normal gravity and microgravity conditions, Int. J. Multiphase Flow, 60, 50–63, (2014).

Ninth International Conference on
TWO-PHASE SYSTEMS FOR GROUND AND SPACE APPLICATIONS
Baltimore, Maryland, USA, September 22-26, 2014

Enhanced Boiling Heat Transfer of FC-72 over Micro-Pin-Finned Surfaces with Jet Impingement

Yonghai Zhang, Jinjia Wei*, Xin Kong, Ling Guo

State Key Laboratory of Multiphase Flow in Power Engineering, Xi'an Jiaotong University
Xi'an 710049, China
E-mail: jjwei@mail.xjtu.edu.cn

Heat transfer characteristics of confined submerged jet impingement boiling of air-dissolved FC-72 on heated micro-pin-finned surfaces are presented. The dimension of the silicon chips is 10 × 10 × 0.5 mm^3 (length × width × thickness). Staggered micro-pin-fins with the four dimensions of 30 × 30 × 60 μm^3, 50 × 50 × 60 μm^3, 30 × 30 × 120 μm^3 and 50 × 50 × 120 μm^3 were fabricated by using the dry etching technique. For comparison, experiments of jet impinging on a smooth surface were also conducted. High-speed visualization was used to supplement trends observed in the heat transfer data. The effect of jet Reynolds number, micro-pin-fins and nozzle-to-surface distance on jet impingement boiling heat transfer were explored.

Fig. 1 shows boiling curves of chip S and staggered micro-pin-fins in submerged jet impingement boiling heat transfer under different experimental conditions, the effects of Reynolds number *Re* and jet-to-surface distance *s*/*d* on the heat transfer of chip S and staggered micro-pin-fins can be obtained. The pool boiling curves are also shown for comparison. In the low heat flux region, heat flux *q* increases linearly with wall superheat ΔT_{sat}. The heat transfer is determined by the temperature gradient, which is further determined by the thermal boundary layer. At a fixed jet-to-surface distance *s*/*d*, with increasing *Re*, the thermal boundary layer thickness decreases because of the perpendicularly direct jet impingement, and thus the heat transfer can be enhanced. In the nucleate boiling region, the boiling curves are greatly affected by *Re*. The heat flux *q* increases for a given wall superheat but the slope decreases as *Re* increases. The large bubbles can be destroyed by perpendicularly direct jet impingement, and the bubbles become smaller with increasing *Re*. After jet impingement, the small bubbles can be taken away by high cross flow rate, resulting in a lower wall temperature. Besides, there exists a certain proportion of heat transfer area for single-phase forced convection heat transfer, and thus the boiling heat transfer is greatly affected by jet velocity. The decreased slope means a large proportion of forced convection heat transfer for higher *Re*. Especially at *Re*=17120 for staggered micro-pin-fins, the slope of boiling curves is largest among all Reynolds numbers and nearly the same as that in the convection heat transfer region. This indicates that the staggered micro-pin-fins are much sensitive to large jet velocity, and the jet flow dominates the flow field. The heat transfer may be controlled by the forced convection. Besides, the departure frequency of bubbles increases and augments single-phase heat transfer considerably with increasing *Re*, and thus increases the q_{CHF}.

For smooth surface as shown in Fig. 1, the heat transfer performance in submerged jet impingement boiling for *Re*=5707, 11414, 17120 is better than that in pool boiling in both single-phase and two-phase heat transfer region. As shown in Fig. 1, staggered micro-pin-fins show different heat transfer performance. In the single-phase heat transfer region, all staggered micro-pin-fins show better heat transfer performance in submerged jet impingement boiling, because the thermal boundary layer thickness decreases due to the perpendicularly direct jet impingement. In the two-phase heat transfer region, the heat transfer performance of all staggered micro-pin-fins in submerged jet impingement boiling is better than that in pool boiling for all three flowrates except for S-PF30-60 and S-PF30-120 at *Re*=5707. The staggered micro-pin-fins with large fin height and small fin gap usually have large micro-convection heat transfer proportion with large flow resistance. At lower *Re*=5707, jet impact force with small flowrate is not strongly enough to overcome large flow resistance for chip S-PF30-60 and S-PF30-120. Meanwhile, jet impact force onto the surface suppresses the bubbles growth and shortens the bubbles' stay time on the surface, and thus weakens the micro-convection, so the nucleate boiling process is highly restrained. However, jet flow can destroy larger bubbles and take them away from the heater at high heat fluxes compared with pool boiling. Consequently, S-PF30-60 and S-PF30-120 show higher critical heat flux than that of pool boiling in the nucleate boiling region at *Re*=5707.

The effect of nozzle-to-surface distance, *s*/*d*, of submerged jet impingement boiling on chip S and different staggered micro-pin-fins at *Re*=5707, 11414, 17120 and ΔT_{sub}=35 K can also be obtained in Fig. 1. It can be found that decrease of nozzle-to-surface distance, *s*/*d*, enhances the potential core and augments single-phase heat transfer considerably at a fixed *Re*, and thus enhances heat transfer for chip S. For staggered micro-pin-fins, CHF enhancement increases as *s*/*d* decreases. At all three Reynolds numbers, small nozzle-to-surface distance, *s*/*d*=1, can obtain largest CHF, but for *s*/*d*=3, a lower wall temperature can be obtained compared with the other two nozzle-to-surface distances.

Besides, it can be seen that all staggered micro-pin-fins show an obvious heat transfer enhancement compared with smooth surface due to heat transfer area enhancement from Fig. 1. The ratios of staggered micro-pin-finned surface area to smooth surface area are 2.2, 3.0 3.4 and 5.0 for chips S-PF50-60, S-PF30-60, S-PF50-120and S-PF30-120, respectively. The value of *h*/*p* is 0.6, 1.0, 1.2 and 2 for chips S-PF50-60, S-PF30-60, S-PF50-120 and S-PF30-120, respectively. In the low heat flux region, there are only a small number of bubbles, and the heat transfer is dominated by the forced convection. As illustrated above, the micro-pin-fins with large fin height and small fin gap usually have large micro-convection heat transfer proportion with large flow resistance. S-PF50s with small value of *h*/*p* can be sensitively affected by jet flow, and thus show better heat transfer performance in the convection heat transfer region than that of S-PF30s with the same fin height,

especially at low *Re* conditions. In fact, we can observe that the heat transfer performance of S-PF30-60 is nearly the same as chip S at low heat fluxes from Fig. 1, indicating that small jet flow velocity only has a little effect on enhancing effective heat transfer area of S-PF30-60. However, with increasing *Re*, large jet flow velocity can overcome flow resistance and enlarge effective heat transfer area. Consequently, S-PF30s and S-PF50s with the same fin height show nearly the same heat transfer performance in the convection heat transfer region at *Re*=17120.

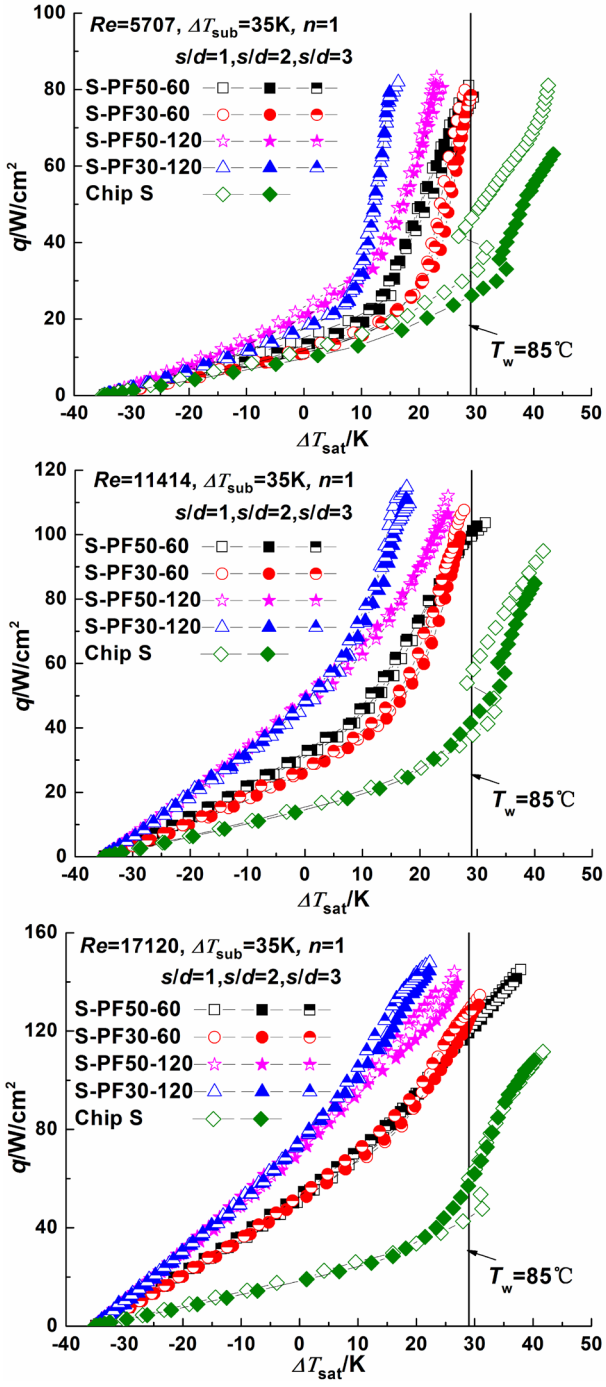

Figure 1 Boiling curves of chip S and staggered micro-pin-fins

In the high heat flux region, jet flow can destroy the bubble and take them away. With increasing *Re* In Fig. 1, at all Reynolds numbers, S-PF120s show better heat transfer performance including CHF and wall superheat than that of S-PF60s with the same fin thickness due to the increase of surface area. Here, heat transfer area enhancement ratio is a key factor in nucleate boiling heat transfer at small Reynolds number. Although S-PF50-120 has a lower flow resistance and thinner thermal boundary layer than that of S-PF30-120, the heat transfer area enhancement ratio, 3.4, is much lower than that of S-PF30-120, 5.0, and thus S-PF30-120 shows lower wall superheat and larger CHF, especially at *Re*=5707. S-PF50-60 has smallest flow resistance and a thinnest thermal boundary layer among all micro-pin-fins, and the heat transfer area difference between S-PF50-60 and S-PF30-60 is not very large, thus S-PF50-60 shows lower wall superheat and larger CHF than S-PF30-60. With increasing *Re*, the thermal boundary layer can be diminished by large jet flow velocity for both smooth surface and micro-pin-fins, and larger velocity can overcome large flow resistance of PF30s to make more effective heat transfer area. As a result, chip S-PF30s show better heat transfer performance than that of S-PF50s with the same fin thickness as shown in Fig. 1, indicating that jet velocity is a key influence factor in the whole heat transfer at large Reynolds numbers. Besides, the slopes of nucleate boiling curves decrease as *Re* increases. For small *Re*, the jet flow can not affect the whole side surfaces, and thus nucleate boiling heat transfer can play an important role on the fin side surfaces at large heat fluxes, resulting in steeper boiling curves. For large *Re*, convective heat transfer dominates the boiling heat transfer process due to larger jet velocity.

In general, the ratio of fin height to fin pitch, *h/p*, and jet velocity are key parameters affecting boiling heat transfer for micro-pin-fins. The bubble nucleations on the bottom and side wall surface are easily affected by the jet flow over the chips when *h/p* is small and/or the jet velocity is large, which prevents the burst of nucleate bubbles and reduces the proportion of nucleate boiling. The micro-convection and thin liquid layer evaporation due to the bubble generation in the gap are the reason for the significant enhancement of boiling heat transfer on micro-pin-fins.

Acknowledgement: We gratefully acknowledge the financial support from NSFC (No 51225601).

References

[1] Martin, H., Heat and mass transfer between impinging gas jets and solid surfaces, Advances in Heat Transfer, vol.13, pp. 1-60(1977)

[2] Brevet, P., and Dejeu, C., et al., Heat transfer to a row of impinging jets in consideration of optimization, International Journal of Heat and Mass Transfer, vol. 45, no. 20, pp. 4191-4200(2002)

[3] Wei, J. J., and Honda, H., Effects of fin geometry on boiling heat transfer from silicon chips with micro- pin-fins immersed in FC-72, International Journal of Heat and Mass Transfer, vol. 46, pp. 4059–4070 (2003)

[4] Agostini, B., Fabbri, M., Park, J. E., et al., State of the Art of High Heat Flux Cooling Technologies, Heat Transfer Engineering, vol. 28, no. 4, pp. 258-281(2007)

[5] Ibuki, K., Umeda, T., and Fujimoto H., Heat transfer characteristics of a planar water jet impinging normally or obliquely on a flat surface at relatively low Reynolds numbers, Experimental Thermal and Fluid Scinence, vol. 33, pp.1226-1234(2009)

Air entrainment and cavity generation in solid-liquid impact

H. Ding*, B.Q. Cheng and C.Y. Zhang

Department of Modern Mechanics, University of Science and Technology of China
96 Jinzhai St, Hefei, China
* hding@ustc.edu.cn

We investigate the fluid dynamics in solid-liquid impact, characterized by the occurrence of air entrainment and cavity generation. The water-entry problems are ubiquitous in nature, ranging from the impact of falling stone with water surface to the water slapping of Basilisk lizard running on water. Many phenomena have been extensively studied previously. Bergmann et al. [1] studied the pinch-off process of a giant air bubble in water by pulling a disk through the water surface. Duez et al [2] showed that hydrophobicity promotes air entrainment by impacting spheres. Aristoff and Bush [3] investigate the influence of Webber and Bond numbers on the water-entry cavity and the resultant cavity regimes. In these phenomena the motion of contact lines, where solid/liquid/gas meet, plays an important role, e.g., a cavity is formed only when the contact line eventually rests on the side of the solid object. However, the manner in which contact line moves and the flow mechanisms that results in pinned contact lines remain unclear. In this talk we mainly consider a cylinder plunging into a liquid pool and focus on the flow mechanisms that results in pinned contact lines and the related flow patterns. The transition of flow phenomena are investigated through experiments and simulations over relevant ranges of Weber ($=\rho U^2R/\sigma$) and Reynolds ($=\rho UR/\mu$) numbers and contact angles, where U is the impact velocity, ρ the density, σ the surface tension, μ the viscosity and R the radius of the solid object.

A sketch of the experimental setup is shown in Fig. 1. A steel sphere or cylinder of radius of 1mm is initially held by an electromagnetic device at a certain height above a water container. After being released, it falls through a vertical tube with a size slightly larger than the cylinder, effectively avoiding any rotation in contact with the water. The impact dynamics is then recorded from the side view by a high-speed camera (up to 0.1 million frames per second).

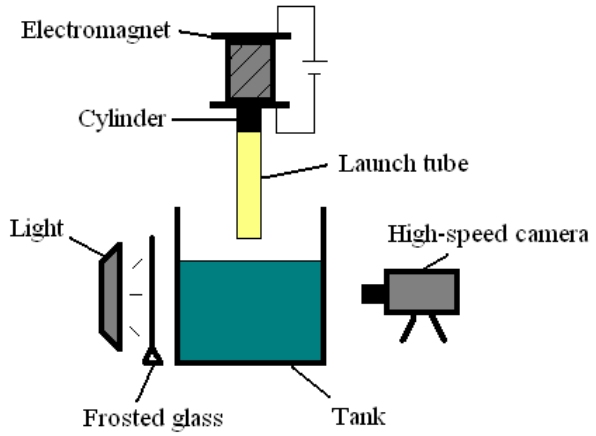

Figure 1: A schematic diagram of the experimental set-up.

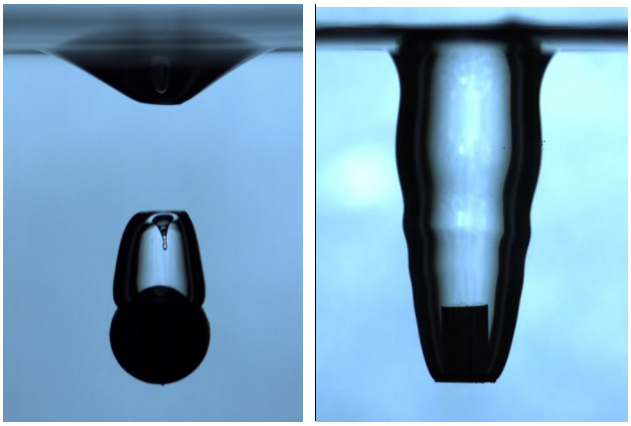

Figure 2: Plunging of a sphere (left) and a cylinder (right) of radius of 1mm into water at a speed of 1.25m/s. The contact angle in both case are about 110º to 120º.

Our experiments indicate that the geometry of the impinging object significantly affects the regime of the air entrainment. Fig. 2 shows that the impact of a sphere produces a bubble attached at the downstream of the sphere while the impact of a circular cylinder generates an open cavity in the similar conditions. Clearly, it is the motion of the contact line that makes the difference.

In order to gain further insights into the flow behavior, we simulate the water-entry process by using a diffuse interface method, which is capable of simulating two-phase flows with large density and viscosity ratios [3] and allows for moving contact lines [4,5]. We consider here a cylinder steadily plunging into water at a constant speed, and the gravitational force is assumed to be negligible in the short duration of impact.

Numerical simulations reproduce all the regimes of air-entrainment observed in experiments, including no cavity, bubble attachment and open cavity, as shown in Fig. 3.

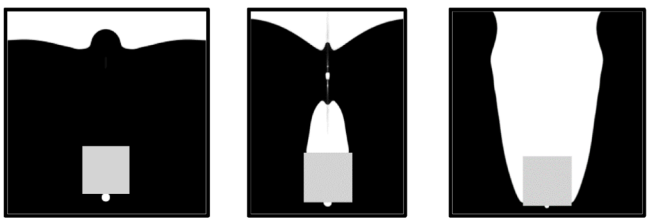

Figure 3: Regimes of air-entrainment in plunging of a cylinder into water: no cavity, bubble attachment and open cavity, as listed from the left to right.

Moreover, the numerical results are validated by comparing against the experiments under the same flow conditions, with respect to the cavity shape and the contact line position, as shown in Fig. 4.

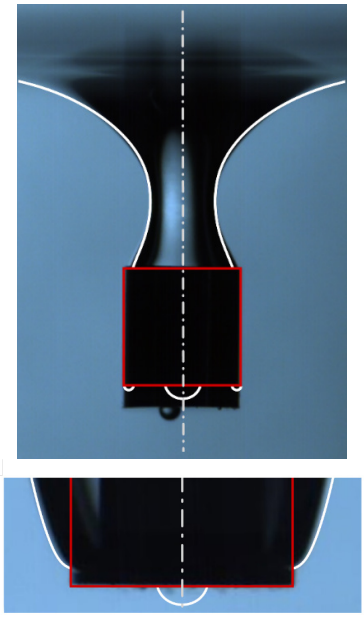

Figure 4: Result comparison for the bubble attachment (upper, We=3.2 and Re=316) and the open cavity (lower, We=16 and Re=706). Red lines represent the geometry of the circular cylinder in simulations and white lines for the interface.

Numerical results suggest that the generation of open cavity is closely associated with pinned contact lines, which is consistent with experiments. Fig. 5 shows Snapshots of cavity shapes in the non-inertial frame attached to the cylinder. Once the contact lines are formed at the cylinder surface, they are quickly decelerated and pinned somewhere near the upstream edge of the cylinder. The subsequent evolution of the interface and flow field at the upstream appears to enter a steady state, although the flow and the interface at the rear of the body is usually unsteady, with the capillary waves that arise from the impact propagating downstream and radially outwards.

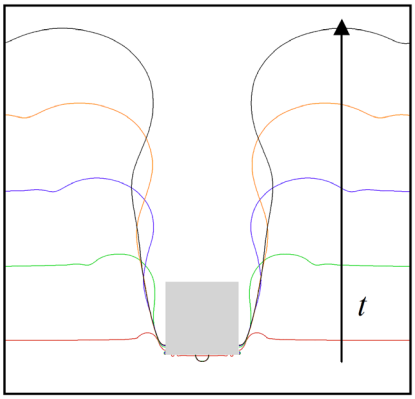

Figure 5: Snapshots of cavity shapes in the non-inertial frame of the cylinder. The arrow indicates the direction of time.

Observation of steady flows around the pinned contact lines suggests that the force balance across the interface in the vicinity of the contact line can be approximated by the Young-Laplace equation,

$$\Delta p = \sigma (1/R_1 + 1/R_2) \quad (1)$$

where R_1 and R_2 are the respective principle radii of curvature. Provided the negligible variation of pressure in the air, a low pressure zone on the liquid side near the contact line is required in order to balance the interfacial force.

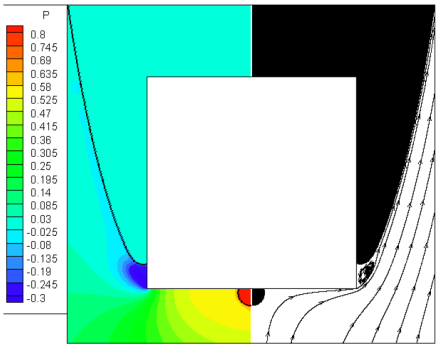

Figure 6: A typical flow pattern for the open cavity regime, at We=30, Re=968 and an advancing contact angle of 90°.

A typical flow pattern for the regime of open cavity is shown in Fig.6, in which small eddies stationary relative to the cylinder occur at the forward side of the cylinder. The streamlines close to the forward face of the cylinder pass around the standing eddies and overlap with the interface. The low pressure at the eddy center arises from the flow acceleration around the cylinder edge, i.e. Bernoulli theorem, and the radial pressure gradient due to the circulation around the vortex. The later mechanism, which is absent in the impact of sphere into water, leads to a decrease of pressure of order ρv_{max}^2, where v_{max} is the maximum circumferential velocity outside the vortex. This explains the earlier appearance of the open cavity in the impact of a cylinder on water than that of a sphere.

Other fluid mechanisms will also be discussed in the talk, such as the dynamic competition between the eddy growth and the contact line motion, and the effect of wettability, thickness and impact speed of the cylinder on the flow behaviors.

References

[1] Bergmann, R., Stijnman, M., Sandtke, M., van der Meer, D., Prosperetti, A. & Lohse, D. Giant bubble pinch-off. Phys. Rev. Lett. 96, 154505/1–4 (2006)

[2] Duez, C., Ybert, C., Clanet, C., Bocquet, L. Making a splash with water repellency. Nat. Phys. 3, 183–183 (2007)

[3] Aristoff, J.M. & Bush, J.W.M. Water entry of small hydrophobic spheres. J. Fluid Mech. 619, 45–78 (2009)

[4] Ding, H. & Spelt, P.D.M. Wetting condition in diffuse interface simulation of contact line motion. Phys. Rev. E 75, 046708 (2007).

[5] Ding, H., Spelt, P.D.M. & Shu, C. Diffuse interface model for incompressible two-phase flows with large density ratios. J. Comput. Phys. 226, 2078–2095 (2007)

[6] Ding, H. & Spelt, P.D.M. Onset of motion of a three-dimensional droplet on a wall in shear flow at moderate Reynolds numbers. J. Fluid Mech. 599, 341–362 (2008)

Electric Field Effects On Bubbles In Microgravity

Ezinwa Elele[1], Dana Qasem[2], John Tang[3], Boris Khusid[4]

New Jersey Institute of Technology, Department of Chemical Engineering, Biological and Pharmaceutical Engineering
University Heights, Newark, NJ, USA
[1] eoe4@njit.edu; [2] dbq2@njit.edu; [3] jt97@njit.edu; [4] khusid@njit.edu

An electric field is known to provide a body force in two-phase flows that mitigates effects of reduced gravity in heat transfer systems [1]. Contrary to conventional field-based microgravity techniques, the main idea behind our electro-hydrodynamic (EHD) method is to apply an alternating current (AC) field directly to a fluid via capacitive coupling [2]. An electrically insulated energized electrode is inserted in a fluid vessel, whereas current techniques utilize a bare energized electrode. A grounded electrode is mounted on an insulated external wall of the fluid vessel, whereas current techniques utilize a bare grounded electrode also placed inside the vessel. To reduce charge accumulation in the system, high voltage pulses alternating in polarity are applied to an energized electrode. The chance of short circuit, sparking, electrochemical deterioration of a fluid and electro-corrosion of the system components would be therefore drastically reduced. These features offer the ability of using EHD phenomena in liquids with much higher electrical conductivity.

In this paper we present results of experiments conducted in microgravity and terrestrial environments. Microgravity tests were conducted in four flights aboard the NASA Zero-Gravity aircraft in Houston, TX, July 30–August 2, 2013. Following [3, 4], experiments were conducted at the boiling regime controlled by the fluid surface tension under normal and microgravity conditions as the heating element size, L_h, was taken such that $L_h \le 2.1L_c$, where $L_c = \sqrt{\gamma_f / g(\rho_f - \rho_v)}$ is the capillary length with the fluid surface tension γ_f, fluid ρ_f and vapor ρ_v densities and gravity acceleration g. The conceptual design of the setup is shown in Fig. 1. Each cuvette was equipped with a platinum temperature sensor (2.3 x 2.0 x 1.3mm; Innovative Sensor Technology, Las Vegas, NV) acting as heater to produce bubbles. The sensor was embedded into a PDMS slab mounted at the bottom of the cuvette such that the open sensor cover was lying in the same horizontal plane as the slab surface (Fig. 1). Experiments were conducted on bubbles formed in boiling distilled water (properties at room temperature: 1 g/cm^3 density, 72 mN/m surface tension, 1 cP viscosity, 80 dielectric constant, $1.5\cdot10^{-4}$ S/m conductivity measured before experiments) and Novec fluid HFE-7100 (3M, St. Paul, MN; properties at room temperature: 1.48 g/cm^3 density, 13.6 mN/m surface tension, 0.61 cP viscosity, 7.4 dielectric constant, $3\cdot10^{-8}$ S/m conductivity, 61°C boiling point); $L_c \approx 2.7$ mm for water and 0.9 mm for HFE-7100. The behavior of a fluid subjected to a time-varying electric field depends on the ratio between the time scale of the field variation, t_e, and the relaxation time of electric charges, $t_{rel} = \varepsilon_0\varepsilon_f / \sigma_f$ with the vacuum permittivity ε_0 and the fluid dielectric constant ε_f and conductivity σ_f; $t_{rel} =$ 5μs for distilled water and 2.2 ms for HFE-7100. Electric charges in both fluids followed the field variation as t_e lied within the range 0.05 to 0.1 s in our experiments.

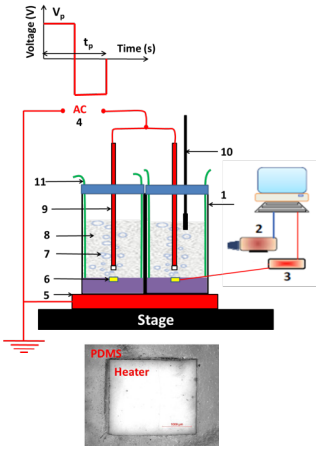

Figure 1: Experimental setup: 1, fluid cell; 2, imaging system; 3, data acquisition system; 4, high voltage AC amplifier controlled by a programmable function generator; 5, grounded electrode; 6, two mini-heaters; 7, bubbles; 8, liquid; 9, energized electrode with insulated tip; 10, surface temperature probe; 11, connections of heaters to DC power.

Each temperature sensor was connected in series with a low voltage DC power supply and a resister of 8.3 Ohm. The voltage drop across each resistor was recorded at 500 Hz by the data acquisition system and used to compute the electrical current through, the voltage drop across the temperature sensor, the sensor resistance and the power produced by the sensor. The sensor resistance was used for calculation of the sensor temperature based on the calibration curve. Each cuvette was charged with 1 mL of either liquid before the flight and then closed with the lid which was intentionally not hermetically sealed as dictated by flight safety requirements. A long energized electrode coated with Teflon was mounted in the cuvette lid such that its tip was located in the vicinity of the heater (Fig. 1). The electrode was connected to the high voltage amplifier to generate an electric field in the fluid.

A low voltage DC power supply was turned on to produce bubbles in a fluid during zero gravity portions of a flight parabola and, for comparison, in ground experiments over the periods of time as those in flight tests. To evaluate the electric field effects on the bubble motion, a train of rectangular voltage pulses of 3-4 kV with polarity alternated

in frequency of 10 – 20 Hz was applied by the high voltage amplifier to the energized electrode during the zero gravity portion of selected flight parabolas and in ground experiments. The fluid flow and the bubble formation and motion were recorded by the camera during the entire flight and in ground experiments. Flight tests confirmed the ability of the EHD method to apply an electric force to a fluid in microgravity via capacitive coupling to electrically insulated electrodes. While water was subjected to high voltage pulses, no electrical short circuit and sparking occurred during flight and ground operations.

As heating was turned on, a large bubble rapidly formed over the heater (Fig. 2). The bubble did not detach during the acceleration portion of the parabola and remained on the heater up to 19 consecutive parabolas. Recorded videos indicate that the bubble was pinned to the heater edges. The bubble pinning caused by capillary forces can be attributed to a substantial difference in wettability between the heater cover (glass with base aluminum oxide) and the PDMS surface. Experiments in microgravity were conducted up to the heater temperature of 150^0C and the heat flux of 0.7 MW/m^2. A similar bubble evolution in distilled water was also observed under normal gravity when heating was periodically switched on and off over periods of time as those in flight tests. When water was continuously heated in ground experiments, a bubble detached the heater after 12 min as the water surface temperature rose to about 65°C (Figs. 3). In the presence of a bubble on the heater, the heat flux of up to 1.2 MW/m^2 and the heater temperature of up to 250°C were recorded in ground experiments.

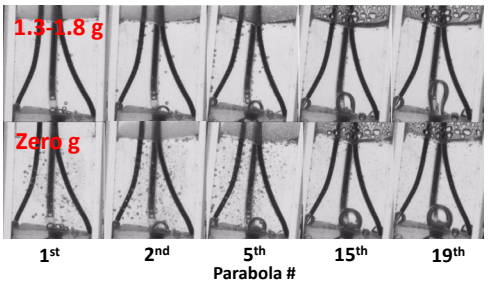

Figure 2: Photos of a bubble formed in water under microgravity and remained on the heater up to 19 consecutive parabolas; heat flux 0.7 MW/m^2, heater temperature 150^0C, rectangular voltage pulses 4kV/20Hz.

A large bubble pinned to the heater was observed to emit sporadically microbubbles in microgravity. Tracking individual microbubbles was used to compute their trajectories around the large bubble and estimate velocities under applied voltage pulses 4kV/20Hz and without a field (Fig. 4). The bubble trajectories in the absence of an electric field resemble streamlines of the thermocapillary flow observed in subcooled nucleate pool boiling in FC-72 and common refrigerants under microgravity and predicted by computer simulations [1, 5]. Comparison of data with and without voltage pulses demonstrates that the EHD forces suppress velocity fluctuations and stabilize the flow pattern and the motion of microbubbles in water under microgravity (Fig. 4). The EHD forces were found to increase the heat flux in water by about 10% at the same superheat. These observations are similar to data reported in Ref. [6] on the DC field contribution to the boiling performance of small heaters in FC-72 under microgravity in parabolic flights. The reason for it can be attributed to the fact that an electric force exerted on growing bubbles in water appears to be relatively weak to remove them away from a heater.

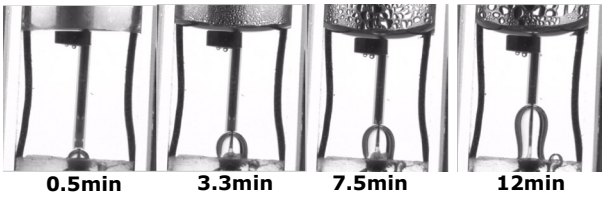

Figure 3: Ground experiments. A bubble detached the heater after 12 min in continuously heated water when the water surface temperature rose to about 65°C.

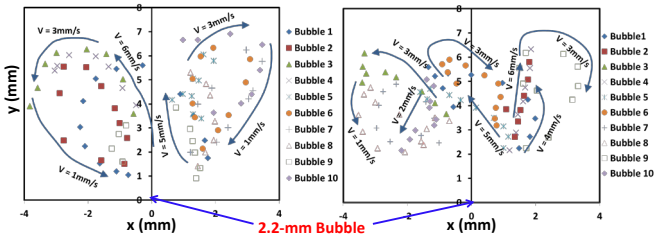

Figure 4: Microgravity. A large bubble in water pinned to the heater emitted microbubbles. Trajectories of individual microbubbles around the large bubble and estimated velocities under 4kV/20Hz (*left*) and without field (*right*).

Acknowledgement
The work was supported by NASA grant NNX09AK06G and NASA/NJIT Space Act Agreement.

References

[1] Di Marco, P., Influence of force fields and flow patterns on boiling heat transfer performance: A review, ASME Journal of Heat Transfer 134, 030801-1-15 (2012)

[2] Elele, E., Shen, Y., Khusid, B., Electrodeless electrohydrodynamic printing of personalized medicines, Applied Physics Letters 97, 233501-1-4 (2010)

[3] Raj, R., Kim, J., Heater size and gravity based pool boiling regime map: transition criteria between buoyancy and surface tension dominated boiling, ASME Journal of Heat Transfer 132, 091503-1-10 (2010)

[4] Raj, R., Kim, J. McQuillen, J., On the scaling of pool boiling heat flux with gravity and heater size, ASME Journal of Heat Transfer 134, 011502-1-13 (2012)

[5] Wu, J., Dhir, V.K., Numerical simulation of dynamics and heat transfer associated with a single bubble in subcooled boiling and in the presence of noncondensables, ASME Journal of Heat Transfer 133, 041502-1-14 (2011)

[6] Di Marco, P., Raj, R., J Kim, J., Boiling in variable gravity under the action of an electric field: results of parabolic flight experiments, Journal of Physics: Conference Series 327, 012039-1-14 (2011)

Bubble Injection to Increase the Thrust of a Nozzle

Xiongjun Wu, Jin-Keun Choi, and Georges L. Chahine

DYNAFLOW INC.
10621-J Iron Bridge Road, Jessup, MD 20794, USA
wxj@dynaflow-inc.com

Evidence of jet thrust increase through injection and growth of bubbles in a water stream has been anecdotally reported by experimentalist and inventors for the past 50 years [1]-[2]. Our recent studies have aimed at investigating the existence and extent of such an augmentation under controlled laboratory settings [3]-[6]. The present work extends the effort to large local Mach numbers.

Using 2D and 3D divergent-convergent nozzles, we have been able to demonstrate net thrust augmentation over a conventional waterjet as high as 70% with injected air volume fractions in the range of 50%. In parallel, we developed and validated two-phase flow numerical codes to simulate and predict the performance of the bubbly nozzle flow. These included a continuum model coupled with bubble dynamics and a coupled Eulerian-Lagrangian model, where the continuum flow field was described by the viscous flow solver 3DYNAFS-VIS© and the bubbles were tracked and their dynamics computed by 3DYNAFS-DSM©.

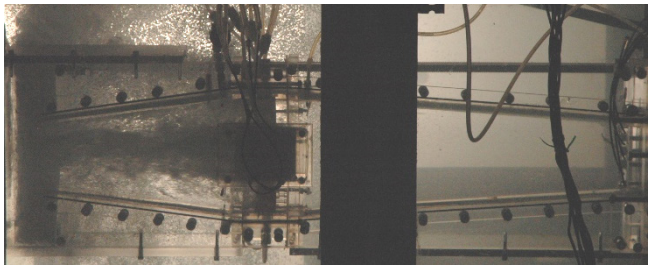

Figure 1: View of the 3-D nozzle experiment setup with air injection.

Figure 1 shows a picture of one of the experimental setups where microporous PTFE sheets were used to inject microbubbles into the flow. Figure 2 shows the percent thrust increase with increased air flow input obtained from numerical simulations and experiments. Both indicate that the air injection becomes more efficient with increased input void fraction. Existing literature indicates that even higher thrust augmentations could be achieved if choked flow conditions could be achieved in a convergent-divergent nozzle [7]-[9]. As the air volume fraction increases, the speed of sound in the bubbly mixture decreases dramatically and could drop to less than 20 m/s, which makes it possible for the local mixture flow velocities to exceed the speed of sound in the medium. This would result in choked conditions at the nozzle throat and result in a supersonic flow in the divergent section of the nozzle. Here we present the results of our study with a convergent-divergent shape nozzle design selected to enable observation of potential choked flow conditions and measurement of thrust augmentation. Figure 3 shows the selected nozzle geometry and Figure 4 shows a sample image of the bubbly mixture flow through the nozzle with nominal void fraction of 15.5% and water flow rate of 50 gpm. The air was injected into the bulk of the liquid upstream of the nozzle using a bundle of long porous tubes located near the axis of the feed pipe.

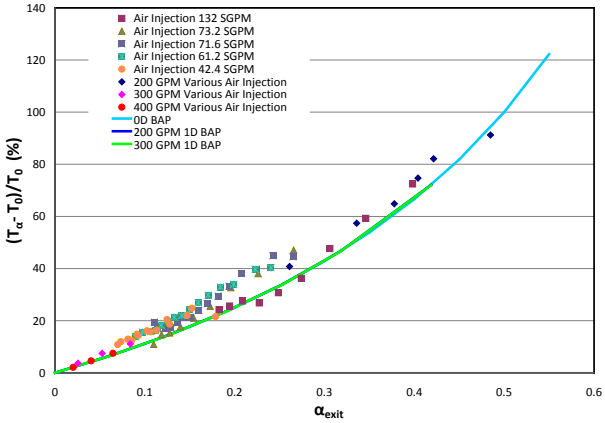

Figure 2. Variation of thrust augmentation with void fraction normalized by thrust in absence of bubble injection.

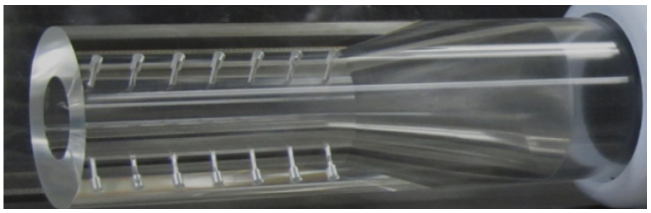

Figure 3. Picture of the convergent-divergent nozzle used in this study. Upstream diameter 2.067 in, throat diameter 1.0 in, and exit diameter 1.065 in.

Extensive measurements were performed at various liquid and air flow rates in order to examine the resulting flow behaviors. Figure 5 shows the mixture pressure and Figure 6 shows the distribution of the average mixture velocity calculated based on the measured water flow rate and local void fraction along the nozzle for several nominal air injection rates while the water flow rate was fixed at 100 gpm. As Figure 5 shows, in the absence of bubble injection or at low void fractions, the pressure in the nozzle divergent section increases toward the exit as the average flow velocity decreases with the increased area. As the void fraction increases the pressure gradient gradually reduces, and then reverses the sign, resulting in a throat pressure higher than the exit ambient pressure. This could indicate a mixture flow in the nozzle similar to that which occurs in a choked two-phase flow, or could result from an effective area available to the liquid flow, which continually decreases between the inlet and the exit due to local variations of the air volume fraction. Although no evidence of a two-phase shock has been observed so far from the flow visualizations, the average mixture velocities and the mixture sound speeds

(estimated from calculations of the void fraction) approach each other, as seen in Figure 6, indicating a possible supersonic flow. Higher injection rates that require modification of the hardware are presently in process.

Figure 4. Photo from a high speed video of the bubbly flow in the convergent divergent nozzle. Water flow rate at 50 gpm and nominal void fraction 15.5%.

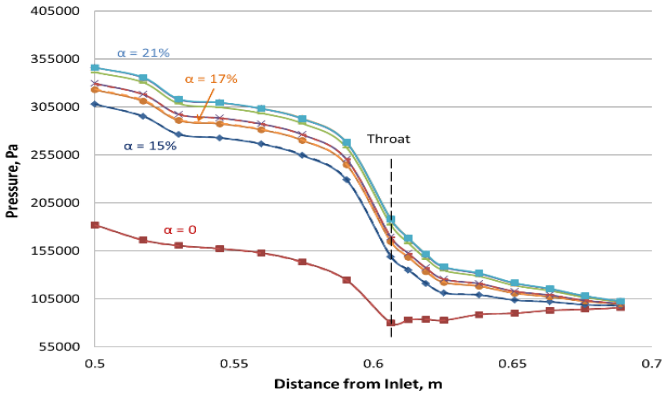

Figure 5. Measured pressure distributions along the axial direction at various void fractions. Water flow rate is fixed at 100 gpm.

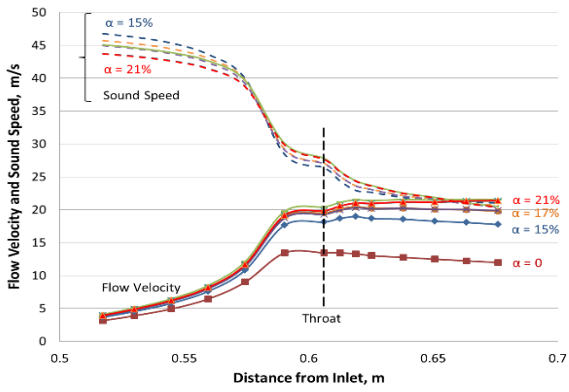

Figure 6. Average mixture velocity and sound speed deduced from void fraction along the length of the nozzle at various nominal void fractions. Water flow rate is fixed at 100 gpm.

In parallel to the experimental study, we have extended the 3D numerical method to handle higher void fractions and enable simulations of high thrust augmentation conditions. Figure 7 illustrates a simulated mixture flow in the nozzle at a void fraction of 30%. Also, a two-fluid model based on the concept that bubble volume change modifies the cross-section area effectively occupied by the liquid in the nozzle has been developed and can explain most of the experimental results including the sign reversal of the pressure gradient. It indicates the need to further increase the speed and void fraction to achieve a supersonic region.

Tests with increased liquid speed and void fraction are on-going to achieve the aforementioned larger cross-over, and updated test results will be reported in the presentation.

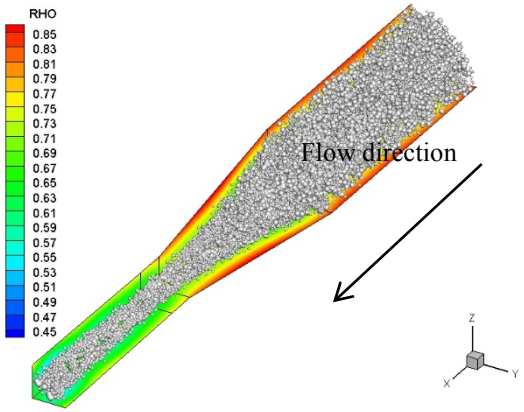

Figure 7. Simulation of bubbly mixture flow in the convergent-divergent flow nozzle using 3DYNAFS©. Water flow rate 100 gpm, initial bubble radii 0.5 and 1 mm, void fraction 30%.

Acknowledgement

This work was supported by the Office of Naval Research under contract N00014-11-C-0482 monitored by Dr. Ki-Han Kim. This support is very highly appreciated.

References

[1] Mottard E.J. and Shoemaker, C.J. "Preliminary Investigation of an Underwater Ramjet Powered by Compressed Air", NASA Technical Note D-991, 1961.

[2] Schell C. and Ornoff H., "Hydro-Pneumatic Ram-Jet", US Patent 3,171,379, 1965.

[3] Wu, X., Choi, J.-K., Singh, S., Hsiao, C-T, and Chahine, G. L., "Experimental and Numerical Investigation of Bubble Augmented Waterjet Propulsion", *Journal of Hydrodynamics*, Vol. 24, No. 5, pp.635-647, 2012.

[4] Singh, S., Choi J.-K., Chahine, G.L., "Optimum Configuration of an Expanding-Contracting-Nozzle for Thrust Enhancement by Bubble Injection", *Journal of Fluids Engineering*, Vol. 134, No. 1, 2012.

[5] Wu, X., Singh, S., Choi, J.-K., Chahine, G.L., "Waterjet Thrust Augmentation using High Void Fraction Air Injection", 29th Symposium on Naval Hydrodynamics, Gothenburg, Sweden, August 2012.

[6] Wu, X., Choi, J.-K., Hsiao, C.-T., Zhang, Q., and Chahine, G. L., "Bubble Augmented Waterjet Propulsion: Numerical and Experimental Studies", 28th Symposium on Naval Hydrodynamics, Pasadena, California, September 12-17, 2010.

[7] Brennen, C., "Fundamentals of Multiphase Flow", Cambridge University Press, 2005.

[8] Singh, S., Fourmeau, T., Choi, J.-K., Chahine, G.L., "Thrust Enhancement through Bubble Injection into an Expanding-Contracting Nozzle with a Throat", *Journal of Fluids Engineering*, 2014 (in press).

[9] Mor, M., Gany, A., "Analysis of Two-Phase Homogeneous Bubbly Flows Including Friction and Mass Addition", *Journal of Fluids Engineering*, Vol. 126, pp.102-109, January 2004.

Bubbles growth behavior in a direct methanol fuel cell under different gravity level

Fang Ye*[1,a], Ziguang Yang[1,b], Hang Guo[1,c], Longyun Xu[1,d], Chongfang, Ma[1,e]

[1]MOE Key Laboratory of Enhanced Heat Transfer and Energy Conservation and Beijing Municipal Key Laboratory of Heat Transfer and Energy Conversion, College of Environmental and Energy Engineering, Beijing University of Technology, 100 Pingleyuan, Chaoyang District, Beijing 100124, China,
[a]yefang@bjut.edu.cn (*Corresponding author), [b]ziguangyang@emails.bjut.edu.cn, [c]hangguo@sohu.com ,
[d]xulongyun@emails.bjut.edu.cn, [e]machf@bjut.edu.cn

Introduction

Direct methanol fuel cells (DMFC) have many benefits to be an attractive power source for small devices in spacecraft: requirements of compact system design, easy refueling, low cost of fuel, quick start-up, ambient temperature and pressure operation.

In direct methanol fuel cells, methanol is directly oxidized on the anode side without any reforming process, while oxygen is introduced into the cathode and is reduced. The electrochemical reactions on anode and cathode of DMFC are as follows:

Anode: $CH_3OH + H_2O \rightarrow CO_2 + 6H^+ + 6e^-$ (1)

Cathode: $\frac{3}{2}O_2 + 6H^+ + 6e^- \rightarrow 3H_2O$ (2)

Passive DMFCs do not use external devices to supply methanol or oxygen, so it has been identified as one of the most promising candidates to replace batteries in micro power applications[1-2]. A lot of experiment an simulation research have been carried out on passive DMFC[3-5], but two phase flow behavior in anode under microgravity has not been studied.

This paper presents the bubble growth behavior at different placement angles in a passive direct methanol fuel cell with transparent anode.

Experimental

The experimental system involves a direct methanol fuel cell, a rotatable platform, an electrical load device, camera, and other auxiliary devices (Fig. 1).

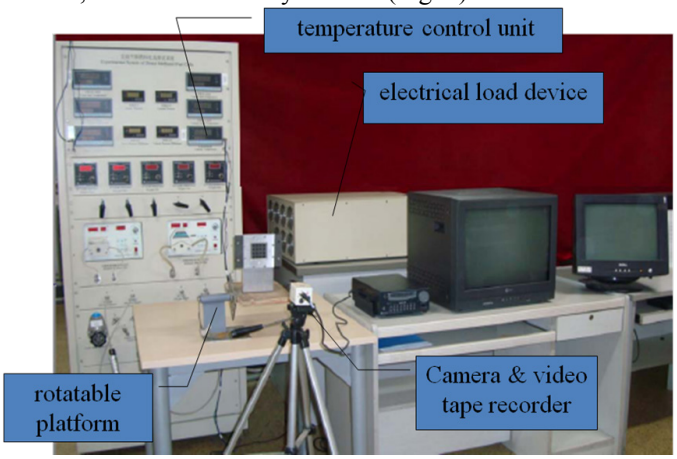

Figure 1: Self made fully passive direct methanol fuel cell and the experimental system.

The fuel cell could be rotatable during the experiments. The angle between the anode normal direction of the fuel cell and the gravity direction is the inclination angle β. (Fig. 2)

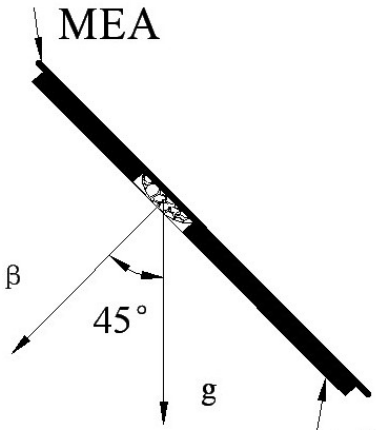

Figure 2: The angle of the cell anode normal direction and gravity direction g is the inclination angle β

Photos of anode of the passive direct methanol fuel cell would be taken when the fuel cell was working (Fig. 3).

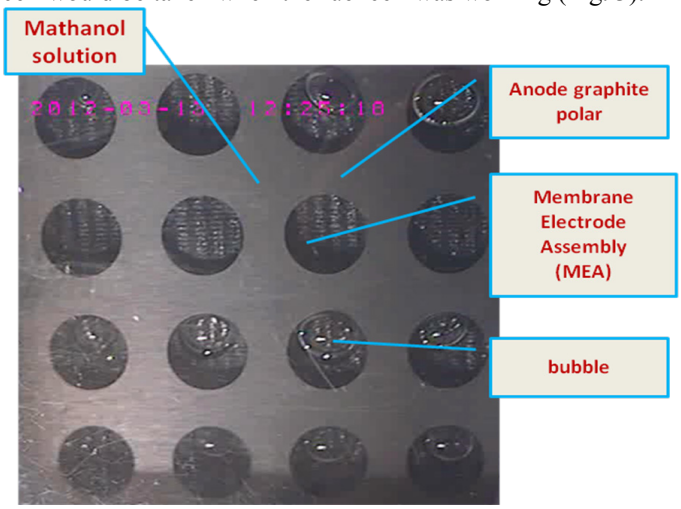

Figure 3: The photo shows the bubbles in the anode of the passive direct fuel cell

Results and discussions

The angle β between fuel cell anode and gravity direction express the force direction on the fuel cell. 30°, 45°, 60°, 90°, 120°, 135°, 150° were selected.

It is found that the bubble growth cycle time, formation position and the diameter of bubble detach from the membrane will have significant difference under different angles. When β < 90°, the growth time will

markedly longer (Fig. 4) than it is at $\beta \geq 90^{o}$ (Fig. 5), and the diameter will be much bigger. When $\beta > 90°$, it will has the bubble formation position not only one again which will has at $\beta < 90°$. There is also some observation when the fuel cell chemical reaction stop in the experiment. Simply analysis about that is presented in this paper as well.

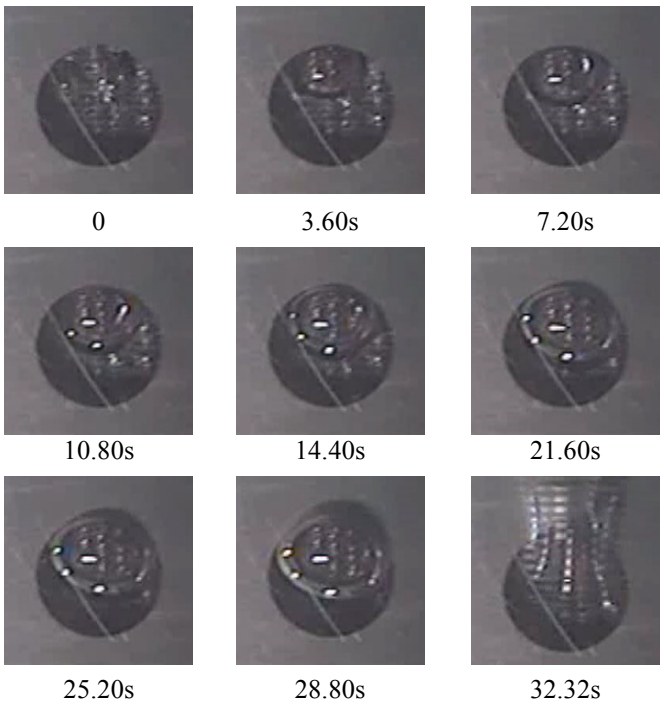

Figure 4: A bubble's growth behavior in 30°inclination angle

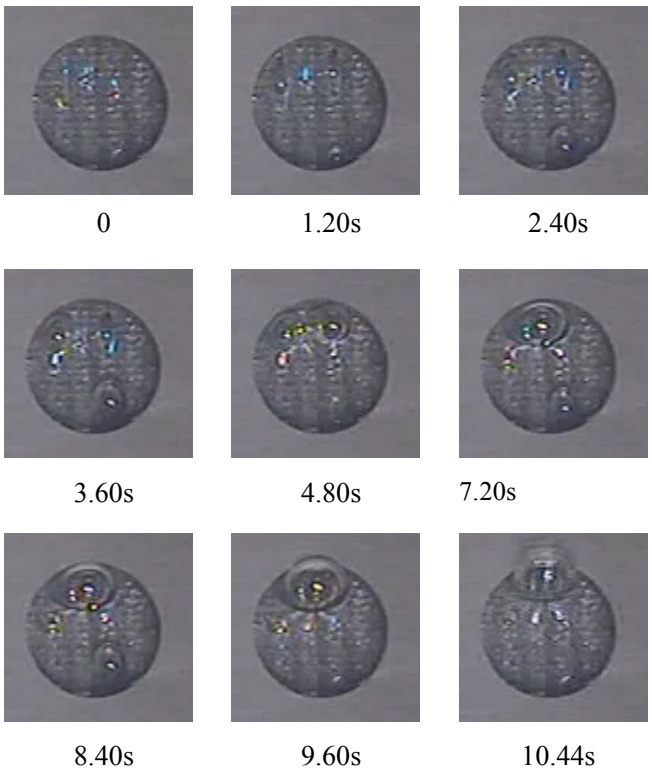

Figure 5: A bubble's growth behavior in 120° inclination angle

Conclusions

Experimental study of a liquid fed passive direct methanol fuel cell has been conducted under different gravity levels.

The gravity effcet is prominent on the bubble growth in the anode of the passive direct methanol fuel cell.

The bubble growth time, formation position and the diameter of bubble detach from the membrane have significant difference at different angles.

When $\beta < 90°$, the growth time will markedly longer than it is at $\beta \geq 90°$, and the diameter will be much bigger.

Acknowledgement

This work is supported by the National Natural Science Foundation of China (Grant Nos.: 50976006, 11102005), Program for New Century Excellent Talents in University (Grant No.: NCET-10-0006), Specialized Research Fund for the Doctoral Program of Higher Education (Grant No.: 20121103110009), and Opening project of national microgravity laboratory, the Chinese Academy of Sciences.

References

[1] T.S. Zhao, C. Xu, R. Chen, W.W. Yang, Mass transport phenomena in direct methanol fuel cells, Progress in Energy and Combustion Science, 35, 275-292 (2009).

[2] O. Gholami, S.J. Imen, M. Shakeri, Effect of non-uniform parallel channel on performance of passive direct methanol fuel cell, International Journal of Hydrogen Energy, 38, 3395-3400 (2013).

[3] B. Bae, B.K. Kho, T. Lim, et. al., Performance evaluation of passive DMFC single cells, Journal of Power Sources, 158, 1256–1261 (2006).

[4] R. Chen, T.S. Zhao, Performance characterization of passive direct methanol fuel cells, Journal of Power Sources, 167, 455-460 (2007).

[5] J.G. Liu, T.S. Zhao, R. Chen, et. al., The effect of methanol concentration on the performance of a passive DMFC, Electrochemistry Communications, 7, 288-294 (2005).

Future ESA experiments in Two-phase Heat and Mass Transfer Research on-board the International Space Station

Balázs Tóth[1)], Olivier Minster[2)], Hans Ranebo[2)] on behalf of
ESA's Science, Payload Development and Operations teams, Science Teams[3)] and Space Industries[4)]

[1)] HE Space Operations for ESA, NL-2201DK Noordwijk, The Netherlands, E-mail: balazs toth@esa-external.com
[2)] ESA-ESTEC, NL-2200AG Noordwijk, The Netherlands, E-mail: olivier.minster@esa.int
[3)] Science Teams: Absolut System (FR), Air Liquide (FR), AIST (JP), Alfa Laval (IT), Airbus Defence and Space (Bremen, DE), AUTh (GR), CEA (FR), CCNY (US), CSI (DE), DIAS (IT), ENEA (IT), ENSMA (FR), EPFL (CH), Euro Heat Pipes (BE), IITK (IN), IMFT (FR), INSA-LYON (FR), IT (RU), KTH (SE) LAPLACE (FR), MARS (IT), NLR (NL), P' (FR), Politecnico di Milano (IT), Selex ES (IT), SIT (JP), SMU (US), Thalès Aliena Space (FR), TUD (DE), UCLA (US), ULB (BE), UNIHEAT (IT), ZARM (DE), Universities of Aix-Marseille (FR), Altai State (RU), Bergamo (IT), Edinburgh (UK), Illinois (US), Kyushu (JP), Liège (BE), Loughborough (UK), Maryland (US), Mons-Hainaut (BE), Ochanomizu (JP), Padova (IT), Pisa (IT), Purdue (US), Toronto (CA), Utsunomiya (JP), York (CA)
[4)] Space Industries: Airbus Defence and Space (Friedrichshafen, DE), QinetiQ Space and Lambda-X

Assessing two-phase heat transfer phenomena, where capillary forces play significant role is often challenging on ground. In the majority of the regimes gravity masks certain processes making the representation of the observations difficult. In some particular cases by creating small scale set-ups, the effect of the gravitational field can be minimised. Nevertheless, this solution imposes further challenges to the diagnostic systems, which are mostly optical.

Therefore, researchers often use microgravity condition, where the influence of gravity (i.e. natural convection, buoyancy) can be significantly reduced. To support such studies, the *European Space Agency* (ESA) makes its various microgravity platforms (e.g. drop tower, parabolic flights, sounding rockets, space missions) available for scientific purposes through the *European Programme for Life and Physical Sciences in Space* (ELIPS). [1]

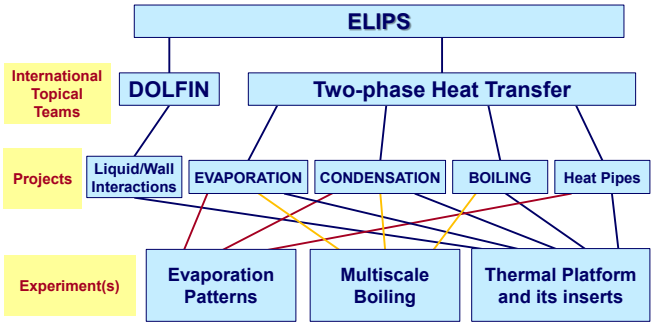

Figure 1: **Two-phase heat transfer experiments on the International Space Station (ISS) and projects in ELIPS**

The aim of the present contribution is to provide an update of the two-phase heat transfer experiments envisaged by ESA, focusing on gas-liquid phase change and wettability related phenomena within the frameworks of the utilisation of the *International Space Station* (ISS). The context of these experiments within the ELIPS programme is pictured in Figure 1. They serve the objectives of the *Liquid-Wall Interactions*, *EVAPORATION*, *CONDENSATION*, *BOILING* and *Heat Pipes* research projects (further details are given below and in [1]), which are coordinated in the framework of the *DOLFIN* (Dynamics of Liquid Film/Wall Interactions) and *Two-phase Heat Transfer* international topical teams. All the experiments are planned to be conducted in the *Fluid Science Laboratory* (FSL) in the Columbus module of the ISS (see Figure 2).

Figure 2: The Fluid Science Laboratory

Evaporation Patterns (historically: Convection and Interfacial Mass Exchange (CIMEX)) aims at studying the evaporation induced convection patterns and associated gas-liquid interface phenomena. Under ESA contract, Airbus Defence and Space (in Friedrichshafen) is responsible for the overall development, QinetiQ Space is responsible to develop the Fluid Cell Assembly and Lambda-X takes care of the optical subsystems of the experiment.

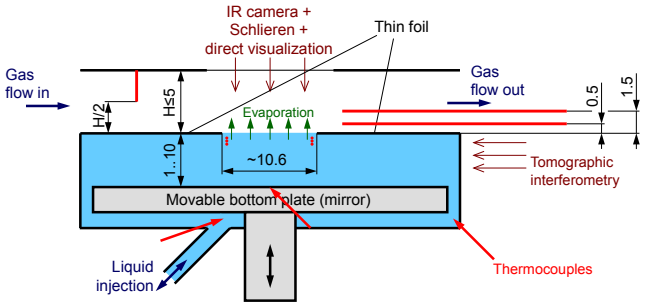

Figure 3: Schematic of the evaporator cell of the *Evaporation Patterns* experiment

The *Multiscale Boiling* (historically: Reference mUltiscale Boiling Investigation (RUBI)) experiment aims at studying the fundamentals of boiling by analysing the behaviour of a single vapour bubble with particular attention to the role and behaviour of the three-phase contact line. Furthermore, *Multiscale Boiling* is designed to quantify the effect of external forces on the bubble dynamics, such as a shear flow or an electric field. The hardware is being developed by Airbus Defence and Space under ESA contract.

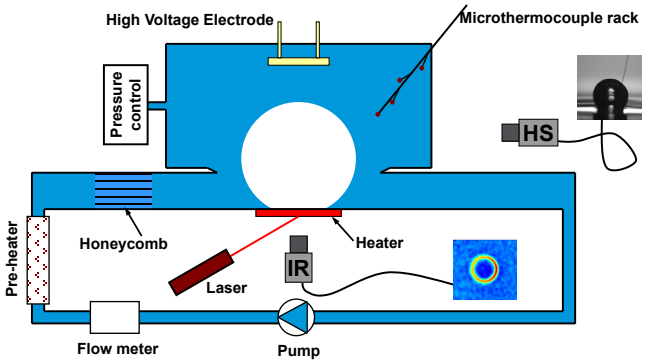

Figure 4: Schematic of the boiling cell of the *Multiscale Boiling* experiment

To allow a relatively simple implementation of fundamentally similar two-phase flow loops with moderately complicated measurement techniques, the concept of *Thermal Platform* was proposed and studied.

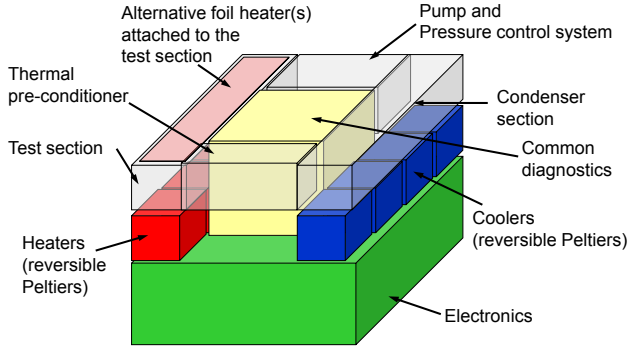

Figure 5: Conceptual schematic of Thermal Platform (the grey transparent object mimics the detachable insert)

Installed into the Fluid Science Laboratory as a standard Experiment Container, the platform will provide for heating and cooling of the test cells of interchangeable flow loops as well as commonly required (primarily optical) diagnostics (see also Figure 5). Two consortia lead by QinetiQ Space and Airbus Defence and Space were contracted in 2012 by ESA to elaborate the potential design of Thermal Platform at phase A level. Both concluded positively on its feasibility. The users of Thermal Platform will include the members of the Heat Pipes, Liquid-Wall Interactions, EVAPORATION, CONDENSATION and BOILING projects.

At the time of the preparation of the present abstract the following experiments and the corresponding inserts to Thermal Platform were identified:

- *Self-rewetting Fluid* targets the assessment of the heat transfer performances of self-rewetting liquid mixtures, with particular attention to the vapour-liquid interface temperature distribution and liquid film thickness distribution as well as film stability and the dry patch formation. The effect of substrate characteristics and different mixtures would be tested in dedicated inserts.
- *Pulsating Heat Pipes* aims at transient and steady Pulsating Heat Pipe thermal performance studies, flow pattern analysis and local pressure fluctuation with various working fluids and geometries exploring also in inertia dominated regimes in large hydraulic diameter tubes.
- *Drop Evaporation* would investigate thermocapillary convection and vapour diffusion processes as well as the effect of electric field on a series of volatile sessile drops.
- *Boiling* would assess the effect of confinement, shear flow and electric field on a vapour bubble. Particular mixtures and the investigation of non-condensable gas impact are among the most significant objectives.
- *Condensation on Fins* targets liquid film thickness distribution characterisation on a single condenser finger for average and local heat transfer coefficient assessment. Surface roughness and the test liquid are among the envisaged experiment parameters.
- *Enhanced Evaporators* targets global heat transfer performance characterisation of multi-scale evaporator structures. Evaporation regimes, wetted area and consequently the three-phase contact line would be characterised together with the critical heat flux (boiling limit) in a capillary pumped loop.
- *Marangoni in Films* aims to better understand heat transport to a volatile liquid film, through film thickness evolution and dynamics characterisation as well as the vapour concentration distribution. Surfactants are considered as a potential parameter.
- *Shear Driven Film* focuses on determining the heat transfer coefficient, liquid dynamics, film thickness evolution, stability and eventual dry spot formation in liquid films under shear flow influence up-to critical heat flux.
- *In-Tube Condensation* targets void fraction, flow regime and stability characterisation as well as heat transfer coefficient (distribution) measurements and film thickness measurements for annular flow regime in various shapes of tube cross sections;

There is obviously room for other experiments to utilise the capabilities provided with Thermal Platform.

References

[1] Tóth, B., Future Experiments to Measure Liquid-Gas Phase Change and Heat Transfer Phenomena on the International Space Station, Microgravity Science and Technology, Volume 24, Number 3, pp 189-194 (2012)

Introduction and Status of hardware development for Boiling and Two-phase Flow Experiments onboard ISS/Kibo

Takashi Kurimoto[1], Satoshi Matsumoto[1], Haruo Kawasaki[1], Kenichiro Sawada[1], Hitoshi Asano[2], Osamu Kawanami[3], Koichi Suzuki[4], Ryoji Imai[5], Yasuhisa Shinmoto[6] and Haruhiko Ohta[6]

[1]Japan Aerospace Exploration Agency, 2-1-1 Sengen, Tsukuba, Ibaraki, 305-8505 Japan
kurimoto.takashi@jaxa.jp
[2]Kobe Univ., Dept. Mechanical Engineering, 1-1 Rokkodai, Nada, Kobe, Hyogo, 657-8501 Japan
[3]Univ. of Hyogo, Dept. Mechanical and System Engineering, 2167 Shosha, Himeji, Hyogo, 671-2280 Japan
[4]Tokyo Univ. Science-Yamaguchi, Dept. Mechanical Engineering, 1-1-1 Daigaku-Dori, Sanyo-Onoda, Yamaguchi, 756-0884 Japan
[56]Muroran Institute of Technology, Dept. Mechanical, Aerospace and Materials Engineering, 27-1 Mizumoto-cho, Muroran, Hokkaido, 050-8585 Japan
[6]Kyushu University, Dept. Aeronautics and Astronautics, 744 Motooka, Nishi-ku, Fukuoka 819-0395 Japan

Introduction

The amount of waste heat would be larger and larger, because space platform size and its power consumption are expected to become bigger and bigger in recent year. In this situation, higher efficiency is required for thermal management system. Boiling and two-phase flow becomes powerful means for this system because boiling is one of the most efficient modes of heat transfer due to phase change. A lot of experiments on boiling were performed to obtain heat transfer coefficient under microgravity conditions. However, they are not concluded how the boiling heat transfer is affected in microgravity.

So the experiment on boiling and two-phase flow under microgravity conditions onboard the International Space Station (ISS) is proposed to investigate the effect of gravity on boiling heat transfer [1-3]. The experiment provides fundamental understandings on the behavior of liquid-vapor flow and the mechanism of heat transfer under microgravity conditions. The knowledge can be applied to the design of high-performance space thermal management systems.

This candidate of space experiment is now ongoing the development phase of experiment equipment. In this paper, the Engineering Model (EM) for the microgravity experiment is introduced and the test in order to verify the performance and feasibility to be used in the Kibo module of ISS is explained.

Experimental Equipment

The target configuration of our experiment is a flow boiling. Pumped loop with preheater, two kind of main heater sections, adiabatic observation section and condenser is employed (Fig. 1). Pure normal-perfluorohexane (nPFH) is used for coolant as a test fluid. After the preliminary design of experiment equipment, the engineering model (prototype) is produced as shown in Fig. 2. The dimension is 500 x 800 x 650 mm and the mass is 140 kg. TPF-EE will be accommodated in the Work Volume (WV) of the Multi-purpose Small Payload Rack (MSPR) onboard the ISS/Kibo.

Using this apparatus, we intend to perform the experiment of the heat transfer with flow boiling. At the same time, we study the mechanism of liquid-vapor behaviors in two-phase flow under the microgravity condition.

Test results

Several tests using the Engineering Model (EM) have been performed to verify the performance and quality which satisfy the scientific and safety requirements and endure the launch and onboard environments. All the test have been cleared. (i.e. Functional Test, Thermal Data Acquisition Test, Vibration Test (Fig. 3), Excitation Force Test, Electromagnetic Compatibility Test, Rack Interface Test, etc.)

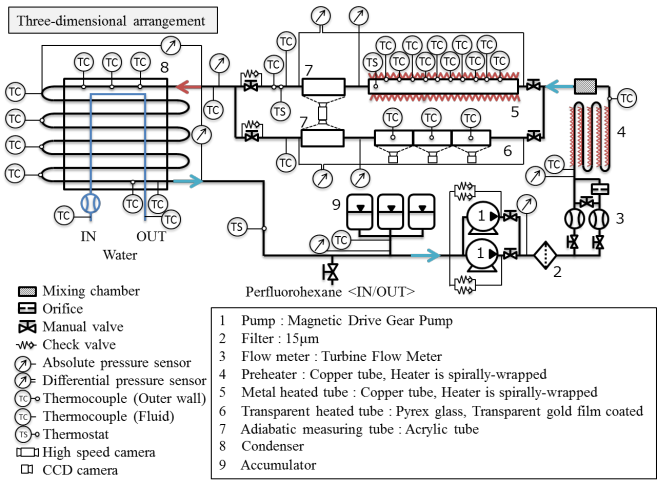

Figure 1: Schematic diagram of pumped loop for TPF-EE.

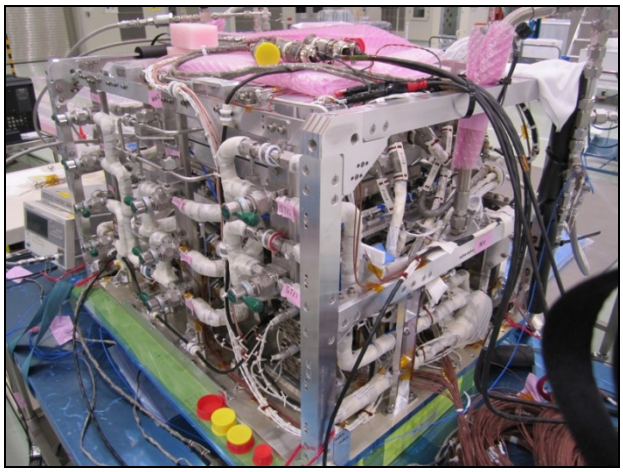

Figure 2: Picture of Engineering Model.

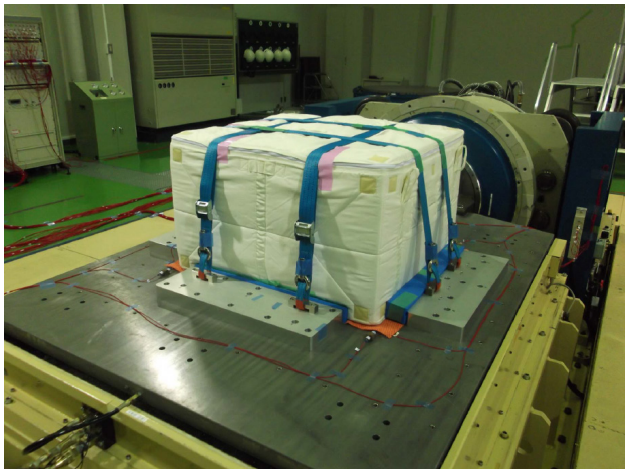

Figure 3: Vibration Test of TPF-EE (launch configuration).

Safety Issue

Hazardous material (perfluoroisobutylene, PFIB) may be produced from the test fluid (nPFH) when temperature of the fluid exceeds 600 ºC during experiment [4]. Unintentional production of this hazardous material will cause loss of crew, injure crew or lead to crew illness.

NASA Payload Safety Review Panel showed the criterion that the highest temperature of nPFH must be controlled below 600 ºC to prevent formation of PFIB.

We performed chemical analysis of nPFH to get more available information for safety analysis and experiment equipment design. The analysis is done to obtain the formation of PFIB from nPFH under several temperature conditions. Analysis results are shown in Table 1.

(1) PFIB was found above 850 ºC.
(2) No PFIB was detected at 600 ºC.

We can design TPF hardware to prevent the maximum temperature of the test fluid from rising up to 600 ºC even if the runaway overheat happened by any chance.

Table 1: Analysis Results of the Test Fluid.

Heating Temperature [ºC]	Percentage of PFIB [%]
1050	36.5
850	8.7
600	0

Milestone

Now we aim to launch and on orbit experiments in 2016 as scheduled in Table 2.

Table 2: Schedule of the Two-Phase Flow experiment.

SDR (System definition review)	Apr. 2010 (approved)
PDR (Preliminary design review)	Jan. 2012 (approved)
Engineering Model manufacturing and Testing	
CDR (Critical design review)	Mar. 2014
Proto Flight Model manufacturing and Test	
PQR (Post-qualification test review)	Oct. 2015
Preparation for flight	
Launch and on orbit experiments	2016

Acknowledgments

The authors gratefully acknowledge all project members participated from Kyushu Univ., Kobe Univ., Univ. of Hyogo, Tokyo Univ. Sci. Yamaguchi, Muroran Institute of Technology, IHI Aerospace Co., Ltd., JAMSS and JSF.

References

[1] Ohta, H., Fujii, K. and Kawasaki, H., Preparation for Flow Boiling Experiment on Board ISS Recent Progress, Fifth International Topical Team Workshop on TWO-PHASE SYSTEMS FOR GROUND AND SPACE APPLICATIONS, September 26-29, 2010, Kyoto, Japan

[2] Baba, S., Sawada, K., Kubota, C., Wada, Y., Shinmoto,Y., Ohta, H., Asano, H., Kawanami, O., Suzuki, K., Imai, R., Kawasaki, H., Fujii, K., Takayanagi, M., Yoda, S., Proposal of Experimental Setup on Boiling Two‐phase Flow on‐orbit Experiments onboard Japanese Experiment Module "KIBO", Journal of Physics: Conference Series vol.327 No.012055 Journal of Physics) (2011)

[3] Fujii, K., Komasaki, M., Kurimoto, T., Kawasaki, H., Sawada, K., Suzuki, K., Asano, H., Kawanami, O., Imai, R., Shinmoto, Y. and Ohta, H., Recent Progress in JAXA Project of Boiling Two-Phase Flow Experiment onboard ISS, J. Physical Science and Application, Vol.2, No.4, 71-79 (2012)

[4] Arnold, W.A. and McQuillen, J., Chemical Characterization and Thermal Stressing Studies of Perfluorohexane Fluids for Space-Based Applications, J. Spacecraft and Rockets, Vol. 44, No. 1, 94-101 (2007)

High-speed imaging system for two-phase flow research on the International Space Station

Jeffrey R. Mackey

Vantage Partners, LLC
3000 Aerospace Parkway, Brook Park, OH 44142, U.S.A.
Jeffrey.R.Mackey@nasa.gov

Nancy R. Hall, Mohammad M. Hasan, James D. Wagner, Henry K. Nahra, Rochelle L. May, Robert L. Butcher and John S. Kolacz

NASA Glenn Research Center, 21000 Brookpark Road
Cleveland, OH 44135, U.S.A.

Hyoungsoon Lee, Christopher Konishi, and Issam Mudawar

Boiling and Two-Phase Flow Laboratory (BTPFL)
Mechanical Engineering Building, 585 Purdue Mall
West Lafayette, IN 47907-2088, U.S.A.

Multi-phase flow studies usually require visual data collection from high-frame rate cameras and/or imaging systems. In heat exchanger studies involving flow boiling [1] as well as flow condensation [2], many challenges exist due to the flow geometries, illumination, spatial resolution and temporal resolution required to capture image data of sufficient quality to accomplish the underlying scientific analysis. Such imaging system challenges are compounded when attempted in space. The unique properties of the radiation environment encountered in the International Space Station (ISS) prohibit the long-term use of many high frame rate imaging systems that are otherwise quite suitable for terrestrial studies.

In this paper we will analyze the design and performance of a moderately high frame rate digital imaging system for two-phase flow studies and examine the effects of cosmic radiation [3] on its various components and on the system as a whole.

At first glance, it may seem appropriate to attempt space-based imaging studies using the same imagers used for ground-based, reduced gravity aircraft or suborbital research studies. Many of these high frame rate imagers come preconfigured with on-board flash memory capable of receiving and storing high resolution images extremely fast. Some are capable of over 13,000 frames per second at 1k x 1k pixel resolution. Although these imaging features are extremely desirable for multi-phase flow analysis, problems associated with their use in space include large size and mass, limiting their use in constrained volumes such as the ISS Fluids Integration Rack (FIR) or in the ISS Glove box. However, the main problem is that many such systems are intolerant of cosmic radiation and are prone to suffer permanent damage that can render the imager useless. The time it takes for such radiation damage to occur may vary greatly because of the random nature of cosmic ray strikes.

In order to study flow boiling and condensation effects in microgravity, a relatively high frame rate imaging system is required to operate nominally aboard ISS for a period of at least one year. Since the experiment volume is limited, it is desirable to design the imaging system to be small, have low mass and be capable of surviving the ISS radiation environment.

The initial Flow Boiling and Condensation (FBCE) imaging system was based on a camera-link architecture and PCI-express bus. This system is suitable for testing multiple cameras simultaneously for development and data gathering purposes and this system has been tested aboard the Zero-G aircraft. Its main components are three 2k x 1k full camera-link 10-tap cameras, three full camera-link frame grabber boards, an ATX motherboard with a X-79 chipset, 64 GB of RAM for image buffering and several solid-state 1 TB hard drives for fast image transfer from RAM and more permanent image storage. This initial PC-based imaging system was tested using a custom flow boiling module with reduced gravity test images shown in Fig. 1 below.

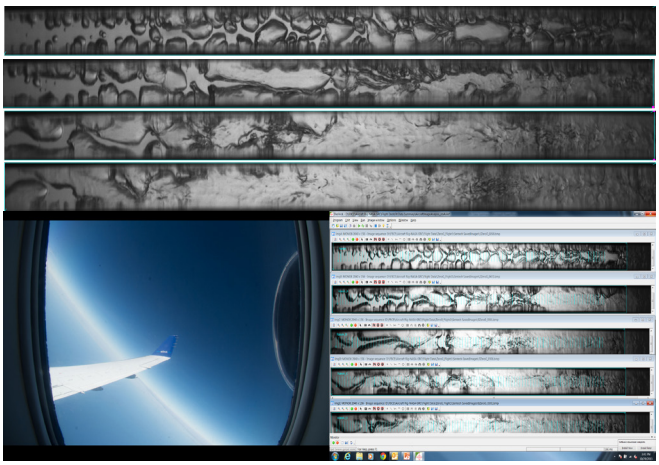

Figure 1: (Top) Images of flow boiling using two heaters in microgravity illustrating development of critical heat flux from top to bottom image. (Bottom) Processed images and view from aircraft during low gravity period.

The flow boiling images were acquired to RAM at a frame rate of 2,217 frames per second during the low-g portion of each parabola. Image transfer to hard drive took several seconds and was thus performed during the hyper-g

portion of each parabola. Operating the imaging system in such a manner allowed low-g portions of every parabola to be captured and stored for post-flight analysis.

A separate part of the FBCE test section involves flow condensation along a metal tube. FC72 is heated in the fluid loop and introduced as vapor into the custom condensation module manufactured at NASA Glenn Research Center in Cleveland, Ohio, U.S.A. A portion of the condensation tube, camera lens, reflective prism and illumination is shown at the top of Fig. 2 while an acquired image is shown in the middle of this figure and wavelength analysis is shown at the bottom of the same figure.

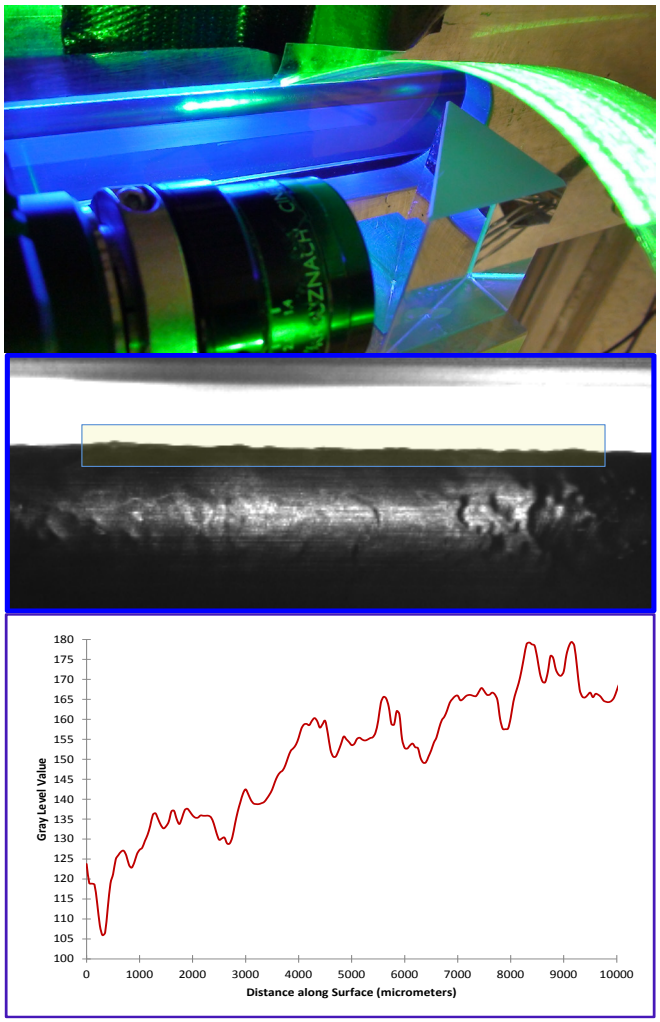

Figure 2: (Top) Camera lens, prism, woven fiber line light, backlight and condensation tube. (Middle) Image captured by PCIe/104 imaging system showing region of analysis in top box. (Bottom) Gray level as a function of position from left to right along the region of analysis.

In order to accommodate volume constraints in the FIR, the updated version of the imaging system was developed as a PCIe/104 stack, which is similar in footprint to the PC-104 stacked computers that have a successful history performing ISS research. There are somewhat greater restrictions on RAM and other attributes when comparing PCIe/104 to ATX or other computer architectures. Our prototype PCI-express 104 stack is equipped with 8 GB of RAM for image buffering, which allows for approximately 10 seconds worth of image data at 2040 x 86 pixel resolution at a frame rate of 4,000 frames per second. This 10 second time duration assumes that 1 GB is reserved for the operating system.

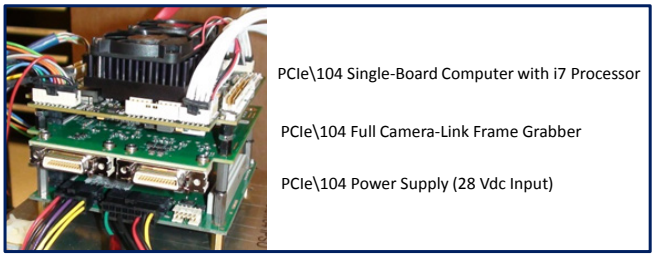

Figure 3: PCIe/104 stack with single-board computer, camera-link frame grabber and power supply.

Once the imaging systems were constructed and tested for functionality, the next step in their characterization was to test them in a radiation environment that will emulate the ISS environment. For this purpose, components and subsystems were taken to the Indiana University Cyclotron Facility (IUCF) in Bloomington, IN and tested in a high energy proton beam [3]. The main components tested in September 2013 involved several candidate cameras and a PCIe frame grabber board. The PCIe/104 systems, including several PCIe/104 single-board computers, a PCIe/104 frame grabber, PCIe/104 power supply and several solid-state hard drives will be tested in March 2014 with results and analysis included in the final paper.

The radiation tests at IUCF were conducted to proton levels of 600 rad, or approximately one year of ISS radiation dose. Cameras that were tested and survived include a Sentech model STC-CMB2MCL (39.4 days MTBF), a Lumenera model LT225M - USB 3.0 Camera (10.2 days MTBF) and a Euresys Grablink Full Frame Grabber (37.9 days MTBF). All of the aforementioned components experienced undesirable issues such as latch-ups and image readout problems but all issues were recoverable by cycling power to the devices under test[1].

References

[1] H. Zhang, I. Mudawar and M. M. Hasan, Flow boiling CHF in microgravity, International Journal of Heat and Mass Transfer, 48, 3107–3118 (2005)

[2] H. Lee, I. Park, C. Konishi, I. Mudawar, et.al., Experimental Investigation of Flow Condensation in Microgravity, J. Heat Transfer 136 (2), 1-11 (2014).

[3] F. A. Cucinotta, M. R. Shavers, P. B. Saganti, J. Miller, Radiation Protection Studies of International Space Station Extravehicular Activity Space Suits,NASA/TP-2003-212051 (2003) http://techreports.larc.nasa.gov/cgi-bin/NTRS

[4] C. C. Foster, S. L. Casey, A. L. Johnson, P. Miesle, N. Sifri, A. H. Skees and K. M. Murray, Riation Effects Test Facility at the Indiana University Cyclotron Facility, http://iuco.indiana.edu/doc/research-pub-radiation-effects-research.pdf

[1] Component names are presented for information purposes only. NASA does not endorse any product in this paper.

Ninth International Conference on
TWO-PHASE SYSTEMS FOR GROUND AND SPACE APPLICATIONS
Baltimore, Maryland, USA, September 22-26, 2014

Interfacial Deformation and Internal Flow during Rotational Breakup of Electrostatic Levitated Droplet

Soma Watahiki[1], Satoshi Matsumoto[2], Akiko Kaneko[1] and Yutaka Abe[1]

[1]University of Tsukuba, Graduate school of System and Information Engineering, 1-1-1, Tennoudai, Tsukuba, Ibaraki 305-8573, Japan
[2]Japan Aerospace Exploration Agency, Institute of Space and Astronautical Science, 2-1-1, Sengen, Tsukuba, Ibaraki, 305-8505, Japan
okahca916@gmail.com

1. Introduction

Under the microgravity environment, liquid can be treated without container due to weightless. Therefore physical properties of materials are expected to be measured with high accuracy [1]. However, in viscosity measurement of a levitated droplet, there has been no method to measure the viscosity of the droplet in the range of 0.1 to 100 Pa.s. A new method for measuring viscosity by applying the principle of Liquid Filament Rheometer (LFR) [2] to rotational breakup of the levitated droplet in that viscosity range has been presented by Tanaka et al. [3]. However, the error in the measurement is about ±30%. In order to establish the viscosity measurement, it is necessary to investigate a force balance between surface tension, inertia, and viscous stresses. However, it was difficult to detect a detailed shape of the droplet due to the restriction of lighting. Moreover, there have been few reports about an internal flow during rotational breakup of a levitated droplet. In this study, the visual observation method for interfacial deformation and internal flow structure of the rotating levitated droplet are presented. Finally, we compare the observation results with those of the filament stretching experiment to investigate the effect of viscous stresses.

2. Experimental apparatus and experimental method

2.1 Rotational breakup of electrostatic levitated droplet

The schematic diagram of the electrostatic levitator is shown in Figure 1. The levitator was composed of a pair of cylindrical electrodes, high voltage amplifiers, laser and detector. At first, a sample was placed on a tip of needle located in bottom electrode. Secondly, positive voltage was applied to the bottom electrode, then the surface of sample was charged positively. Thirdly, negative voltage was applied to upper electrode. Finally, coulomb force lifts up the charged sample in the opposite direction of gravity. In this method, there is no restoring force on the sample, so it is necessary to control the sample position. The position of the sample is detected by He-Ne laser and position detector, and adjusting the voltage of the upper electrode through PID algorithm. The experiment is performed in normal pressure at room temperature. Droplet, which diameter is from 2.0 to 2.6 mm, was levitated in the air. Standing waves are generated in a chamber, and the waves produce a torque on the droplet to induce a rotation by a pair of orthogonal positioned acoustic drivers (loudspeakers) [4]. The fluorescent dye (Rhodamine 6G) and the fluorescent particles were mixed in the glycerol droplet for visual observation of the shape and the internal flow. To illuminate the equatorial plane of the droplet, the laser beam (ND:YAG Laser) is expanded into a sheet using a cylindrical lens. The fluorescent image of the levitated droplet was visualized by a high-speed video camera.

2.2 Filament Stretching Experiment

The schematic diagram of the filament stretching device is shown in Figure 2. It has upper and lower disks of 2.0 mm diameter made of aluminum. A glycerol liquid bridge containing fluorescent particles is formed in the gap between two disks. The lower disk was attached to a height adjuster, and then moved downwards manually. All experiments were performed under the room temperature. The liquid bridge is illuminated by a sheet light of a Nd:YAG laser in a vertical plane, and visualized by a high-speed video camera.

3. Results and discussion

Figure 3 shows snapshots of the levitated droplet. The images are of the top of the droplet. The equatorial plane of the droplet was illuminated by the laser beam. In order to observe the internal flow inside the rotating droplet,

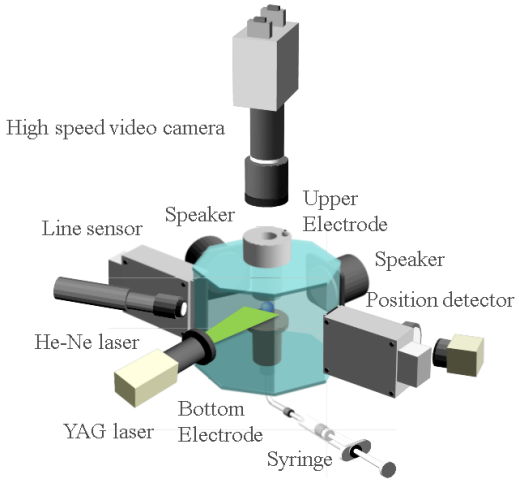

Figure 1: Schematic diagram of the electrostatic levitator.

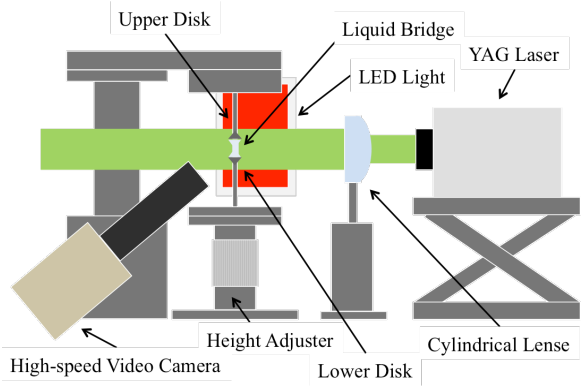

Figure 2: Schematic diagram of the filament stretching device

the image coordinate system of each of the observed images is subjected to rotary coordinate transformation. Therefore, it is necessary to obtain the rotational angle of the droplet. Figure 4 represents a method to obtain the rotational angle of the droplet. As shown by a circle in blue in Figure 4 (a), a brightness distribution along a circumference centering at the center of the rotation center of the droplet is determined. Each peak indicated by arrow in Figure 4 (b) represents a point where the surface of the droplet and the circle intersect. The x-axis represents angle along the circle and the y-axis is the brightness distribution along the circle. The rotation angle of the droplet is determined by intermediate angle between the first peak and second peak on the brightness distribution.

Figure 5 shows the evolution of the midpoint diameters of both the levitated droplet and the liquid bridge. In horizontal axis, 0 second means the time droplet broke up. The midpoint diameters of both the levitated droplet and the liquid bridge were decreased rapidly just before the breakup. The data shows a similarity between the midpoint diameter profile of the levitated droplet and that of the liquid bridge.

Figure 6 (a) shows a trajectory of six particles which were located nearly in the center of the droplet just before the droplet. The direction of each particle is indicated by arrow. This result represents that the directions of the particles and the velocities of the particles are different in the various position inside the droplet. This suggests that the internal flow inside levitated droplet during the rotational breakup is multidimensional. Figure 6 (b) shows a trajectory of the particles inside the liquid bridge just before the breakup. This result shows the internal flow of the liquid bridge during breakup is similar to that of the droplet during rotational breakup.

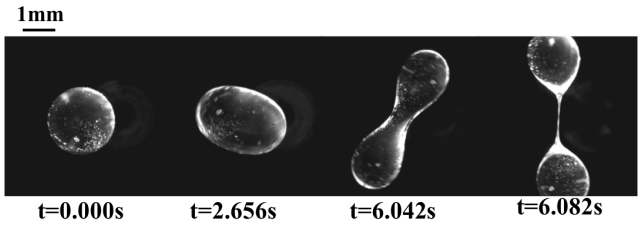

Figure 3: Snapshots of rotating levitated droplet.

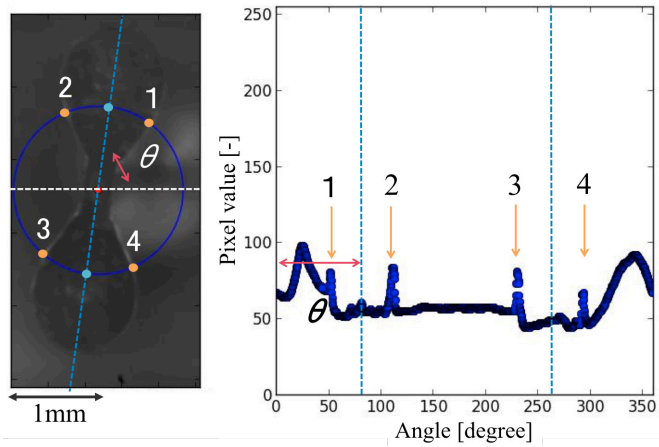

Figure 4: The method to obtain the rotational angle of the droplet, (a) The image of the levitated droplet, (b) The brightness distribution along a circumference centering at the center of the rotation center of the droplet

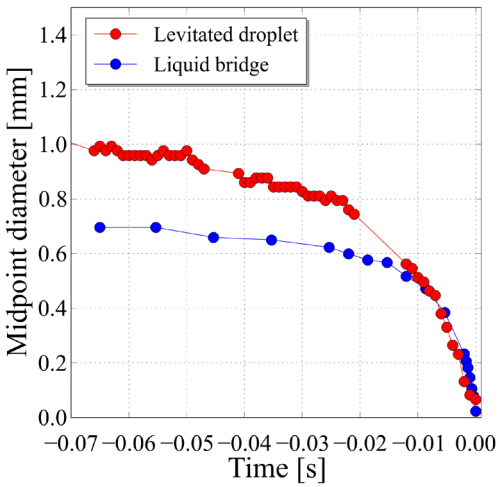

Figure 5: Midpoint diameter versus time.

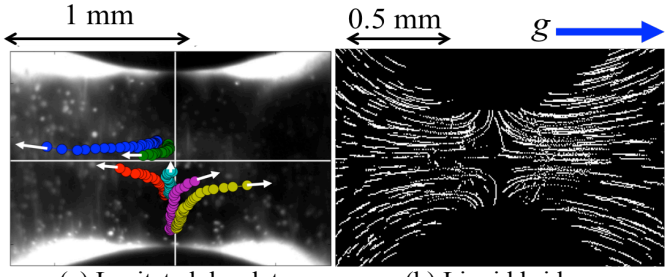

Figure 6: Trajectory of particles.

4. Conclusion

1. The visual observation method for interfacial deformation and internal flow structure of the rotating levitated droplet are presented.
2. The evolution of the midpoint diameter of the levitated droplet is similar to that of the liquid bridge in the filament stretching experiment.
3. The trajectory of the particles inside the levitated droplet during the rotational breakup agrees qualitatively with that of the liquid bridge during the breakup, and also suggests that the internal flow of them are multidimensional.

References

[1] Ishikawa, T., Okada, J. T., Paradis, P. F. and Watanabe, Y., Thermophysical Property Measurements of Liquid Gadolinium by Containerless Methods, International Journal of Thermophysics, 31, pp. 388-398. (2010)

[2] McKinley, G. H. and Tripathi, A., How to Extract the Newtonian Viscosity from Capillary Breakup Measurements in a Filament Rheometer, Journal of Rheology, vol.44, pp.653-671, (2000)

[3] Tanaka, R., Matsumoto, S., Kaneko, A. and Abe, Y., Viscosity Measurement using Breakup of a Levitated Droplet by Rotation, Interfacial Phenomena and Heat Transfer, Vol.1, pp. 181-194. (2013)

[4] Busse, H. and Wang, T. G., Torque Generated by Orthogonal Acoustic Waves – Theory, Journal of the Acoustical Society of America, 69, pp. 1632-1638. (1981)

The interaction of a rising bubble and a particle in oscillating fluid as a part of a flotation process.

… Dmitriy Lyubimov[1], Tatyana Lyubimova[1,2], Lyudmila Klimenko[2]

[1]Perm State University, Theoretical Physics Department, 15, Bukireva Str., 614990, Perm, Russia
[2]Institute of Continuous Media Mechanics UB RAS, 1, Ak. Koroleva Str., 614990, Perm, Russia
lyubimova@psu.ru, lyudmilaklimenko@gmail.com

Particle-bubble interactions are known to play an important role in many technological and physical processes, including acoustic coagulation, supersonic techniques in medicine, and flotation. Flotation is an energy-efficient and eco-friendly process, and it has been applied in almost all sectors of the economy. The improving the efficiency of flotation is a high priority.

Flotation is a complex process that is affected by many parameters. In flotation enrichment technology, separation is largely achieved by the difference in the ability of particles to be retained at the interface. Hydrophobic particles adhere to air bubbles and float to the pulp surface, forming a mineralized froth, whereas hydrophilic particles do not adhere to the bubbles and remain in the slurry.

One of the current tendencies in the intensification of mass transfer processes, including flotation, is based on ultrasound exposure (see, for example [1,2]). The main disadvantages of the available techniques are the inability to treat the entire contents of a flotation cell using the ultrasonic method and the impossibility to apply these techniques to industry. Therefore the existing methods of ultrasound action on the flotation process need to be improved, which requires the development of an adequate theory of particle-bubble interaction in the ultrasound field.

Many papers in the literature deal with theoretical studies of the behavior of a single bubble in liquid under the action of external variable forces (see, for example [3,4]). An expression for the force arising between the bubble and the particle in the acoustic field can be found in [5-8]. However, the authors [5-8] take into account only monopole oscillations of the bubble, which is not sufficient.

There is also a series of works on the radiation force acting on a solid particle in a vibrational field in the cases of perfect [3,9,10] and viscous fluid [11]. However, these expressions have not been applied to the case in which the vibrational field is scattered by the bubble.

In flotation theory, the bubble-particle interaction can hardly be modeled without referring to the hydrodynamic approach. However, the existing theories of the flotation process are either of empirical nature [12, 13] or do not account for the action of the external fields [14, 15].

Thus, despite extensive investigations, the role of hydrodynamic and structural parameters in the implementation of different flotation processes is still not well understood. Moreover, there are no well-defined optimization criteria, and the obtained relations are mainly of an empirical nature and require refinement. It is necessary to elaborate the appropriate theories and models that will account for the behavior and interaction of the particles and bubbles that are subject to vibrations.

We investigate the behavior of a single solid heavy particle in the vicinity of a gas bubble placed in an incompressible fluid. The system is located in a long cylindrical tube with a diameter d (Figure 1) that is larger than the bubble and particle, i.e. $d \gg R_b \gg R_p$ (R_b, R_p are bubble and particle radii). Since the velocity of the external flow is assumed to be constant, it appears to be reasonable to use the reference frame of this flow. The system is subjected to a gravity field and external vibration (ultrasound) field.

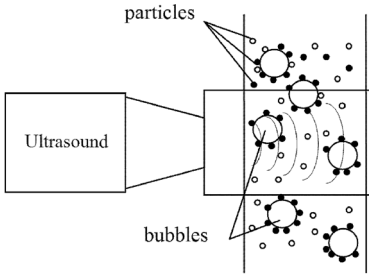

Figure 1: Scheme of the setup.

We consider a small particle with a radius less than 50 μm. A particular feature of flotation of such a particle is that the main stage of the elementary flotation event is the transportation of particles to the bubbles surface. The particle is under the influence of the average force generated by a pulsating flow, Stokes force and buoyancy force. The momentum equation for a particle is written as:

$$\vec{F}_{vib} - \frac{9}{2R_p^{\,2}}\eta\left(\frac{d\vec{r}}{dt} - \vec{V}\right) + \left(\rho_s - \rho\right)\vec{g} = 0 \qquad (1)$$

where ρ_S is particle density, ρ, η are density and dynamic viscosity of the liquid, $\vec{V}$ is the velocity of flow past the bubble in the absence of particle, which according to [16], is given by:

$$\vec{V} = \frac{uR_b}{2r}\left[\frac{\vec{r}}{r^2}\left(\vec{k}\cdot\vec{r}\right) + \vec{k}\right] - u\vec{k} \qquad (2)$$

where $u = gR_b^2/3\nu$ is the rising velocity of the bubble with respect to the external flow and $\vec{k}$ is the direction of bubble motion.

The frequency ω is assumed to be so high that the thickness of the Stokes boundary layer $\delta = \sqrt{2\nu/\omega}$ (where ν is the kinematic viscosity of the fluid) is much less than the bubble and particle radii. In this case, a pulsating flow around the bubble and the particle can be described using the inviscid fluid model. The expression for the average force generated by a pulsating flow of perfect fluid can be found in [3,9,10] and a per unit volume it can be written as:

$$\vec{F}_{vib} = \frac{3}{4}\rho \frac{\rho_s - \rho}{\rho_s + \frac{1}{2}\rho} \nabla \overline{U^2} \,. \quad (3)$$

Another restriction for the frequency range is that the sound wavelength at the vibration frequency is at least one order larger than the bubbles radius. In this case the vibrations can be considered translational and harmonic. We assume that the vibration amplitude b is small compared to the particle radius $b \ll R_p$ and deviation of the bubble surface from spherical one does not exceed the bubble radius, which leads to the restriction $bd \ll R_b^2$. These assumptions permit linearizing Euler equation for the pulsating velocity field around the bubble.

The pulsating velocity field includes the imposed field and scattered fields of the monopole and translational motions:

$$\vec{U} = \vec{U}_{vib} + \vec{U}_r + \vec{U}_d = \vec{U}_{vib} + \left(\vec{U}_{vib} \cdot \vec{r}_b\right) \frac{\omega^2 R_b}{\left(\omega^2 - \omega_0^2\right)} \frac{\vec{r}}{r^3} - \\ -\vec{U}_{vib} \frac{R_b^3}{r^3} + \left(\vec{U}_{vib} \cdot \vec{r}\right) \frac{3R_b^3}{r^4} \frac{\vec{r}}{r} \quad (4)$$

Here $\vec{U}_{vib} = b\omega \vec{j} \cos \omega t$ is the velocity of oscillatory at a sufficient distance from the bubble, b is the vibration amplitude, $\vec{j}$ is the direction of vibrations, $\omega_0 = c/R_b \sqrt{3\rho_g/\rho}$ is the natural frequency of radial bubble oscillations, ρ_g is gas density in the bubble, c is the sound speed in gas, $\vec{r}_b$ is the radius vector of the bubble center under the assumption that the origin of the coordinate system coincides with the center of the tube.

It should be noted that at a large distance from the bubble, the most essential contribution to the force is due to the interference of the external vibration field and the field scattered by the bubble, which suggests that considering only monopole oscillations of the bubble (as for example in [6]) will be inadequate.

Solving equations (1) - (4) we obtain the trajectories of the particle motion.

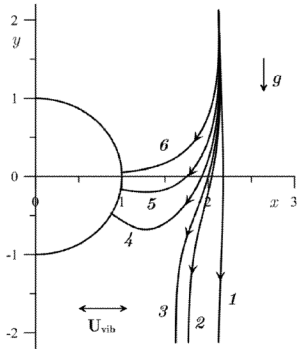

Figure 2: The trajectories of particle motion: 1 - in the absence of vibrations, 2 – 0.16 W/sm^2 , 3 - 0.31 W/sm^2 , 4 - 1.1 W/sm^2 , 5 - 2.5 W/sm^2 , 6 - 4.2 W/sm^2 .The vibrations are directed along the x-axis and the gravitational force is directed along the y-axis.

The calculations show that in the absence of vibrations at a distance of about one bubble diameter, the influence of the bubble on particle motion is inconsequential the particle trajectories are nearly vertical (Figure 1b, curve 1). When subjected to vibrations, the particle trajectories are gradually distorted, and at a certain value of vibration parameters the particles adhere to the bubble surface (Figure 1b, curve 2-6).

The trajectories of the particle motion in the pulsating field have been constructed. It has been found that even moderate vibrations may lead to a multifold increase in the capture cross section. Therefore it possible to significantly affect the attachment-separation processes, which increases the efficiency of the flotation process as a whole.

This work was carried out under the framework of the France-Russia program of scientific collaboration APKYS and supported by the Administration of the Perm Krai (under contract N C 26/205) and French national program ICEEL Carnot.

References

[1] Aldrich, C., Feng, D.,. Effect of particle size on flotation performance of complex sulphide ores. Miner. Eng. 12, 701-707. (1999)

[2] Ozkan, S. G., Beneficiation of magnesite slimes with ultrasonic treatment. Miner. Eng. 15, 99-101. (2002)

[3] Lyubimov, D. V., Lyubimova, T. P., Cherepanov, A. A., Behavior of a drop (bubble) in a non-uniform pulsating flow. Adv. Space Res. 29, 667–672. (2002)

[4] Rensen, J., Bosman, D., Magnaudet, J., Ohl, C.-D., Prosperetti, A., Tgel, R., Versluis, M., Lohse, D., Spiraling bubbles: How acoustic and hydrodynamic forces compete. Phys. Rev. Lett. 86, 4819–4822. (2001)

[5] Alekseev, V. N., 1991. Forces acting between a bubble and solid particles in a sound field. Akust. Zh. 37, 597.

[6] Doinikov, A. A., Zavtrak, S. T., 1996. Interaction force between a bubble and a solid particle in a sound field. Ultrasonics 34, 807– 815.

[7] Gor'kov, L. P., 1961.O silah, dejstvujushhih na maluju chasticu v akusticheskom pole v ideal'noj zhidkosti. Dokl. Akad. Nauk SSSR 140, 88.

[8] Miller, D. L., Nyborg, N. L., Whitcomb, C. C., 1979. Platelet aggregation induced by ultrasound under specialized conditions in vitro. Science 205, 505

[9] Krasil'nikov, V. A., Krylov, V. V., 1984.Vvedenie v fizicheskuju akustiku, M. Nauka.

[10] Settnes, M., Bruus, H., 2012. Forces acting on a small particle in an acoustical field in a viscous fluid. Phys. Rev. E. 85, 016327.

[11] Danilov, S. D., Mironov, M. A., 2000. Mean force on a small sphere in a sound field in a viscous fluid. J. Acoust. Soc. Am. 107, 143–153.

[12] Gaudin, A. M., 1957. Flotation, McGraw-Hill, New York.

[13] Dobby, G. S., Finch, J. A., 1987. Particle size dependence in flotation derived from a fundamental model of the capture process. Int. J. Miner. Proces. 21, 241–260.

[14] Nguyen, A.V., 1999. Hydrodynamics of liquid flows around air bubbles in flotation: a review. Int. J. Miner. Process 56, 165-205.

[15] Phan, C. M., Nguyen, A. V., Miller, J. D., Evans, G. M., Jameson, G. J.,2003. Investigations of bubble–particle interactions. Int. J. Miner. Proces. 72, 239–254.

[16] Landau, L. D., Lufshits, E. M., 2001. Theoretical physics, Phismatlit, Moscow.

Ninth International Conference on
TWO-PHASE SYSTEMS FOR GROUND AND SPACE APPLICATIONS
Baltimore, Maryland, USA, September 22-26, 2014

Finite Amplitude Propagation of Acoustic Waves in Bubbly Liquids Based on Nonlinear Evolution Equations

Tetsuya Kanagawa

Department of Engineering Mechanics and Energy, University of Tsukuba
1-1-1 Tennodai, Tsukuba 305-8573, Japan
kanagawa@kz.tsukuba.ac.jp

1. Introduction

As in the active control of cavitation phenomena in rocket tank, pressure wave propagation in bubbly liquids has long been examined as one of the most important problems in two-phase flow systems. Some recent theoretical studies [1-3], which been taken the compressibility of liquid phase into account, clarified the existence of two types of propagation modes, i.e., Slow mode and Fast mode. Figure 1 illustrates the conceptual diagram of the linear dispersion relation.

Slow mode has been known as a classical propagation mode discovered in a pioneering paper by van Wijngaarden [1], where the compressibility of liquid phase was discarded. On the other hand, Fast mode is induced by the liquid compressibility [2-4]. Waves in Fast mode are sometimes called precursor, because the phase velocity of which exceeds the sound speed in liquid. Although many theoretical works have been carried out, the propagation properties of waves in Fast mode have not been investigated in detail.

Toward the enhancement and establishment of many engineering applications such as the space utilization, a number of basic studies should be unified. Our goal is unifying a theoretical framework of pressure waves in bubbly liquids based on derivation of evolution equations describing wave behaviors. Our previous study [5] has already derived two types of wave equations for nonlinear propagation of waves in Slow mode, i.e., the Korteweg-de Vries-Burgers (KdVB) equation for a long wave in a low frequency and the Non-Linear Schroedinger (NLS) equation for an envelope of short wave in a moderately high frequency (see Fig. 2).

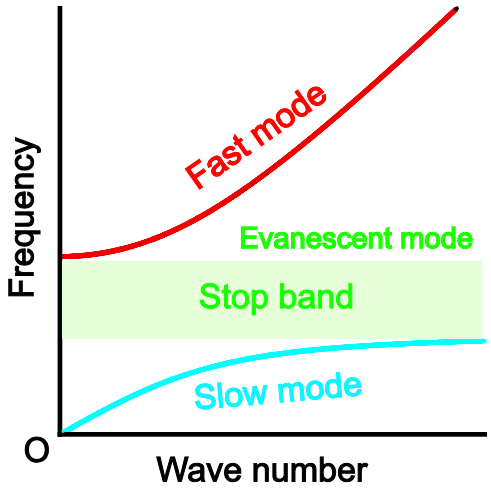

Figure 1: Conceptual diagram of the linear dispersion relation.

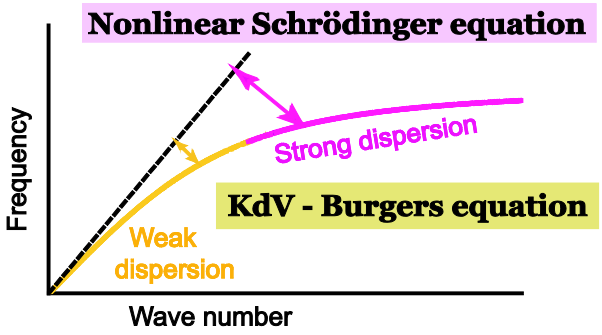

Figure 2: Slow mode and two types of resultant wave equations by Kanagawa *et al.* [5].

2. Problem statement

The present study treats the waves in Fast mode with a brief review of those in Slow mode [5]. We shall decompose Fast mode into Band A and Band B (see Fig. 3). Band A and Band B correspond to a short wave in very high frequency and a long wave in moderately high frequency slightly above the cutoff frequency, respectively. Utilizing a methodology of the method of multiple scales with parameter scaling proposed by Kanagawa *et al*. [5], we shall derive a wave equation for Band A in Fast mode.

3. Derivation of wave equations

The propagation of plane waves in Fast mode in a compressible liquid containing many small spherical gas bubbles is examined. For simplicity, the viscosity in gas phase, heat conduction in gas and liquid phases, phase change across the bubble wall, gravitation, and Reynolds stress, are disregarded.

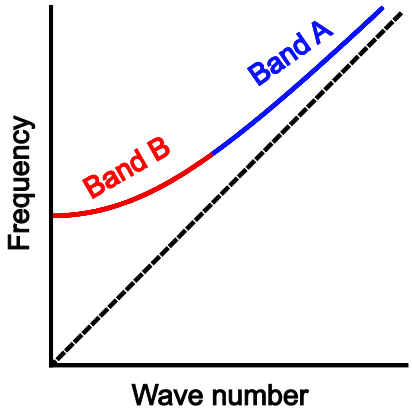

Figure 3: Fast mode, which is decomposed into Band A and Band B.

We employ the set of basic equations in a two-fluid model proposed by ourselves [3], which are composed of conservation equations of mass and momentum in gas and liquid phases, the Keller equation for bubble wall motion, the state equations in gas and liquid phases, mass conservation equation inside the bubble, and the balance equation of normal stresses at bubble-liquid interface (see, the explicit form in Ref. [4]). By the use of the method of multiple scales with the choices of scaling relations of physical parameters appropriate to the wave concerned, we can derive various types of wave equations from the basic set.

In our previous study [5], the set of parameter scaling appropriate to low- and high-frequency bands in Fig.2 has been determined as

$$\left(\frac{U}{c_{L0}},\frac{R_0}{L},\frac{\omega}{\omega_B}\right)=\begin{cases}O(\sqrt{\varepsilon}),O(\sqrt{\varepsilon}),O(\sqrt{\varepsilon}) & (\text{for KdVB})\\ O(\varepsilon^2),O(1),O(1) & (\text{for NLS})\end{cases} \quad (1)$$

where U, L, and ω are a typical propagation speed of waves, wavelength, and frequency of incident waves, respectively; c_{L0} is the sound speed in an unperturbed liquid; R_0 is the initial bubble radius; and ω_B is the eigenfrequency of spherical oscillations of single bubble.

Equation (1) yields two types of nonlinear evolution equations (i.e., the KdVB and NLS equations) via a straightforward and systematic calculation [5]. Let us proceed to the formulation of Band A in Fig.3. We define the set of parameter scaling for Band A, as

$$\left(\frac{U}{c_{L0}},\frac{R_0}{L},\frac{\omega}{\omega_B}\right)=(O(1),O(1),O(1)), \quad (2)$$

Substituting Eq. (2) into the basic set [4], we have the following resultant equation from the leading order of approximation:

$$A_1\frac{\partial^4 f}{\partial t^4}+A_2\frac{\partial^4 f}{\partial t^2\partial x^2}+B_1\frac{\partial^3 f}{\partial t^3}+B_2\frac{\partial^3 f}{\partial t\partial x^2} + C_1\frac{\partial^2 f}{\partial t^2}+C_2\frac{\partial^2 f}{\partial x^2}=0, \quad (3)$$

where t is the time; x is the spatial coordinate normal to the wavefront; f is a dependent variable (e.g., the liquid pressure, bubble radius, etc.); the coefficients in third-order derivatives, A_1 and A_2, denote the dispersion effects, those in fourth-order derivatives, B_1 and B_2, denote the dissipation effects, these coefficients include the initial void fraction, liquid viscosity, and so on. The explicit form of coefficients is not shown since its complexity. Note that all the symbols in Eq. (2) have been nondimensionalized.

4. Conclusion

The resultant Eq. (3) governs the linear propagation of waves in Band A of Fast mode, i.e., very high frequency short wave. In the wave propagation process, the dispersion effect and dissipation effect compete with each other; the former is induced by bubble oscillations and the latter is owing to the acoustic radiation from oscillating bubbles and the liquid viscosity. Furthermore, a wave equation for Band B will also be presented.

Acknowledgments

This work was carried out with the aid of the Japan Society for Promotion of Science (223218 & 245892). The authors sincerely thank for this grant.

References

[1] van Wijngaarden, L. “On the equations of motion for mixtures of liquid and gas bubbles,” *Journal of Fluid Mechanics*, **33,** 465-474 (1968).

[2] Khismatullin, D. B. and Akhatov, I. S., “Sound-ultrasound interaction in bubbly fluids: Theory and possible applications” *Physics of Fluids*, **13**(12), 3582-3598 (2001).

[3] Egashira, R., Yano, T. and Fujikawa, S., “Linear wave propagation of fast and slow modes in mixtures of liquid and gas bubbles,” *Fluid Dynamics Research*, **34,** 317-334 (2004).

[4] Yano, T., Egashira, R. and Fujikawa, S., “Linear analysis of dispersive waves in bubbly flows based on averaged equations,” *Journal of Physical Society of Japan*, **75,** 104401 (2006).

[5] Kanagawa, T., Yano, T., Watanabe, M. and Fujikawa, S. “Unified theory based on parameter scaling for derivation of nonlinear wave equations in bubbly liquids,” *Journal of Fluid Science and Technology*, **5**(3), 351-369 (2010).

Phenomenological model for annular two-phase friction pressure drop under microgravity condition

Jiajun Xia, Zhencheng Huang, Wan wu, Xingbin Zhang, Zhenhui He

Center for Space Technology, Sun Yat-sen University
Daxue Road 1st Sun Yat-sen University Zhuhai Campus, Zhuhai, China
xiajiajun_2010@hotmail.com

Nomenclature

We	Weber number	μ	dynamic viscosity (Pa·s)
g	nomal gravity (m/s^2)	P	pressure drop/Pressure (Pa)
δ	annular film thickness (mm)	L	pipe length (m)
R	pipe radius (mm)	s	slip ratio
D	pipe diameter (mm)	*Subscripts*	
o	sensity (kg/m^3)	G	gas
σ	surface extension (N/m)	L	liquid

Two-phase flows occur in more and more space operations as the fast development of space technology. Compared with single phase systems, two-phase systems can meet the high requirement of future thermal management and thermal control systems in spacecraft, and also, the temperature stability of two-phase systems is also better than single phase systems.

Under microgravity condition, a two-phase friction correlation is important for predicting pressure drop. However, there is no proper model or theory yet according to the recent research. Thus using groud model to predict two phase pressure drop is a method may be considered.

In this paper we will analyze the feasibility of using the phenomenological model proposed by Jesus Moreno Quiben and John R. Thome 2007 to predict the annular two-phase pressure drop under microgravity, and based the Thome model, A modified model from groud condition is proposed.

The Jesus Moreno Quiben and John R. Thome (2007) model[1] is propose for Freon working medium, and it covers all two-phase flow patterns such as stratified flow, slug flow, annular flow etc. As the microgravity experimental data we obtained through literature suvey are all annular flow conditions(see table 1). This paper only analyze the annular correlation of Jesus Moreno Quiben and John R. Thome model.

Table 1: Experimental data for Feron two-phase friction pressure drop under microgravity

Sources	Working medium	Flow geometry D(mm)/L(mm)	Flow pattern[a] (number)
Nguyen[2]	R12	12.7/1.63	A(60)
Hurlbert[3]	R12	11.1/1.22	A(107)
CHEN, I et al.[4]	R114	15.8/1.83	A(43)

[a] A-annular

The core of the annular correlation of JR.Thome model is the annular friction factor:

$$(fi)_{annular} = 0.67\left[\frac{\delta}{2R}\right]^{1.2}\left[\frac{(\rho_L-\rho_G)g\delta^2}{\sigma}\right]^{-0.4}\left[\frac{\mu_G}{\mu_L}\right]^{0.08}[We_L]^{-0.034} \quad (1)$$

Then the friction pressure drop can be calculated as:

$$\frac{\Delta P}{L} = 2\frac{fi\cdot\rho_G\cdot(u_G-u_L)^2}{(D-2\delta)} \quad (2)$$

Under microgravity conditon, the gravitational acceleration is 9.8e-6 kg/m^{2}s, According to the experimental data obtained, the data set changed to the flowing expression:

$$(fi)_{annular} = 0.32\left[\frac{\delta}{2R}\right]^{0.55}\left[\frac{(\rho_L-\rho_G)g\delta^2}{\sigma}\right]^{0.2}\left[\frac{\mu_G}{\mu_L}\right]^{0.09}[We_L]^{-0.004} \quad (3)$$

Use equation (3) to predict the two-phase annular pressure drop under microgravity conditions. The result is shown in Figure 1. Among the 210 experiment data, nearly 71% are within $\pm 30\%$ error band(Figure 1).

Figure 1 shows the statistical comparision between the 210 experimental data points and the phenomenological model by Jesus Moreno Quiben and Thome(2007). The result show is not so satisfactory. Even though nearly 71% of the data within $\pm 30\%$ error band, the result indicates the accuracy can be improved by modifying the model.

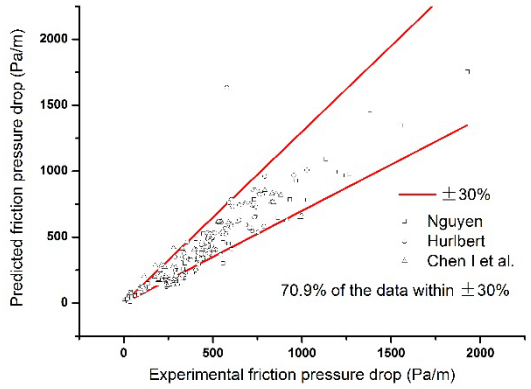

Figure 1: Experimental pressure drop data compared to the phenomenological model by Jesus Moreno Quiben and Thome(2007),use equation (3)

The phenomenological model accounts for the effects of flow pattern, interfacial waves and it can be shown from the expression of the friction factor $(fi)_{annular}$.

Most researchers agree that gas-liquid slip ratio has a significant effect on the two-phase pressure drop. The gas-liquid velocity ratio is defined as:

$$s = \frac{u_G}{u_L} \tag{4}$$

Then take the slip ratio s into consideration. Add s in to modify the expression of the annular friction factor, According to the experiment data. A new data set for $(fi)_{annular}$ is proposed:

$$(fi)_{annular} = 0.166\left[\frac{\delta}{2R}\right]^{0.55}\left[\frac{(\rho_L-\rho_G)g\delta^2}{\sigma}\right]^{-0.115}\left[\frac{\mu_G}{\mu_L}\right]^{0.07}[We_L]^{-0.07}[s]^{-0.95} \tag{5}$$

Use equation (5) to predict the two-phase annular pressure drop under microgravity conditions. The result is shown in Figure 1. Among the 210 experiment data, nearly 82% are within ±30% error band and 42% are within ±10% error band (Figure).

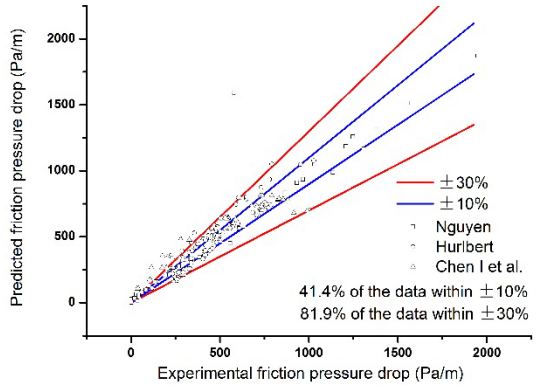

Figure 2: Experimental pressure drop data compared to the modified phenomenological model(based on the model by Jesus Moreno Quiben and Thome(2007)),use equation (5)

Figure 2 shows the comparison between the 210 experimental data points and the modified phenomenological model with slip s added in. The modified phenomenological model give a better prediction, nearly 82% of the data withina ±30% error band and 42% of the data withina ±10% error band.What's more, the absolute pressure drop of most data points that beyond ±30% error band are below 500Pa/m(relatively small pressure drop), and the predict result is bigger the experimental value, It means the predicted result can be uesd and will not cause big design redundancy. The comparison shows that by taking slip ratio s into consideration can improve the accuracy of the prediction.

The phenomenological model is new and predict the two-phase pressure drop in a different way from the conventional pressure drop model. It accounts for the effect of flow patterns and interfacial waves, however the two-phase flow mechenism is still unrevealed, especially under microgravity conditions. The modified phenomenological model based on the model by Jesus Moreno Quiben and Thome(2007) can give a relatively good prediction of two-phase friction pressure drop for nomal design of Freon two-phase systems under microgravity conditions. but further research to reveal microgravity two-phase mechanism is still needed.

References

[1] J. M. Quibén and J. Thome, "Flow pattern based two-phase frictional pressure drop model for horizontal tubes, Part II: New phenomenological model," Int. J. Heat Fluid Flow, 2007.

[2] N. Nguyen, "Analytical and Experimental Study of Annular Two-Phase Flow Friction Pressure Drop Under Microgravity," 2009.

[3] K. Hurlbert, Flow dynamics for two-phase flows in partial gravities. 2000.

[4] H. Shen, C. W. Tam, and I. CHEN, "Measurements and correlation of two-phase pressure drop under microgravity conditions," … Thermophys. …, 1991.

Two-Phase Heat Transfer Mechanisms within Plate Heat Exchangers: Experiments and Modeling

Valentin Solotych and Jungho Kim

University of Maryland, Department of Mechanical Engineering
College Park, Maryland, USA
solotych@gmail.com

Two-phase flow heat exchangers have been shown to have very high efficiencies, but the lack of a dependable model and data precludes them from use in many cases. Herein a new method for the measurement of local convective heat transfer coefficients from the outside of a heat transferring wall has been developed, which results in accurate local measurements of heat flux during two-phase flow. This novel technique uses a chevron-pattern corrugated plate heat exchanger (PHE) consisting of two specially machined Calcium Fluoride (CaF_2) plates and the refrigerant HFE7100, with heat flux values up to 10 W/cm^2 and flow rates up to 300 kg/m^2-s. As CaF_2 is largely transparent to IR radiation, the simultaneous visualization of the flow within the PHE is accomplished through use of a mid-range (3.0-5.1 µm) IR-Camera.

CaF_2 is an inorganic compound that acts as in insulator. In order to provide uniform heating to the working fluid several approaches were considered. A widely used Indium tin oxide (ITO) layer on the flat side of the plates would provide joule heating of the substrate but would also block IR-Radiation since ITO is only transparent in the visible range. A thin layer of Gold was also considered, which would create similar problems as the ITO coating, whereas Gold would have a very high reflectance in the IR which would make the data evaluation rather cumbersome. Lately Hu et. al. [1] discovered that a thin layer of singled wall carbon nanotubes (CNT) can provide films that are on the order of 200 Ohms/square with a transmittance in the IR-Range of greater than ~ 80% [2].

For amplification of the signal obtained by the IR camera, one CaF_2 plate is coated with Kapton-Tape, which acts as a thermal insulator. Kapton-Tape is fairly transparent in the IR-Range, therefore both sides of the Kapton-Tape are applied with a very high emissive paint. The liquid facing side of the tape is completely covered with a uniform layer of commercially available black paint. The other side of the tape, which is covered with adhesive, is only partially covered with a highly emissive substrate, since otherwise it would block the thermal radiation from the liquid side. Therefore 1 mm square dots that can resolve the true temperature with 3 mm spacing (center to center) where applied on the adhesive side of the Kapton-Tape. As Kapton-Tape acts as a thermal insulator, the spacing was determined to be able to create a temperature map under the Kapton-Tape. Knowing the temperature distribution on both sides of the tape it is possible to calculate the heat flux and thereby enable the calculation of heat transfer coefficient values.

The Kapton-Tape is 50 um thick, therefore it is very important to keep the thickness of the black dots to a minimum since large differences in dot thickness would create a wrong reading. Therefore a thin layer of Chromium was deposited first on the adhesive side to ensure that the dots are opaque and would not allow for any radiation to pass from the top black paint layer. Chromium is a metal and has a relatively low emissivity. To increase the emissivity and keep the thickness to a minimum, a CNT layer was applied using the technique described in [3].

In order to get the true temperature values from the IR-Data the optical properties of all involved materials need to be known. In addition to that, CaF_2 has similar properties as glass, meaning that reflections at each interface of the CaF_2 occur which need to be accounted for in the calculation. A comprehensive ray-tracing calculation needs to be performed which is explained in [4].

To allow for simultaneous flow visualization with an optical high speed camera, the second plate was only coated with transparent tape, in order to create the same thermal boundary and to allow visualization of the flow. Figure 1 shows the schematic of the test

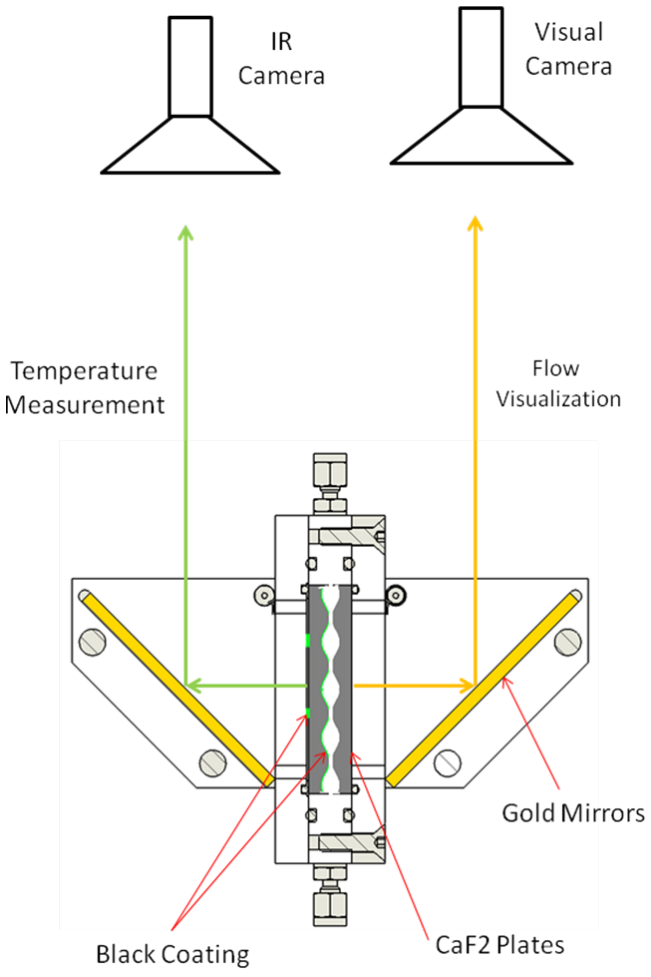

Figure 1: Schematics of Flow Visualization and Temperature Measurements

CaF_2 is a brittle material which can therefore be complicated to machine. Due to cost and stability considerations, the size of the plates are 50 x 100 x 5 mm. With this size we ensure that the plates provide enough corrugations to enable perfect mixing of bubbles and liquid and thereby entry effects would disappear. Additionally the plates provide a geometry that is relevant for 2-phase cooling within PHE. Figure 2 shows a picture of the machined CaF_2 plate covered with Kapton-Tape and the schematic of its dimensions.

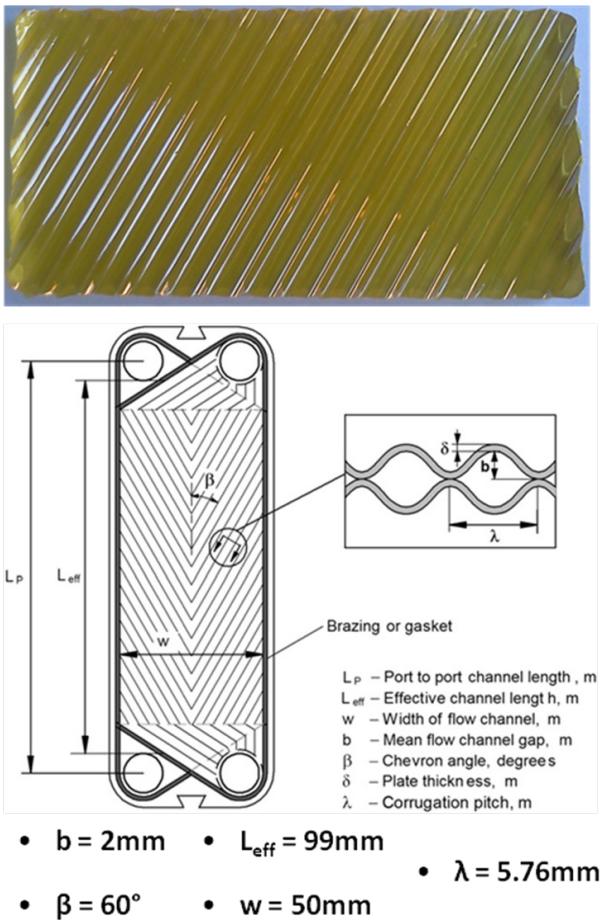

Figure 2: Top: Photograph of the CaF_2 for optical flow visualization, covered with transparent Kapton-Tape. Bottom: Schematic of the dimensions of the plate.

The pairing of high-resolution IR imaging and heat transfer coefficients of the flow allows for the evaluation of the two-phase distribution and better understanding of the heat transfer mechanism during evaporation in a plate channel. The theoretical basis for the technique is given along with a detailed description of the test apparatus and data reduction procedure. The technique is evaluated for accuracy by comparison with established single phase heat transfer data from the literature. Using this technique we hope to extrapolate further models of two-phase heat transfer and provide reliable data under this regime.

References

[1] Hu, L., Gruner, G., Hornbostel, B., Electrowetting devices with transparent single-walled carbon nanotube electrodes, Applied Physics Letters, 90, 093124 (2007)

[2] Hu, L., Gruner, G., Hecht, D., Infrared transparent carbon nanotube thin films, Applied Physics Letters, 94, 081103 (2009)

[3] Gokhale, V., Sherendova, O., McGuire, G., Infrared Absorption Properties of Carbon Nanotube/Nanodiamond Based Thin Film Coatings, Journal of Microelectromechanical Systems, Volume:23 ,Issue: 1, 191 - 197 (2014)

[4] Kim, T., Kommer, E., Kim, J., Measurement of two-phase flow and heat transfer parameters using infrared thermometry, International Journal of Multiphase Flow, 40, 56-67 (2012)

Ninth International Conference on
TWO-PHASE SYSTEMS OR GROUND AND SPACE APPLICATIONS
Baltimore, Maryland, USA, September 22-26, 2014

Flow Boiling Critical Heat Flux Measurements in Reduced Gravity

Henry K. Nahra
NASA-Glenn Research Center
21000 Brookpark Rd., Cleveland, OH 44135
henry.k.nahra@nasa.gov

Mohammad M. Hasan, Nancy R. Hall, James D. Wagner, Rochelle L. May, Robert L. Butcher, John S. Kolacz
NASA-Glenn Research Center
21000 Brookpark Rd., Cleveland, OH 44135

Jeffrey R. Mackey
Vantage Partners, LLC
3000 Aerospace Parkway, Brook Park, OH 44142, U.S.A.

Ramaswamy Balasubramaniam
National Center for Space Exploration Research
21000 Brookpark Rd., Cleveland, OH 44135

Hyoungsoon Lee, Christopher Konichi, and Issam Mudawar
Purdue University
Mechanical Engineering Building, 585 Purdue Mall
West Lafayette, IN 47907-2088

Introduction

Power and heat dissipation demands for future manned space missions are on the rise. The challenge posed to future NASA missions is to achieve the mission's objective with minimum mass, including the mass of the thermal management systems. Performance enhancement and mass and volume reduction in future manned space missions can achieved with flow boiling and condensation as the two crucial mechanisms for heat transport. It is crucial to achieve higher optimal flow rates and coolant liquid velocity in two phase systems which effectively result in an inertial flow that is insensitive to body and interfacial forces [Ref. 1, 2].

In this work, measurements of the critical heat flux were carried out in low and normal gravity as a function of the velocity of the working fluid (FC-72) for a wide range of liquid velocity, wide range of subcooling and for inlet quality of up to 30%. The results from the low gravity experiments are presented in this paper.

Low Gravity Testing

Hardware Description

An aircraft rig was built to conduct the flow boiling experiments on board the Zero-G Corp parabolic aircraft. The rig consisted of the structural frame which was aircraft-flight qualified, a preheater to heat the fluid to the proper thermodynamic properties before entering the Flow Boiling Module (FBM) test section, an air cooled condenser to condense and bring down the fluid's temperature, a filter for fluid filtration, a positive displacement-gear pump and flow controller to provide the pumping function, an accumulator for pressure fluctuation/spikes dampening during boiling and a turbine flow meter to measure the FC-72 flow rate. A degassing system based on circulating the heated fluid through an FC-72 reservoir is used to degas the working fluid and reduce the non-condensable content in FC-72.

Flow Boiling Module: The Flow Boiling Module (FBM) consisted of two parallel heated surfaces (made from Oxygen free copper) in which the FC-72 was vaporized as it flowed through the test module. Each heated surface was capable of delivering 200 W. Heating was provided from heating elements matched up in resistance to ensure uniformity in heat flux. The flow channel was 2.5x5x100mm. Flow boiling was observed using a high speed camera.

Low Gravity Flow Boiling Critical Heat Flux Measurements and Results

Approximately 5-6 low gravity parabolas were needed to achieve Critical Heat Flux (CHF) for a given flow condition. The fluid was heated to near saturation by the preheater. The FBM heat flux incrementally increased on both sides to heat the fluid uniformly until CHF was reached. At the point of CHF, the temperature of both heated surfaces were observed to rise sharply until reaching 130 C that triggered the shutdown circuitry, in turn shutting down the heat from the heating elements within 1 second.

The heat flux that resulted in the sharp rise in temperature was identified as the critical heat flux. The test runs performed with both sides heated were also repeated with single side heating.

Plots of temperature, velocity and heating data for a series of parabolas in pursuit of the critical heat flux are shown in Fig. 1 for a mass flow rate of 2.5 g/s. Plots in red and blue show the temperature- time behavior and the transient sharp rise in temperature. The data plotted in green show the heat flux as a function of time, the step increase after each parabola, and the decrease to zero heating at shutdown, whereas the data in bright green show the velocity of the fluid.

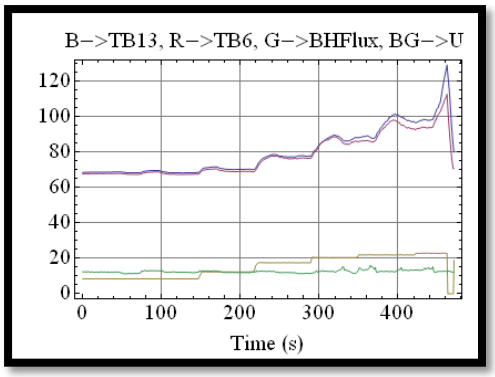

Figure 1: Experimental temperature, liquid velocity and heat flux data as a function of time.

The critical heat flux at 2.5 g/s flow rate for 5 parabolas is shown in Fig. 2 as a function of $\Delta T = T_{Wall|Max} - T_{Sat|in}$. For this flow rate, the critical heat flux was measured at 22.5 W/cm^2. The critical heat flux increased with increasing flow rate. At a flow rate of 40 g/s, the critical heat flux in low gravity with both sides heating was measured at 41 W/cm^2. Flow visualization of CHF is shown in Fig. 3, showing a series of high-speed images captured during each of the parabolas leading to the CHF at a flow rate of 2.5 g/s.

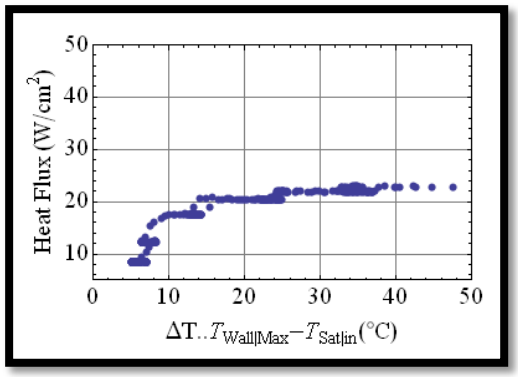

Figure 2: Critical Heat Flux as a function of ΔT.

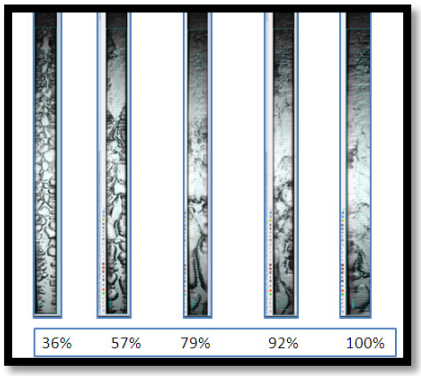

Figure 3: Percentage of CHF (22.5 W/cm^2) achieved in each of the 5 parabolas performed at 2.5 g/s.

These results are samples of the large amount of data on CHF as measured in both ground and reduced gravity environments. This paper presents the results of the CHF measurements for the various parameters including flow velocity, subcooling and thermodynamic quality.

References

[1] Mudawar, I., Hasan, M.M. "Science Requirements Document for Flow Boiling and Condensation Experiment", January 2014.

[2] H. Zhang, I. Mudawar and M. M. Hasan, Flow boiling CHF in microgravity, International Journal of Heat and Mass Transfer, 48, 3107–3118 (2005)

Floating on Air

Detlef Lohse, Tuan Tran, Andrea Prosperetti, Chao Sun

Physics of Fluids, Faculty of Science & Technology, University of Twente, The Netherlands
E-mail: d.lohse@utwente.nl

At the impact of a liquid droplet on a smooth surface heated above the liquid's boiling point, the droplet either immediately boils when it contacts the surface (''contact boiling''), or without any surface contact forms a Leidenfrost vapor layer towards the hot surface and bounces back (''gentle film boiling''), or both forms the Leidenfrost layer and ejects tiny droplets upward (''spraying film boiling'') (see Fig. 1). We experimentally determine conditions under which impact behaviors in each regime can be realized [1] (see Fig. 2). We also show that the spreading factor of impacting droplets on the heated surfaces, defined by the maximal lateral extension of the droplet divided by the original droplet diameter, in both gentle and spraying film boiling regimes shows a universal scaling with the Weber number We, which is much steeper than for the impact on nonheated (hydrophilic or hydrophobic) surfaces.

We develop a theory for the scaling of the spreading factor with Weber number, Stokes number, and a new dimensionless number, which is connected with the Peclet number and the Jacob number [2]. This theory also makes predictions for the scaling of the vapor velocity shooting out under the droplet and for the height of the vapor layer, all as functions of above dimensionless parameters. We also offer first interferometric measurements of the vapor thickness under the droplet and compare them with the predictions [3].

Next, we extend our work to the impact of droplets on superheated *structured* surfaces [2]. The structures on the surface lead to an earlier onset of the gentle film-boiling regime as compared to the smooth case, due to the enhanced heat transfer between surface and liquid. For large interspacing between the pillars on the structured surface we can rescale the data such that the onset of the gentle film boiling regimes becomes universal.

Finally, we describe the surprising formation of upward-directed liquid jets that emerge during the spreading phase of the droplets in the contact-boiling regime on structured surfaces [2]. We never observed similar jets in the case of a smooth surface. The occurrence of the jet and its velocity vary depending on the surface structures, surface temperature, and impact velocity. That this type of jets occurs during the spreading stage makes the phenomenon very different from those that occur during the retracting stage of impact on unheated surfaces. In Fig. 3, we show a series of images taken during the impact of a water droplet falling with a velocity of 1.3 m/s on a structured surface heated to 300ºC (the time origin t = 0 ms is taken as the moment the drop first touches the surface). Shortly after the initial contact, the liquid at the bottom of the droplet spreads out horizontally, whereas the top surface still remains spherical. At the same time, a stream of small droplets shoots up from the base of the spherical cap as shown in the

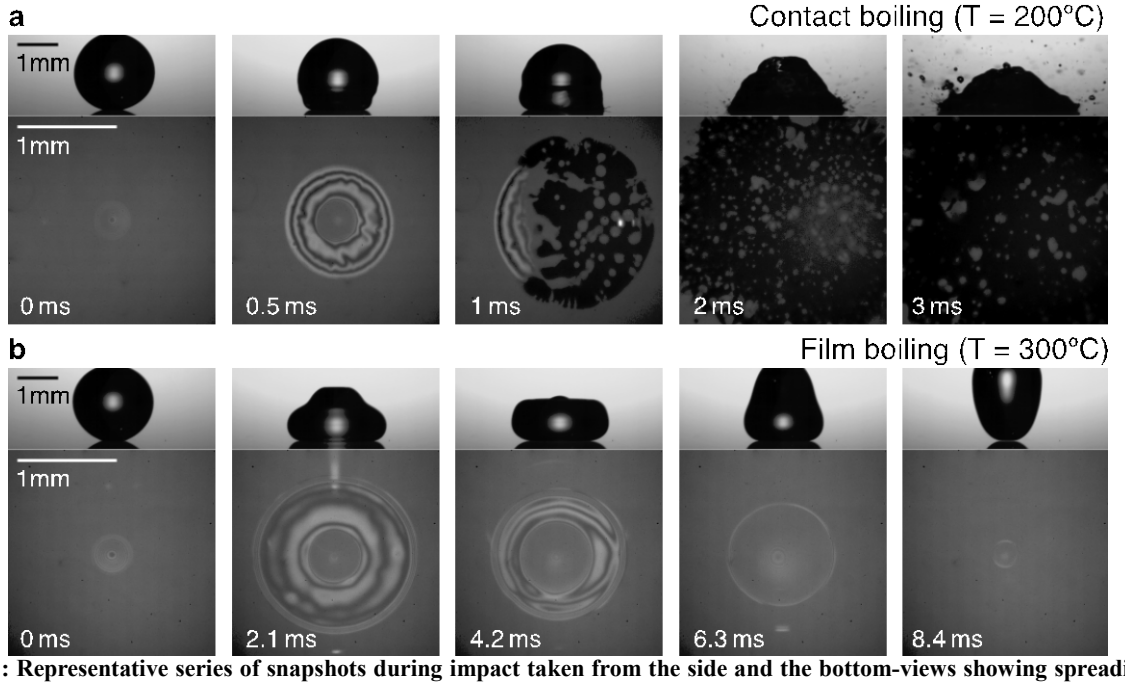

Figure 1: Representative series of snapshots during impact taken from the side and the bottom-views showing spreading and boiling processes of droplet impact on a smooth sapphire surface in (a) contact boiling regime, and (b) film boiling regime. In both cases, the impacting drop has diameter 2 mm, velocity 0.26 m/s, and Weber number 1.9.

image taken at t = 0.83 ms. These droplets are presumably caused by the bursting of vapor bubbles forming on the lower liquid surface.

The ejection of small droplets is then followed by a liquid jet shooting vertically upward from the center of the flattened drop. One possible explanation is that the expansion of vapor bubbles underneath the spreading drop applies a collective pressure to the liquid bulk and eventually causes the liquid in the middle to shoot up.

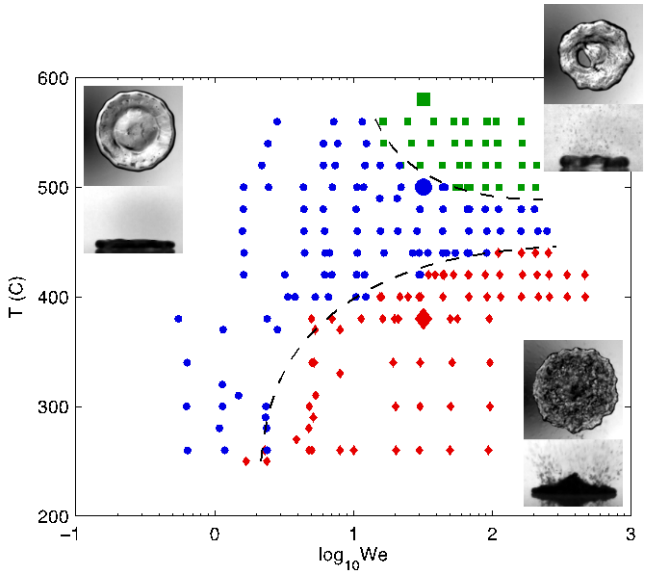

Figure 2: Phase diagram for water droplet impact on a heated surface showing three separate regions: contact boiling regime (red solid diamonds), gentle film boiling regime (blue solid circles), spraying film boiling regime (green solid squares). Each region has an inset illustrating the typical droplet impact behavior in that regime. The dashed lines between different regimes are drawn to guide the eye.

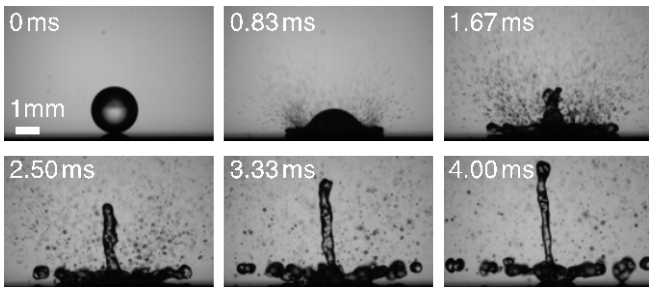

Figure 3: Jet formation during the impact of a water droplet on a structured surface (I = 4µm, H = 2µm) heated to 300°C. The diameter of the drop is 2.2 mm, and the impact velocity is 1.3 m/s.

References

[1] T. Tran, H. J. J. Staat, A. Prosperetti, C. Sun, and D. Lohse, Drop Impact on Superheated Surfaces, *Physical Review Letters* **108**, 036101 (2012)

[2] T. Tran, H.J.J. Staat, A. Susarrey-Arce, T.C. Foertsch, A. van Houselt, H.J.G.E. Gardeniers, A. Prosperetti, D. Lohse, and C. Sun, Droplet impact on superheated micro-structured surfaces, *Soft Matter* **9**, 3272-3282 (2013).

[3] R. C. A van der Veen, T. Tran, D. Lohse, and C. Sun, Direct measurements of air layer profiles under impacting droplets using high-speed color interferometry, *Physical Review E* **85**, 026315 (2012)

Alcohols and Alkanes Sessile Droplets Evaporation into Air: an Empirical Model for Convective Evaporation

Florian Carle and David Brutin

Aix-Marseille University, CNRS, IUSTI UMR 7343, 13013 Marseille, France
florian.carle@etu.univ-amu.fr, david.brutin@univ-amu.fr

The classically used models consider evaporation as a quasi-steady process controlled by the diffusion of vapor into the air, and the whole system is assumed to be isothermal at the ambient temperature. However, when two type of fluids (alcohols and alkanes) are let to evaporate on heated substrates while a side view camera measures their evaporation flux rate with accuracy, droplets tend to see their evaporation flux rate underestimated by this model mostly due to convection contribution. This experimental study aims to understand how atmospheric convective transport in the vapor phase influences evaporation in order to developed an empirical model that describes with accuracy the evaporation flux rate. The Rayleigh number is used to analyze the contribution of natural convection and an empirical is developed combining diffusive and convective transport for each type of fluid. The influence of the molecular chain length (and the increasing number of carbon atoms) is also being discussed.

Sessile droplets are widely found in day-to-day life; it might be a coffee spilt [1], rain onto a waterproof raincoat [2] or again, water falling onto a cooking plate [3]. However, despite the vast number of studies and publications devoted to droplets for almost half a century, the fundamental phenomenon of the evaporation of sessile droplets is still a field that attracts a high level of interest due to its wide applicability and its complexity.

For the purpose of this experimental study, two types of linear carbon chain fluids have been chosen to be evaporated onto heated substrates: alcohols; from CH_4O (methanol) to $C_7H_{16}O$ (heptanol), and alkanes; from C_5H_{12} (pentane) to $C_{10}H_{22}$ (decane). The fluids, obtained from Sigma Aldrich, are anhydrous with a purity of 99% or higher and contain only one compound except for hexane that is a mixture of isomers. The fluids have been used without any treatments prior to the experiments. All fluids properties can be found in Table 1.

Table 1: Fluids properties at T_m = 40°C and P = 1013 hPa, except for P_{sat} and γ, T = 20°C.

Fluids		M_w [g/mol]	ρ_v [18] [kg/m^3]	ν_v [18] [μm^2/s]	L_v [18] [kJ/kg]	T_{sat} [K]	P_{sat} [18] [hPa]	γ [19] [mN/m]	L_c [mm]
Methanol	CH_4O	32	0.486	21.7	1111	333.3	13.8	22.5	1.7
Ethanol	C_2H_6O	46	0.322	28.5	857	346.6	5.83	22.3	1.7
Propanol	C_3H_8O	60	0.159	51.8	664	369.9	2.4	23.7	1.74
Butanol	$C_4H_{10}O$	74	0.082	81.3	423	390.2	1.17	24.6	1.78
Pentanol	$C_5H_{12}O$	88	0.059	119	505	411.2	0.2	25.6	1.81
Hexanol	$C_6H_{14}O$	102	0.238	27.3	486	430.3	0.1	24.5	1.73
Heptanol	$C_7H_{16}O$	116	0.010	611	440	488.2	0.015	26.2	1.82
Pentane	C_5H_{12}	72	3.37	2.17	357	309.1	57.9	16	1.65
Hexane	C_6H_{14}	86	1.27	5.47	335	341.7	17.6	18.4	1.72
Heptane	C_7H_{16}	100	0.48	13	317	371.4	5.33	19.3 [20]	1.72
Octane	C_8H_{18}	114	0.18	33	303	398.6	1.47	21.7	1.8
Nonane	C_9H_{20}	128	0.07	81.7	295	424	1.33	22.9	1.82
Decane	$C_{10}H_{22}$	142	0.03	208	263	447	0.195	23.9 [20]	1.85

Properties are given at T_m = 313 K (unless otherwise indicated) to have medium values of the properties for all the experiments, however, properties temperature dependencies have been taken into account in all calculations. Moreover, through this article, properties have either been measured in our laboratory or are accompanied by their reference. The experimental set-up, based on our previous work [4], enables evaporation dynamics measurements of alcohols and alkanes droplets. Alcohols and alkanes are fairly wetting due to their low surface tension and therefore induce small contact angles (lowest contact angle $\theta_{pentane}$ = 18°, and highest contact angle $\theta_{heptanol}$ = 37°).

Alcohols droplets are then let to evaporate onto PFC substrates whereas alkanes droplets are deposited onto PTFE substrates. Substrates have been chosen for their surface energies inducing a good wetting ie: low initial contact angles, and pinning of the triple line during the large part of the evaporation. However, the dissolution of the PFC substrates by alkanes forced us to use PTFE substrates instead for this type of liquid. The evaporation takes place inside a test cell that is large enough to ensure a constant vapor concentration far from the droplet and below saturation, to prevent potential external perturbations. The air inside the test cell is renewed before each evaporation to make sure previous evaporations do not influence the laters. The substrate is heated by spherical polyimide thermo foil heater regulated by a PT-100 sensor with a PID regulator at 0.1°C with a range from ambient air to 60°C. The ambient pressure and temperature are also recording while droplets evaporate. The error measurement on temperatures are 0.1°C. Once all the fluids have been evaporated for temperatures from ambient to +35°C above ambient, the evaporation flux rate have been measured for each case and divided by the initial radius R_0 to be able to compare all experimental data. This quantity will be called global evaporation flux rate hereinafter.

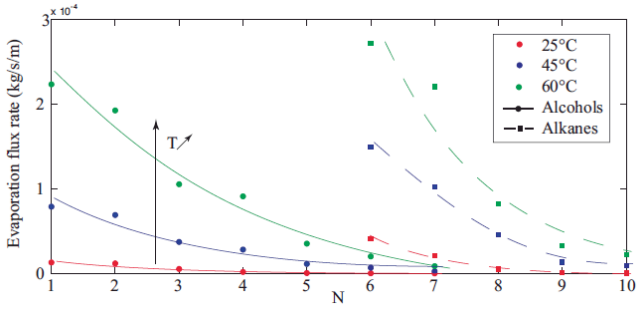

Figure 1: Chain length dependence of the evaporation flux rate for alcohols (circles), alkanes (square) at 25, 45 and 60°C and N is the number of Carbone in the chain. Lines are not a fit of the data but are provided to only guide the eye.

Figure 1 shows the global evaporation flux rate as a function of the number of carbon inside the molecules chain for various temperatures. One can notice a decrease of the evaporation flux rate with the increase of the molecular chain. This observation is valid both for alcohols and alkanes and to some extent for each temperature.

Considering that both diffusion and convection are significant in our problem, the evaporation flux rate E can be express as the sum of diffusive evaporation E_D, described by the following equation and convective evaporation E_C [5].

$$-\frac{dm}{dt} = \pi R D \Delta c f(\theta),$$

Therefore, the dimensionless evaporation flux rate can be define as $E^* = E/Ed = 1 + E^*_C$ where E^*_C is the dimensionless evaporation rate due to convection. For this last part, the description can be done through the Rayleigh number Ra. Figure 2 shows the dimensionless convective evaporation flux rate E^*_C as a function of the Rayleigh number for the two types of fluids. Rayleigh number goes from less than 1 for Heptanol to up to 23000 for Pentane.

This figure first evidences that the convective regime of each compound vapor is laminar (critical Rayleigh number for turbulent flow induced by a horizontal heated plate is $Ra_C = 2x10^7$ [6]). In the case of short molecules (lowest number of Carbone in alcohols and alkanes chains), the motion of the vapor around the droplet is far from being purely diffusive (Ra > 200 for alcohols and Ra > 1500 for alkanes) and convection induces a strong concentration gradient between droplet interface and the above air.

In order to integrate the convective part into the model, each set of data has been fitted with a power law ($E^*_C = C_1 Ra^{C2}$) giving a pair of coefficients C_1 and C_2 per fluid (see Table 2). The first coefficient C_1 strongly increases with the number of Carbone atoms for both fluids. On another hand, the coefficient C_2 is almost constant for all the fluid with an average value of 0.966 with a standard deviation of 0.368. These coefficients are only depending of the physical properties since no other experimental parameters have been changed. However, there is no obvious behavior matching the physical properties and coupling phenomenon should be taken into account.

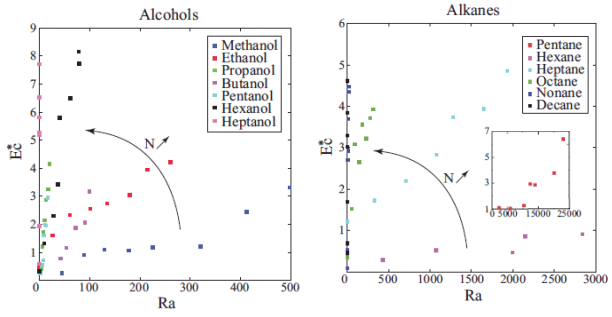

Figure 2: Variation of the dimensionless evaporation term E_C as a function of the Rayleigh number for alcohols (left) and alkanes (right). The inset is a zoom out of Pentane data.

These coefficients can be integrated inside the expression of the dimensionless global evaporation and by employing the ideal gas law, we can write the following equation:

$$E = \frac{4RDM_vP_v}{\hat{R}T_s}\left(1 + C_1\left[\frac{g\frac{\partial\rho}{\rho_v\partial T}\Delta TR^3}{\nu_v\alpha}\right]^{C_2}\right)$$

where M is the molar mass, P is the pressure (considered at saturation as the substrate temperature for the vapor), the subscript v specifying the consideration of the vapor and s the substrate and R is the ideal gas constant.

Table 2: Fitting coefficients C_1 and C_2 for alcohols (left) and alkanes (right).

N	Alcohol	C_1	C_2
1	Methanol	5.35×10^{-3}	1. 02
2	Ethanol	3.21×10^{-2}	0.90
3	Propanol	1.62×10^{-2}	1.07
4	Butanol	1.82×10^{-2}	1.07
5	Pentanol	5.79×10^{-2}	1.39
6	Hexanol	1.46×10^{-1}	0.98
7	Heptanol	9.78	0.38

N	Alkane	C_1	C_2
5	Pentane	9.29×10^{-6}	1.32
6	Hexane	5.78×10^{-3}	0.64
7	Heptane	5.38×10^{-2}	0.59
8	Octane	2.87×10^{-1}	0.46
9	Nonane	1.61×10^{-1}	1.14
10	Decane	6.19×10^{-1}	1.62

In summary, an empirical model has been developed in order to take into account the contribution of the atmospheric convection in the vapor phase during the evaporation of sessile droplets since purely diffusive models underestimate the evaporation flux rate in the case of heated substrates. This empirical model gives a good agreement wherever the substrate temperature or the fluid. However, for temperature near the ambient conditions, the model may require a refinement. This study has also highlighted that the number of carbon atoms in the chain and its length have a strong influence on the evaporation. In order to take into account this phenomenon, empirical coefficients have been given for number of carbon atom for both alcohols and alkanes. We are currently working on a theoretical approach in order to identify the physical parameters that play a role in the coefficients values. In a near future, we would like to improve this empirical model to make it universal, with initial conditions a wide as possible, depending only on the molecule composition of the fluid.

References

[1] Deegan, R. D., Bakajin, O., Dupont, T. F., Huber, G., Nagel, S. R., and Witten, T. A., Nature 389 , 827–829 (1997).
[2] Gelderblom, H., Mar´ın, A´ . G., Nair, H., vanHouselt, A., Lefferts, L., Snoeijer, J. H., and Lohse, D., Physical Review E 83(2) , 026306, (2011).
[3] Leidenfrost, J. G., De aquae communis nonnullis qualitatibus tractatus, Ovenius, (1756).
[4] Carle, F., Sobac, B., and Brutin, D., Journal of Fluid Mechanics 712 , 614–623, (2012).
[5] Kelly-Zion, P., Pursell, C., Vaidya, S., and Batra, J. Colloids and Surfaces A: Physicochemical and Engineering Aspects 381(1–3) , 31–36, (2011).
[6] Incropera, F. P., Lavine, A. S., and DeWitt, D. P. Fundamentals of Heat and Mass Transfer, John Wiley & 216 Sons, (2011).

Comparing the measured vapour concentration field surrounding an evaporating pendant deposited droplet with numerical simulations

S. Dehaeck, A. Rednikov & P. Colinet

Université Libre de Bruxelles (ULB), Transfers, Interfaces and Processes (TIPs),
Fluid Physics Unit, Avenue F.D. Roosevelt, 50, C.P. 165/67, 1050 Brussels
sam.dehaeck@ulb.ac.be, pcolinet@ulb.ac.be

Evaporation of a deposited droplet (sessile or pending) in ambient air is in many cases controlled by the slow process of evacuating the generated vapour away from the droplet by diffusion. As was already shown by e.g. [1], [2], this leads for droplets with contact angles below 90° to local evaporation rates which vary considerably along the interface of the drop, and in particular diverge at the contact line. To test these predictions experimentally, accurate local evaporation rate measurements are necessary. To date, such measurements are very rare in literature and are generally not possible without considerable hypotheses (e.g [3], [4]). In the present contribution, it will be shown that the technique of vapour interferometry is capable of performing such local evaporation rate measurements. Additionally, we will demonstrate how the technique is also capable of measuring the interfacial temperature and global evaporation rate.

In vapour interferometry, a classical Mach-Zehnder setup is used to measure the variations in the refractive index that are generated by the different concentration levels of the vapour throughout the vapour cloud. A typical recorded raw image is shown in Figure 1.

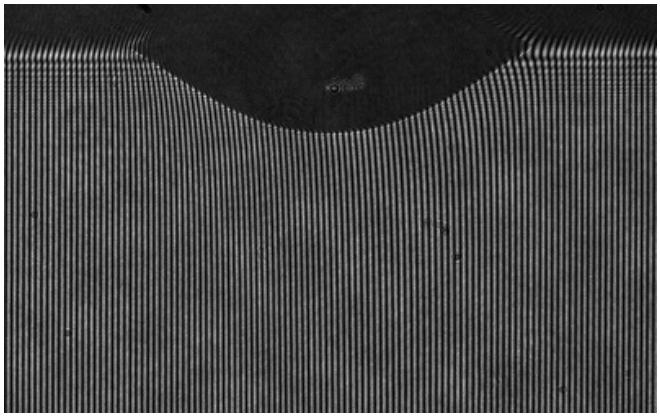

Figure 1: Typical raw interferometric image of a pending deposited evaporating droplet.

This image is then analyzed with the Fourier transform techniques described in e.g. [5] to yield the 2D projection of the (supposedly axisymmetric) refractive index field. With the help of the inverse Abel transform algorithm described in [6], one is able to convert this projection into a true 2D cut of the refractive index field. Knowing the refractive index of the investigated pure vapour, this refractive index field can be transformed into the mole fraction. First results using this approach were obtained by Toker and Stricker [7]. A typical measured mole fraction field is shown in Figure 2.

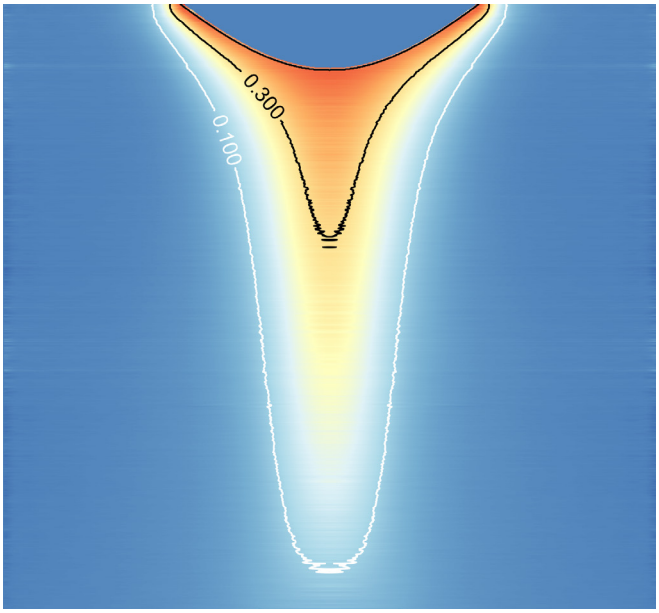

Figure 2: Example of a measured mole fraction field around an evaporating pending droplet

From this mole fraction field, one can find the interfacial temperature of the drop by assuming that the extracted mole fraction at the drop interface corresponds to the saturation mole fraction, which is uniquely linked to the temperature (for a given total pressure, i.e. ambient, and assuming a perfect gas mixture). Through the extraction of concentration profiles normal to the detected droplet interface and calculating the gradient at the droplet interface, it is possible to obtain the local evaporation rate through the following formula:

$$J_l = -\frac{M_v P_{tot} D_v}{R T_{amb}(1-\chi_\sigma)} \frac{\partial \chi}{\partial n}$$

Here, M_v is the molar mass of the liquid (we use HFE-7000), P_{tot} is the total pressure, T_{amb} is the ambient temperature, R is the universal gas constant, D_v is the vapour diffusion coefficient and the last factor is the normal gradient of the molar fraction at the interface. Values of the global evaporation rate can be obtained by integrating this local evaporation rate over the droplet interface. As detailed in [8], we also found a way to extract the global evaporation rate by performing the integration of a 'pseudo'-local evaporation rate over any given iso-concentration contour. A good agreement is found between the different methods of evaluating the global evaporation rate, including the direct

side-measurement of the droplet shape (though this last method is much more perturbed by noise).

At last year's workshop, we have shown some quantitative results found for an evaporating pendant droplet of HFE-7000. This showed that the vapour plume deviated significantly from the pure-diffusion case. In addition, the measured global evaporation rate turned out to be up to 4 times larger than the pure-diffusion prediction and this already for a droplet with a radius of 2mm. These results are now published in [8].

In the present contribution, we will show the results of the simulation based on a boundary-layer theory that is also detailed in [8]. This simulation corresponds to the opposite limit of large Grashof number (as compared to the pure-diffusion calculation which corresponds to small Grashof numbers). In this simulation, the gas flow surrounding the measured droplet interface is calculated in quasi-stationary conditions. A non-Boussinesq approach is required as density variations in the gas can be up to four times larger than the ambient air density. Moreover, physical properties such as gas viscosity also vary significantly throughout the vapour cloud. A typical resulting mole fraction field is shown in Figure 3 using coordinates made dimensionless by the contact radius.

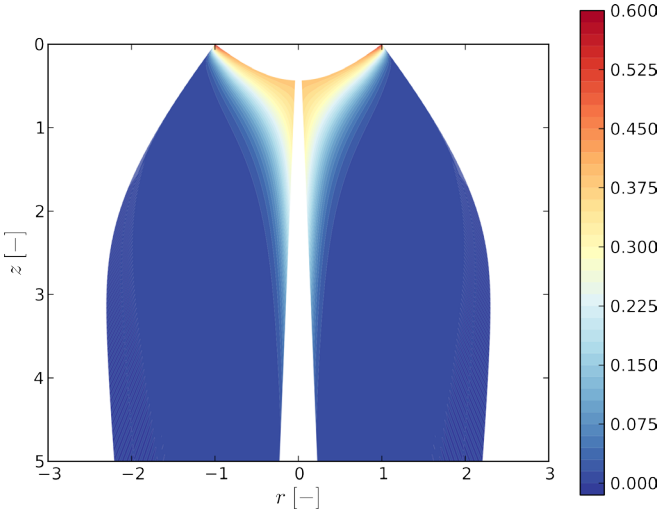

Figure 3: Calculated mole fraction field surrounding an evaporating pendant droplet of 1.81mm radius.

Apart from the typical boundary-layer computational domain, this field also shows qualitatively the same vapour cloud geometry as was experimentally measured. Important points to note are that the boundary layer and the numerical domain start at the contact line with a zero thickness, and the results are not accurate in its vicinity. Progressing the calculation downstream, the numerical domain expands rapidly. In the center of the droplet, no accurate results can be obtained either, as the tangential velocity component ceases to be larger than the normal one.

Now concerning the boundary conditions at the interface of the droplet, different possibilities have been explored. The simplest one, often considered in literature, is that of a stagnant interface with a uniform temperature equal to the ambient one. However, as our vapour concentration measurements also allow quantifying the interfacial temperature and have shown that a temperature decrease of 11°C occur from the contact line to the centre (for our pendant droplet of HFE-7000), this boundary condition is certainly questionable. Therefore, a second calculation was ran where the measured interfacial temperature was prescribed as a boundary condition, but still keeping the interface stagnant. Finally, we also performed a full numerical simulation inside the droplet to check whether the Marangoni stresses due to the measured interfacial temperature gradients could lead to interfacial velocities large enough to influence the vapour cloud geometry.

Comparing these three calculations showed that neglecting the interfacial temperature drop will lead to an overestimation of 35% of the global evaporation rate. On the other hand, neglecting the induced Marangoni flows can lead to an underestimation of up to 17%. A comparison of the local and global evaporation rates with the experimental results also shows that the simulation including the Marangoni flows yields the best agreement. Detailed results and comparisons will be given during the presentation.

In conclusion, we have found that experimental results obtained by vapour interferometry concerning local and global evaporation rate are satisfactorily confirmed by a simulation based on boundary-layer theory, while they strongly disagree with the classical pure-diffusion calculation. These simulations have also shown revealed an essential convective role of the Marangoni flow even in the gas phase, which is to be taken into account when running a full simulation. For the gas flow, a non-Boussinesq approach is recommended, including density and viscosity variations with vapour concentration.

References

[1] Deegan, R.; Bakajin, O.; Dupont, T.; Huber, G.; Nagel, S. & Witten, T. "Contact line deposits in an evaporating drop" Physical Review E, 62, 756-765 (2000)

[2] Popov, Y. "Evaporative deposition patterns: Spatial dimensions of the deposit" Phys. Rev. E, 71, 036313 (2005)

[3] Girard, F.; Antoni, M. & Sefiane, K. "Use of IR thermography to investigate heated droplet evaporation and contact line dynamics." Langmuir 2011, 27, 6744−6752.

[4] Dhavaleswarapu, H.; Migliaccio, C.; Garimella, S. & Murthy, J. "Experimental investigation of evaporation from low-contact-angle sessile droplets" Langmuir, 2010, 26, 880-888 (2010)

[5] Takeda, M.; Ina, H. & Kobayashi, S. "Fourier-transform method of fringe-pattern analysis for computer-based tomography and interferometry" J. Opt. Soc. Am., 72, 156-160 (1982)

[6] Fagrich, M. E. & Chehouani, H. "A simple Abel inversion method of interferometric data for temperature measurement in axisymmetric medium" Optics and Lasers in Engineering, 50, 336-344 (2012)

[7] Toker, G. & Stricker, J. "Holographic study of suspended vaporizing volatile liquid droplets in still air.", Int. J. Heat Mass Transfer, 39, 3475−3482, (1996)

[8] Dehaeck, S.; Rednikov A. & Colinet, P. "Vapor-Based Interferometric Measurement of Local Evaporation Rate and Interfacial Temperature of Evaporating Droplets", Langmuir, doi: 10.1021/la404999z, (2014)

On the Effect of Ambient Gas, Heat Transfer, and Thermal Patterns During Evaporation of Small Droplets

Yuki Fukatani[1], Takaaki Wakui[1], Suhaila Hussain[1],
Masamichi Kohno[1,2,3], Yasuyuki Takata[1,2,3],
Khellil Sefiane[4] and Jungho Kim[5]

1 Dept. of Mechanical Engineering, Kyushu University
2International Institute for Carbon-Neutral Energy Research (I2CNER), Kyushu University
3CREST, Japan Science and Technology Agency,
4School of Engineering, University of Edinburgh Kings Buildings, Mayfield road Edinburgh, EH9 3JL, United Kingdom
5 Dept. of Mechanical Engineering College Park, University of Maryland, MD 20742, USA
y.fukatani@heat.mech.kyushu-u.ac.jp

The evaporation of small sessile droplets deposited on a solid substrate has been widely studied in the past few decades due to its fundamental importance for many industrial and biological applications such as spray cooling, inkjet technology, and medical diagnosis of blood diseases. Previous studies of droplet evaporation have concluded that evaporation mainly occurs at the edge of the droplet near the three-phase contact line [1], and that there are two modes of the droplet evaporation: constant contact angle and constant contact area [2]. Thus far, different evaporative mechanisms have been reported depending on parameters such as wettability [3], thermal properties of the substrate [4], and atmosphere [5] in addition to the physical properties of the droplet.

Thermal patterns and hydrothermal waves (HTWs) within volatile droplets such as alcohols and refrigerants have attracted the attention of the scientific community since they were first discovered [6]. Conventional hydrothermal waves have thus far been observed in thin liquid layers whose interfaces were subjected to a lateral temperature gradient. On the other hand, the temperature difference is spontaneously self-driven during evaporation of volatile droplets. Theoretical linear stability analysis has shown that the role of thermocapillary Marangoni stress and advection are the key contributors to the instability [7]. Hydrothermal waves have recently been found to be bulk waves that extend across the entire droplet volume and affect the temperature and heat-flux distributions on the solid substrate and ultimately influence the droplet evaporation rate [8]. Despite the numerous studies carried out in this topic, details of the mechanism and the effect of thermal patterns and HTWs on the energy transport are not completely understood.

The objective of this study is to clarify the role of ambient gas and its effect in the evaporation of sessile droplets. The aim is a better understanding of the interplay between local thermal field at solid-liquid interface and the evaporation process. A schematic illustration of the experimental apparatus is shown in Figure 1. Experiments are conducted in Nitrogen environment with varying water and ethanol humidity levels. We aim to elucidate the role of ambient gas and its composition on evaporation and temperataure and heat flux distribution. The droplets which are degassed beforehand are deposited on the substrate using a syringe and allowed to evaporate freely into the surrounding gas. The liquids used here are FC-72 and water.

An IR (FLIR SC4000, with a spectral range of 3µm-5µm and a resolution of 18 mK) camera and a CCD camera (SENTECH, STC-TB152USB) were used to determine the temperature/heat flux distribution at the solid-liquid interface and profile of evaporating droplet, respectively. The shape of the FC-72 droplet during evaporation is shown in Figure 2.

The heat flux and temperature distribution at the solid-liquid interface was obtained using a multilayered substrate consisting of a silicon wafer coated with a thin thermal insulator that was partially transparent to IR [9]. Time varying profiles of the evaporating drop were used to find the area averaged, time resolved wall heat transfer. Examples of the data after processing are shown on Figure 3 for FC-72.

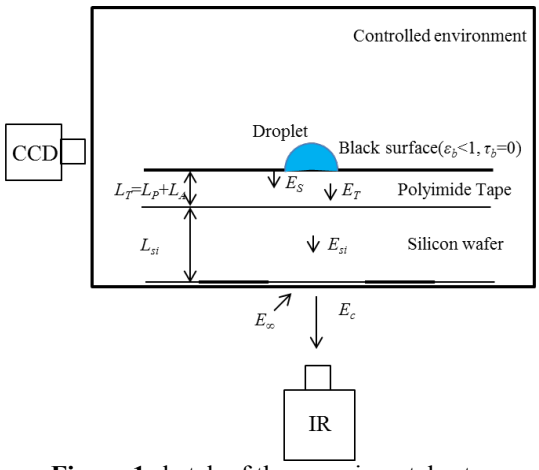

Figure 1 sketch of the experimental setup

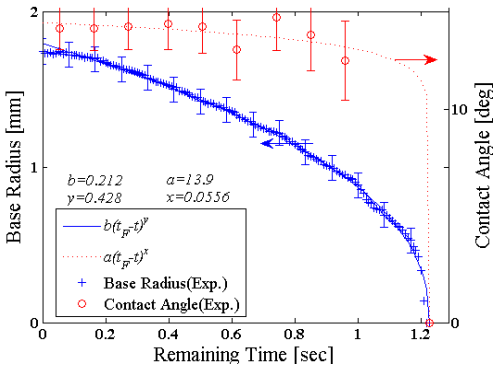

Figure 2 Base radius and contact angle evolution for a FC-72 droplet.

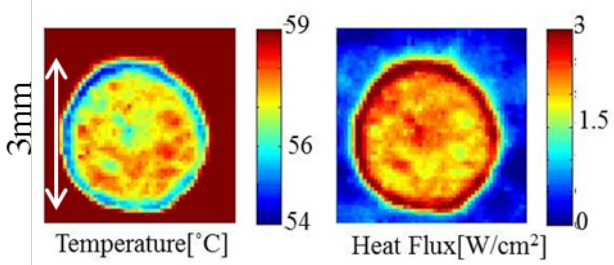

Figure 3 Evaporation of a FC-72 droplet. Temperature (Left) and heat flux distribution (Right) on the bottom surface.

The multilayer substrate consisting of a silicon wafer, polyimide, adhesive and black paint is shown schematically on Figure 1. To obtain temperature variations within the multilayer and the heat flux at the solid-fluid interface, an unsteady heat conduction problem was solved. A 1-D heat conduction approximation could be applied to the multilayer since the temperature gradient is much larger in the x-direction than in the other directions. To ascertain the accuracy of the IR heat-flux measurements, the energy required to evaporate a drop, calculated as $Q_{vol} = \rho_l V_i h_{lg}$, where ρ_l is the liquid density, h_{lg} is the evaporative latent heat, and V_i is the deduced initial droplet volume, was compared to the integrated IR heat flux over the droplet lifetime [$Q_{IR} = \int_0^t \int A_b(t)\dot{q}''\mathrm{dA}(t)\mathrm{dt}$ where A_b is the drop base surface area] for each test. The agreement was within ~22% for each substrate temperature.

Preliminary tests were conducted using HFE-7100 droplets. The normalized area-integrated heat transfer as a function of the base radius during the evaporation of is shown in Figures 4(a), (b). The data show that the curve deviates from the linear trend when humidity is present in the ambient gas. This may imply that when the ambient gas comprises water vapor, the heat transfer depends more on the surface rather than the perimeter of the drop. Effects of thermal and species gradients on the evaporation of sessile droplets will be discussed in the presentation.

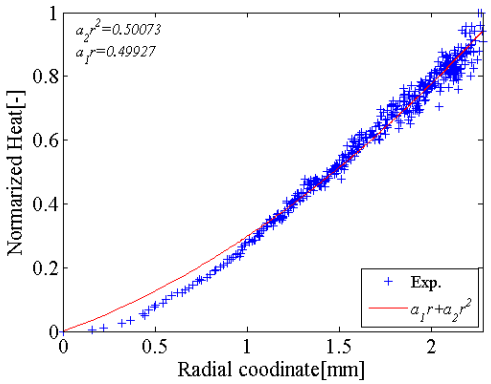

(a) pure N_2 environment

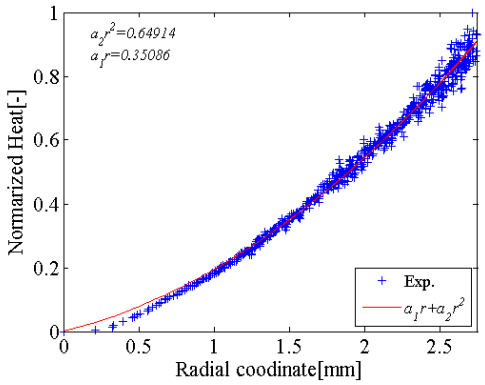

(b) N_2+water environment

Figure 4 Area-integrated heat transfer as a function of base radius for HFE-7100 droplets at ambient temperature (26 °C).

[1] Deegan, R. D., Bakajin, O., Dupont, T. F., Huber, G., Nagel, S. R., & Witten, T. A. Contact line deposits in an evaporating drop. Physical Review E - Statistical Physics, Plasmas, Fluids, and Related Interdisciplinary Topics, 62(1 B), 756-765. (2000).

[2] Picknett, R. G., & Bexon, R. The evaporation of sessile or pendant drops in still air. Journal of Colloid and Interface Science, 61(2), 336-350. (1977).

[3] Bourgès-Monnier, C., & Shanahan, M. E. R. Influence of evaporation on contact angle. Langmuir, 11(7), 2820-2829. (1995).

[4] Sefiane, K.; Bennacer, R. An expression for droplet evaporation incorporating thermal effects. Journal of Fluid Mechanics, 667, 260-271. (2011).

[5] Sefiane, K., Wilson, S. K., David, S., Dunn, G. J., & Duffy, B. R. On the effect of the atmosphere on the evaporation of sessile droplets of water. Physics of Fluids, 21(6). (2009).

[6] Sefiane, K., Moffat, J. R., Matar, O. K., & Craster, R. V. Self-excited hydrothermal waves in evaporating sessile drops. Applied Physics Letters, 93(7). (2008).

[7] Karapetsas, G., Matar, O. K., Valluri, P., & Sefiane, K. Convective rolls and hydrothermal waves in evaporating sessile drops. Langmuir, 28(31), 11433-11439. (2012).

[8] Sefiane, K., Fukatani, Y., Takata, Y., & Kim, J. Thermal patterns and hydrothermal waves (HTWs) in volatile drops. Langmuir, 29(31), 9750-9760. (2013).

[9] Kim, T. H., Kommer, E., Dessiatoun, S., & Kim, J. Measurement of two-phase flow and heat transfer parameters using infrared thermometry. International Journal of Multiphase Flow, 40, 56-67. (2012).

Influence of Interfacial Transport Phenomena on Internal and External Flow Behavior around an Acoustically Levitated Droplet

Atsushi Goda[1(a)] , Koji Hasegawa[3(b)], Akiko Kaneko[1(c)] , Yutaka Abe[1(d)]

University of Tsukuba, [1]Institute of engineering Mechanics and System, [2]Graduate school of System and Information Engineering, Research, [3]Kogakuin University, Department of Mechanical Engineering
[1,2]1-1-1 Tennoudai, Tsukuba, Ibaraki, 305-8573, Japan, [3]2665-1, Nakano-machi, Hachioji-shi, Tokyo, Japan
s1011161@u.tsukuba.ac.jp[(a)], kojihasegawa@cc.kogakuin.ac.jp[(b)], kaneko@kz.tsukuba.ac.jp[(c)] , abe@kz.tsukuba.ac.jp[(d)]

1. Introduction

A container is necessary in order to hold the solution in ground environment. On the other hand, container - less processing using levitation techniques could prevent influence from the wall surface. Acoustic levitation is one of levitation techniques which have some nonlinear behavior such as the internal flow, external flow, and the interfacial deformation. It is widely known that an acoustic streaming is also appeared around a levitated droplet by an acoustic wave, and complex flow is also generated inside and outside the droplet. In ground environment, toroidal vortices are observed around an acoustically levitated droplet [1]. It is indicated that flow field around a levitated droplet affects the rate of mass transfer [2]. However experimental knowledge about the interaction between flow behavior and transport phenomena of the droplet is not enough.

The purpose of this study is to investigate about interaction between internal, external flow behavior and interfacial transport phenomena of an acoustically levitated droplet. Here, we visualized the external flow around a levitated droplet and investigated the time series change of the surface temperature and the size of the levitated droplet.

2. Experimental apparatus and experimental method

Figure 1 shows schematic of the experimental apparatus and method for measuring the external flow of the levitated droplet. The experimental apparatus consist of a test section and measuring devises. A sine wave signal generated via a function generator is inputted to the ultrasonic transducer through a power meter and an amplifier. Then, ultrasonic wave is transmitted from the horn which is connected to the transducer. The ultrasonic wave is reflected by the reflector and forms standing wave. Droplet is injected by a syringe and levitated at the node of the standing wave.

The external flow around the levitated droplet is visualized by illuminating entrained tracer particles. Tracer particles which is about 5 [μm] in diameter are generated by a nebulizer. Flow configuration of the levitated droplet is measured by PIV and trajectory of particles which consisted by the multi exposure images. In order to evaluate the evaporation process, the size and surface temperature was measured. The size and the surface temperature of the levitated droplet were measured by the images taken with a high-speed camera and a thermography, respectively.

In this experiment, the resonance frequency of the transducer is 19.4 [kHz]. The distance between the horn and the reflector is 47.5 [mm]. The sound pressure level at antinode is set at 158-164 [dB]. In the present study, three kinds of fluids are used, water, ethanol, and hexane. Table 1 shows the physical properties of sample at 25 [deg C]. The saturated vapor pressure is characteristically difference. Aspect ratio is defined as a ratio of major axis divided by minor axis.

Table 1: The physical properties of the test fluid

Liquid	Density [kg/m^3]	Viscosity [mPa·s]	Surface tension [mN/m]	Vapor Pressure [Pa]
Water	1000	1.00	72.8	2333
Ethanol	789	1.20	22.3	5849
Hexane	655	0.29	18.4	16162

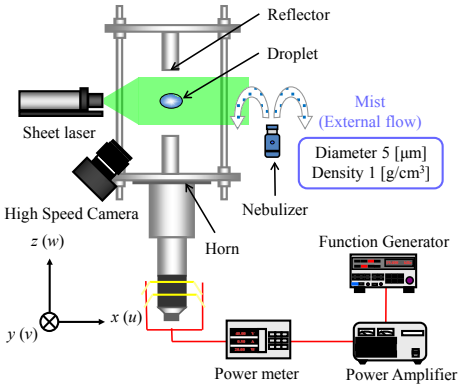

Figure 1: Schematic of the experimental apparatus

3. Results and discussion

Figure 2 shows average velocity vector fields around an acoustically levitated droplet. The velocity vector consisted of average of measurement of 1 [s]. Figure 2 (a) shows a water droplet, (b) shows an ethanol droplet, and (c) shows a hexane droplet. In the case of the water droplet, the surrounding fluid flows from the side of the droplet and flow out to the lower and upper of the droplet. The circular vortex which is considered as toroidal vortex is observed around the bottom of the levitated water droplet. In the case of the ethanol and hexane droplet, the direction of the flow becomes opposite from the case of water, and the toroidal vortex is observed around the top and bottom of the droplet. Additionally in the case of the ethanol and hexane droplet, the external flow is accelerated near the droplet surface as the saturated vapor pressure of the droplet becomes higher. Then, we have expanded the imaging area using microscope lens, and focused on the flow structure in the vicinity of the droplet interface.

Figure 3 shows the flow trajectory in the vicinity of the droplet interface. The white line is the path of particles by multi exposure for 0.1 [s]. Here, mixed solution of ethanol and water which were mixed at the ratio 25, 50, 75 [wt%] are used.In the case of the 50,75,100 [wt%] aqueous solutions of ethanol droplet and the hexane droplet small circular vortex was observed around the droplet. But in the

case of the water droplet and 25 [wt%] aqueous solution of ethanol droplet, the vortex was not observed.

The circulating vortex inflows from the side of the droplet, and is directed into the top and bottom of the droplet along the interface. Then, before reaching the top and bottom end, it is circulated back to the sides. In terms of flow direction, the flow behavior is consistent by the case of the non-volatile fluid. In the present study, as the concentration of ethanol in the droplet increases, the scale of the circular vortex decreases. And the scale of the circular vortex which generated around the hexane droplet is smaller than the case of the ethanol droplet.

Figure 4 shows results of a quantitative evaluation about the scale of the circular vortex. The scale of the circular vortex is defined as the length from the existing area of the circular vortex to the droplet interface. The horizontal axis in Figure 4 (a) is the droplet diameter and vertical axis is the scale of circulating vortex in the vicinity of the droplet interface. Figure 4 (a) shows the tendency that the concentration of ethanol increases, the scale of circulating vortex becomes smaller, but not all of them are adapted. The horizontal axis of Figure 4 (b) is the droplet aspect ratio, and vertical axis is the scale of circulating vortex. In a droplet containing ethanol component, the scale of circular vortex shows that as the aspect ratio becomes higher, the scale of the circular vortex becomes larger. Therefore, the circular vortex generated in the vicinity of the interface may be related to concentration gradient of the droplet. Thus we suggested a correlation of the flow behavior and the evaporation behavior of the droplet.

Figure 5 shows the time series change of the surface area and surface temperature of the levitated droplet. The horizontal axis in Figure 5 (a) is the time, and the vertical axis is the surface area. In the case of the ethanol droplet, 80 [%] of the surface area was reduced by 300 [s]. In the hexane droplet, 95 [%] of the surface area was also reduced by 100 [s] too. The volatile droplets evaporate quickly unlike the water droplets. Therefore, the volatile gas component may be present in the test section. It is likely to be the concentration gradient appears around the droplet. Next we focus on the change of the surface temperature. The horizontal axis in Figure 5 (b) is time, and the vertical axis is the minimum surface temperature of the levitated droplet measured by thermography. In the case of the water droplet, surface temperature decreases immediately after levitation. Then it becomes constant. In volatile droplets, surface temperature decreases immediately after the levitation, and surface temperature becomes constant. Then the surface temperature increases, and this is different tendency from water droplet. The cause of this behavior is considered that the decrease in the temperature is the endothermic due to the evaporation of the droplet, and the increase in surface temperature is the exothermic reaction due to the condensation of present water vapor.

4. Conclusion

(1) In the case of the water droplet, toroidal vortex generated around the bottom of the droplet. In the ethanol and the hexane droplet, two toroidal vortices were observed around the top and bottom of the droplet, and two toroidal vortices were also generated in the vicinity of the droplet interface.

(2) Comparing with the ethanol and the hexane droplet, the higher saturated pressure generated the smaller circular vortex at the interface.

(3) Surface temperature on the droplet decreases when it levitated, and also its volume decreases. This is considered to be the effect of volatility.

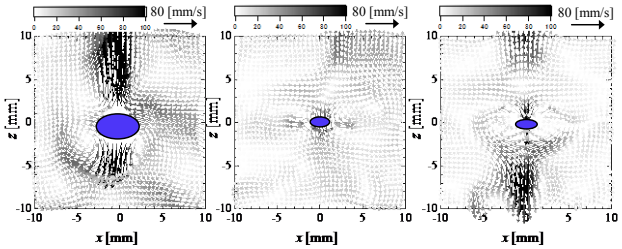

(a) Water (b) Ethanol (c) Hexane

Figure 2: Average velocity vector fields around a droplet

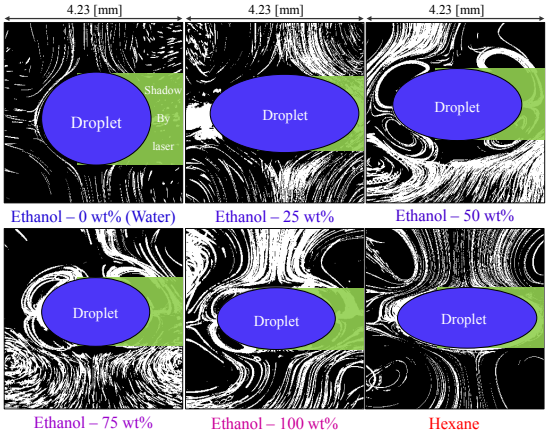

Figure 3: The flow trajectory in the vicinity of the interface

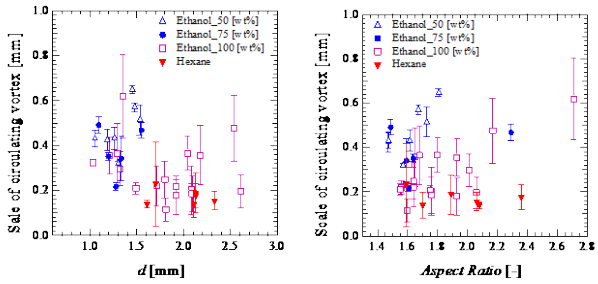

(a) Diameter (b) Aspect ratio

Figure 4: Scale of the circular vortex in the vicinity of the droplet interface

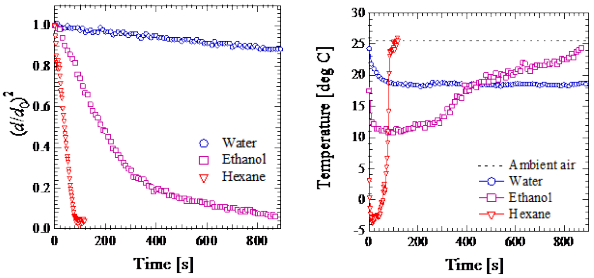

(a) Surface area (b) Surface temperature

Figure 5: Time series change of evaporation process

References

[1] K. Hasegawa, et al. "Visualization measurement of streaming flows associated with a single-acoustic levitator" Microgravity Science and Technology, Vol.21(1), pp.9-14, 2009.

[2] A. L. Yarin, et al. “Evaporation of acoustically levitated droplets”, J. fluid Mech., Vol.399, pp.151-204, 1999.

Levitation stability and restoring force of an acoustically levitated droplet

Koji Hasegawa[1 (a)], Taku Furukawa[1], Hiroyasu Ohtake[1], Yutaka Abe[2]

Department of Mechanical Engineering, Kogakuin University[1]
2665-1, Nakano-machi, Hachioji, Tokyo, Japan[1]
Graduate School of Systems and Information Engineering, University of Tsukuba[2]
1-1-1 Tennodai, Tsukuba, Ibaraki, Japan[2]
E-mail: kojihasegawa@cc.kogakuin.ac.jp [(a)]

1. Introduction

Acoustic levitation is based on the production of a standing wave with equally spaced nodes and antinodes between the horn and reflector[1]. This levitation technique is expected to be used in the field of the analytical chemistry and manufacturing new materials in order to prevent the heterogeneous nucleation and contamination by container-less processing. However, there was always a strong concerns of the levitation force and stability of droplet with acoustic levitator over the decades[1-4]. Although it is crucial to understand the non-linear behavior of an acoustically levitated droplet, it is still unclear in what way the levitation force/stability can be improved experimentally.

The purpose of this study is to improve the levitation stability and investigate the mechanism of restoring force on an acoustically levitated droplet.

2. Experimental approach

Figure 1 shows a schematic of experimental setup. Acoustic levitator consisting of a transducer and a reflector generates a standing wave between transducer-reflector gaps. An acoustic standing wave is generated from a transducer through a bottom horn and reflected at a top reflector surface. Acoustic standing wave provides the radiation pressure arising from a vertically oriented in the gap. This allows a droplet to levitate at the pressure nodes. The characteristics of the levitated droplet was recorded through a high speed video camera and a computer.

It is numerically suggested that remarkable enhancement of the single-axis acoustic levitation force is achieved by properly curving the surface to reinforce the levitation stability in the test section[2]. In order to investigate the effect of geometric parameter of the levitator on stability of levitated droplet, we used different reflectors based on the result by Xie et. al.[2]. Figure 2 shows a schematic of two types of reflector. Figure 2(*a*) is the flat reflector (R∞) which we have been used in the early studies. Figure 2(*b*) is the spherically curved reflector (R36) which is developed in this study. Curvature of the concave reflector is 36 [mm] which is calculated and developed. Table 1 shows the experimental conditions in this study. Frequency generated from function generator was roughly 19.4 [kHz]. A transducer-reflector gap was set at approximately 47 [mm]. Sound pressure was set between 0.3-10.9 [kPa]. Sound pressure was measured with the probe microphone (Bryel&Kjaer, Type4182). We used water as a test sample. Aspect ratio is the equatorial-to-polar ratio of radii which is derived from photographs.

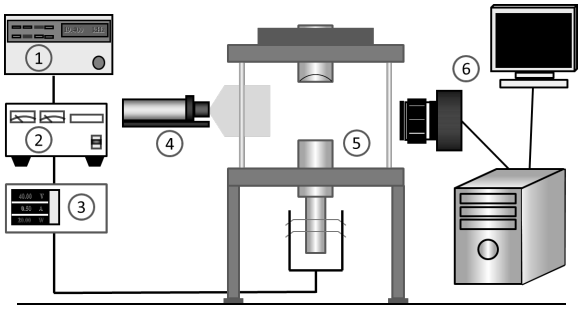

① Function generator
② Power amplifier
③ Power meter
④ Light
⑤ Test section
⑥ High-speed video camera

Figure 1: Schematic of experimental setup.

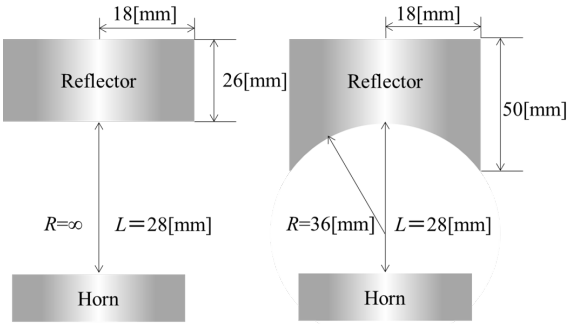

(*a*) Flat type (*R*=∞) (*b*) Concave type (*R*=36 [mm])

Figure 2: Geometry of each reflector.

Table 1: Experimental conditions.

Input frequency [kHz]	19.4
Temperature [ºC]	22±8
Humidity [%]	45±10
Equivalent diameter [mm]	0.3-7.0
Sound pressure [kPa]	0.3-10.9
Test sample	Water
Aspect ratio [-]	0.8-7.5
Wavelength [mm]	17.7
Wavenumber [1/mm]	0.3

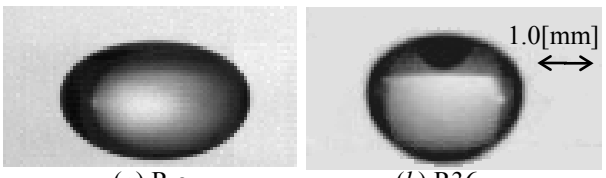

(*a*) R∞ (*b*) R36

Figure 3: The levitated droplet with each reflector.

3. Experimental result and discussion

Figure 3 shows photographs of the levitated water droplet with each reflector. Equivalent diameter and sound pressure are 4.2 [mm] and 3.4 [kPa] in both cases. In terms of interfacial deformation, it is found that the aspect ratio of curved reflector is smaller than that of flat reflector even same conditions.

Figure 4 shows experimental and theoretical results of relation between normalized equivalent diameter and sound pressure with different reflector. The equivalent diameter is normalized with wavelength of sound wave. During levitating droplet by acoustic levitator, it is difficult to be stable drop levitation in either case of the sound pressure becomes too low to counteract the gravity, or it becomes too high to keep the stability and integration of the drop. In the former case, the droplet falls down. Whereas in the latter case, the droplet is remarkably oscillated and then broken up. Breaking up the droplet leads to atomization. Therefore the sound pressure of acoustic fields needs to be tuned in suitable condition. Its lower limit to sustain a droplet is described by King[3]. While its upper limit calculated by Donilov et al.[4] represents upper threshold pressure. In comparison with theoretical results by King and Danilov et.al,. Droplets with flat reflector were levitated in the predicted region. On the other hand, droplets with curved reflector were levitated beyond its region.

Figure 5 shows the translational motion of the droplets with different reflector. Equivalent diameter and sound pressure are 3.7 [mm] and 3.4 [kPa] in both cases. The steady translation was occurred on the droplet with the flat reflector. Whereas, the droplet with the curved reflector was levitated in more stable condition. In comparison with the amplitude of former case, that of the latter case decreased by around 80% due to the difference of sound pressure distribution around each droplet.

Our interest here is the difference of sound pressure distribution between the flat reflector and spherically curved reflector. Even though a measurement of sound pressure distribution under the levitation of droplet has not been achieved because of disturbance by microphone, we have tried to visualize the sound pressure distribution without any droplet. Figure 6 shows sound pressure distribution with each reflector. In the case of the flat reflector, maximum and minimum sound pressure were 4.0 and 0.6 [kPa]. In the case of the curved reflector, maximum and minimum sound pressure were 4.1 and 0.3 [kPa]. It is confirmed that the acoustic standing wave were formed in both case. It is found that horizontal sound pressure gradient with the curved reflector was lower than that with the flat reflector at levitated position(y/λ=0.22). This indicates that droplet with curved reflector is less disturbed by surrounding sound pressure distribution.

4. Conclusions

We investigated the levitation stability and investigate the mechanism of restoring force on acoustically levitated droplet by using different reflectors. The translation of the droplet was recorded by high speed video camera and estimated quantitatively. It is shown that translational amplitude of droplet with curved reflector was drastically smaller than that with flat reflector because of the lower sound pressure gradient around the levitated droplet.

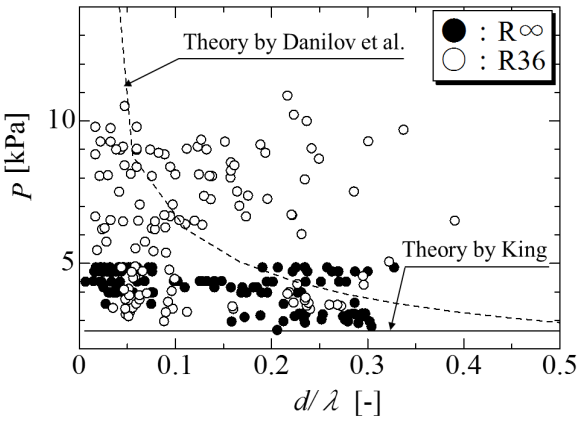

Figure 4: Relation between normalized equivalent diameter and sound pressure.

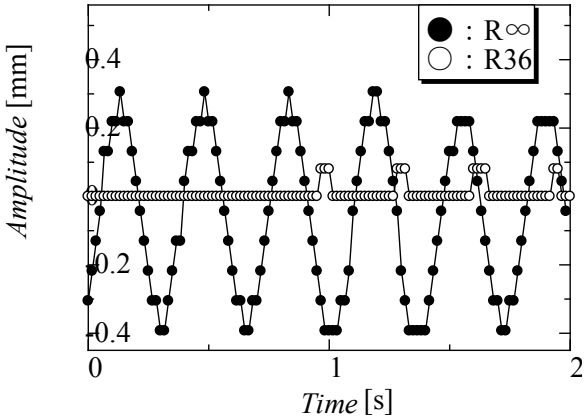

Figure 5: The translational motion of the droplets.

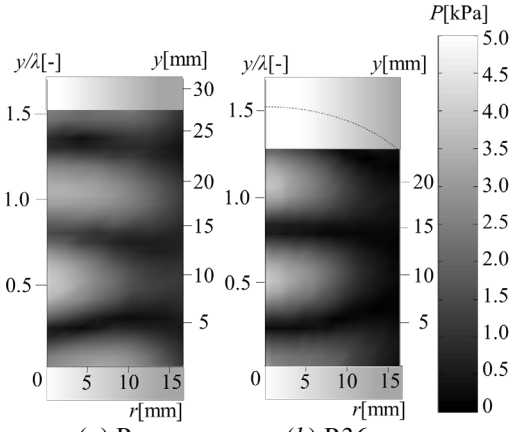

Figure 6: Sound pressure distribution with each reflector.

References

[1] Yarin, A. L., Pfaffenlehner, M. and Tropea, C., On the Acoustic Levitation of Droplets, J. Fluid Mech., Vol. 356, 65-91 (1998).

[2] Xie, W. J. and Wei, B., Dependence of Acoustic Levitation Capabilities on Geometric Parameters, Physical Review E, Vol. 66, 026605-1-11 (2002).

[3] King, L. V., On the Acoustic Radiation Pressure on Spheres, Proc. R. Soc. London, Ser. A Vol. 147, 212-240 (1934).

[4] Danilov, S. and Mironov, M., Breakup of a Droplet in a High-intensity Sound Fields, J. Acoust. Soc. Am., Vol. 92, 2747-2755 (1992).

A new concept for investigating heat transfer mechanisms during spray cooling

Matthias Winter, Tatiana Gambaryan-Roisman, Peter Stephan

Institute for Technical Thermodynamics & Center of Smart Interfaces, Technische Universität Darmstadt
Alarich-Weiss-Str. 10, 64287 Darmstadt, Germany
pstephan@ttd.tu-darmstadt.de

A new concept for an extended study on the heat transfer mechanisms during spray cooling, with regard to electronics cooling is presented in the following.

To remove the steady increasing amount of waste heat from electronic devices, contemporary technologies using single-phase air or water cooling verge their limits. Since electronics typically have a limitation of working temperature of approximately 75°C, new technologies using two-phase heat transport mechanisms are necessary to meet future demands in cooling. Spray cooling enables a very high heat transfer capability due to a very good uniformity of liquid distribution on the cooled surface. So far, most studies on spray cooling focus on the enhancement of heat transfer by testing and optimizing different surface structures.

Hsieh and Yao [1] investigated the advance of capillary forces to ensure a passive liquid distribution on micro-structured silicon surfaces using water as working fluid. They found that the topography of the surface has an effect to reach higher heat transfer rates than on a smooth surface when working in thin film and partial dry-out evaporation regime, while no influence of the surface topography could be determined in flooded and dry-out regime. Silk et al. [2] did a study varying a broad range of geometrical parameters as size and distance of cubic stud structures using degassed and non-degassed PF-5060 as working fluid. They conclude that the smaller the size and distance of the studs, the higher the CHF, with highest CHF measured with non-degassed working fluid. To determine the heat transfer in the vicinity of the three-phase contact-line, Sodtke et al. [3,4] studied spray impingement on copper surfaces with geometrically well-defined micro-milled triangular grooves and pyramids. They visualized the length of the three-phase contact-line, due to film break-up, using a high-speed IR video camera and found that at already low surface superheat, the dissipated heat flux increases if the liquid film breaks up. A study of spray cooling using water on micro-porous surfaces varying the thickness and particle size of the porous structure has been done by Kim et al. [5]. They found no clear dependency of particle size on heat transfer but they found that the thickness of a porous layer influences heat transfer performance.

Additional studies as parameter studies on the angle the liquid is sprayed on the surface, liquid sub-cooling and so on were performed up to now. The lack of fundamental investigations of the heat transfer mechanisms governing the heat transfer induces the need for further studies.

The subject of the present work is to distinguish between to two main heat transfer mechanisms of spray cooling, namely single-phase convection and evaporation. The concept led to a new setup that allows determining the amount of the condensate of condensed vapor and the excess liquid separately. The setup consists of a closed loop system with pure working fluid under saturated conditions without non-condensable gases. Different micro-milled and porous sintered surface structures have been tested and compared to a polished surface.

The following approach was chosen to distinguish between convective and evaporative transferred heat:
The total heat $\dot{Q}$ consists of the convective transported heat $\dot{Q}_c$ and the heat transported by evaporation $\dot{Q}_v$:

$$\dot{Q} = \dot{q} A_{proj} = \dot{Q}_c + \dot{Q}_v \quad (1)$$

with

$$\dot{Q}_c = \dot{q}_c A_{proj} = h_c A_{proj}(t_w - t_\infty), \quad (2)$$

$$\dot{Q}_v = \dot{q}_v A_{proj} = h_v A_{proj}(t_w - t_{sat}) = \dot{M}_v \Delta h_v, \quad (3)$$

where A_{proj} is the projected area of the surface, h_c the convective heat transfer coefficient, h_v the evaporative heat transfer coefficient, t_w the wall temperature, t_∞ the temperature of fluid out of the boundary layer, t_{sat} the saturation temperature, $\dot{M}_v$ the mass flow of condensate, and Δh_v the enthalpy of evaporation.
The convective mass flow $\dot{M}_c$ is calculated as

$$\dot{M}_c = \dot{M} - \dot{M}_v \quad (4)$$

with

$$\dot{M}_v = M_v / \tau_{meas}, \quad (5)$$

where $\dot{M}$ is the measured mass flow at the nozzle outlet, M_v the measured mass of condensate, and τ_{meas} the duration of the collection of M_v.
The heat flux for the convective heat flux $\dot{q}_c$ depends on the heat capacity of the liquid $c_{p,l}$ and the difference of the excess fluid temperature t_c and fluid inlet temperature t_f:

$$\dot{q}_c = c_{p,l}(t_c - t_f)\dot{M}_c / A_{proj}. \quad (6)$$

The evaporative heat flux $\dot{q}_v$ is defined as

$$\dot{q}_v = \frac{\dot{M}_v}{A_{proj}} c_{p,l}(t_{sat} - t_f) + \Delta h_v + c_{p,v}(t_v - t_{sat}), \quad (7)$$

where $c_{p,v}$ is the heat capacity of the vapor and t_v the vapor temperature.
Three different heat transfer coefficients, a global one *h,* a convective one h_c and an evaporative one h_v are calculated using the individual heat fluxes $\dot{q}_i$ as:

$$h_i = \dot{q}_i / \Delta t_w \quad (8)$$

with the wall superheat Δt_w

$$\Delta t_w = t_w - t_{sat}. \quad (7)$$

The pressure inside the test cell p_{cell} is used to calculate the saturation temperature t_{sat} using the specific fluid properties from NIST Standard Reference Database 23, REFPROP 9.0, and fluids datasheets by 3M™.

In this study the working fluids methanol and Novec™-7000 are used. Results of heat transfer measurements using methanol as working fluid on a polished copper surface with $R_a \approx 0.3\mu m$ and $A_{proj}=\pi$ cm² are presented in figure 1-3. The liquid sub-cooling is $\Delta t_f =$

$t_{sat} - t_f = 3$ K. During the measurement, the heat flux is increased stepwise until the surface temperature reaches 75 °C or CHF occurred.

The global heat transfer coefficient h is plotted versus the heat flux $\dot{q}$ with variable mass flow $\dot{M}$, see figure 1.

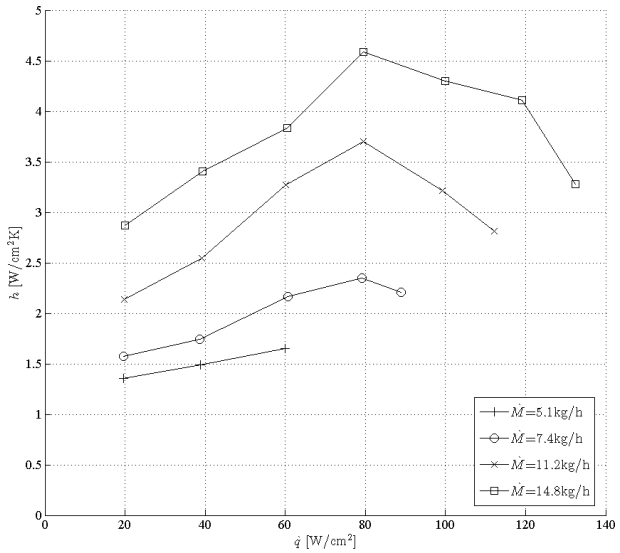

Figure 1: global heat transfer coefficient h over heat flux $\dot{q}$ for varying mass flow $\dot{M}$ (polished; methanol, $\Delta t_f = 3$ K.)

With increasing heat flux $\dot{q}$, the global heat transfer coefficient h increases slightly, with higher values, the higher the mass flow $\dot{M}$. When a maximum value is reached, the heat transfer coefficient decreases with further increasing heat flux. This analysis hypothesis, that with increasing $\dot{q}$ and $\dot{M}$, the heat transfer increases, which is correct for the global view, but does not give specific information about the convective and evaporative heat transfer.

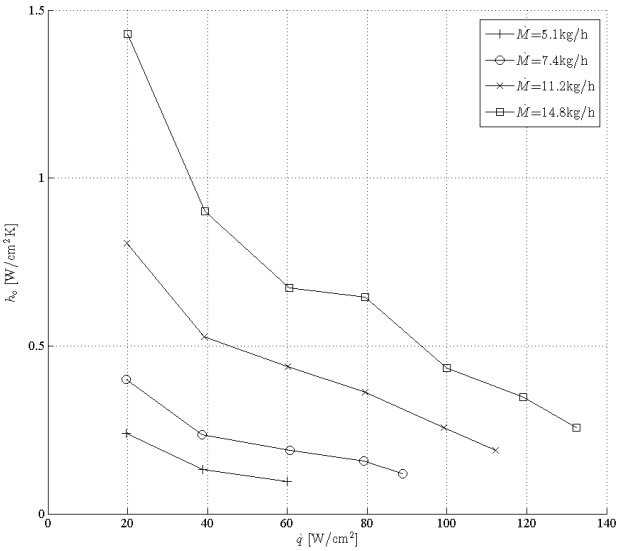

Figure 2: conv. heat transfer coefficient h_c over heat flux $\dot{q}$ for varying mass flow $\dot{M}$ (polished; methanol, $\Delta t_f = 3$ K.)

To analyse the convective and evaporative heat transfer, both heat transfer coefficients, h_c and h_v, are plotted versus heat flux in figure 2 and figure 3. The convective heat transfer coefficient h_c is higher at higher mass flux $\dot{M}$, but decreases with increasing $\dot{q}$, see figure 2. In figure 3, the evaporative heat transfer coefficient h_v is plotted versus $\dot{q}$. Again, h_v is higher at higher mass flux $\dot{M}$, but increases with increasing $\dot{q}$ at moderate heat fluxes, and then seem to reach a maximum value. This trend is consistent with the observed maximum global heat transfer coefficient in figure 1. We conclude that (for the tested parameters and for this surface configuration) the global heat transfer is dominated by evaporation compared to convection at high heat fluxes

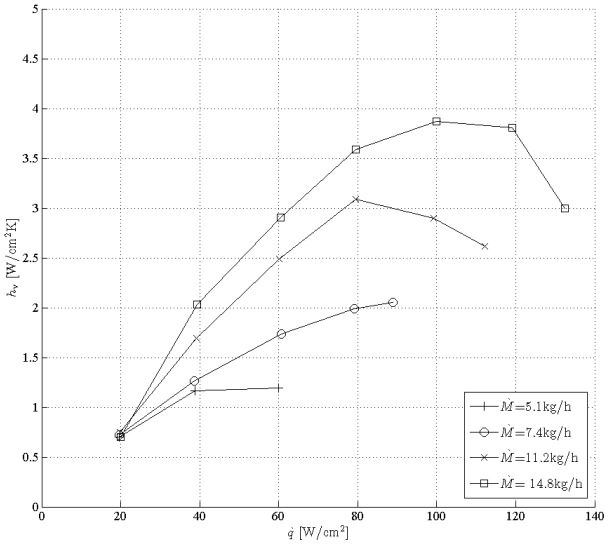

Figure 3: evap. heat transfer coefficient h_v over heat flux $\dot{q}$ for varying mass flow $\dot{M}$ (polished; methanol, $\Delta t_f = 3$ K.)

Summary and Conclusions

The presented experimental approach allows distinguishing between heat transfer by convection and by evaporation during spray cooling. Analyzing these heat transfer contribution for variable mass fluxes and heat fluxes leads to a better understanding of the basic heat transfer modes. Further optimization of spray cooling systems can make use of these findings.

References

[1] Hsieh, C.-C., Yao, S.-C., Evaporative heat transfer characteristics of water spray cooling on micro-structured silicon surfaces, International Journal of Heat and Mass Transfer, 49, 962-974 (2006)

[2] Silk, E.A., Kim, J., Kiger, K., Impact of Cubic Pin Finned Surface Geometry Upon Spray Cooling Heat Transfer, Proceedings of IPACK, 73003 (2005).

[3] Sodtke, C., Untersuchungen zur Sprühkühlung an mikrostrukturierten Oberflächen, Ph.D. Thesis, Technische Universität Darmstadt (2007)

[4] Sodtke, C., Stephan. P., Spray cooling on micro structured surfaces. International Journal of Heat and Mass Transfer, 50, 4089–4097 (2007)

[5] Kim, J., You, S., Choi, S.U., Evaporative spray cooling on plain and microporous coated surfaces, International Journal of Heat and Mass Transfer, 47, 3307-3315 (2004)

Temperature Evolution during the Evaporation of a Sessile Droplet

Aziz Maatar[1, a], Salah Chikh[1,b], Mebrouk Ait-Saada[1,c] and Lounès Tadrist[2,d]

[1] USTHB, Faculty of Mechanical and Process Engineering, LTPMP, Alger, Algeria
[2] Aix Marseille Université, IUSTI, CNRS UMR 7343, Marseille, France
[a] maataraziz@gmail.com, [b] salahchikh@yahoo.fr, [c] m_aitsaada@yahoo.fr, [d] lounes.tadrist@polytech.univ-mrs.fr

The evaporation of a sessile droplet is a phenomenon encountered in many practical applications such as micro-lenses manufacturing, DNA analysis, inkjet printing and many others. It has a simple geometry but it involves several coupled mechanisms that render its analysis quite complex. Accounting for the contact line dynamics, the evaporation kinetics, the droplet interface tracking and the fluid motion inside and outside the droplet makes it a difficult problem. According to the literature survey, numerous analytical, experimental and numerical studies were carried out for the attempt to reveal some non-answered questions [1-3]. However, most of the numerical works have assumed the quasi-steady state, which is a good approach but only for the less or non-volatile liquids with slow variation of evaporation parameters [4, 5]. Though, some authors dealt with volatile liquids such as (tetrachlorethylene, ethanol–fuel oil mixtures and methanol) [6- 8] in order to analyze the volatility effects.

The present study is devoted to the analysis of heat and mass transfer during the sessile droplet evaporation. A numerical investigation is carried out with a transient diffusion model. Thermal diffusion is considered in all three phases (substrate, liquid droplet and surrounding air) whereas mass diffusion is invoked only in the surrounding air. Results are presented in terms of temperature evolution during the evaporation. Three reference points are considered and analyzed: the hottest point i.e. the droplet base center, the droplet apex i.e. the coldest point and the contact line which is a singular point.

An axis-symmetric computational domain is considered; it encompasses a cylindrical disk of great extent representing the substrate, a spherical cap droplet deposited on it and the surrounding gas where the evaporated liquid diffuses. In order to solve the governing equations for concentration and temperature, some assumptions are made. A pure liquid droplet with a pinned contact line is considered. It is assumed of small size so that the fluid motion inside it is neglected.

The unsteady thermal diffusion and mass diffusion equations are written as:

$$\rho c \frac{\partial T}{\partial t} = \frac{1}{r}\frac{\partial}{\partial r}\left(rk\frac{\partial T}{\partial r}\right) + \frac{\partial}{\partial z}\left(k\frac{\partial T}{\partial z}\right) \quad (1)$$

$$\frac{\partial C}{\partial t} = \frac{1}{r}\frac{\partial}{\partial r}\left(rD\frac{\partial C}{\partial r}\right) + \frac{\partial}{\partial z}\left(D\frac{\partial C}{\partial z}\right) \quad (2)$$

Coupling of thermal and concentration fields occurs at the drop surface through the saturation concentration and the energy balance which take the following forms:

$C_i = C_{sat}\,(T_i)$

$$k_L \left.\frac{\partial T}{\partial n}\right|_L - k_G \left.\frac{\partial T}{\partial n}\right|_G = D\frac{\partial C}{\partial n} L_{LG}$$

To solve these equations numerically, the finite volume method is used for the discretization and the ADI method is adopted for solving the transient equations.

A zonal and structured mesh is used with refined grids close to interfaces; 250 x 250 nodes are used and the cell size is $\Delta r = \Delta z = R/50$, where R is the droplet base radius. On the other hand, the time step should be less than 4×10^{-5} s to ensure stability.

A computer program is developed and implemented to solve Eqs.(1) and (2). The temperature and concentration fields are determined. The obtained results from the computer code are validated with the previous results found in the literature and a good agreement is found.

We focus in this work on the time evolution of temperature at three critical points in the droplet: the droplet apex "T_A", droplet base (center) "T_B" and contact line "T_{CL}". This allows to analyze heat transfer behavior and to deduce thermal diffusion time in the drop. Results for water and ethanol droplets on a 4 mm thick PTFE substrate are presented.

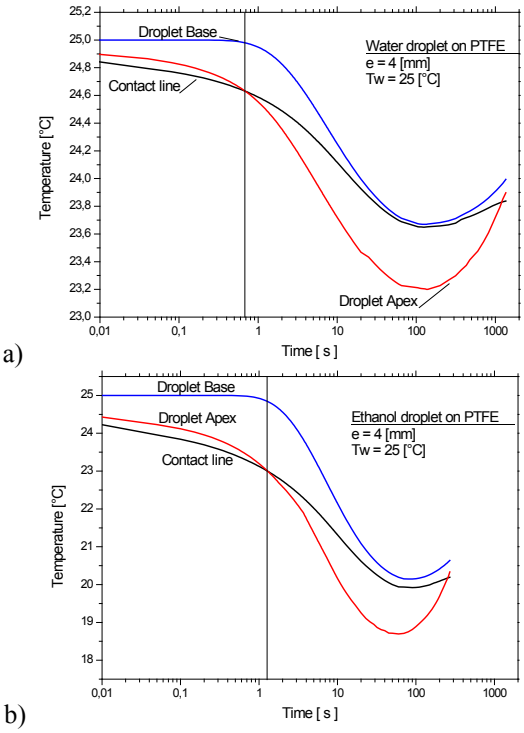

Figure 1: Time evolution of specified points in the droplet (a. water and b. ethanol) for non-heated conditions.

We present first the non-heated case where the initial temperature equals 25°C and the lower surface of the

substrate "Tw" is kept at 25°C as well. Hence, we notice that the time evolution of the three points are similar for both liquid droplets (see Fig. 1), but they differ on the cooling magnitude and the droplet lifetime which is shorter for ethanol droplet. It is shown that the substrate affects the contact line temperature T_{CL} at the beginning of evaporation. Initially, for a very short period of time, part of energy needed for evaporation is supplied by the substrate which makes the contact line temperature smaller than the apex temperature as indicated in Fig.1. For the remaining of the droplet evaporation the coldest point is the apex.

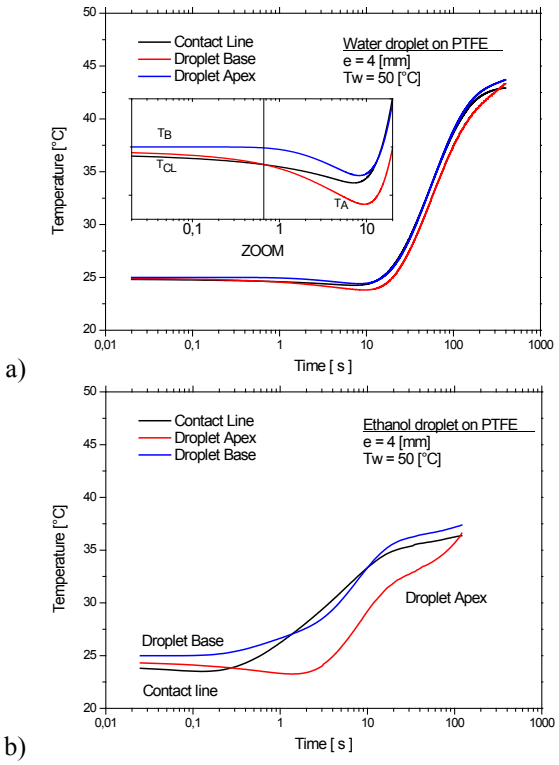

Figure 2: Time evolution of specified points in the droplet (a. water and b. ethanol) for heated conditions.

The substrate plays an important role when it is heated; it delays the moment at which the temperature of these points starts increasing. At the first stage of evaporation for a period less than 1 second, the droplet behaves as if it is non-heated and the temperature of the contact line is the coldest as in case of Fig.1. During the second stage T_w imposed at the bottom surface of the substrate yields the heating of the droplet; then we observe increase of the temperature. We notice that the contact line temperature increases higher than the droplet base center.

References

[1] Song, H., Lee, Y., Jin, S., Kim, H.Y., Yoo, J. Y., Prediction of sessile drop evaporation considering surface wettabilityPrediction of sessile drop evaporation considering surface wettability, Microelectronic Engineering, 88, 3249–3255, (2011).

[2] Lee, K.S., Cheah, C.Y., Copleston, R.J., Starov, V.M., Sefiane, K., Spreading and evaporation of sessile droplets: Universal behaviour in the case of complete wetting, Colloids and Surfaces A: Physicochem. Eng. Aspects, 323, 63–72, (2008).

[3] Ait Saada, M., Chikh, S., Tadrist, L., Numerical investigation of heat and mass transfer of an evaporating sessile drop on a horizontal surface, Physics of Fluids, 22, 112-115, (2010).

[4] Hu, H., Larson, R. G., Evaporation of a sessile droplet on a substrate, J. Phys.Chem. B, 106, 1334, (2002).

[5] Ait Saada, M., Chikh, S., Tadrist, L., Evaporation of a sessile drop with pinned or receding contact line on a substrate with different thermophysical properties, I. J. Heat Mass Transfer, Vol.58, Issues 1–2, 197–208, (2013).

[6] Chen, P., Understanding the dynamic surface tension of solutions containing volatile organic compounds (VOCs), Colloids and Surfaces A: Physicochemical and Engineering Aspects, 192, 195, (2001).

[7] Hallett, W.L.H., Beauchamp-Kiss, S., Evaporation of single droplets of ethanol–fuel oil mixtures, Fuel, 89, 2496, (2010).

[8] Bin, L., Bennacer, R., Bouvet, A., Evaporation of methanol droplet on the Teflon surface under different air velocities, Applied Thermal Engineering, 31, 3792, (2011).

Role of Surface Charges in Drop-Evaporation-Triggered "Coffee-Stain" Formation

Siddhartha Das

Department of Mechanical Engineering, University of Maryland,
College Park, MD 20740, USA
sidd@umd.edu

In this paper we shall analyze the role of particle surface charges in coffee-stain formation during evaporation of electrolyte drops on charged surfaces. Recent study by Das et al. [1] demonstrated that evaporation of electrolyte drops on charged surfaces induced a streaming electric field triggering an electroosmotic transport that massively altered the particle-deposition pattern. Here, we shall discuss the possible electrophoretic effects of this streaming electric field in case the particles suspended inside the drop are charged. We shall consider both rigid and soft colloidal particles. By controlling the charge on the particles (be it soft or rigid), it will be possible to actually control the "coffee-stain" (e.g., its rate of formation or the extent of heterogeneities in the particle distribution within the stain) in a manner that has been hitherto unexplored.

Drop-evaporation-induced "coffee-stain" formation has been an extremely important problem at the interface of multiphase fluid mechanics and colloid science and has motivated a large number of applications in disciplines ranging from nanoscale manufacturing to biotechnology [2]. The physical principle of the process is rather simple, albeit the mathematical modeling remains a big challenge – the evaporation of a liquid drop triggers an advective transport directed towards the three phase contact line (TPCL) of the drop which forces the suspended colloidal particles to assemble at the TPCL forming the "coffee-stain".

In a recent study, Das et al. [1] studied an important modification of this problem. They considered the evaporation of an electrolyte drop on a charged surface. Presence of a charged surface in contact with an electrolyte solution triggers a double-layered distribution of charges, known as electric double layer (or EDL) [3]. The pressure-driven transport, intrinsically associated evaporation-triggered flow, leads to the downstream advection of the charge density gradient within the EDL and this triggers a streaming electric field (see Fig. 1). Das et al. [1] theoretically demonstrated massive influence of this electric-field-induced electroosmotic transport in altering the deposition dynamics of the particles during the "coffee-stain" formation (see Fig. 2).

In this paper, we shall investigate the effect of this streaming electric field in dictating the electrophoretic transport (in case the suspended particles are charged) and the manner in which the resulting "coffee-stain" gets affected. We shall consider both soft and rigid suspended particles.

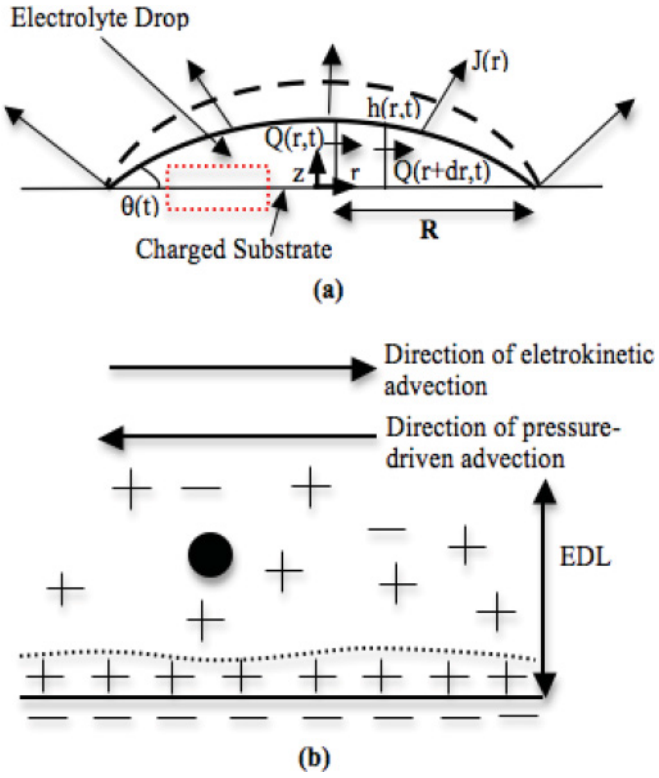

Figure 1: Schematic illustrating the generation of the EDL-induced-electroosmotic transport [1].

While the evaporation-induced "coffee-stain" formation with rigid suspended particles has been routinely used for different applications [2], the

"coffee-stain"-like deposition for soft particles (e.g., microgels) are being recently probed for novel applications [5]. Of course in none of the previous studies of evaporation-induced particle deposition (and associated self-assembly) – be it for rigid or soft particles – the role of the particle surface charge has been probed.

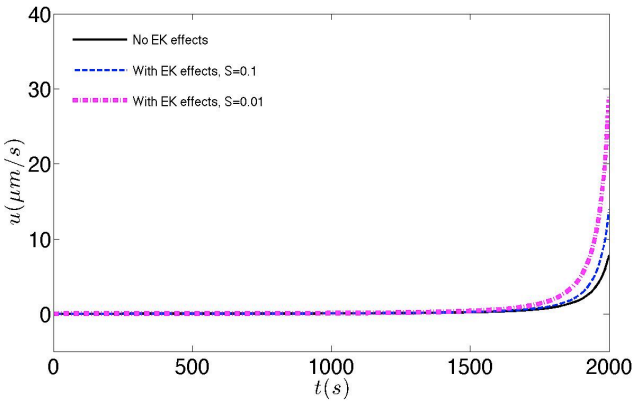

Figure 2: Variation of the deposition speed of the particles in presence of streaming-field-induced electroosmotic or electrokinetic (EK) transport. Results are shown for different values of dimensionless ionic Peclet number S [1,4] that dictate the magnitude of the streaming electric field. Figure taken from Ref. 1.

For both the rigid and soft charged particles, two distinct issues will be of concern. Firstly, the manner in which the EDL formed around the particles get polarized in presence of the induced streaming potential and how that dictates the electrophoretic transport of these particles. Here an essential ingredient is the appropriate description of the EDL charge distribution at zero field condition. For example, for the soft charged particle, the charge is not localized at the particle surface; rather this soft charged interface is described by a layer of charged polyelectrolyte resident on a rigid sphere [6]. Our model will appropriately account for this structural specificities, as well as boundary conditions at the interface of the poleyelectrolyte layer and the rigid surface (please note that by changing this boundary condition it is possible to demarcate between the cases where the polyelectrolyte coating is on a metallic surface or on a dielectric surface like glass). The second key ingredient, also having different extent of influences depending on the rigidity of the particle, is the collective dynamics of the particles during the deposition. This becomes specially important given the fact that the particles may be identically charged inducing repulsive interactions. For soft surfaces, the repulsive interactions may get even more magnified given the fact the polyelectrolytes may undergo Steric repulsions (on account of dynamics such as interpenetration of polyelectrolyte chains [7]) in addition to the electrostatic repulsion.

In summary, this study will present the first calculations on the effect of charge on surfaces of dispersed rigid and soft particles in the drop-evaporation-induced "coffee-stain" formation. The calculations will have immense bearing towards appropriate designing of experiments that employ evaporation-triggered particle assembly for a myriad of technological applications.

References

[1] Das, S., Chakraborty, S., Mitra, S. K., Ring stains in the presence of electrokinetic interactions, Physical Review E, 85, 046311-1–046311-8 (2012).

[2] Deegan, R. D., Bakajin, O., Dupont, T. F., Huber, G., Nagel, S. R., Witten, T. A., Capillary flow as the cause of ring stains from dried liquid drops, Nature, 389, 827–829 (1997).

[3] Hunter, R. J., *Zeta Potential in Colloid Science*, Academic, London (1981).

[4] Chakraborty, S., Das, S., Streaming-field-induced convective transport and its influence on the electroviscous effects in narrow fluidic confinement beyond the Debye-Hückel limit, Physical Review E, 77, 037303-1–037303-4 (2008).

[5] Zhou, J., Wang, G., Marquez, M., Hu. Z., The formation of crystalline hydrogel films by self-crosslinking microgels, Soft Matter, 5, 820–826 (2009).

[6] Ohshima, H., Theory of electrostatics and electrokinetics of soft particles, Science and Technology of Advanced Materials, 10, 063001-1–063001-13 (2009).

[7] Khan, S. J., Pierce, F., Sorensen, C. M., Chakrabarti, A., Self-assembly of ligated gold nanoparticles: Phenomenological modelling and computer simulations, Langmuir 25, 13861–13868 (2009).

Multiphase Systems Under Vibrations in Different Gravity Conditions

T.P. Lyubimova

Institute of Continuous Media Mechanics UB RAS
1, Koroleva Str., 614013, Perm, Russia
lubimova@psu.ru

It is known that vibrations exert strong influence on the behaviour of multiphase systems. They are able to stabilize equilibrium states which were unstable in the absence of vibrations and to create new equilibrium states. The simplest example of this is the Kapitza pendulum [1] (the pendulum with oscillating point of suspension). Kapitsa considered the case of small-amplitude high frequency oscillations of the suspension point by splitting the motion into the fast and slow components and introducing an effective potential to describe the slow component. The stable equilibrium states of the pendulum correspond to the minima of the effective potential. It was found that vertical high frequency vibrations of the suspension point can stabilize the state with the inverted bob position, i.e. the state with the bob above the point of suspension and horizontal high frequency vibrations of the suspension point create new stable equilibrium state with the inclined position of the pendulum [1,2]. Similar effects were observed for hydrodynamical systems in [3]: vertical high frequency vibrations were able to stabilize the equilibrium state of a two-layer system subjected to gravity in which more dense fluid is located above less dense one, preventing the occurrence of the Rayleigh-Taylor instability and horizontal high frequency vibrations created new stable equilibrium state with the inclined fluid interface.

In experiments [4] it was found that under sufficiently intensive horizontal vibrations the planar interface of two immiscible fluids subjected to the gravity field becomes unstable and the formation of the frozen wave is observed. The theoretical investigation of this phenomenon was carried out in [5] using high frequency (inviscid) approach. It was shown that the development of frozen waves is related to the Kelvin-Helmholtz instability. The case of viscous fluids subjected to the horizontal vibrations of finite frequency and amplitude was studied in [6]. Additionally to Kelvin-Helmholz instability the parametric instability zones were found. In [7-9] discissed phenomena were studied experimentally and numerically for fluids with large viscosity contrast. Formation of the periodical patterns on the diffused interface of two miscible fluids subjected to the gravity field and tangential vibrations was investigated experimentally in [10]. In the framework of future space experiment VIPIL on ISS it is planned to study the vibration effects on miscible fluids and near critical fluids in microgravity conditions. Preliminary terrestrial experiments performed for the two-phase near critical H2 under magnetic compensation of gravity [11,12] have shown that the dynamics of fluid interface subjected to vibrations strongly depends on the gravity level. For the tangential vibrations, in the first stage of the process the interface dynamics is similar to the frozen wave formation in the terrestrial conditions. However, further evolution leads to the formations of the band pattern. Besides, differ from the case of non-zero gravity, for zero gravity conditions there is no instability threshold. The question on the physical mechanisms of the wavelength selection is discussed in the present paper.

The problem of the vibrational dynamics of multiphase systems consisting of fluid with solid, liquid or gaseous inclusions is very important for both microgravity and terrestrial conditions. Theoretical analysis of the behaviour of a rigid particle in a container filled with the liquid and subjected to the translational high frequency vibrations was carried out in [13,14] in the inviscid approximation. It was shown that there arise the average vibrational attraction to the nearest wall. These theoretical predictions were confirmed experimentally in [15]. The interaction of two rigid particles in oscillating liquid was performed in [16,17] in the inviscid approximation. It was shown that under vibrations perpendicular to the line connecting the particle centers there arises the average attraction force and under vibrations parallel to this line – the average repulsion force. In [18] experiments were performed in which two spheres made of stainless steel were introduced in the glycerol mixtures of three different viscosities and subjected to the horizontal vibrations of different frequencies and amplitudes. The equilibrium distance between the particles was determined at which the transition from the attraction force at large distances between the sphere surfaces to the repulsion force at small distances takes place. In [19] the interaction of ensemble of particles in a liquid subjected to vibrations was studied experimentally. It is found that the particles form the chains oriented perpendicular to the vibrations and located at equal distances from each other.

Investigation of the average shape of deformable inclusions in a fluid subjected to high frequency vibrations in zero gravity conditions performed by the minimization of corresponding functional shows that the squeezing of inclusion in the direction of vibration axis takes place [20]. In the case of drop the squeezing is related to the Bernoulli effect and in the case of bubble – to mean Reynolds stress structure at the interface. Additionally, vibrational attraction to the nearest wall takes place.

At finite frequencies considerable role is played by resonance phenomena. Investigation of forced oscillations of the drops and bubbles in oscillating fluid shows that these are translational oscillations of inclusion as a whole with the frequency equal to the vibration frequency. The oscillation phase coincides with the container oscillation phase for the drop and opposite to that for the bubble. In the case of bubble the amplitude of the inclusion displacement is twice larger than the vibration amplitude (in a reference frame of container). Such forced oscillations were observed in the space experiments on the dynamics of the bubbles in a vibrating liquid performed in [21]. The interaction of the modes leads to the secondary, non-linear, resonance of forced oscillations, for which the frequency of excitation is

found to be twice lower than the frequency of lowest mode of eigen-oscillations. Forced oscillations become unstable at the vibration frequencies satisfying the synchronism condition [22]. This parametric resonance differs from well known Faraday waves: it is excited not at the frequencies twice higher than eigen-frequencies but at the frequencies equal to the sums of frequencies of neibouring eigen-modes. The theoretical predictions on parametric instability of forced oscillations of the drop (bubble) in oscillating liquid were confirmed in experiments under magnetic compensation of gravity.

The oscillations of the sessile drop on oscillating rigid substrate were studied in [23-25] taking into account the contact line dynamics.

The work was supported by the Government of Perm Region (Contract number C-26/212)

References

[1] Kapitsa, P.L., Dynamic stability of a pendulum when its point of suspension vibrates, Sov. Phys. JETP, 21 (5), 588-592 (1951); Kapitza, P.L., Pendulum with a vibrating suspension, Usp. Fiz. Nauk, 44, 7-15 (1951)

[2] L.D. Landau, E.M. Lifshitz (1960). *Mechanics*. Vol. 1 (1st ed.). Pergamon Press.

[3] Wolf, G.H., The dynamic stabilization of the Rayleigh-Taylor instability and the corresponding dynamic equilibrium, Z. Physik, 227, 291-300 (1961).

[4] Wolf, G.H., Dynamic stabilization of the interchange instability of a liquid-gas interface. Phys.Rev.Lett., 24 (9), 444-446 (1970).

[5] Lyubimov, D.V., Cherepanov, A.A., On the development of steady relief on fluid interface in a vibrational field, Fluid Dynamics, 21, 849-854 (1987).

[6] Khenner, M.V., Lyubimov, D.V., Belozerova, T. S., Roux, B., Stability of plane-parallel vibrational flow in a two-layer system, Eur. J. Mech. B/Fluids, 18, 1085-1101 (1999).

[7] Ivanova, A.A., Kozlov, V. G., Evesque, P. Fluid Dynamics, 36 (3), 362–368 (2001).

[8] Jalikop, S.V., Juel, A., J. Fluid Mech., 640, 131-150 (2009).

[9] Yoshikawa, H.N., Wesfreid, J.E., J. Fluid Mech. 675, 223-248 (2011).

[10] Legendre, M., Petitjeans, P., Kurowski, P., C. R. Mecanique, 331, 617-622 (2003).

[11] Gandikota, G., Chatain, D., Amiroudine, S., Lyubimova, T., Beysens, D. Faraday instability in a near-critical fluid under weightlessness Phys. Rev. E, 89, 013022 (2014).

[12] Gandikota, G., Chatain, D., Amiroudine, S., Lyubimova, T., Beysens, D. Frozen-wave instability in near-critical hydrogen subjected to horizontal vibration under various gravity fields, Phys. Rev. E, 89, 012309 (2014).

[13] Lugovtsov V.A., Sennitsky V.L., Dokl. Akad. Nauk SSSR, 289(2), 314 (1986).

[14] Lyubimov D.V., Lyubimova T.P., Cherepanov A.A. On a motion of solid body in a vibrating fluid, Convective Flows, Perm, 61 (1987).

[15] Hassan, S., M., Lyubimova, T., Lyubimov, D., Kawaji, Effects of vibrations on particle motion near a wall: Existence of attraction force. Int. J. Multiphase Flow, 32 (9), 1037-1054 (2006).

[16] Lyubimov, D.V., Cherepanov, A.A., Lyubimova, T.P., The motion of solid body in a liquid under the influence of a vibrational field, Reviewed Proc. of the First Int. Symp. on Hydromechanics and Heat/Mass Transfer in Microgravity, Gordon and Breach, 247-251 (1992).

[17] Lyubimov, D.V., Cherepanov, A.A., Lyubimova, T.P., Roux, B., Vibration influence of a two-phase system in weightlessness conditions, J. Physique IV, 11 (Pr6), 83-90 (2001).

[18] Klotsa D., Swift M.R., Bowley R.M., King P.J., Interaction of spheres in oscillatory fluid flows, Phys. Rev. E, 76, 056314 (2007).

[19] Klotsa D., Swift M.R., Bowley R.M., King P.J., Chain formation of spheres in oscillatory fluid flows, Phys. Rev. E, 79, 021302 (2009).

[20] Lyubimov, D.V. Cherepanov, A.A., Lyubimova, T.P., Roux, B. Deformation of gas or drop inclusion in high frequency vibrational field. Microgravity Quarterly, 6 (2-3), 69-73 (1996).

[21] Kawaji, M., Ichikawa, N., Kariyasaki, A., Tryggvason, B.V., Large Bubble Motion in a Fluid Ce11 under Microgravity: ISCAP Experiments on the Effects of g-jitter and Forced Vibration, Journal of the JASMA, 16 (4), 245-254, (1999).

[22] Lyubimov, D.V., Cherepanov, A.A., Lyubimova, T.P., Beysens, D., Roux, B., Meradji, S., Behaviour of isolated bubble (or drop) in oscillating liquid. Third International Conference on Multiphase Flow. ICMF-98, 8th-12th June, 1998, Lyon, France. Book of Abstracts, 1.2-2.

[23] Lyubimov, D.V., Lyubimova, T.P., Shklyaev, S.V., Behavior of a drop on an oscillating solid plate, Phys. Fluids 18, 012101 (2006).

[24] Fayzrakhmanova, I.S., Straube, A.V., Stick-slip dynamics of an oscillated sessile drop, Phys. Fluids, 21, 072104 (2009).

[25] Benilov, E.S., Billingham, J. Drops climbing uphill on an oscillating substrate, J. Fluid Mech., 674, 93–119, (2011).

Convective fluid flows with evaporation: analytical, numerical and experimental investigations

Olga Goncharova[1, 2], Yuriy Lyulin[2], Ekaterine Rezanova[1] and Oleg Kabov [2, 3]

[1] Altai State University, Department of Differential Equations, Lenin ave., 61, 656049 Barnaul, Russia, gon@math.asu.ru
[2] Institute of Thermophysics SB RAS, Ac. Lavrentieva ave., 1, 630090 Novosibirsk, Russia
[3] Tomsk Polytechnic University, Institute of Power Engineering, Department of Theoretical and Industrial Heat Systems Engineering, Lenin Avenue, 30, 634050 Tomsk, Russia

The processes of convection, accompanied by evaporation at an interface, are studied experimentally, numerically and theoretically in the present time. Scientific activity in this direction is determined by the experiments in the frame of the CIMEX project of the European Space Agency [1]. The experiments devoted to investigations of the features of the convective fluid flows in an open cavity and in an open horizontal layer under conditions of co-current gas flows are carried out in the Institute of Thermophysics SB RAS [2]. The experiments are an important motivation for improvement of theoretical understanding of convection and mass transfer processes in the domains with interfaces. The mathematical modeling of the fluid flows demands the study of various problems of the thermal gravitational, thermocapillary and thermodiffusive convection in the fluids and of interaction of convection and interfacial processes. Evaporation process under action of the inert gas flow induces an intensive heat and mass transfer through the gas-liquid interface. It causes a temperature gradient between bottom and interface, that leads to the appearance of the buoyancy convection within liquid layer. The inert gas flow induces the shear stress at interface; strong evaporation at the initial section of interface leads to an interfacial temperature gradient which induces a countercurrent motion of liquid relative to the gas flow. It is evident that the structure of the convective flows should depend on various factors: on gas flow rate, on evaporator temperature, on size of liquid pool etc. In the CIMEX experiments not only the features of convective flows but also intensity of evaporation in the moving and stationary horizontal liquid layers are studied. A schematic of a flow structure that can be realized in the liquid layer being under action of the gas flow is shown in the Fig. 1. Average evaporation mass flow rate of the horizontal evaporating liquid layer (HFE-7100 or Ethanol) under shear stresses of the inert gas flow (Nitrogen) relative to the gas velocity, the gas/liquid temperature and the liquid depth, is measured experimentally (Fig. 2). It is shown that with an increase of the liquid depth the average evaporation mass flow rate has a local maximum. The local maximum significantly depends on the gas/liquid temperature. With the growth of the gas/liquid temperature, the local maximum is shifted to the larger value of the liquid depth.

Mathematical modeling of the fluid flows with an interface, new exact solutions illustrated the two-layer fluid flows with evaporation, numerical investigation of the evaporative convection in an open cavity and comparison of the experimental, theoretical and numerical results will be presented in the paper. Construction of the exact solutions of special type is the important part of the theoretical investigations [3]. In the problem statement with given gas flow rate Q the exact solutions allow to model the two-layer flows of the fluids with evaporation at the thermocapillary interface. It is shown that the longitudinal temperature gradient along the interface (A) or along the rigid boundaries (A_1, A_2) of a channel determines the flows. The values of the temperature gradient A are found, which provide the experimental value of the specific evaporation mass flow rate (M). The flow features with respect to the height of the liquid and gas layers and to the type of the gas-liquid system are demonstrated. Influence of the height of the liquid and gas layers on evaporation intensity is confirmed. The analytical results coincide qualitatively with the results of the physical experiments. Figures 3 and 4 demonstrate the examples of the two layer fluid flows in the case of the experimental values of the height of the liquid (l) and gas (h) layers under normal and low gravity (g).

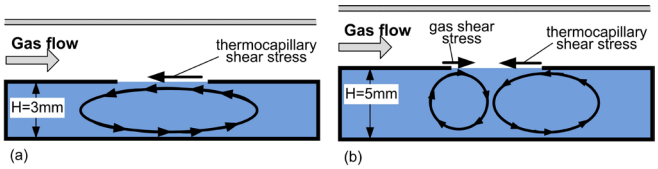

Figure 1: Liquid flow structure.

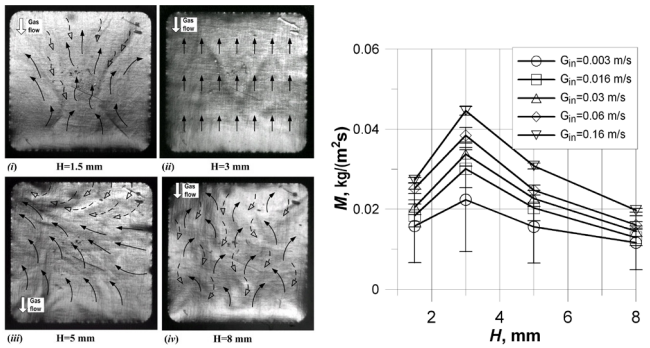

(a) **(b)**

Figure 2: **(a)** Shadowgraph snapshots of the gas-liquid interface; **(b)** Evaporation flow rate against the liquid depth, T=20° C.

Two types of the boundary condition for vapor concentration are studied: the case, when the vapor concentration is equal to zero and the case of absence of vapor flux on the upper

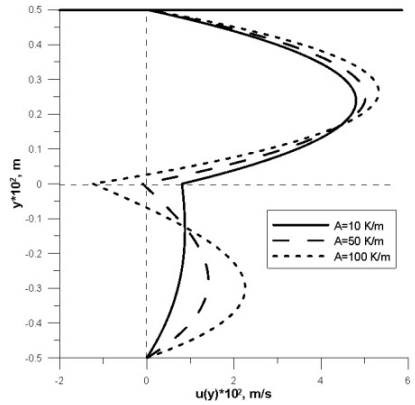

(a)

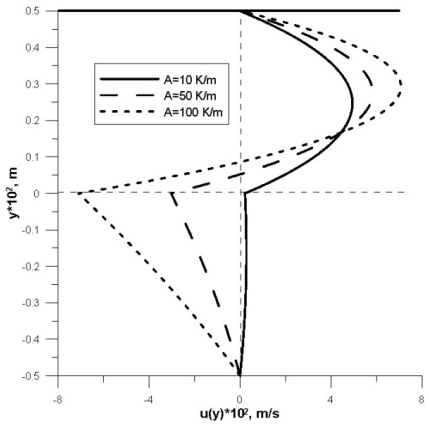

(b)

Figure 3: Examples of the velocity profiles of the two-layer flows (HFE7100 - nitrogen); problem statement with given gas flow rate $Q = 2*10^{-4}$ kg/(m*s) at **(a)** g = 9.81 m/s^2 and **(b)** $g = 9.81*10^{-2}$ m/s^2; case of zero vapor flux at the upper rigid boundary; here $l=0.5*10^{-2}$ m, $h=0.5*10^{-2}$ m, $A_1=0$. ***Effects of free interfacial longitudinal temperature gradients A.*** A = 10 K/m, A_2 = 35.7 K/m: **(a)** $M=3.495*10^{-5}$ kg/(m^2*s), **(b)** $M=3.492*10^{-5}$ kg/(m^2*s) (solid lines); A = 50 K/m, A_2 = 178 K/m: **(a)** $M=1.754*10^{-4}$ kg/(m^2*s), **(b)** $M=1.746*10^{-4}$ kg/(m^2*s) (dashed lines); A= 100 K/m, A_2 = 356 K/m: **(a)** $M=3.525*10^{-4}$ kg/(m^2*s), **(b)** $M=3.492*10^{-4}$ kg/(m^2*s) (dense dashed lines).

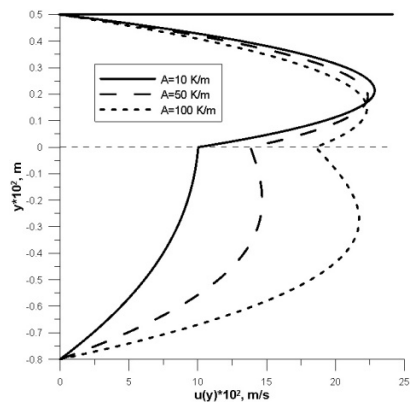

(a)

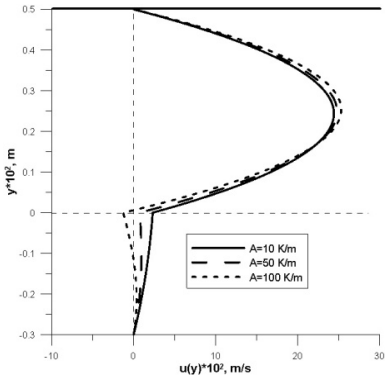

(b)

Figure 4: Examples of the velocity profiles of the two-layer flows (HFE7100 - nitrogen) at g = 9.81 m/s^2; problem statement with given gas flow rate $Q = 10^{-3}$ kg/(m*s) at; case of zero vapor flux at the upper rigid boundary; here $h=0.5*10^{-2}$ m, $A_1=0$. ***Effects of the free interfacial longitudinal temperature gradients A.*** A = 10 K/m: **(a)** $l=0.8*10^{-2}$ m, A_2 = 26.1 K/m, $M=1.7461*10^{-4}$ kg/(m^2*s), **(b)** A_2 = 52.8 K/m, $M=1.7469*10^{-4}$ kg/(m^2*s) (solid lines); A = 50 K/m: **(a)** $l=0.8*10^{-2}$ m, A_2 = 130 K/m, $M=8.7321*10^{-4}$ kg/(m^2*s), **(b)** $l=0.3*10^{-2}$ m, A_2 = 264 K/m, $M=8.7496*10^{-4}$ kg/(m^2*s) (dashed lines); A =100 K/m: **(a)** A_2 =261 K/m, $M=1.74684*10^{-3}$ kg/(m^2*s), **(b)** A_2 =528 K/m, $M=1.7538*10^{-3}$ kg/(m^2*s) (dense dashed lines).

boundary of the channel (Figs. 3, 4).

The numerical investigations of fluid motion in a rectangular cavity with a non-deformed thermocapillary boundary are carried out. The simulations are performed for the experimental liquids filled cavities with different aspect ratio under conditions of evaporation at interface. Topology of the convective fluid flows and the characteristics of the vortex structures will be presented. Analytical, numerical and experimental results are compared and analyzed.

Acknowledgments. The authors gratefully acknowledge the support of the Russian Foundation for Basic Research (project No. 14.08.00163).

References

[1] Scheid, B., Margerit, J., Iorio, C.S., Joannes, L., Heraud, M., Queeckers, P., Dauby, P.C., Colinet, P., Onset of thermal ripples at the interface of an evaporating liquid under a flow of inert gas, Experiments in Fluids, 52 (5), 1107-1119 (2012)
[2] Lyulin Y., Kabov O., Evaporative convection in a horizontal liquid layer under shear–stress gas flow, Int. J. Heat Mass Transfer 70, 599-609 (2014)
[3] Goncharova, O.N., Hennenberg, M., Rezanova E.V., Kabov, O.A., Modeling of the convective fluid flows in the two-layer systems with evaporation in the presence of the normal or anomalous thermocapillary effects, Interfacial Phenomena and Heat Transfer, 1 (4), 317-338 (2013)

Experimental Investigation of Heat Transfer Characteristics Due to Evaporation of Shear-driven Liquid Film Flow

Tomoki Hirokawa[1], Masahiko Murozono[1], Oleg Kabov[2], Yasuhisa Shinmoto[1] and Haruhiko Ohta[1]

[1]Department of Aeronautics and Astronautics, Kyushu University, 744 Motooka, Nishi-ku, Fukuoka, Japan
[2]Institute of Thermophysics, Russian Academy of Science, Siberian branch, 630090, Novosibirsk, pr. Lavrentyev 1, Russia
hirokawa@aero.kyushu-u.ac.jp

Introduction

In recent years, by the development of electronic techniques, the density of dissipated heat from a semiconductor chip tends to increase. In near future, the higher performance of thermal management system is required for the improvement of the existing cooling systems by convective liquid or air. The powerful methods by using phase change attract much attention for the cooling both of small semiconductor chips and power electronics. For the heat transfer by nucleate boiling or two-phase forced convection, the formation or the consumption of liquid film underneath bubbles or around the vapor core flow, respectively, becomes a key factor which determines the cooling ability. However, the motion of liquid-vapor interface cannot be controlled directly but controlled indirectly via the behavior of vapor phase. To realize the liquid film flow ideal for the individual cooling requirement, behaviors of liquid film are attempted to be regulated by the interfacial shear force exerted by the vapor flow. To clarify the interaction between the phases under variable combinations of flow rates and heat fluxes, the heat transfer across the shear-driven liquid film flow with the co-current gas flow of different component is investigated.

Experimental apparatus and procedure

Figure 1 shows the test loop, which is composed of a pump, pre-heater, a test section, a separator and heat exchanger for cooling. The test fluids are pure water as a liquid phase and nitrogen as a gas phase. The test loop is exposed to the atmosphere at the vent valve in the downstream of the test section, and only water is circulated.

As shown in **Figure 2**, the test section is composed of an aluminum block, heating copper blocks, channel walls of stainless steel flanges and observation window made of Pyrex glass. The liquid film is introduced from a rectangular thin slit along the heating surface with a width of 30mm and a heated length of 100mm. Since the heating surface is divided into 10 segments along the flow direction by using separated copper heating blocks with individual cartridge heaters, the local heat transfer performance is evaluated even

Table 1: Experimental conditions.

Channel height	H	5mm
Channel width	w	30mm
Nozzle height	h_N	1mm
Test section outlet pressure	P_{out}	1atm
Gas inlet temperature	$T_{g,in}$	20°C
Liquid inlet temperature	$T_{l,in}$	20°C
Liquid film Reynolds number	Re_l	18.4
Gas Reynolds number	Re_g	0-6380
Heat flux	q	0-280kW/m^2

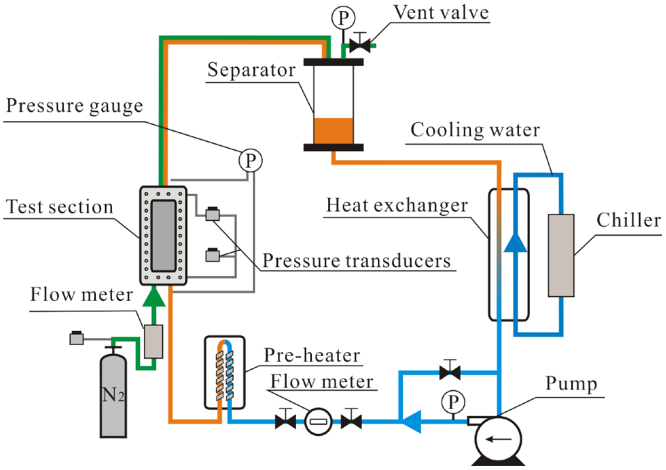

Figure 1: Outline of test loop.

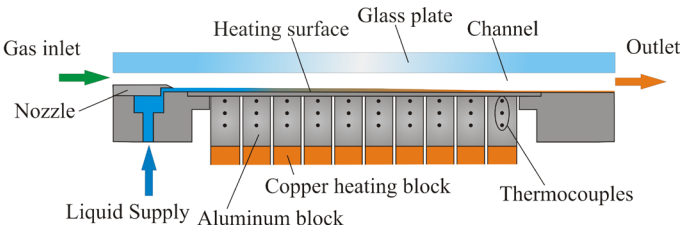

Figure 2: Structure of test section.

in the case of local dryout at the downstream locations. A local heat transfer coefficient is defined by using differences between the local heating surface temperature and local liquid film temperature, which is evaluated by the following procedure. By using the temperature gradient along the flow direction obtained by an unheated preliminary experiment for the same inlet liquid temperature and gas Reynolds number as those for the heated experiment, the temperature of liquid film flowing in the 1st segment is evaluated. The procedure is important because the heat loss of liquid film at the upstream unheated section cannot be negligible owing to the large temperature difference between the liquid film and gas flows. On the other hand, the liquid film temperature at the 10th heated segment is regarded as the same as the temperature at the outlet. The liquid film temperatures at the 2nd to 9th segments are estimated here by the linear interpolation of these temperatures. The top view of liquid film behavior and its rupture is recorded by a high-speed video camera. The experimental conditions are given in **Table 1**.

Results and discussion

Figure 3 shows liquid film behaviors for the variation of gas Reynolds numbers as 0, 2552, 5104 and 6380 under

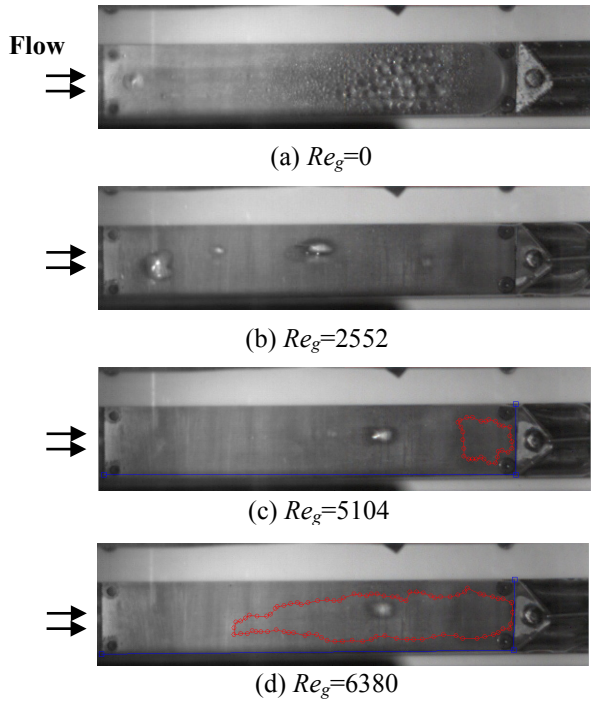

Figure 3: Top view of Liquid film behavior and its rupture at q=23kW/m^2.

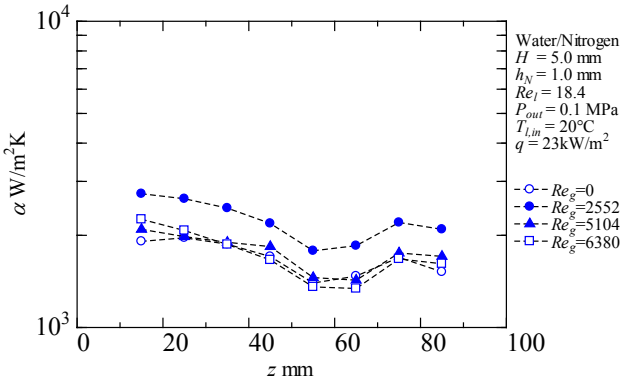

Figure 4: Local heat transfer coefficient at Re_l=18.4, $T_{l,in}$=$T_{g,in}$=20°C, q=23kW/m^2.

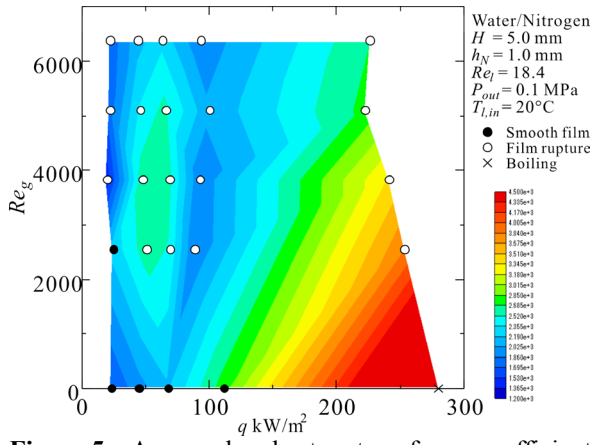

Figure 5: Averaged heat transfer coefficients at $T_{l,in}$=$T_{g,in}$=20°C, Re_l=18.4.

liquid inlet temperature 20°C and heat flux 23kW/m^2. At gas Reynolds number 0, i.e. no shear stress at the surface of the liquid film flow, there are no bubbles but condensing droplets attached to the upper glass plate at the downstream. At gas Reynolds numbers of 5104 and 6380, a liquid film rupture occurs. This rupture is initiated at the downstream edge of heating surface and dried area is extended with increasing gas Reynolds number. Enhanced interfacial shear stress increases the velocity in the liquid film and decreases simultaneously its thickness. At high gas Reynolds numbers, the presence of liquid film flow along the side wall and a part of upper glass plate is observed.

Figure 4 shows local heat transfer coefficients at gas Reynolds numbers varied from 0 to 6380 and heat flux 23kW/m^2, where the data from the 1st and the 10th segments are omitted because of larger heat loss to the flanges contacted the heating surface. At gas Reynolds number 2552, in which the emergence of dried area is not observed, heat transfer coefficient becomes higher than those for other Reynolds numbers for all local positions. At gas Reynolds numbers of 5104 and 6380, the heat transfer coefficients decrease at the downstream compared to gas Reynolds number 2552. The extension of dried area deteriorates the heat transfer to the level of no inlet gas flow.

Figure 5 shows the heat transfer coefficients as averaged values of those at 8 segments. Black solid symbols indicate the case where no rupture in the liquid film is observed. Under the conditions represented by open circles, the rapture of liquid film occurs and the dried area is extended in the downstream. Under the conditions of zero gas Reynolds number and the highest heat flux tested, indicated by cross marks, nucleate boiling occurs. At high heat flux larger than 100kW/m^2, with increasing gas Reynolds number, heat transfer deterioration occurs because of the extension of dried area. On the other hand, at low heat flux, heat transfer enhancement occurs with increasing gas Reynolds number. The blank area at higher heat flux in the figure represents the combinations of Reynolds number and heat flux where dryout accompanied by the temperature excursion occurs at the segment(s) in the downstream.

Conclusions

To improve the performance of cooling system by evaporation of thin liquid film, co-current gas and liquid flow were realized by the independent control of each flow rate. Experiments were performed by using water and nitrogen gas under atmospheric pressure and the followings were concluded.

1. At low Reynolds number, heat transfer coefficient increases at higher heat flux, where the liquid film thickness becomes thinner by the enhanced evaporation or nucleate boiling occurs.
2. At high heat flux, the heat transfer coefficient decreases with increasing gas Reynolds number because the liquid film thickness becomes thinner by the enhanced interfacial shear stress exerted by the vapor flow of increased velocity and the rupture of liquid film occurs at the downstream of the heating surface.

The formation of disturbance waves in downward annular flow

Alekseenko S.V., Cherdantsev A.V., Cherdantsev M.V.*, Isaenkov S.V., Markovich D.M

Institute of Thermophysics of SB RAS
Lavrentiev Ave., 630090, Novosibirsk, Russia
secret.gear@gmail.com

The annular-dispersed flow is presented by liquid film which flows on inside walls of tube and fast-moving gas core in the center of the flow. The wavy structure of film is presented by disturbance waves and ripple waves. The disturbance waves are large waves which are coherent over long distances. Disturbance waves are separated by thin base film areas. Small-scale ripple waves cover both disturbance waves and base film.

The disturbance waves play important role in heat and mass transfer processes. It was revealed that liquid is entrained in gas core, mainly from the crests of disturbance waves (Woodmansee & Hanratty 1969). The most part of experimental works is dedicated to investigation of disturbance wave properties in developed annular-dispersed flow, i.e. on large distances from the inlet. In several papers the downstream evolution of the system of disturbance waves is studied. It was found that the velocity of individual disturbance waves may be varied in the same flow conditions. Velocity difference leads to coalescence of disturbance waves. Due to coalescence, passing frequency of disturbance waves decreases downstream (Hall Taylor & Nedderman 1968). Without coalescence, disturbance waves were found to travel with constant speed over large distances (Hall Taylor et al. 1963). Zhao et al. (2013) studied the film thickness records obtained with conductance technique at different downstream distances. They observed that the isolated waves of large amplitude (>1.6 of the mean film thickness) first appear at the distances of 5-10 pipe diameters below the inlet. Above this area, waves with high frequency and relatively low amplitude were observed.

The process of formation of disturbance waves is still unclear. To study this process, field measurements of film thickness in the vicinity of the inlet are necessary. High frequency and velocity of the waves make strong demands to both spatial and temporal resolution of the measurements technique. Brightness-based laser-induced fluorescence technique is used in present paper, since it fits the mentioned requirements.

Using this technique, the structure of disturbance waves and their interrelation to the ripples was recently investigated (Alekseenko et al. 2009). It was found that all the ripples are generated at the back slopes of disturbance waves. The subsequent evolution of ripples depends on initial position of a ripple's appearance. Ripples generated farther from the disturbance wave's front travel with low velocity over the base film behind parent disturbance wave until the following disturbance wave absorbs them. Ripples generated closer to the disturbance wave's front, move with high speed over the crest of disturbance wave and disappear near its front. In accordance with observations of Woodmansee & Hanratty (1969) these 'fast ripples' disappear because of being disrupted into droplets by the gas shear. Thus, new qualitative and physically-based definition of disturbance waves can be suggested as follows. A wave is considered to be a disturbance wave if the fast ripples are generated on its back slope. Of course, this definition can be used as the practical criterion of identification of disturbance waves only with film thickness measurements resolved in both space and time with proper resolution.

In present experiments, downward air-water annular flow was organized in vertical acrylic resin tube with inner diameter 15 mm was used as working channel. Liquid was introduced as a film through a tangential ring-shaped slot, so the annular flow regime started at the inlet. Experiments were conducted under the following conditions: liquid Reynolds number Re=140-400; gas flow velocities V_g=18-57 m/s. The area of interrogation was one longitudinal section of the pipe with length of 100 mm, beginning at the inlet. This section was illuminated by continuous 2 W 532 nm laser, converted into narrow vertical laser sheet. Fluorescent dye (Rhodamine 6G) was dissolved in working liquid in low concentration. Laser light was re-emitted by fluorescent matter at different wavelength. The emitted light was captured by high-speed camera through orange optical filter. Local brightness of fluorescent light was measured simultaneously in 500 points; thus, spatial resolution was 0.2 mm/pixel. Camera frame rate was 10 kHz. For each set of flow conditions record of 2 seconds was obtained. Thus video 500x1 pixels with 20000 frames was obtained and then transformed into the bitmap picture 500x20000 pixels. Each value of brightness was recalculated into the value of film thickness (see Alekseenko et al. 2012). Thus we obtain two-dimensional matrix $h(x,t)$ (Fig.1). Here h is the film thickness, x - the distance from the inlet, and t - time from start of record.

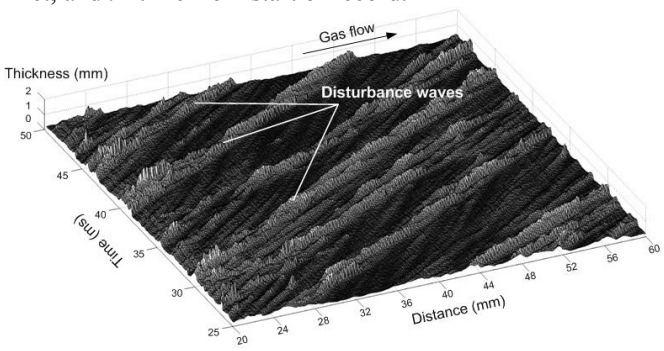

Figure 1: The fragment of $h(x,t)$ matrix for Re=300 and V_g=43 m/s.

For high gas velocities, disturbance waves, covered by the fast ripples, can be seen in the working area. They are formed through coalescence of high-frequency low-amplitude waves, appearing at the inlet. At lower gas velocities, no disturbance waves were observed within the area of measurements. Obviously, formation of disturbance waves at low gas velocities occurs further downstream.

To quantitatively investigate the disturbance waves formation and the first stages of their development, we analyze the time-spectra of film thickness obtained at different distances from the inlet. Since disturbance waves have high amplitudes and carry the main part of liquid (Han et al. 2006 estimate it as 60-80%), they make the most significant contribution into the power spectrum of a film thickness record. The frequencies corresponding to the maximum of power spectra were found.

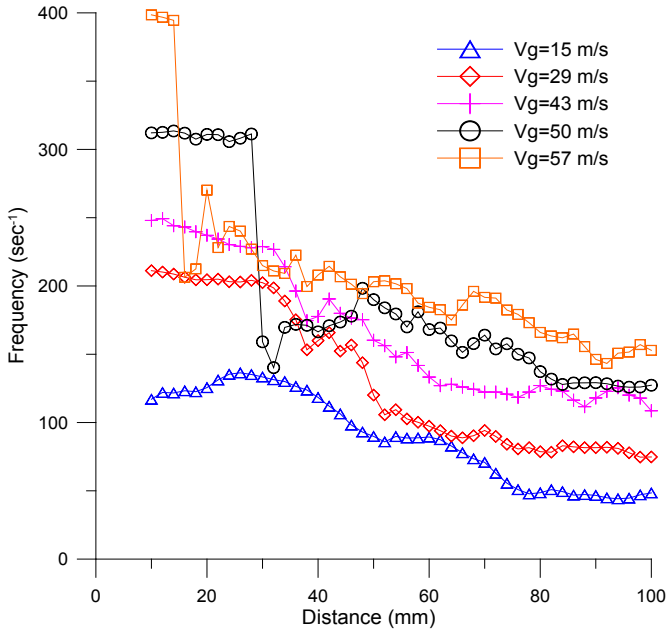

Figure 2: The maximum of power time-spectra in dependence from distance from the inlet. Re=300.

Fig. 2 shows change in the main frequency with downstream distance. The initial frequency is very high; it corresponds to the frequency of initial waves appearing at the inlet. This frequency grows with gas velocity. At the lowest gas velocity initial frequency decreases gradually. Analysis of *h(x,t)* surface shows that in such conditions initial waves are not stable; they decrease in amplitude and loose initial shape. At high gas velocities, the initial frequency undergoes sudden drop. The drop is closer to the inlet at higher the gas velocities. In terms of spectra, this drop can be explained as follows. Two main peaks coexist in the spectra; the one at higher frequency corresponds to the initial waves, and the one with lower frequency corresponds to the disturbance waves that start to occasionally appear from the beginning as well. Amplitude of the high-frequency peak gradually decreases downstream, whereas the amplitude of low-frequency peak increases downstream. The frequency drop corresponds to the moment when the amplitude of the low-frequency peak overcomes that of the high-frequency peak. This denotes that the disturbance waves pattern starts dominating in the wavy structure of liquid film. Further downstream the low-frequency peak gradually shifts towards the lower frequencies. This most likely happens due to acts of coalescence of disturbance waves. The acts of coalescence are relatively rare and they do not change the number of waves as abruptly as it occurs in process of a disturbance wave formation. Thus, this process is not accompanied by drops in the main frequency.

References

[1] Alekseenko, S.V., Antipin, V., Cherdantsev, A., Kharlamov, S., Markovich, D.,. Two-wave structure of liquid film and wave interrelation in annular gas–liquid flow with and without entrainment, Phys. Fluids, 21, 061701:061704. (2009)

[2] Alekseenko, S., Cherdantsev, A., Cherdantsev, M., Isaenkov, S., Kharlamov, S., Markovich, D.,. Application of a high-speed laser-induced fluorescence technique for studying the three-dimensional structure of annular gas–liquid flow, Exp Fluids, 53, 77–89 (2012)

[3] Hall-Taylor, N.S., Hewitt, G.F., Lacey, P.M.C., The motion and frequency of large disturbance waves in annular two-phase flow of air–water mixtures, Chem. Eng. Sci., 18, 537–552 (1963)

[4] Hall-Taylor, N.S., Nedderman, R.M., The coalescence of disturbance waves in annular two phase flow, Chem. Eng. Sci. 23, 551–564 (1968)

[5] Han, H., Zhu, Z., Gabriel, K., A study on the effect of gas flow-rate on the wave characteristics in two-phase gas–liquid annular flow, Nucl. Eng. Des., 236, 2580–2588 (2006)

[6] Woodmansee, D.E., Hanratty, T.J., Mechanism for the removal of droplets from a liquid surface by a parallel air flow, Chem. Engng. Sci., 24, 299-307 (1969)

[7] Zhao, Y., Markides, C.N., Matar, O.K., Hewitt, G.F.,. Disturbance wave development in two-phase gas–liquid upwards vertical annular flow, Int J Multiphase Flow, 55, 111–129 (2013)

Acknowledgements

This work was supported by Russian Foundation for Basic Research (projects 13-08-01400a, 14-08-31514) and by President of Russian Federation (project MK-5997.2014.1).

Simple Model for Calculation of Film Thickness and Heat Transfer in a Turbulent Liquid Film

P. I. Geshev

Institute of Thermophysics
Lavrentyev Ave. 1, Novosibirsk, Russia
Geshev@itp.nsc.ru

The model for calculation of a thickness and heat transfer through a turbulent film, moving by gravity and friction forces is offered. The elementary approximation of turbulent viscosity giving the cubic law of decay in a viscous sublayer and logarithmic law for velocity far from a wall is used. The analytic formula for a film thickness depending on Reynolds's number and on the friction factor of gas stream is derived. Comparison of calculated thickness with experimental data available in the literature shows that the deviation is maximum at laminar-wave modes and can reach 10-20 %.

Let's consider liquid layer of a thickness δ flowing down on an inclined surface with inclination angle α relative to horizon. At free surface of a film the friction stress arising under action of gas stream is applied. The averaged equations are

$$\frac{d}{dy}\left(\nu+\nu_T(y)\right)\frac{du}{dy}=-g\,\sin\alpha\,, \tag{1}$$

$$\frac{d}{dy}\left(a+a_T(y)\right)\frac{dT}{dy}=0 \tag{2}$$

where $u(y)$ and $T(y)$ are velocity and temperature in a film, y is co-ordinate perpendicular to a wall, g is acceleration of gravity, ν, ν_T and a, a_T are molecular and turbulent viscosities and thermal diffusivity, respectively. Dakler [1] was the first who considered this problem by using Prandtl's "mixing length" concept for ν_T.

The Reynolds's number of a film is obtained from (1)

$$\mathrm{Re}=\int_0^{\delta}\frac{u\,dy}{\nu}=\delta_-^3\int_0^{\delta_+}d\eta\int_0^{\eta}\frac{F/\delta_-+\left(1-\xi/\delta_+\right)}{\delta_+^2\left(1+\varphi(\xi)\right)}d\xi\,,$$

where $F=\tau_i/\left[\rho\left(\nu\,g\,\sin\alpha\right)^{2/3}\right]$, τ_i is friction stress of gas stream, $\mathrm{Re}=Q/(\rho\nu)$, Q is the liquid flow rate, $\varphi=\dfrac{\xi^3}{A+B\xi^2}$, A=1125, B=2.5. From the last formula for Reynolds number after transformation we obtain

$$\mathrm{Re}==\delta_-^2\left[Ff_1(\delta_+)+\delta_-f_2(\delta_+)\right], \tag{3}$$

where functions f_1 and f_2 are

$$f_1(\delta_+)=\frac{1}{\delta_+^{\,2}}\int_0^{\delta_+}\frac{(\delta_+-\eta)d\eta}{1+\varphi(\eta)}\,, \tag{4}$$

$$f_2(\delta_+)=\frac{1}{\delta_+^{\,3}}\int_0^{\delta_+}\frac{(\delta_+-\eta)^2\,d\eta}{1+\varphi(\eta)}\,. \tag{5}$$

Functions f_1 and f_2 depend only on δ_+. These functions are shown in a Fig. 1.

Two dimensionless thicknesses δ_+ and δ_- are connected by the additional formula (6) followed from definition of δ_+:

$$\delta_+^2=\delta_-^2\,(F+\delta_-)\,, \tag{6}$$

$$\delta_+=v_*\delta/\nu\;;\quad v_*=\sqrt{\tau_w/\rho}\;;\quad \tau_w=\rho g\delta\,\sin\alpha+\tau_i\,.$$

Analysis of solutions of system of equations (3)-(6) permits to build the expressions

$$\delta_-=\frac{\delta_+}{\left[\left(\delta_++F\delta_+^{1/3}\right)^2+F^3\right]^{1/6}}\,, \tag{7}$$

$$\delta_+=\left\{\mathrm{Re}\left[W(F,\mathrm{Re})+C(\mathrm{Re})\right]\right\}^{1/2}, \tag{8}$$

$$W(F,\mathrm{Re})=\frac{F+\mathrm{Re}^{1/3}}{F/2+\mathrm{Re}^{1/3}/3}\,, \tag{9}$$

$$C(\mathrm{Re})=\frac{2\,\mathrm{Re}/170}{\sqrt{\left[\ln\left(10+\mathrm{Re}/170\right)\right]^2+170/\mathrm{Re}}}\,. \tag{10}$$

Approximations (7)-(10) give values δ_-, deviating from the exact model (3)-(6) less than 2 % as it is shown in Fig.2. In Fig. 3 comparison of approximations (7)-(8) with models [2, 4] and experimental data [4-6] is done.

Let's consider separately two cases: a) film on a vertical surface ($F=0$, $\alpha=\pi/2$); b) film which is carried away by a stream of gas along a horizontal surface ($\alpha=0$, $F=\infty$). From formulae (7)-(8) it is obtained for a dimensional film thickness:

a) $$\delta=\left\{\frac{\nu^2}{g}\,\mathrm{Re}\left[3+C(\mathrm{Re})\right]\right\}^{1/3}, \tag{11}$$

b) $$\delta=\nu\left\{\frac{\rho}{\tau_i}\mathrm{Re}\left[2+C(\mathrm{Re})\right]\right\}^{1/2}. \tag{12}$$

Heat transfer coefficient for the film is defined by the formula for the Nusselt number (obtained from (2)):

$$Nu_*=\frac{q_w\cdot\left(\nu^2/g\right)^{1/3}}{\Delta T\cdot\kappa}=\frac{1}{\delta_-\,f_T\left(P;\delta_+\right)}\,, \tag{13}$$

$$f_T(P,\delta_+)=\frac{1}{\delta_+}\int_0^{\delta_+}\frac{d\eta}{1+P\varphi(\eta)}\,, \tag{14}$$

where q_w is heat flux density, ΔT is characteristic temperature difference, κ is heat conductivity of liquid, $P=\mathrm{Pr}/\mathrm{Pr}_t$ is the ratio of molecular and turbulent Prandtl's numbers. We use the value $\mathrm{Pr}_t=0.9$, suggested often in near wall turbulence models. Results of calculation of Nu_* for freon-21 and for water are shown in Fig. 4.

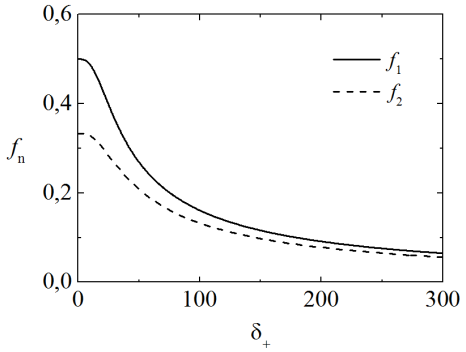

Figure 1: Functions f_1 and f_2 *vs.* value δ_+.

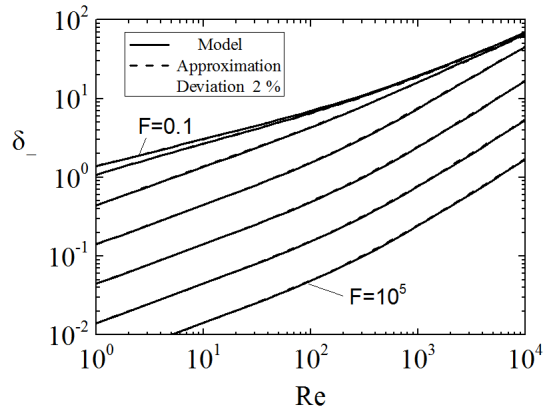

Figure 2: Comparison of the exact model (3)-(6) with approximation (7)-(8).

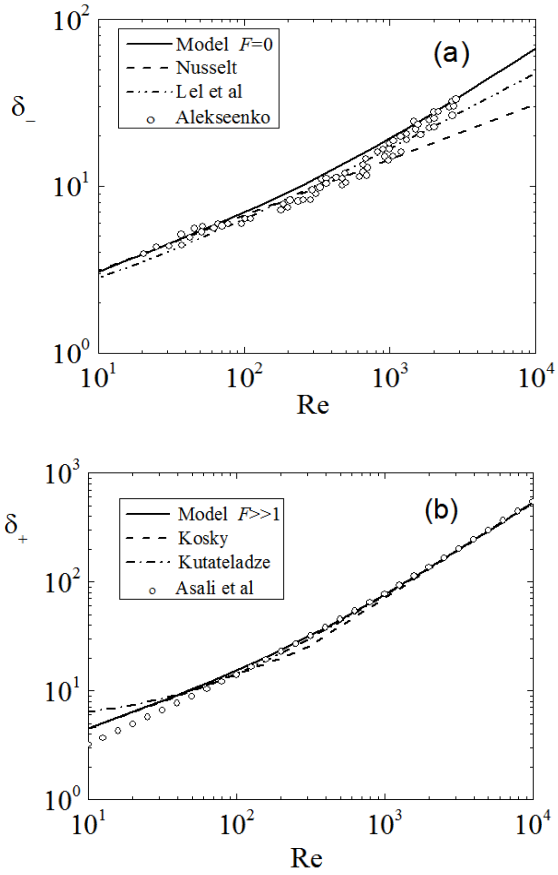

Figure 3: Comparison of approximations (7)-(8) with experimental data [4-6].

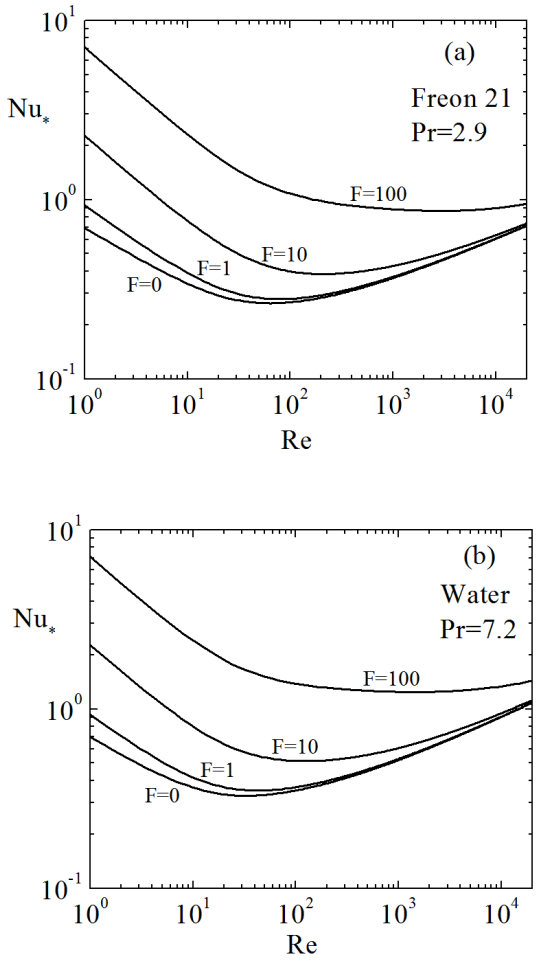

Figure 4: Heat transfer coefficient Nu_* *vs.* Re for (a) freon-21 and (b) water for various friction factors F.

References

[1] Dukler A.E., Fluid mechanics and heat transfer in vertical falling-film system, Chem. Engng Prog. Symp. Ser V. 56, No. 30, P. 1 (1960).

[2] Kutateladze S.S. Fundamentals of Heat Transfer, Edited by R.D. Cess, Chapter 15. "Academic Press" (1963).

[3] Kosky P. G., Thin-liquid films under simultaneous shear and gravity forces, Int. J. Heat Mass Trans., V.14, No.8, P.1220–1224 (1971).

[4] Alekseenko S.V., Nakoryakov V.E., Pokusaev B.G., Wave Flow of Liquid Films, Begell, 313 pp (1994).

[5] Lel V.V., Al–Sibai F., Leefken A., Renz U., Local thickness and wave velocity measurement of wavy films with a chromatic confocal imaging method and a fluorescence intensity technique, Experiments in Fluids, V. 39, P. 856–864 (2005).

[6] Asali J.C., Hanratty T.J., Andreussi P., Interfacial drag and film height for vertical annular flow, AIChE Journal, V. 31, No. 6, P. 895–902 (1985).

Two-phase flows in channels with chemically patterned walls

Elizaveta Gatapova[1], Vladimir Ajaev[1,2], and Oleg Kabov[1]

[1]Institute of Thermophysics SB RAS, Lavrentyev Ave., 1, Novosibirsk, 630090, Russia
[2]Department of Mathematics, Southern Methodist University, Dallas TX 75275, USA
gatapova@itp.nsc.ru, ajaev@mail.smu.edu, kabov@itp.nsc.ru

The development of novel approaches to drag reduction in channel flows is important for many applications such as microfluidics and microscale heat transfer. Recent experimental studies of vapor-liquid channel flow past a chemically patterned surface show that vapor bubbles tend to accumulate at the hydrophobic regions on the wall, leading to the suggestion that this effect can be used to reduce the overall viscous resistance of the two-phase flow at a fixed pressure gradient [1]. The mechanism of reduction is due to liquid slippage at the surfaces of the attached bubbles. This effect is analogous to drag reduction at the structured surface with gas phase trapped between the elements of the structure, as discussed in our previous work [2].

Sbragaglia and Prosperetti [3] investigated the effect of a large number of nearly flat bubbles attached to a solid substrate on viscous single-phase viscous flow near the solid. They showed that the effect can be described by introducing the effective slip length and derived the following formula for this quantity,

$$\lambda_{eff} = \frac{8}{9\pi}\frac{\beta R}{1-\beta}$$

where β is the fraction of the area covered by bubbles and R denotes the wetting radius, assumed the same for all bubbles. However, the limitation of this approach is that it completely neglects the effects due to finite heights of the bubbles. The objective of the present work is to investigate the interplay between the effects of slippage at bubble surfaces and the obstruction of the channel due to finite height of each bubble.

The analysis in the present study is based on the standard lubrication-type approach [4] applied both for the flow inside the bubble and the liquid flow in the channel. We note that even though the fluid phase inside the bubble is vapor, it can still be described by equations of viscous flow since the Reynolds number of this flow is small due to small size of the system. The geometric configuration is that shown in Fig. 1, with channel walls chemically patterned by an array of parallel hydrophobic stripes and the flow being driven by the pressure difference between the two ends of the channel. The characteristic lengths in the vertical and horizontal directions are given by the height and the length of the channel, respectively; the characteristic flow velocity is that of the pressure-driven flow, so the problem can be nondimensionalized based on the following scales,

$$L_x = d$$
$$L_y = L >> d$$
$$U = \frac{(P_L - P_R)d^2}{\mu_l L}$$

where μ_l is the viscosity of the liquid. The use of these scales allows us to formulate the equations for flows both inside and outside each bubble in terms of non-dimensional variables as follows,

$$u_{yy} = p_x$$
$$\mu\hat{u}_{yy} = \hat{p}_x$$

where the parameter μ is the ratio of the vapor-to-liquid viscosities and the pressure is scaled by the imposed pressure difference between the two ends of the channel.

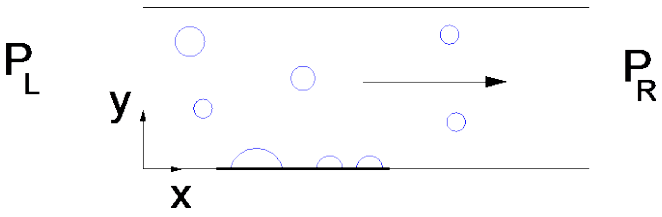

Figure 1: Sketch of a two-phase flow in channel with patterned walls showing attachment of vapor bubbles in hydrophobic regions at the walls.

The boundary conditions at the liquid-vapor interface are given by

$$u_y = \mu\hat{u}_y \quad \text{at} \quad y = h(x),$$
$$u = \hat{u} \quad \text{at} \quad y = h(x)$$

The standard no-slip condition is used at the solid walls. The conditions on the flow rates in the two phases are

$$Q_l = \int_h^L u\,dy = \text{const.}$$
$$Q_v = \int_0^h \hat{u}\,dy = 0$$

where the first condition reflects the mass conservation of the liquid and the second is based on the fact that the flow inside the bubble is a re-circulation without any gas leaking out of the bubble. We note that our lubrication-type approach may in fact break down in the parts of the bubble near the contact lines, but we assume that such local break-down does not affect the validity of the approximation away from the contact line. The measure of the improvement of flow rate due to bubbles is the ratio of the flow rates with and without their presence, defined by

$$G = \frac{Q_l}{Q_l^0}$$

This quantity can be expressed in terms of the local height of the vapor bubble and the viscosity ratio according to

$$G = (1-h)^3\left[4 - \frac{12\mu(1-h)}{h+4\mu(1-h)}\right]$$

The results based on this formula are shown in Fig. 2 for three different viscosity ratios. The plot indicates that the most significant enhancement of the flow due to the effect of slippage is achieved at smaller values of the viscosity ratio and at bubble heights of approximately 0.1 of the total channel height. As the viscosity ratio is increased, the effects of finite bubble height become dominant, so the transport rates in channel with bubbles are in fact lower than without them.

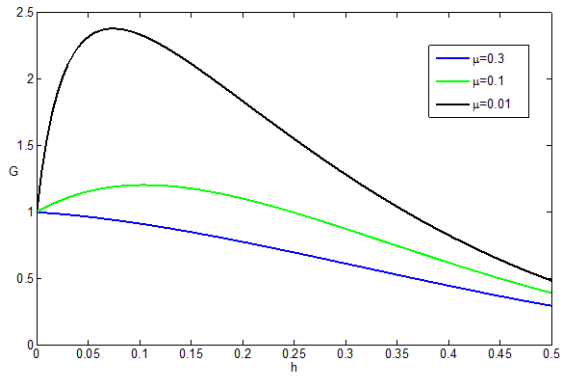

Figure 2: The ratio of flow rates with and without attached bubbles for several different values of the viscosity ratio.

For small bubble height, an approximate analytic formula for G can be derived using the Taylor series expansion. This formula can then be used to estimate the critical value of the viscosity ratio below which the transport enhancement is expected. These results are summarized by

$$G \sim 1 + 3\left(\frac{1}{4\mu} - 1\right)h, \qquad \mu^* = \frac{1}{4}$$

This approximate result is clearly consistent with the plots shown in Fig. 2 since the two values of the viscosity ratio showing the improved transport rate are below ¼, while the value showing no improvement due to attached bubbles is above that critical value. We note that in most practical applications the values of the viscosity ratio are small so that the increase in the flow rate due to slippage over the attached bubbles can be very significant.

References

[1] Kabov O.A. et al. Rivulet/droplet dynamics and boiling incipience in microgravity: parabolic flights experiments, Fifth International Topical Team Workshop on Two-Phase Systems for Ground and Space Applications, Kyoto, Japan, September 26-29, *Book of Abstracts,* p. 61, (2010).

[2] Ajaev V.S., Gatapova E.Ya., Kabov O.A., Rupture of thin liquid films on structured surfaces, Phys. Rev. E, Vol. 84, Issue 4, 041606 (7 pages), (2011).

[3] Sbragaglia M., and Prosperetti A, Effective velocity boundary condition at a mixed slip surface, J. Fluid Mech., Vol. 578, pp. 435-451, (2007)

[4] Oron, A., Davis, S., Bankoff, S., Long-scale evolution of thin liquid films, Reviews of Modern Physics, 69:3, pp. 931-938 (1997).

Annular flow instability in microgap channels

Caleb Holloway, Ahmed Kaffel, Avram Bar-Cohen and Amir Riaz

University of Maryland, Mechanical Engineering
College Park, MD 21076
ariaz@umd.edu

Two-phase flow in microgap channels offers high impact thermal management capability and is the foundation for the emerging "embedded cooling" paradigm of electronic cooling [1,2,3]. Within the regime of annular flow the thermal performance of microgap coolers improves when flow quality increases from moderate to high values. This occurs because higher rates of heat transfer accompany the thin liquid layers, which are characteristic of the prevailing annular flow regime in this range of qualities. However, with further increase in flow quality the evaporating liquid film breaks up into rivulets and dry patches on the heated surface. The average heat transfer rate then depends on the fraction of the wetted surface and the thickness of liquid layers. This local dryout typically leads to a decreasing average heat transfer coefficient. However, if the average wetted area is sufficiently large and the average liquid film sufficiently thin, high rates of heat transfer can still be achieved well past the onset of local dryout and up to a critical flow quality. The determination of the optimal operating conditions associated with critical flow quality is thus necessary to operate two-phase microgap coolers consistently at high thermal efficiency under large thermal loads.

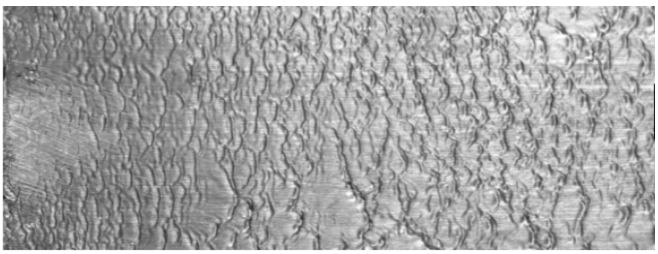

Figure 1: Interfacial patterns in an annular flow in a microgap channel.

In this study we show that specific interface deformation patterns, as shown in Figure 1, result from hydrodynamic and thermocapillary instability and govern the overall rate of heat transfer in microgap coolers. We show that the amplitude and wavelength of interfacial waves are affected by inlet mass flow rate and inlet flow quality. It has also been found that heated liquid films at a given inlet quality rupture and split into well defined structures from specific interfacial wave patterns. These developments suggest that quantitative relationships can be found between thin film characteristics and the primary microgap channel parameters that depend on inlet mass flow rate, inlet flow quality, refrigerant type and cooler geometry.

In order to quantify such behavior, the focus of this study is on the classification of flow regimes with the help of experiments, stability analysis and direct numerical simulation. Experiments were designed to reveal the basic interfacial structure of liquid films subject to gas shear under adiabatic conditions. The linear stability analysis was employed to the determine the interface structure associated with small scale flow disturbances from a fundamental perspective. Results of the linear stability analysis were compared with experimental observations with respect to the wavelength of the waves at the interface. The wavelength was measured in the experiments by visual inspection as well as with the image density profile technique. For the linear stability analysis, the wavelength with the highest growth rate was selected. This comparison relies on the void fraction obtained from the standard Baroczy correlation, which has an expected standard deviation of $\pm 20\%$. Within this range of uncertainty, the comparison reveals a relatively good agreement between the experimentally observed interfacial waves and the prediction of the most unstable waves from the linear analysis. A reverse estimation of void fraction was also carried out by wavelength matching. In this approach the wavelength given by the linear stability analysis was matched exactly with the average wavelength observed experimentally for a specific void fraction. The void fraction thus obtained from the linear stability analysis was found to be in good agreement with the void fraction obtained from the Baroczy correlation for a fixed set of flow conditions. These comparisons are instrumental in developing confidence in the physical relevance of the linear stability analysis, which was subsequently employed to explore the fundamental flow behavior over a wider range of parameters. Direct numerical simulations were also carried out to extend the physical understanding to nonlinear wave interaction.

Experiments are carried out with the coolant, FC-72, that is stored in an atmospheric reservoir and pumped with a Fluid-o-Tech magnetically coupled gear pump

and DC motor. The flow rate is measured with a Kobold DPM Pelton wheel flow sensor and the liquid temperature with an Omega T-type thermocouple probe, before it proceeds into a resistive coil heater (evaporator). The evaporator pre-heats the subcooled liquid to a targeted level of vapor quality based on an energy balance calculation. Power is measured and applied to the evaporator with a BK Precision XLN10014 DC power supply. Before the two-phase flow enters the test section, the pressure and temperature is measured with a Gems 2200 pressure transducer and an Omega T-type thermocouple probe, respectively.

The two-phase flow then proceeds through the micro-gap test section and visually captured using a Nikon D2X SLR with a Nikkor PC Micro 85mm lens and Speedlight flash. The pressure drop across the channel is measured with a Setra 230 pressure transducer and the outlet temperature with an Omega T-type thermocouple probe. A Flat Plate FG5X12-10 liquid-to-liquid brazed plate heat exchanger condenses the two-phase mixture before it flows back into the reservoir. The flow loop consists of Swagelock stainless steel plumbing and data is measured using a National Instruments CompactDAQ system with a NI 9214 thermocouple, NI 9205 analog voltage, and NI 9203 analog current module. The adiabatic visualization of the micro-gap test section was performed for three mass fluxes, G = 220 kg/m^2-s, 420 kg/m^2-s, and 620 kg/m^2-s, corresponding to flow rates of 0.5 mL/s, 1.0 mL/s, and 1.5 mL/s For a given mass flux, the desired vapor quality entering the adiabatic micro-gap channel was controlled using the pre-heater and varied from approximately 40 to 85%, in four steps. Visualization was performed for each distinct mass flux and vapor quality case when a quasi-steady state condition was reached.

A linear stability analysis is carried out to determine growth characteristics of small amplitude disturbances imposed on a steady, two-phase annular flow. Such perturbations likely arise from slight non-uniformities of inlet flow in physical systems. Perturbations grow to form finite amplitude structures observed in the experiments. The time required for the transition from small amplitude to the fully developed profile depends on the initial amplitude of disturbances. When the initial amplitude is sufficiently large the linear regime of growth may be bypassed altogether. We assume initial disturbances to be small so that linear stability analysis is applicable. The wavelength of the fastest growing waves predicted by the linear stability analysis is compared with the observed experimental wavelength. The Baroczy correlation is used to find the void fraction, which is required as input by the linear stability analysis.

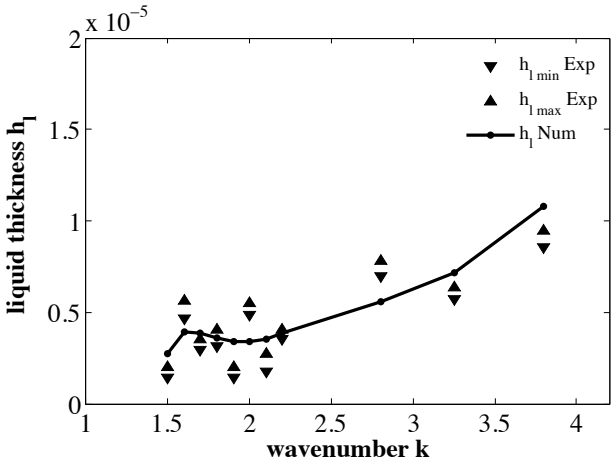

Figure 2: Thickness of the liquid film, h_1, versus the wavenumber k for different experimental cases.

The stability results may be influenced by the uncertainty in the film height that is obtained from the Baroczy correlation for the void fraction. In order to investigate this effect, liquid film thickness is varied to determine the void fraction for which the linear stability analysis gives the same wavelength as the experimentally observed average value. Figure 2 shows the liquid film thickness, h_1, based on this void fraction as a function of the wavelength, k. The values of h_1 obtained from the Baroczy correlation associated with the experimentally observed average value for k are shown as vertical lines. The variation of experimental results reflects the uncertainty related to the measurement of flow velocities. Figure 2 shows a reasonable agreement between h_1 obtained from the linear stability analysis and from the experiments.

References

[1] Kopp, B.A., Ouellette, E.A., Billups, A.J., "Thermal design considerations for wide bandgap transistors," Microw. J., 43, pp. 110-118, (2000).

[2] Bar-Cohen, A., Albrecht, J.D., Maurer, J.J., "Near-Junction Thermal Management for Wide Bandgap Devices," Compound Semiconductor Integrated Circuit Symposium, pp. 1-5, (2001).

[3] Bar-Cohen, A., "Gen-3 Thermal Management Technology: Role of Microchannels and Nanostructures in an Embedded Cooling Paradigm," J. Nanotechnol. Eng. Med., 4(2), pp. 1-3, (2013).

Numerical Modeling of Bubbly Two-Phase Flow in a Vortex Separator

Jingsen Ma, Chao-Tsung Hsiao, and Georges L. Chahine

DYNAFLOW, INC.
10621-J Iron Bridge Road, Jessup, MD 20794
Emails: jingsen@dynaflow-inc.com; ctsung@dynaflow-inc.com;
glchahine@dynaflow-inc.com

Development of a phase separator capable of efficiently and reliably separating gas-liquid mixtures in wide ranges of void fractions, flow rates, and levels of gravitational force is of great interest for both space and ground applications. This paper addresses the modeling of the flow in a vortex phase separator that we have been developing for future testing by NASA on the International Space Station [1][2]. In this separator centrifugal force is induced by high speed tangential injection of the bubbly mixture in a cylindrical chamber to generate a cavitating vortex core for gas capture. Through a combination of swirl, cavitation, and rectified gas diffusion, the separator is capable of extracting gas out of even very low void fraction mixtures into the central gaseous core of the vortex (see Figure 1). This separator has already been successfully tested on three reduced gravity flights [2]. Numerical modeling and simulation of the two-phase flow in the separator complements experimentation and allows consideration of a much large range of the parameters than feasible without constructing and testing many separators. This provides needed information to understand the physics and to guide system design and optimization.

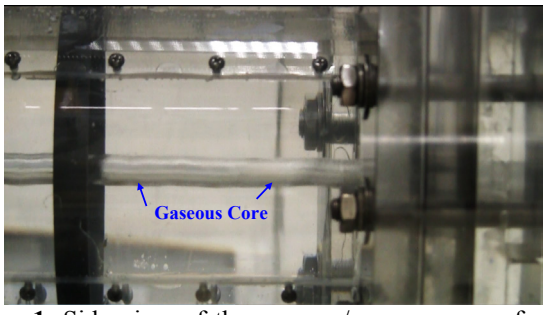

Figure 1. Side view of the gaseous/vaporous core forming on the axis of the phase separator.

We present here an Eulerian Lagrangian method [3]-[5] to model the two-phase medium in the vortex flow. This integrates a Discrete Singularity Model (DSM) for dispersed microbubbles with a continuum viscous description of the two-phase medium. DSM simulates the bubble dynamics following the Rayleigh-Plesset-Keller-Herring equation and tracks their motions in a Lagrangian fashion. Non-uniformities around the bubble are accounted for using surface averaged quantities for the bubble dynamics. A two-way coupling between DSM and the continuum is realized through the local mixture density associated with the bubbles volume change and positioning. The mixture density is determined by the local void fraction computed via a Gaussian scheme, which smoothly spreads and conserves the contribution of a bubble to the void fraction in neighboring continuum cells. In addition, a level set method in the Eulerian solver models free surfaces and large cavities [5]. Schemes are used to smoothly transition microbubbles that have grown beyond a threshold size into tracked liquid-gas interfaces such as the vortex gas/vapor core. This method is applied here to simulate the capture of bubbles into the vortex, which leads to the formation of a stable gaseous quasi-cylindrical core.

Figure 2 shows that a multi-block grid was generated for numerical simulations of the vortex separator which has a swirl chamber with two orifices of different sizes connecting the swirl chamber to two external chambers. The pressure distribution inside the vortex separator is shown in Figure 3. It is seen that a low pressure vortex core is formed in the axis of the swirl chamber where the gaseous cores forms.

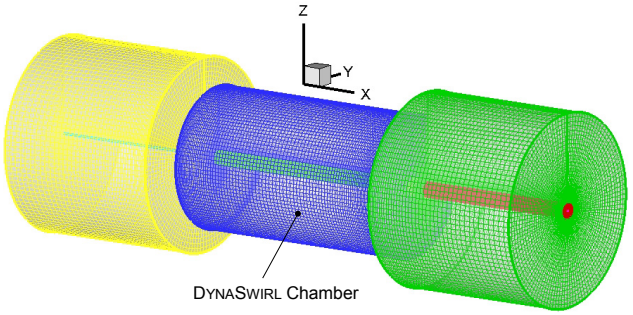

Figure 2. A multi-block grid generated for numerical simulation of the vortex separator.

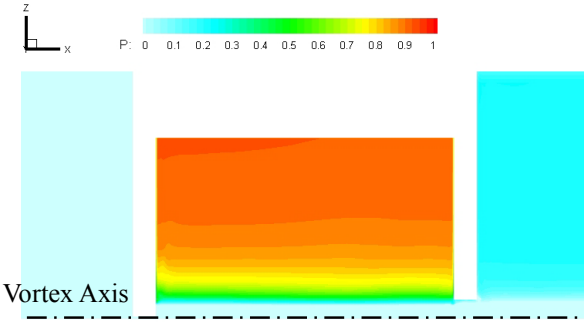

Figure 3. Pressure contour inside the vortex separator shown in half of domain.

Figure 4 shows a snapshot of the bubble distribution after injection into the swirl chamber from the wall tangential inlet. Figure 5 shows the behavior of a bubbly stream entering from the top side of the frame into a line vortex and illustrates bubble trajectories for different initial bubble radii and for two values of the body force. The effect of gravity can be seen by comparing the left (0 g) and right (1 g) panels. In absence of gravity, the bubbles get stratified depending on their size with the larger bubbles tending to

enter into the core region earlier than the smaller bubbles. In addition, all bubbles moves into the vortex core faster. On the other hand, in presence of earth gravity stratification is much more complex as the two acceleration fields – gravity and the rotation field - compete. At the beginning of the bubble trajectory, as the larger bubbles move downwards gravity slows their motion towards the vortex core center with some tending even to escape from the vortex influence. However this is gradually changed and the trend reverses as the bubbles arrive below the core axis elevation. Later, as in the case of no gravity, the two acceleration fields add up and the bubbles of larger sizes move much faster into the vortex core.

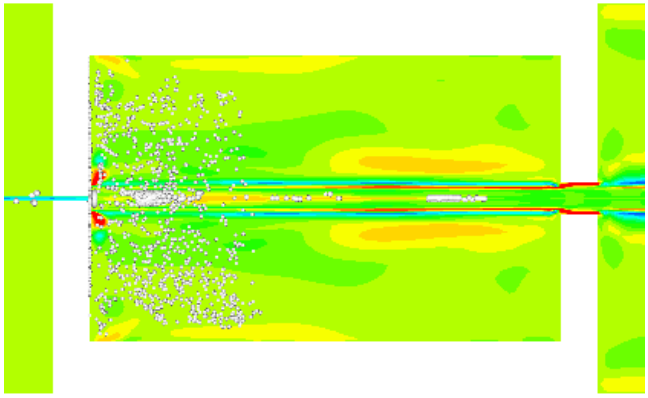

Figure 4. Bubble distribution and rotational velocity contours inside the vortex separator shortly after the bubbles were injected from the chamber tangential wall inlets.

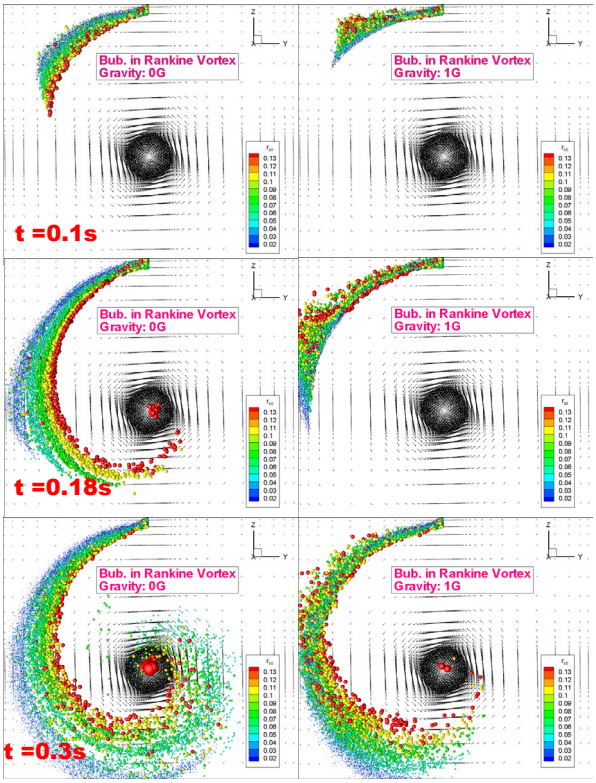

Figure 5. The effects of gravity on bubbles entrained in a line vortex flow. Comparison of trajectories of bubbles of different initial bubble sizes as they are captured in the vortex core.

This simulation shows the relative importance of gravity effects on the bubble capture in the separator vortex core, and highlights the fact that tests on earth and in zero gravity may not produce the same results making scaling studies necessary.

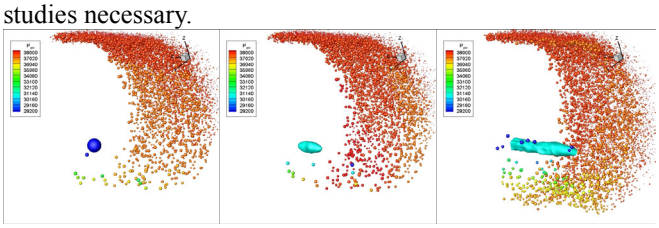

Figure 6. Time sequence of bubble capture and the development of a cavitation core on the axis of the vortex. The bubbles are colored by their gas pressure. The aqua blue iso-surface is the gas/vapor-liquid interface resulting from discrete large free surface formation.

Figure 5 results imply that a gaseous vortex core will be formed on the axis of the swirl chamber as the bubbles coalesce on the vortex axis. This can be modeled by enabling the coalesced bubbles to form a large cavity, which can be tracked as a gas-liquid interface. This can be achieved with the help of the level set method in the continuum two-phase viscous model. As the bubbles grow beyond a selected size and/or merge to increase volume beyond that size, the code initiates tracking them as gas-liquid gridded interfaces, which is detected via a level set method. As seen in Figure 6, an elongated cavity then forms along the axis of the vortex and develop into a gaseous-vaporous tube.

The gas in the cavity can then be sucked out of the axis through an orifice. The balance flow formed through gas capture and extraction is the next challenge of this modeling project and will be addressed in the presentation.

Acknowledgments:

We are grateful for NASA's support under Grant No. NNX11AO76A.

References

[1] Chahine, G.L. and Kalumuck, K.M., Swirling Fluid Jet Cavitation Method and System for Efficient Decontamination of Liquids, US Patent, 6,221,260, April 4, 2001.

[2] Wu, X. and Chahine, G.L., Development of a DYNASWIRL® Phase Separator for Space Applications, In 50th AIAA Aerospace Sciences Meeting, Nashville, TN, AIAA 2012.

[3] Hsiao, C.-T., Chahine, G.L., Numerical Study of Cavitation Inception due to Vortex/Vortex Interaction in a Ducted Propulsor, Journal of Ship Research, 52, 114-123, 2008.

[4] Hsiao, C.-T., and Chahine, G.L., Effect of Gas Diffusion on Bubble Entrainment and Dynamics around a Propeller, Journal of Hydrodynamics, 24(6), 809-822, 2012.

[5] Hsiao, C.-T., Wu, X., Ma, J. and Chahine, G. L. Numerical and Experimental Study of Bubble Entrainment due to a Horizontal Plunging Jet, International Shipbuilding Progress, 60, 435-469,2013.

Gravitational effect on performance of a Direct Methanol Fuel Cell

Fang Ye*[1,a], Cuiping Lv[1,b], Hang Guo[1,c], Feng Wu[1,d], Jianfu Zhao[2,e], Chongfang, Ma[1,f]

[1]MOE Key Laboratory of Enhanced Heat Transfer and Energy Conservation and Beijing Municipal Key Laboratory of Heat Transfer and Energy Conversion, College of Environmental and Energy Engineering, Beijing University of Technology, 100 Pingleyuan, Chaoyang District, Beijing 100124, China,

[2]National Microgravity Laboratory, Institute of Mechanics, Chinese Academy of Science, No.15 Beisihuanxi Road, Beijing 100190, China

[a]yefang@bjut.edu.cn (*Corresponding author), [b]lvcuiping@emails.bjut.edu.cn [c]hangguo@sohu.com, [d]wufeng@emails.bjut.edu.cn, [e]jfzhao@imech.ac.cn, [f]machf@bjut.edu.cn

Introduction

Direct methanol fuel cells (DMFC) have many benefits to be an attractive power source for small devices in spacecraft: requirements of compact system design, easy refueling, low cost of fuel, quick start-up, ambient temperature and pressure operation.

In direct methanol fuel cells, methanol is directly oxidized on the anode side without any reforming process, while oxygen is introduced into the cathode and is reduced. The electrochemical reactions on anode and cathode of DMFC are as follows:

Anode: $$CH_3OH + H_2O \rightarrow CO_2 + 6H^+ + 6e^- \quad (1)$$

Cathode: $$\frac{3}{2}O_2 + 6H^+ + 6e^- \rightarrow 3H_2O \quad (2)$$

Many researchers performed experiments of cell performance[1-4] and fluid flow[4-7] in DMFCs in normal gravity condition. However, only few papers reported experimental study of fuel cells in microgravity. Guo H., Zhao J. F. and Liu X. et al. (2009) experimentally investigated proton exchange membrane fuel cells (PEMFC) performance under different gravity conditions[9]. A serpentine flow field was adopted on the cathode side. They found that in normal gravity, the liquid water accumulates in the bottom of the vertical flow channels of cathode flow bed and cannot discharge effectively; but in microgravity, gas pushes the accumulated liquid water from the bottom of the channels to the outlet of cathode flow bed. Guo H., Zhao J. F. and Lv C. P. et al. (2008) reported their experiments of direct methanol fuel cells with gold plated stainless steel bipolar plates and preliminary analysis of the effect of gravity on mass transfer in DMFC[10]. Their experimental results indicated that carbon dioxide bubbles stagnation in channels results in a negative influence on the mass transfer and performance of direct methanol fuel cells in microgravity when the DMFC operates at high current density.

In this paper, the influence of gravity on power output performance of a liquid fed DMFC was investigated experimentally.

Experimental

The experimental system involves a direct methanol fuel cell, a oxygen tank, a oxygen flow rate controller (Cole Parmer, CZ-32907-67), a liquid flow rate meter (Cole Parmer, CZ-32908-43), a peristaltic pump (BT01), a data acquisition unit (AQU1216) and other auxiliary devices (Fig. 1). The flow rate controller can control the flow rate of oxygen from 0 to 1000 standard cubic centimeter per minute (SCCM) with an error of 1% of full scale. The liquid flow rate meter can precise control the liquid flow rate from 0 to 50.0 ml/min with an error of 2% of full scale. The accuracy of the 8 channel data acquisition unit is 0.1%, the frequency of measurement is 1000Hz.

A miniature direct methanol fuel cell consists of a membrane electrode assembly (MEA), two bipolar plates, a transparent anode end plate, a stainless steel cathode end plate and sealing gaskets.

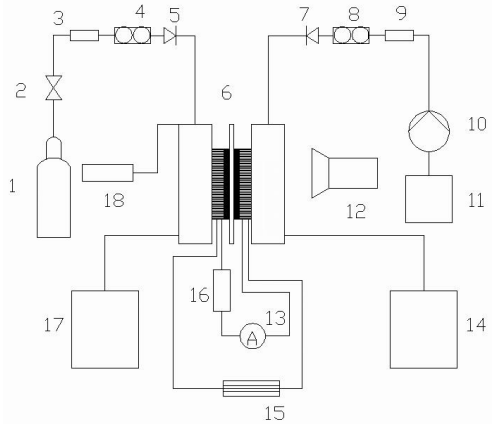

1: oxygen tank; 2: regulator; 3, 9: filters; 4: flow rate controller; 5, 7: one-way valves; 6: DMFC; 8: flow rate meter; 10: peristaltic pump; 11: liquid storage bag; 12: video camera; 13: current transmitter; 14: liquid collector; 15: data acquisition unit; 16: electric resistors; 17: exhaust collector; 18: temperature control and heating unit.

Figure 1: Experimental system .

In the present experiments, all channels on the anode side were vertical, and the anode feeding header pipe was in the bottom of flow bed, and the discharge header pipe was on the top for CO_2 bubbles removal. Oxygen gas with purity of 99.999% was fed as oxidant reactant without humidification.

In each microgravity experiment, the capsule, in which the experimental set-up was fixed, was released from upper storey of a drop tower after the fuel cell ran at 80 °C for 70 min. Capsule free falling in the drop tower of the National Microgravity Laboratory of Chinese Academy of Sciences could create 3.6s effective microgravity environment, which residual gravity acceleration was less than 10^{-2} g_0 (g_0, ground gravity acceleration, 9.81 m/s^2).

Results and discussions

Fig. 2 shows six parameters‘ signal value before and after release the cabin when fuel cell in-situ worked with 99.6 mA/cm^2.

Three electric loads with different value of resistance, are used as the external circuit load of DMFC, respectively. For every circuit load, experiments of the electric output performance of DMFC in normal gravity and microgravity were carried out, respectively.

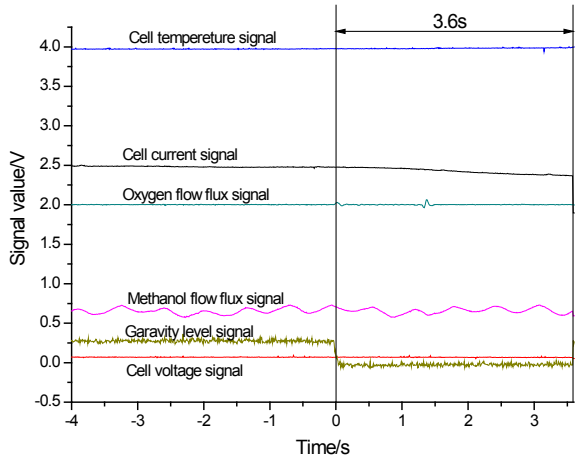

Figure 2: Typical course of free fall experiment in the Drop Tower Beijing (NMLC) with current density 99.6 mA/cm^2

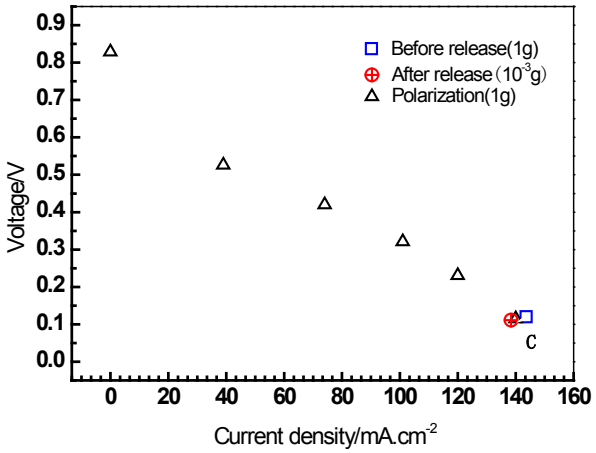

Figure 3: Cell performance under different gravity level

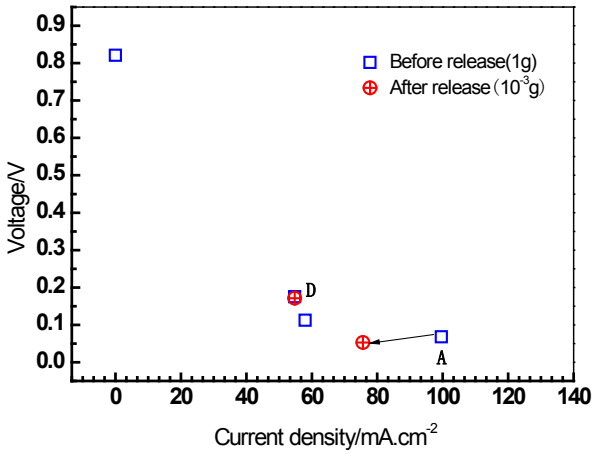

Figure 4: Performance at 99.6mA/cm^2 and 54.8mA/cm^2.

Difference of cell voltage vs. current density characteristics between normal gravity condition and micro gravity condition was obvious. The difference is larger- at higher current density (Fig. 3, 4). From data in Fig. 3 in concentration polarization region of the direct methanol fuel cell, it is known that mass transfer governs electric power generation of DMFC. Without the buoyancy lift force, the penetration in gas diffusion layer and flow in channels of CO_2 are slower and the discharge of CO_2, which is a product of anode electrochemical reaction, becomes more difficult in microgravity. Therefore, the accumulation of CO_2 bubbles in channels is more serious at higher current density in microgravity environment. Large amounts of CO_2 reduce the free area, which is necessary to the flow and penetration of methanol solution from channels to the catalyst layer. This weakens the anode electrochemical reaction and cause concentration polarization at the anode, which reduces the cell performance [7].

Conclusions

Experimental study of a liquid fed direct methanol fuel cell has been conducted in different gravity conditions.

The gravitational effect on power performance of DMFC is considerable when the concentration polarization is dominant in fuel cells operation.

Acknowledgement

This work is supported by the National Natural Science Foundation of China (Grant Nos.: 50976006, 11102005), Program for New Century Excellent Talents in University (Grant No.: NCET-10-0006), Specialized Research Fund for the Doctoral Program of Higher Education (Grant No.: 20121103110009), and Opening project of national microgravity laboratory, the Chinese Academy of Sciences.

References

[1] Scott, K. Taama W. M., et al., 1999, "Engineering aspects of the direct methanol fuel cell system". Journal of Power Sources, 79(1), 43-59

[2]Yang W. M., Chou S. K., Shu C., 2007, "Effect of current-collector structure on performance of passive micro direct methanol fuel cell". Journal of Power Sources, 164(2), 549-554

[3]Zhang J., Yin G. P., Lai Q. Z., et al, 2007, "The influence of anode gas diffusion layer on the performance of low-temperature DMFC". Journal of Power Sources, 168(2), 453-458

[4] Scott K., Argyropoulos P., et al., 2001, "Electrochemical and gas evolution characteristics of direct methanol fuel cells with stainless steel mesh flow beds". Journal of Applied Electrochemistry, 31(8), 823-832

[5] Nordlund J., Picard C., et al., 2004, "The design and usage of a visual direct methanol fuel cell". Journal of Applied Electrochemistry, 34(8), 763-770

[6] Lu G. Q., Wang C. Y., 2004, "Electrochemical and flow characterization of a direct methanol fuel cell". Journal of Power Sources, 134(1), 33-40

[7]Yang H., Zhao T. S., et al., 2005a, "In situ visualization study of CO2 gas bubble behavior in DMFC anode flow fields", Journal of Power Sources, 139(1-2), 79-90

[8]Guo H., Zhao J. F., Liu X. et al., 2009, "Experimental study of performance of proton exchange membrane fuel cells in short-term microgravity condition" (in Chinese). Journal of Engineering Thermophysics, 30(8), 1376-1378

[9]Guo H., Zhao J. F., Lv C. P., et al., 2008, "Experimental study of fuel cells performance in short term microgravity condition" (in Chinese). Journal of Engineering Thermophysics, 29(5), 865-867

Qualification of a Degassing Method for FC-72/PF-5060

Sebastian Fischer[1)], Peter Stephan[1,2)]

1) Institute for Technical Thermodynamics, Technische Universität Darmstadt,
Alarich-Weiss-Straße 10, D-64287 Darmstadt, Germany
Email: fischer@ttd.tu-darmstadt.de
2) Center of Smart Interfaces, Technische Universität Darmstadt,
Alarich-Weiss-Straße 10, D-64287,Darmstadt, Germany

Fully fluorinated hydrocarbons are widely used in evaporation and boiling experiments, both under normal gravity and under microgravity conditions.

Apart from their low vaporization enthalpy when compared to water, which reduces the necessary power consumption of the experiment heaters, the non-toxicity and non-flammability of these fluids make them a first choice from the safety point-of-view. The most commonly used fully fluorinated hydrocarbon used in evaporation and boiling experiments under microgravity is FC-72/PF-5060 (e.g. in [1-3]). The acronyms "FC" and "PF" stand for "Fluorinert Compound" and "Performance Fluid", respectively. Both fluids have equal thermo-physical properties according to the manufacturers data sheets [4,5] rendering them identical. N-perfluoro-hexane is the main component of FC-72/PF-5060, but due to the extremely high costs of the pure substance, it is only scarcely used, usually in space-experiments [6,7], where exchange of contaminated experiment fluid is not possible. The major disadvantage of these experiment fluids is however their ability to dissolve large quantities of non-condensable gases. In order to carry out reliable experiments, the fluids must therefore be carefully degassed to eliminate the influence of non-condensable gases onto the evaporation or boiling processes investigated.

In figure 1 the schematics of the degassing facility used within this work is displayed. Herein, black, green, red and blue connections indicate experiment fluid, non- condensable gas, evaporator thermalization circuit and condenser thermalization circuit piping, respectively. The evaporators and the condenser have been built from large diameter vacuum tubing encompassed by copper tubing of the thermalization circuits to ensure a low leakage rate. After fluid is filled into evaporator 1 through a filter and valve V-1, it is in a first step evaporated into the evacuated rest of the degassing facility (valve V-2 open, all other valves closed). This step eliminates suspended particles from the fluid and possible contaminations by high boiling components, which can later be removed through valve V-3. Condensing liquid

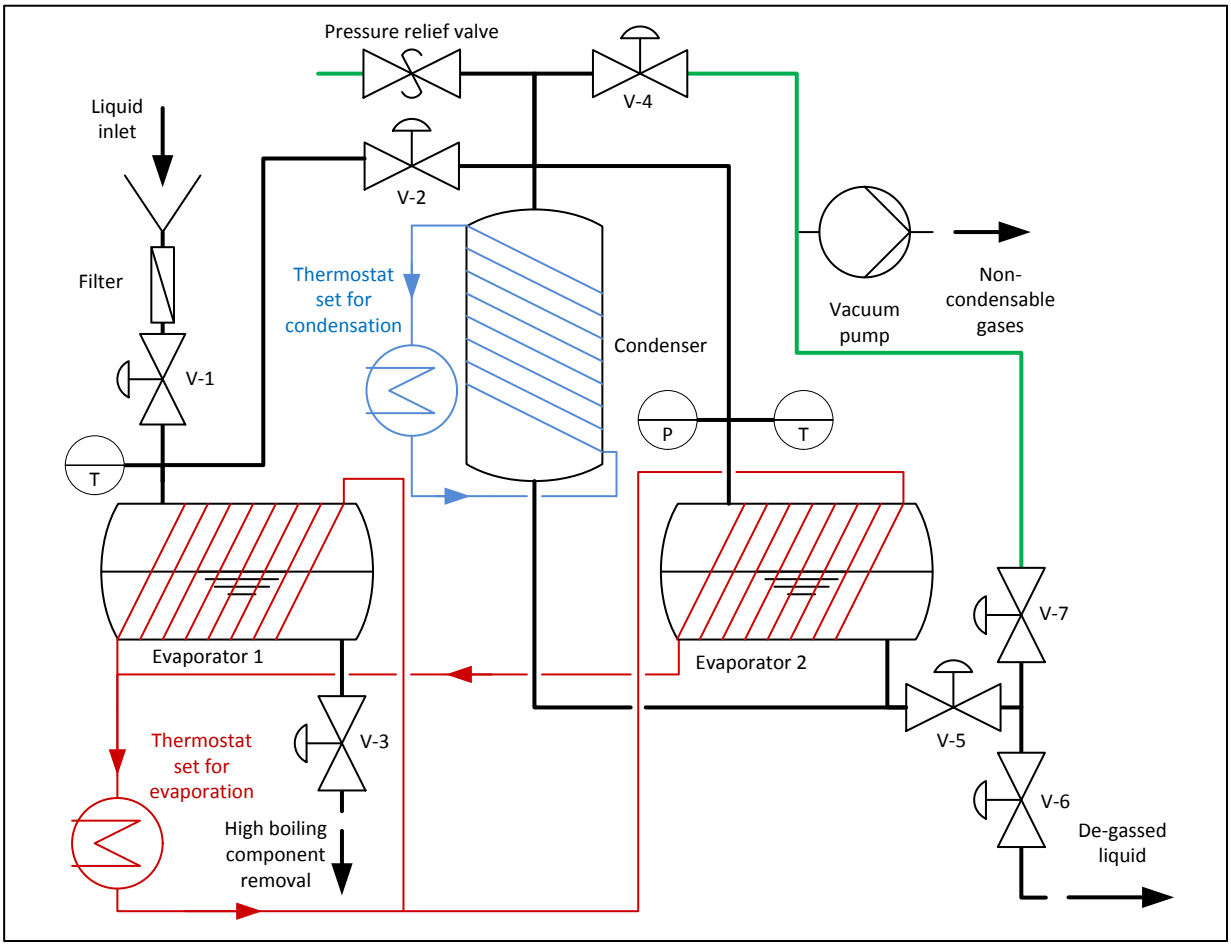

Figure 1: Schematics of the degassing facility

is fed from the condenser to evaporator 2, which slowly fills up due to gravity. After all experiment fluid has been evaporated from evaporator 1, valve V-2 is closed and the fluid is evaporated and re-condensed in the now closed loop for several hours. In regular intervals valve V-4 is opened to suck out non-condensable gases from the top of the condenser. By opening valves V-6 and V-7 the connected experimental setup can be evacuated. Afterwards, valve V-7 is closed and V-5 is opened, thus filling the experimental setup with now degased liquid from evaporator 2.

The reliability of this degassing method is checked by means of comparative analysis through gas chromatography–mass spectrometry (GC-MS). In figure 2 an excerpt of the relevant part of the mass spectra of a not degassed FC-72 sample (left) and a degassed FC-72 sample (right) is shown. Most of the peaks are specific to FC-72 and represent energy minima caused by internal re-arrangements of the molecules. In the excerpt of the spectrum from the not degassed sample however, three further peaks are present: One at a mass-to-charge ratio of 28 indicating the presence of Nitrogen (relative abundance 8.29), one at a mass-to-charge ratio of 32 indicating the presence of Oxygen (relative abundance 3.92) and one at a mass-to-charge ratio of 4 indicating the presence of Helium. The sample was never exposed to Helium above atmospheric concentration, but Helium was used to flush the GC-MS system prior to the measurements, thus its appearance in the first spectrum. Nitrogen and Oxygen however were dissolved in the FC-72 from exposure to the atmosphere. In the mass spectrum of the degassed FC-72 sample the relative abundances of Nitrogen and Oxygen are strongly reduced (0.82 and 0.37, resp.). This corresponds to a reduction of the non-condensable gas content of 90.3 %. With the Henry constant of air in FC-72 of $H = 5.4 \times 10^{-8}$ mole gas/(mole liquid Pa) [8] and assuming saturation of the not degassed sample an initial non-condensable gas content of 4.25×10^{-3} mole gas/mole liquid can be calculated. After the degassing procedure the non-condensable gas content is therefore reduced to less than 4.13×10^{-4} mole gas/mole liquid.

References

[1] Schweizer, N. Stephan, P., Experimental study of bubble behavior and local heat flux in pool boiling under variable gravitational conditions, Multiphase Science and Technology, Vol. 21, pp. 329–350 (2009)

[2] Di Marco, P., Raj, R., Kim, J., Boiling in variable gravity under the action of an electric field: results of parabolic flight experiments, Journal of Physics: Conference Series, Vol. 327, pp. 1-13 (2011)

[3] Baba, S., Ohtani, N., Kawanami, O., Inoue, K., Ohta, H., Experiments on dominant force regimes in flow boiling using mini-tubes, Frontiers in Heat and Mass Transfer, Vol. 3, pp. 1-8 (2012)

[4] 3M Performance Materials, FC-72 datasheet, http://multimedia.3m.com/mws/mediawebserver?mwsId=66666UgxGCuNyXTtnxTE5XF6EVtQEcuZgVs6EVs6E666666--&fn=prodinfo_FC72.pdf (2000)

[5] 3M Performance Materials, PF-5060 datasheet, http://multimedia.3m.com/mws/mediawebserver?mwsId=SSSSSuH8gc7nZxtUM8tZl8_BevUqe17zHvTSevTSeSSSSSS--&fn=prodinfo_pf5060.pdf (2003)

[6] Tóth, B. et al., Future Experiments to Measure Liquid-Gas Phase Change and Heat Transfer Phenomena on the International Space Station, Microgravity Sci. Technol., Vol 24, pp. 189–194 (2012)

[7] Dhir, V. K., Warrier, G. R., Aktinol, E., Chao, D., Eggers, J., Sheredy, W., Booth, W., Nucleate Pool Boiling Experiments (NPBX) on the International Space Station, Microgravity Sci. Technol., Vol 24, pp. 307-325 (2012)

[8] You, S. M., Simon, T. W., Hong Y. S. and Bar-Cohen, A., Effects of Dissolved Gas Content on Pool Boiling of a Highly Wetting Fluid, J. Heat Transfer, Vol. 117, pp. 687-692 (1995)

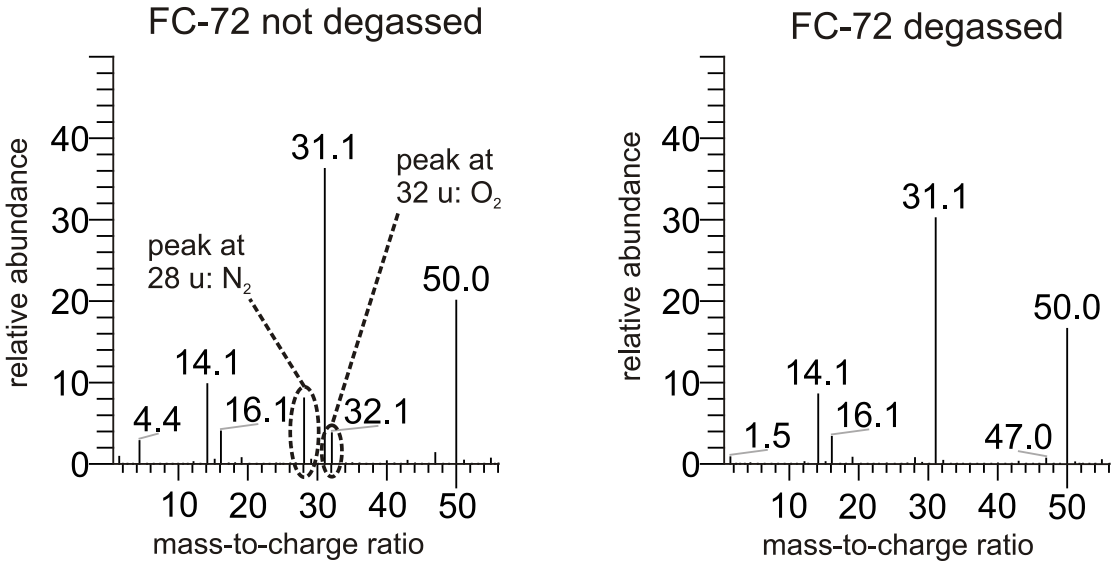

Figure 2: Comparison of the mass spectra excerpts of a not degassed FC-72 sample (left) and a degassed FC-72 sample (right)

Numerical simulations of thermo-convective instabilities in a sessile drop of ethanol under evaporation in microgravity conditions

Sergey Semenov, Florian Carle, Marc Medale, David Brutin

Aix-Marseille Université, Technopôle de Château-Gombert, Laboratory IUSTI UMR 7343 CNRS
5 Enrico Fermi street, 13453 Marseille cedex 13, FRANCE
sergey.semenov@univ-amu.fr

1. Introduction

The thermo-capillary instability, also called thermal Marangoni instability, develops during the evaporation of fluids when the gradient of surface tension is high enough. When the fluid surface is static, the instabilities are created in response to temperature gradients due to the variation of surface tension with temperature. They were observed for the first time by Henri Benard by optical method in liquid layers [1]. Similar thermo-capillary instabilities develop in an evaporating sessile drop placed on a heated substrate.

Our studies of the sessile drop evaporation are intended to bring a new knowledge into the field and improve our understanding of complex physical processes taking place in evaporating drops. In particular, our 2D numerical model of an unsteady process of evaporation of a sessile drop of ethanol under microgravity conditions shows a quantitative agreement (within experimental error bars) with the experimentally measured evaporation rate, and demonstrates the process of development of axisymmetric thermoconvective instabilities. The fact that the instabilities observed in real experiments (by means of infrared thermography) are not axisymmetric motivates us for the extension of current 2D problem into three dimensions and future numerical modelling of an equivalent 3D problem.

2. Experimental observations

Few experimental studies have been found in the literature: study of thermo-capillary convection in an open ring by Schwabe et al. [2] and hydrothermal waves (HTWs) in volatile drops by Sefiane et al. [3]. Microgravity would confirm the thermal origin of these thermo-capillary instabilities and show experimentally that gravity has no influence on the development of instabilities.

The drop configuration has been studied among others by Brutin et al. [4] and Sobac et al. [5] by means of infrared thermography, respectively, at room temperature and for heated substrates. Different fluids were used: water drops, FC - 72, ethanol and methanol. Upon drops evaporation, thermo-capillary instabilities develop spontaneously and grow. Fig. 1 shows these HTWs in two evaporating drops for two different levels of gravity [6].

In normal gravity due to evaporative cooling a temperature gradient develops between the apex of the drop and the triple line, resulting in a surface tension gradient. The thermal gradient therefore generates the thermocapillary instabilities. These HTWs are observed near the three-phase contact line where the majority of evaporation takes place. They circulate around the apex of the drop and spaced at a quasi-constant angle of rotation around the axis of symmetry of the drop.

In microgravity the temperature gradient is much less clear but the apex maintains a temperature below that of the contact line. In this configuration the HTWs have the same pattern as in normal gravity but their movements are not as ordered. This is partly due to vibrations that disrupt the flight of the aircraft and result in insignificant jitter of the microgravity level. Despite this lack of stability, the evolution of the number of HTWs is similar regardless of the gravity level.

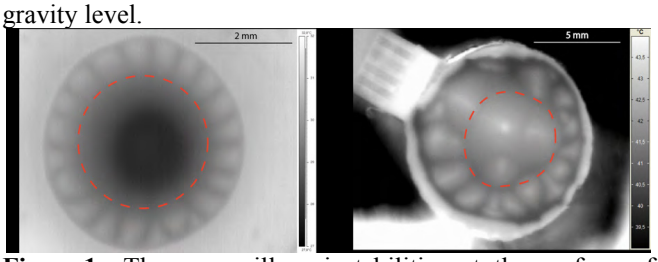

Figure 1: Thermo-capillary instabilities at the surface of ethanol drops: a) normal gravity, b) microgravity. The radiuses of drops are less than the capillary lengths for corresponding gravity levels.

3. Numerical simulations

Only two numerical studies of unsteady (time-dependent) evaporation of a sessile drop have been found in the literature: study of drop oscillations by Korenchenko et al. [7] and study of HTWs in evaporating sessile drops by Karapetsas et al. [8]. The last one has shown a qualitative, but not quantitative, agreement with experimental observations.

3D numerical simulations were performed in the laboratory IUSTI in order to study if there are values of control parameters for which non-axisymmetric solutions appear. For these calculations we made the assumption of "frozen time" for which the geometry does not change allowing us to identify various branches of stationary states with a numerical method of asymptotic continuation [9]. As we show in Figs. 2 and 3, we found numerically a fundamental branch of axisymmetric solutions and two bifurcating branches of non-axisymmetric solutions. One of them is represented in Fig. 3.

Thus the 3D numerical model proves the existence of non-axisymmetric solutions. However the local evaporation rate at the drop surface in this model does not correspond to a real experimental situation, when evaporation rate is limited by the vapour diffusion. Therefore the next step on our way to a physically correct model is a creation of an axisymmetric 2D numerical model and its validation against experimental evaporation rate. The successful validation of 2D model then can be followed in future by its extension to three dimensions with physically correct boundary conditions.

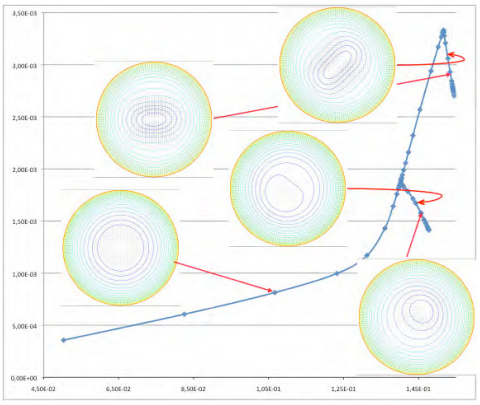

Figure 2: Bifurcation diagram (abscissa: dimensionless density of the evaporation flux; ordinate: dimensionless average speed in the drop), e/d = 0.36, Bo = 1.

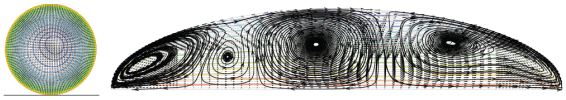

Figure 3: Top view and cross-section of the drop on a forked branch composed out of non-axisymmetric solutions.

3.1. Validation of axisymmetric 2D numerical model

3.1.1. Steady-state problem

Our first 2D numerical model is based on a particular experimental setup: a drop of ethanol on top of heated cylindrical substrate, evaporating into ambient atmosphere in normal gravity. The problem was solved under steady-state approximation. The model showed an agreement with the experimental evaporation rate within 10% error.

The solution bifurcations for this axisymmetric problem are related to different patterns of flow in the surrounding atmosphere, but not in the drop. The flow pattern within the drop was same (one thermo-capillary vortex) for a wide range of substrate temperatures.

3.1.2. Unsteady problem

Another 2D numerical model is based on the parabolic flight experiment: a drop of ethanol on top of heated substrate, evaporating into a closed chamber under microgravity conditions. The problem was solved in its unsteady formulation under the condition of pinned triple line. Fig. 4 shows the comparison of numerical evaporation rate (red line) with the experimental one (black line). The discrepancy at the beginning of the evaporation is due to the fact that in the real experiment there is a stage of drop injection and spreading (gradual increase of the evaporation rate). However the numerical model does not take into account the drop injection and spreading, and therefore numerical evaporation starts instantly, resulting in a very high evaporation rate at the beginning. After this initial stage, the evaporation rates become more or less constant, showing a good agreement.

3.2. Thermo-convective instabilities

It turned out that the solution of unsteady problem (*section 3.1.2*) revealed thermo-convective instabilities within the drop (Fig. 5), which did not appear in the equivalent steady-state problem (*section 3.1.1*). This result is very important, because it demonstrates a big qualitative difference between unsteady and steady-state approaches. *It shows that steady-state approximation of the problem is not suitable for the study of thermo-convective instabilities.* Instead, the unsteady formulation of the problem must be used in order to study these instabilities.

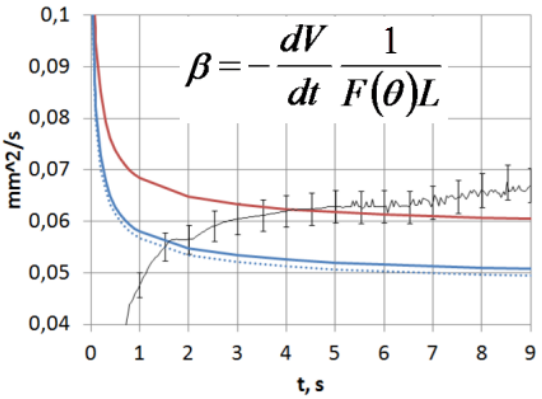

Figure 4: Drop evaporation rate: (red line) – numerical model with convection due to Stefan flow, (black line) – experiment, (blue line) – numerical model for a pure diffusion, (dotted blue line) – semi-empirical theory for a pure diffusion. V is the droplet volume, t is time, L is the contact line radius, $F(\theta)$ is the function of contact angle.

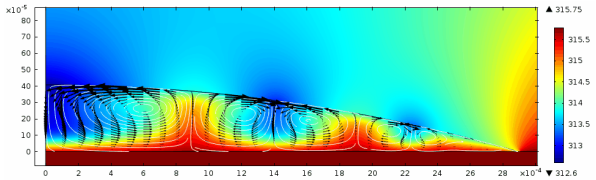

Figure 5: Thermo-convective instabilities within the evaporating drop of ethanol (numerical model, unsteady problem). Colour represents the temperature field. Animation: www.vk.com/doc6449478_285143123

References

[1] Bénard, H., Les tourbillons cellulaires dans une nappe liquide. – Méthodes optiques d'observation et d'enregistrement, Journal de Physique Théorique et Appliquée, 10, 254 – 266 (1901)

[2] Schwabe, D., Zebib, A., Sim, B.-C., Thermocapillary Convection in Open Cylindrical Annuli. Part 1. Experiments Under Microgravity, Journal of Fluid Mechanics, 491, 239 – 258 (2003)

[3] Sefiane, K., Fukatani, Y., Takata, Y., Kim J., Thermal patterns and hydrothermal waves (HTWs) in volatile drops, Langmuir, 29, 9750 – 9760 (2013)

[4] Brutin, D., Sobac, B., Rigollet, F., Le Niliot, C., Infrared visualization of thermal motion inside a sessile drop deposited onto a heated surface, Exp. Therm. Fluid Sci., 35, no. 3, 521 – 530 (2011)

[5] Sobac, B., Brutin, D., Thermocapillarity instabilities in an evaporating drop deposited onto a heated substrate, Physics of Fluids, 24, 032103 (2011)

[6] Carle, F., Sobac, B., Brutin, D., Hydrothermal waves on ethanol droplets evaporating under terrestrial and reduced gravity levels, J. Fluid Mech., 712, 614 – 623 (2012)

[7] Korenchenko, A.E., Beskachko, V.P., Oscillations of a sessile droplet in open air, Physics of fluids, 25, 112106 (2013)

[8] Karapetsas, G., Matar, O.K., Valluri, P., Sefiane, K., Convective rolls and hydrothermal waves in evaporating sessile drops, Langmuir, 28, 11433 − 11439 (2012)

[9] Medale, M., Cochelin, B., A parallel computer implementation of the asymptotic numerical method to study thermal convection instabilities, J. Comp. Physics, 228, 8249 – 8262 (2009)

Bubble Generation and Sizing in Fresh and Salt Water

A. Leaman Nye, X. Wu, G.L. Chahine

DYNAFLOW, INC
10621-J Iron Bridge Road, Jessup, MD, USA
Abigail@dynaflow-inc.com

Microbubbles were generated in fresh and salt water using a swirling cavitating jet and were measured using high speed photography and an acoustic technique. Salinities were varied in the range 15-100 g/kg. Measured bubble size distributions were consistent between the two measurement methods. Sizes were found to skew to smaller radii as salinity increased, with mean bubble radius reductions from freshwater values to the highest salinity tested of between 33%-95% for different bubble generation flow conditions.

Introduction

Of key interest in many bubbly flow applications is the determination of the influence of salinity on bubble sizes and bubble numbers – properties that have direct impacts on bubble rise velocity and residence time, shape, surface area to volume ratio, etc. The mechanisms by which salinity affects the physical processes governing bubble evolution, namely: generation, coalescence, dissolution, and breakup, are not well understood. Salt influences these processes directly by changes in physical parameters such as increasing density, surface tension, and viscosity, and decreasing vapor pressure. In addition, salt has more subtle influences on bubble interface properties that are difficult to model directly [1]. Salt has also been shown to inhibit coalescence through repulsive forces generated through the alignment tendencies of its component sodium and chlorine ions at bubble interfaces [2]. In studies of bubble fragmentation in fresh and saltwater it was found that bubble breakup in saline conditions resulted in up to a fivefold increase in bubble numbers - attributed to the combined influence of salt and surfactants at bubble interfaces [3].

Here we describe acoustic and optical measurements of bubble size distributions (BSDs) generated using a cavitating jet in different salinity conditions.

Experiments

Bubbles were generated in a flow loop (**Figure 1**) comprised of a series of 2 in. internal diameter pipes through which water could be pumped at rates up to 30 gpm from a reservoir of fresh or salt water. Salinity was manipulated by the addition of Instant Ocean® seasalt [4] at mass fractions of the total freshwater mass in the system in the range 15 to 100 g/kg. Flow was pumped from the reservoir and diverted through a swirling cavitating bubble generator [5] before entering a vertical test section that housed two pairs of hydrophones with resonant frequencies $f_0 = 50kHz$ and $f_0 = 250kHz$ for analysis of acoustic propagation across the bubbly flow. The walls of the bypass were made of transparent Plexiglas so that optical measurements could be made simultaneously. The loop was closed by the return of the two-phase flow to the reservoir.

At sufficiently large flow rates, the low pressure center at the center of the bubble generator vortex chamber can drop below vapor pressure, hence inducing formation of cavitation bubbles (see Figure 2). The two-phase core flow is extracted from the swirl chamber through an exit orifice and the bubble population is filtered by the presence of a fine screen that removes larger bubbles. The resulting bubble distributions in freshwater contain bubbles with radii smaller than 150 mm, and void fractions in the range $[10^{-5}, 10^{-1}]$. Fresh and saltwater flow rates for the present study were in the range $[9.9, 13.2]$. These flow rates generated measured freshwater void fractions in the range $[1.7 \times 10^{-5}, 1.1 \times 10^{-4}]$.

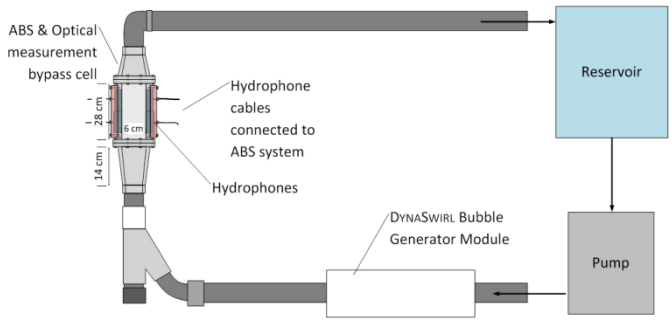

Figure 1: Schematic of the bubble generation loop.

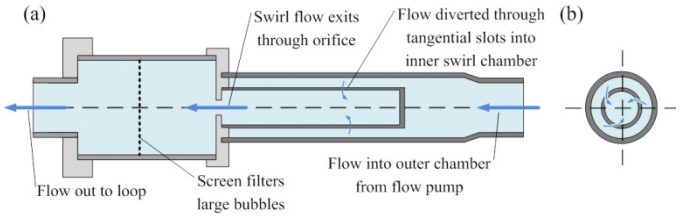

Figure 2: Schematic of the cavitating swirling jet (a) axial cross-section, (b) radial cross-section of annular chambers.

Bubble size distributions were measured using the ABS ACOUSTIC BUBBLE SPECTROMETER® system (ABS) [6]-[7] that uses an inverse acoustic method to determine bubble sizes and void fractions. The ABS analyses signals produced by short monochromatic bursts of sound over a range of frequencies transmitted through the medium between an emitter and a receiver hydrophone. Phase speed, u, and attenuations, v, can be deduced at each acoustic frequency by comparison of the sent and received signals. The ABS derives BSDs from measurements of u and v by solution of an ill-posed pair of Fredholm Integral equations of the first kind using novel algorithms that employs a constrained optimization technique.

The ABS BSDs are validated using those obtained simultaneously from high speed video data (HSV). Five thousand images were collected with a HSV camera with a macro lens and additional lens extensions that was focused on a region of the flow located directly between the ABS

hydrophones. The optical data was calibrated using measurements of pixel size and depth of field. These are critical in accurately determining BSDs and typically have values of a few microns and millimeters respectively. HSV images were then processed and analyzed using image analysis software. Post processing included subtraction of backgrounds and thresholding to remove shadows from bubbles outside of the depth of field. Bubbles identified through this procedure were then counted and binned according to their size to produce BSDs for each sample.

Results and Discussion

Figure 3 shows ABS (red triangles) and HSV (green circles) data for one salinity condition of 25 g/kg at four different flow rates. The acoustic and optical data agree well. As the flow rate increases, void fractions generated by the cavitating swirling flow also increase, with peak values of the BSD increasing by an order of magnitude over the range of flow rates shown.

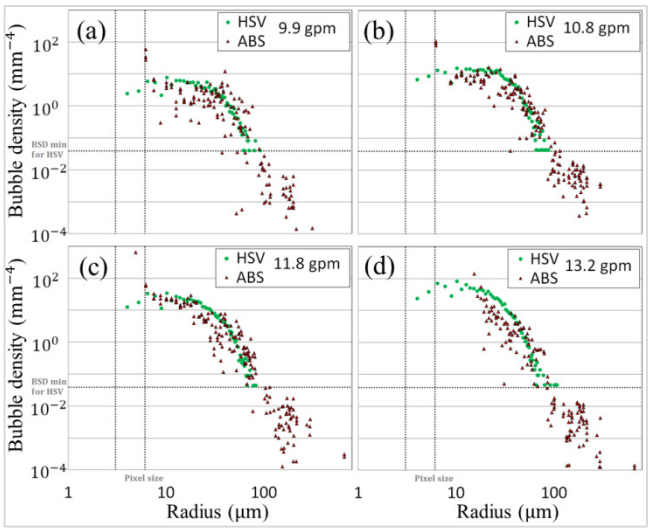

Figure 3: Bubble density distributions comparing ABS (red triangles) and HSV (green circles) data at salinity 25 g/kg and (a) 9.9 gpm, (b) 10.8 gpm, (c) 11.8 gpm, (d) 13.2 gpm.

Figure 4 plots BSDs from HSV at a flow rate of 13.2 gpm for freshwater (red symbols) and with increasing salinity (symbols colored through the spectrum with purple indicating the largest salinity of 100 g/kg). The BSD is skewed to smaller radii with salinity increase, with the peak bubble density increasing from 61 mm^{-4} at $R = 10.3\mu m$ in freshwater to $255 mm^{-4}$ at $R = 6.6\mu m$ for 100 g/kg.

Figure 5 plots the percentage change in mean radius, defined as the average overall radii bins in the binned bubble number distribution, $\overline{R} = \sum_{ibin} R_{ibin} n_{ibin} / \mathrm{N}$ with N being the total number of bubbles, relative to freshwater values with increasing salinity under different flow conditions. All flow conditions show a similar trend in reduction of the mean radii with salinity, having percentage reductions in $\overline{R}$ between 33% and 52% at a salinity of 100 g/kg.

Conclusions

The influence of salinity on bubbles generated by a cavitating jet has been studied using acoustic and optical methods. Bubble size distributions have been shown to skew to lower radii with increasing salinities. Mean radii of distributions decrease with salinity with the greatest reductions achieved at larger flow rates and larger void fractions. It is not clear yet how physical mechanisms such as cavitation, coalescence and bubble breakup are affected individually by the presence of salt. Studies are currently in progress to investigate these in more detail.

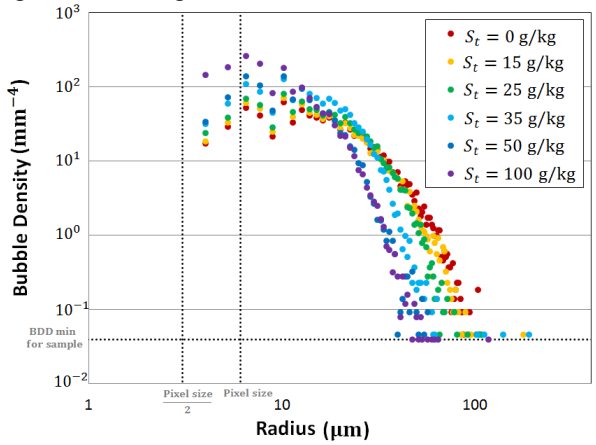

Figure 4: Bubble density distributions from HSV measurements for a flow rate of 13.2gpm. Color spectrum indicates increasing salinity cases from red to purple.

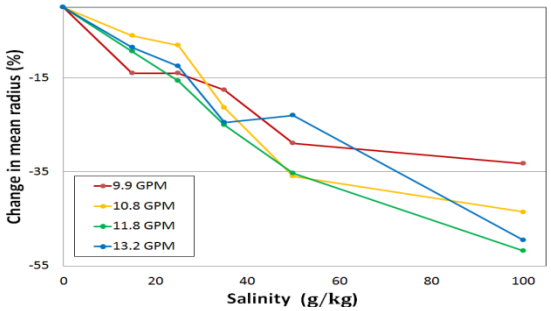

Figure 5: Percentage change in mean radius with increasing salinity at different flow rates.

References

[1] Rosen, M., Surfactants and interfacial phenomena, John Wiley & Sons, New York, 295 (1978)

[2] Henry, C., Dalton, C., Scruton, L., Craig, V., Ion-specific coalescence of bubble in mixed electrolyte solutions, J. Phys. Chem., 111, 1015-1023 (2007)

[3] Slauenwhite, D., Johnson, B., Bubble shattering: differences in bubble formation in fresh water, J. Geophys. Res. - Oceans, 104, 3265-3275 (1999)

[4] Atkinson, M., Bingham, C., Elemental composition of commercial seasalts, J. Aquaricult. & Aq. Sci., 8, 39-43 (1997)

[5] Chahine, G., Choi, J.-K., Hsiao, C.-T., Development of a bubble generator suitable for Spallation Neutron Source (SNS) shock mitigation applications, DOE Phase II Report (2012)

[6] Duraiswami, R., Prabhukumar, S., Chahine, G., Bubble counting using an inverse acoustic scattering method, J. Acoust. Soc. Am., 104(5), 2699-2717 (1998)

[7] Chahine, G., Kalumuck, K., Cheng, J.-Y., Frederick, G. Validation of bubble distribution measurements of the ABS Acoustic Bubble Spectrometer with high speed photography, 4th Int. Symp. on Cavitation, Pasadena, USA (2007)

Effect of high-frequency normal vibrations on critical heat flux of subcooled film boiling

V.V. Konovalov, T.P. Lyubimova, O.A. Kabov

Institute of Continuous Media Mechanics, UB RAS
1, Ak. Koroleva, Perm, Russia
Kutateladze Institute of Thermophysics SB RAS
1, Ac. Lavrentieva, Novosibirsk, Russia
konovalov@icmm.ru, lubimova@psu.ru, okabov@gmail.com

In microgravity regime of film boiling occurs at much lower values of heat flux in the system than in normal conditions [1]. This is due to the fact that usually gravity, but, rather, due to its buoyancy, is the mechanism that separates the vapor bubbles formed on the heater surface and removes them off, preventing thereby the early onset of the first boiling crisis. In its absence thermocapillary convection mechanism goes to the forefront [2], but can not be as effective in the transportation of vapor bubbles as the effect of buoyancy.

Experiments on various boiling liquids in weightlessness [3] show that under these conditions the liquid - vapor interface is the most stable in the so-called subcooled film boiling when the temperature in the liquid volume is maintained lower then the saturation temperature. In this case the liquid - vapor interface tends to the completely stable state when no phase transition exist and all heat supplied to the interface is removed in the process of heat conduction in the liquid.

In the experimental work [4] it is shown that the above stability of the interface can be implemented in the presence of gravity field directed to the heating surface, when the Rayleigh - Taylor instability of heavy fluid overlying the layer of light vapor should arise, which in this case is completely suppressed with phase transition at a certain critical heat flux of subcooling. This phenomenon is observed only in the case of sufficiently thin vapour films, allowing in [5] to build his theory using approximations "shallow water" and "creeping " flow.

A more complete study on the basis of long-wave approximation is made in [6], where not only studied linear stability, but also presents the results of weakly nonlinear analysis and numerical simulation of the dynamics of the phase boundary subcooled or saturated film boiling. For the case with subcooling supercriticality stable regimes were found including the space-periodic regime and alternative "traveling waves" regime.

In this work we have studied the linear stability of the liquid - vapor interface of subcooled film boiling when the effects of the phase transition and the impact of high-frequency normal vibrations exist. It is known from the literature, high-frequency normal vibrations have a stabilizing effect on the Rayleigh - Taylor instability moving the instability region to the direction of long-wave perturbations and reducing the perturbation growth rates [7,8].

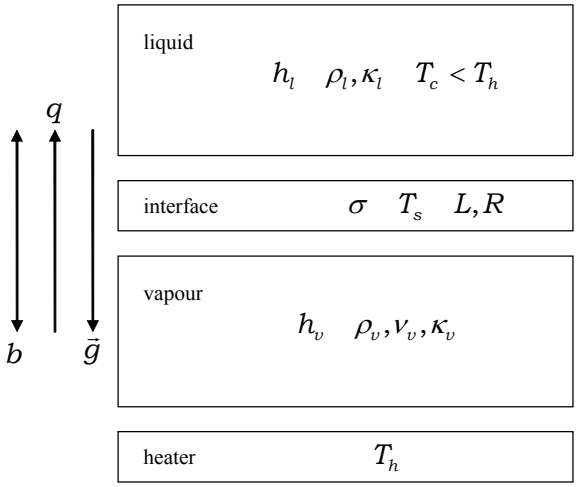

Figure 1: The system configuration and parameters.

The sketch view of the system configuration and parameters one can see in Fig. 1. On a flat horizontal solid heater surface maintained at a temperature T_h, greater than the liquid saturation temperature T_s, the vapor formed a film having thickness h_v and separating the heater from the liquid layer having thickness h_l. The outer surface of the liquid is maintained at a temperature T_c lower than the saturation temperature. The system is effected by high-normal vibration with a given amplitude of vibration velocity b. The other system parameters are the following: g – the gravity accelaration; ρ_l and ρ_v – the densities of the liquid and the vapour, corresponding; σ – the surface tension coefficient; ν_v – the liquid kinematic viscosity; κ_l и κ_v – the heat conductivity of the liquid and the vapour, corresponding; q – the heat flux of subcooling, L – specific heat of vapour generation, R – the parameter managing the speed of the phase transfer.

Usual values of the parameters for the system "water - water vapor" are the following [6]:

$$g = 981\, cm \cdot s^{-2}$$
$$\rho_l = 0.96\, g \cdot cm^{-3}$$
$$\rho_v = 0.6 \cdot 10^{-3}\, g \cdot cm^{-3}$$
$$\eta_v = \rho_v \nu_v = 1.26 \cdot 10^{-4}\, g \cdot cm^{-1} \cdot s^{-1}$$
$$\sigma = 59\, dyn \cdot cm^{-1}$$

$$\kappa_l = 6.8 \cdot 10^4 erg \cdot cm^{-1} \cdot s^{-1} \cdot \mathrm{K}^{-1}$$
$$\kappa_v = 2.4 \cdot 10^3 erg \cdot cm^{-1} \cdot s^{-1} \cdot \mathrm{K}^{-1}$$
$$L = 2.3 \cdot 10^{10} erg \cdot g^{-1}$$
$$R = 5.5 \cdot 10^{-1} g \cdot cm^{-2} \cdot s^{-1} \cdot \mathrm{K}^{-1}$$

It's easy to show that the heights of stable layers of the liquid and the vapour – h_l и h_v, the heat flux of subcooling q, and the temperatures T_h, T_c и T_s are related by the statements:

$$h_v = \frac{H}{\frac{\kappa_l (T_s - T_c)}{\kappa_v (T_h - T_s)} + 1}, \qquad q = \frac{\kappa_v (T_h - T_s) + \kappa_l (T_s - T_c)}{H}$$

Here $H = h_l + h_v$ is the total height of stable layers of the liquid and the vapour.

By the analysis like in [5,6] we get the following equation managing the liquid - vapor interface dynamics in the long-wave and linear approximations:

$$\frac{\partial h}{\partial t} = \frac{h_v^3}{12 \rho_v \nu_v} \left((\rho_l - \rho_v) g \frac{\partial^2 h}{\partial x^2} - \sigma \frac{\partial^4 h}{\partial x^4} \right) - \frac{q}{\rho_v} \frac{\left(\frac{1}{h_l} + \frac{1}{h_v} \right)}{L + R^{-1} \left(\frac{\kappa_l}{h_l} + \frac{\kappa_v}{h_v} \right)} h$$

Here $h = h(x,t)$ is the local height of the vapour layer.

The equation given above allows the completely stable state of the liquid - vapor interface, if $q \geq q_{\mathrm{cr}}$. The value of the critical heat flux of subcooling without vibrations is given by the statement:

$$q_{\mathrm{cr}\ b=0} = \frac{h_v^3}{48 \nu_v} \frac{g^2 (\rho_l - \rho_v)^2 \left(L + R^{-1} \left(\frac{\kappa_l}{h_l} + \frac{\kappa_v}{h_v} \right) \right)}{\sigma \left(\frac{1}{h_l} + \frac{1}{h_v} \right)}$$

The effect of the high-frequency vibrations can be accounted the following replace:

$$(\rho_l - \rho_v) g \frac{\partial^2 h}{\partial x^2} \to (\rho_l - \rho_v) g \frac{\partial^2 h}{\partial x^2} - \frac{1}{2} (\rho_l - \rho_v) \tilde{b}^2 \frac{\partial h}{\partial x}$$

$$\tilde{b} = b \frac{1}{1 - \frac{2\rho_v}{\rho_l + \rho_v} \frac{1}{\exp(2kh_v) - 1}}$$

Here k is the wave number of the liquid - vapor interface perturbations having the form $h(x,t) = h(t) e^{ikx}$. For the case of the thin vapour layer when $kh_v \ll 1$:

$$\tilde{b} \approx -b \frac{\rho_l + \rho_v}{\rho_v} kh_v$$

It can be shown that the effect of high-frequency normal vibration is to reduce the critical heat flux of subcooling, and their effect decreases with decreasing thickness of the vapor film. Significance of the effect may be estimated with the magnitude of the following factors:

$$f_1 = b^2 \frac{\rho_l^2}{\rho_v^2} \frac{h_v^2}{g d_{\sigma g}^3}, \qquad d_{\sigma g} = \sqrt{\frac{\sigma}{\rho_l g}}$$

Thus, when the film thickness is of the order of one hundredth of a centimeter appreciable effect of high-frequency normal vibrations can be expected, in the case if the vibration velocity is of the order a few centimeters per second. When $f_1 \gg 1$.

This work was done under financial support of the program "The integral project of the institutes of SB, UB and FEB RAS № 12-C-1-1006".

References

[1] Straub, J. Boiling heat transfer and bubble dynamics in microgravity, Advances in Heat Transfer, Issue 35, Pages 57-172 (2001)

[2] Marek, R., Straub, J. The origin of thermocapillary convection in subcooled nucleate pool boiling, Int. J. Heat Mass Transfer, Issue 44, Pages 37-53 (2001)

[3] Oka, T., Abe, Y., Mori, Y.H., Nagashima, A. Pool boiling of n-pentane, CFC-113 and water under reduced gravity: parabolic flight experiments with a transparent heater, J. Heat Transfer Trans. ASME, Issue 117, Pages 408-417 (1995)

[4] Abbassi, A., Winterton, R.H.S., The non-boiling vapour film, Int. J. Heat Mass Transfer, Issue 32, Pages 1649-1655 (1989)

[5] Tanaka, H., On the stability of vapour film in pool film boiling, Int. J. Heat Mass Transfer, Issue 31, Pages 129-134 (1988)

[6] Panzarella, C.H., Davis, S.H., Bankoff, S.G., Nonlinear dynamics in horizontal film boiling, J. Fluid Mech, Issue 402, Pages 163-194 (2000)

[7] Wolf, G.H., Dynamic stabilization of the interchange instability of a liquid-gas interface, Phys. Rev. Lett., Issue 24, 9, Pages 444-446 (1970)

[8] Troyon, F., Gruber, R., Theory of dynamic stabilization of the Rayleigh-Taylor instability, Phys. Fluids, Issue 14, 10, Pages 2069-2073 (1971)

Ninth International Conference on
TWO-PHASE SYSTEMS FOR GROUND AND SPACE APPLICATIONS
Baltimore, Maryland, USA, September 22-26, 2014

Diffusive growth of carbon dioxide bubbles

Devaraj van der Meer, Oscar Enríquez, Chao Sun, Detlef Lohse and Andrea Prosperetti

University of Twente, Physics of Fluids Group.
Drienerlolaan 5, 7522NB Enschede, The Netherlands
d.vandermeer@utwente.nl

A gas dissolved in a liquid at a pressure P and temperature T will escape the solution whenever its concentration exceeds the saturation concentration, given by Henry's law: ($c_{sat} = k_H(T)P$). Such a supersaturated state can be induced by a temperature increase or decompression from equilibrium conditions. Gas escapes by diffusion through the free surface or, given appropriate nucleation conditions, by forming bubbles. The latter are most readily observed in the bubbling of a carbonated beverage, but the phenomenon can occur in several other geological, biological and industrial systems such as volcanic magma, underground oil reservoirs, molten polymers, metals and glasses, or the tissues and blood stream of scuba divers undergoing decompression sickness.

We perform an experimental study of the controlled growth of a single CO_2 bubble at high pressure (~ 6 atm) in a low supersaturation regime, which is an order of magnitude smaller than that of a typical carbonated beverage. In this situation, growth is expected to be quasi-static (advection caused by the moving bubble boundary is negligible), and only due to the diffusion of the gas through the liquid phase, with the bubble radius, R, evolving proportionally to $t^{1/2}$ [1].

Despite fulfilling the quasi-static growth condition in our experiments, thanks to a small and accurately controlled supersaturation, we find significant differences with the theoretical predictions for purely diffusive bubble growth. We trace back the differences to several combined effects of the concentration profile around the bubble, which we disentangle in [2]: In the early phase, the interaction with the surface on which the bubble grows slows down the process. In contrast, in the final phase, before bubble detachment, the growth rate is enhanced by the onset of density-driven convection. We show that the bubble growth is affected by prior growth and detachment events, though they are up to 20 minutes apart.

The experiments are performed in the system shown in figure 1 and described in detail in [3]. They start with a water-CO_2 solution equilibrated at pressure P_0 and temperature T_0. We supersaturate the solution through a small isothermal pressure drop. The nucleation site is provided by a hydrophobic micro-cavity of radius 10 μm etched in the center of a small rectangular silicon chip (8 mm by 6 mm) The bubble grows without translating, pinned to the nucleation site, until it reaches a size at which buoyancy forces it to detach. After this, another bubble grows from the same site in a process that can go on for hours.

The spherically symmetric mass transfer problem of a bubble growing in an unbounded, supersaturated gas-liquid solution can be solved analytically [1]. The initial (equilibrium) concentration of gas is given by $c_0 = k_H P_0$, where k_H, Henry's coefficient, is a decreasing function of temperature specific for a given gas-liquid pair. Decreasing the pressure to P_s renders the solution supersaturated. A bubble with an initial radius R_0 is placed in such a supersaturated liquid at $t = 0$. Initially, the concentration is c_0 everywhere, and far from the bubble it remains so at all times. It can be shown that in our experimental conditions, the influence of surface tension is limited to the very first instants of growth. Hence, the gas concentration at the bubble boundary is constant and given by $c_s = k_H P_s$.

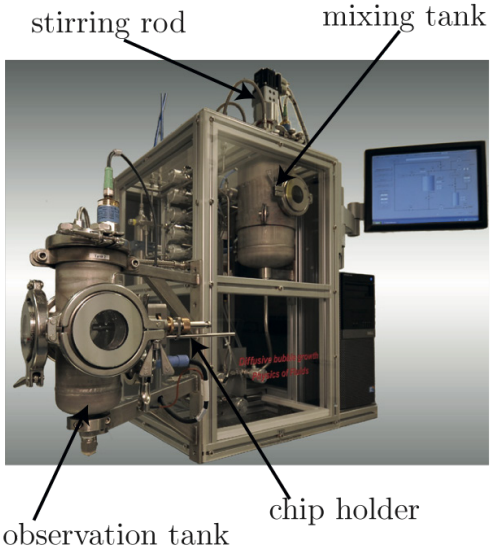

Figure 1: Experimental system. A saturated aqueous solution of CO_2 is prepared in the mixing tank and part of it transferred to a smaller observation tank. Here the mix is supersaturated by means of a small, isothermal pressure drop. In order to avoid residual currents in the observation tank, the liquid is allowed to rest for thirty minutes after filling before the pressure is dropped. Temperature is kept stable by circulating water from a refrigerated cooler through a hose wrapped around the tank. A bubble grows from a hydrophobic micro-pit etched on a silicon wafer, which is held horizontally by the chip holder. The process is imaged through a window in the tank using a long-distance microscope objective with diffuse backlight through a window in the opposite side.

The evolution of the concentration gradient around the bubble in time is found by solving the diffusion equation, and the gas flow induced by this gradient determines the bubble growth rate. In dimensionless form, the asymptotic solution for the evolution of the bubble radius, valid for t >> 1 and R >> 1 is:

$$\bar{R} \approx \left[\gamma + (1+\gamma)^{1/2}\right] x \equiv Sx$$

Here $\gamma = [(c_0\text{-}c_s)/2\pi\rho]^{1/2}$ and $x = [2D(c_0\text{-}c_s)t/\rho R_0^2]^{1/2}$ with $D = 1.97 \times 10^{-9}$ m^2s^{-1} the diffusivity of CO2 in water. As the bubble grows, the radial extension, δ, of the concentration profile around it grows as well. This distance soon becomes of equal size or larger than the bubble itself.

Figure 2 (top) reflects all the differences we find in our experiments with respect to theory. (i) Starting with the red symbols, which denote the first bubble that grows in experiments with different pressure drops, we see that the derivative dR/dx does not rise as fast as the full analytical solution (black solid line) towards the asymptotic value (dotted line). (ii) Furthermore, the experimental values reach a plateau value which is 20–40% lower than the theoretical one. (iii) After some time, when $x \sim 20$, dR/dx starts increasing and eventually surpasses the asymptotic limit. (iv) Finally, the blue symbols, which represent the second bubble that emerges from the nucleation site, initially do not follow the same path as the previous one.

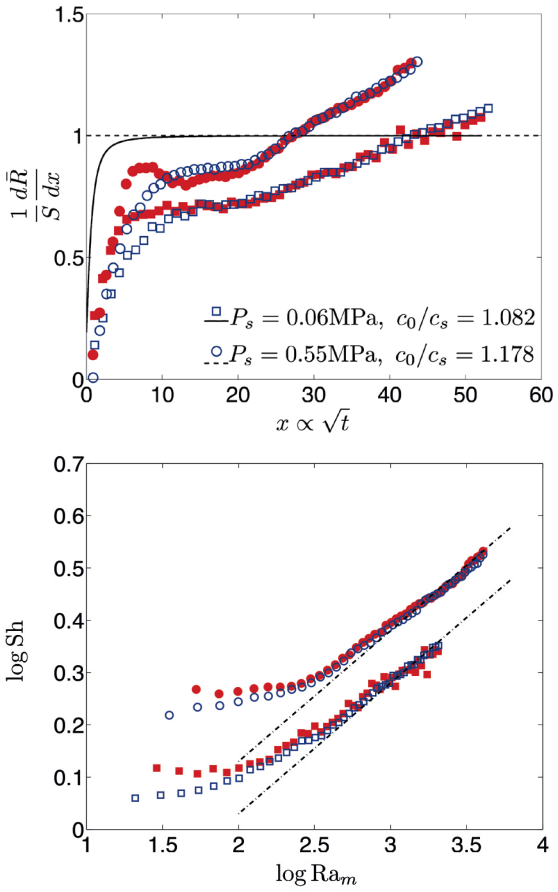

Figure 2: Bubble growth after dropping the pressure from 0.65 to 0.6 MPa (squares) and from 0.65 to 0.55 MPa (circles). The top graph shows the derivative of the radius with respect to $t^{1/2}$ both experimentally (symbols) and theoretically (lines). The local maximum observed for the red circles corresponds to a slight initial overshoot and oscillation of the pressure controller, and therefore is not present in the second bubble. The bottom graph shows the same data re-casted as Sherwood and Rayleigh numbers. The lines here indicate power a law exponent of 1/4, consistent with natural convection around a sphere.

The first two differences can be attributed by the interaction of the bubble with the silicon substrate on which it grows. The latter acts like an obstacle to mass transfer, reducing the effective area through which gas flows into the bubble. The size of the excluded area can be reasonably approximated through geometrical arguments by the intersection of the concentration profile length, δ, with the silicon chip.

The third difference is caused by the onset of density driven convection due to the lower density of the CO_2 depleted fluid that surrounds the bubble compared to the bulk density. This is supported by recasting the data in terms of the dimensionless mass transfer coefficient (Sherwood number, Sh) and the mass transfer Rayleigh number (Ra_m) as shown in Figure 2 (bottom). After an approximately constant value of Sh, the power law relation $Sh \sim Ra^k$ with exponent k = ¼, indicated by the dashed lines, is consistent with natural convection around a sphere.

The last difference, the slower initial growth of the second bubble is due to the different initial condition felt by it. Upon detachment, the first bubble leaves behind a region with a smaller CO_2 concentration. The extension L of this region can be estimated by reformulating the diffusion problem, introducing a linear concentration profile of length L as initial condition and solving numerically, with L as a fitting parameter used to match the experimental data.

References

[1] P.S. Epstein and M.S. Plesset, On the stability of gas bubbles in liquid-gas solutions, J. Chem. Phys. 18., 1505 (1950)

[2] O.R. Enríquez, C. Sun, D. Lohse, A. Prosperetti and D. van der Meer, The quasi-static growth of CO2 bubbles, J. Fluid Mech., 741, R1 (2014)

[3] O.R. Enríquez, C. Hummelink, G-W. Bruggert, D. Lohse, A. Prosperetti, D. van der Meer and C. Sun, Growing bubbles in a slightly supersaturated solution, Rev. Sci. Instrum., 84, 065111 (2013).

VOID FRACTION MEASUREMENT OF TWO PHASE FLOWS INSIDE MINICHANNELS USING A CAPACITANCE PROBE

F. Creatini[1*], P. Di Marco[1], S. Filippeschi[1], M. Mameli[2]

[1]Università di Pisa, DESTEC, Largo Lucio Lazzarino 2, 56122 Pisa, Italy
[2]Università di Bergamo, Viale Marconi 5, 24044 Dalmine (BG), Italy
[*]Corresponding author: francescocreatini89@gmail.com

1 INTRODUCTION

Void fraction plays a crucial role in characterizing two-phase flows in terms of convective heat transfer coefficients and, moreover, in predicting flow pattern transition. The interest is renewing in recent years due to the development of more accurate measurement techniques. Several void fraction measurement techniques are discussed in literature, depending on the application and whether a volumetric, cross sectional or local measurement is required [1].

A possible measurement technique makes use of an optical sensor in order to detect the variation of the refraction index between the liquid and vapor phases [2, 3]. Another technique employs the variation of the dielectric constant to generate an output voltage signal proportional to the capacitance of the two-phase flow between a couple of electrodes. The technique, hereinafter called capacitance technique, is non intrusive and relatively simple to implement. Furthermore, it is suitable for both volumetric and cross sectional measurement. The available literature data concerning the use of a capacitance probe are mainly focused on two-phase flows inside small diameter tubes [4, 5].

In the present paper the design and implementation of a capacitance probe for void fraction measurement of the two-phase flows inside a tube of capillary dimensions is presented. A preliminary finite element simulation is also performed, showing how the variation of the thickness of the dielectric material separating the two-phase flow from the electrodes, as well as the electrodes aperture, affect the probe capacitance. Finally, a capacitance probe design has been selected based on literature data, finite element simulations and tests.

2 FINITE ELEMENT SIMULATIONS

A finite element simulation has been performed in order to optimize the design of the capacitance sensor in terms of maximum capacitance and linearity of the output voltage signal.

The capacitance between the electrodes is determined by solving the Poisson's equation, once the geometry of the sensor as well as the properties of both the two-phase flow and the dielectric material separating the fluid from the electrodes have been assigned.
The Poisson's equation reads:

$$\mathrm{div}\,(\mathbf{D}) = \rho \qquad (1)$$

where **D** is the electric displacement vector field, and ρ is the charge density. The relative permittivity used in the finite element simulation are and $\varepsilon_r = 80$ and $\varepsilon_r = 1$ for the liquid and vapor phases, respectively.

The thickness of the dielectric material as well as the electrodes aperture is varied in order to investigate their effect on the probe capacitance. A pure slug flow can be assumed a priori in case of a tube of capillary dimension and no attention must be paid to flow pattern identification, as in [5].

The cross sectional local void fraction is defined by the ratio of the cross section of a circular vapor bubble centered along the longitudinal axis of the tube to the total cross section of the tube.

The simulation results are presented in terms of the capacitance of the two-phase flows plotted against the cross sectional local void fraction. The simulation results related to the variation of the electrodes aperture are shown in Figure 1. The results refer to the case without dielectric layer, as shown in Figure 2.

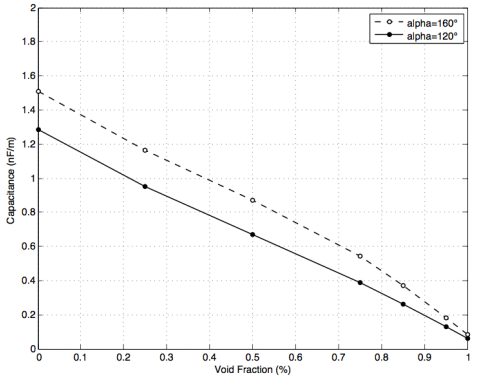

Figure 1: Capacitance for Different Electrodes Aperture.

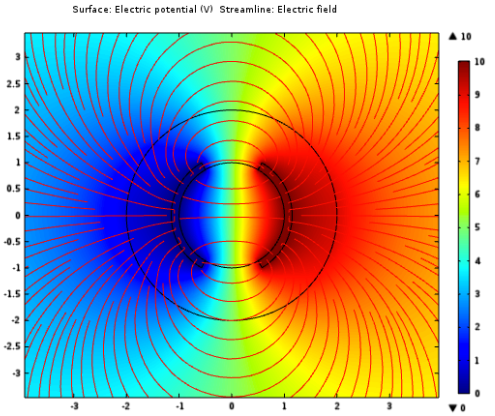

Figure 2: Electric Potential and Electric Field Lines for a Couple of Electrodes.

The results highlight that, by reducing the electrodes aperture the maximum capacitance decreases. Therefore, in order to optimize the performances of a capacitance probe in terms of maximum capacitance, the electrodes aperture shall

be as high as possible. On the other hand, the linearity of the output voltage signal is better for a small electrodes aperture.

Since the interest of the present paper is directed towards the void fraction measurement of two-phase flows inside a tube of capillary dimension, the solution resulting in a more linear output signal is preferable. The solution is even more preferable, when the linearity of the signal is better for a high void fraction, as it is the case.

The simulation results related to the variation of the thickness of the dielectric layer are shown in Figure 3. The results refer to electrodes with an aperture α=120°.

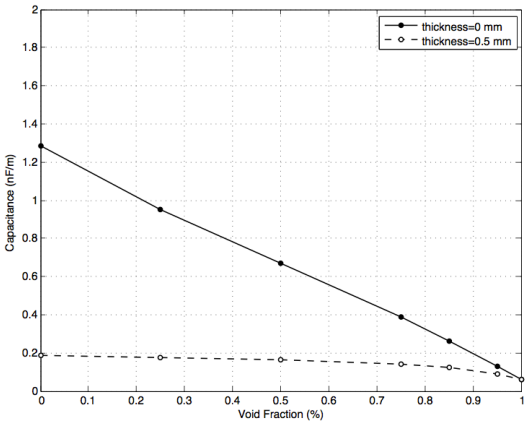

Figure 4: Capacitance for Different Dielectric Layer Thickness.

The maximum capacitance clearly drops by increasing the thickness of the dielectric layer. Clearly, the best performances in terms of maximum capacitance are obtained in the limit of thickness tending to zero.

3 EXPERIMENTAL SETUP

The experimental setup is divided in two parts: a test cell and a recirculation section.

The test cell is the capacitance probe shown in Figure 4. It consists of a couple of concave copper electrodes with an aperture α=120°. The electrodes must be separated from the fluid to prevent electrical discharge. Therefore they are positioned on the external surface of a plastic material tube (ID: 2.0mm, OD: 2.5mm) and kept in place by shrinking a heat sensible material tube.

As shown in Figure 5, the capacitance probe is mounted in series with a glass tube in order to allow the two-phase flow visualization just before it enters the probe. The tested working medium is water. An injection device, constituted by a syringe driven by a stepping motor allows the formation of both static and low velocity (up to 0.1m/s) vapor bubbles. A metering valve regulates the mass flow rate of the pump to the desired value.

The output voltage signal measured by an impedance meter is associated to the void fraction value resulting from the elaboration of the two-dimensional image captured by a high-speed camera and then compared with the results coming from the finite element simulation. Considering the symmetry of the system the volumetric void fraction can be easily calculated by multiplying the two-dimensional image of the bubble by 2π.

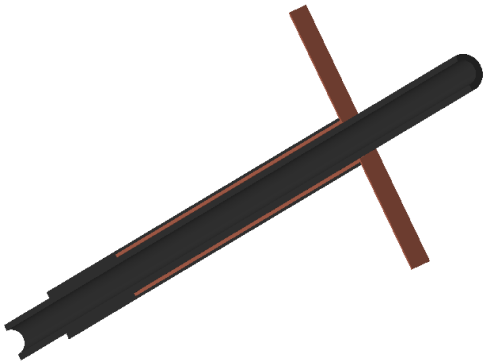

Figure 4: Section View of the Capacitance Probe

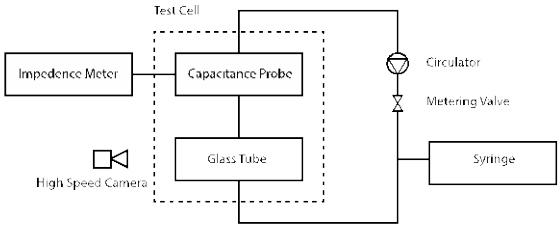

Figure 5: Test Rig

4 CONCLUSIONS AND FUTURE WORK

The finite element simulations highlight the importance of the thickness of the dielectric layer separating the electrodes from the fluid as a design parameter. In particular, the sensitivity of the capacitance probe to void fraction variation increases as the thickness of the dielectric layer is reduced.

Moreover, for an electrode aperture of α=120°, the linearity of the output signal increases at high void fraction, i.e. in the region of greater interest for the present study.

The next step will be to fix the electrodes directly on the internal diameter of the tube, and paint the surface in contact with the two-phase flow with a dielectric material to achieve electrical insulation with a small thickness of material.

REFERENCES

1. [1] J. R. Thome, Engineering data book III, first ed., Wolverine Tube, Inc. publication, 2004
2. [2] N. Abuaf, O. C. Jones Jr. and G. A. Zimmer, Optical probe for local void fraction and interface velocity measurements, Review of Scientific Instruments 49 (1978) 1090
3. [3] B. Stankovic, An experimental study on the local void fraction measurements in large diameter vertical pipes using optical fiber probes, Thesis dissertation, McMaster University, Canada, 1997
4. [4] H. Canière, Flow pattern mapping of horizontal evaporating refrigerant flow based on capacitive void fraction measurements, Doctoral dissertation, Universiteit Gent, Belgium, 2009
5. [5] K. De Kerpel, B. Ameel, C. T'Joen, H. Canière and M. De Paepe, Flow regime based calibration of a capacitive void fraction sensor for small diameter tubes, International Journal of Refrigeration 36 (2013) 390-401

Development of A Long-Distance Loop Heat Pipe for Ground Application

Hosei Nagano and Masataka Mitomi

Department of Aerospace Engineering, Nagoya University
Furo-cho, Chikusa-ku, Nagoya, Aichi, Japan
nagano@nuae.nagoya-u.ac.jp

Loop heat pipes (LHPs) are two-phase heat transfer devices that use evaporation and condensation of a working fluid to transfer heat and use capillary forces developed in fine porous wicks to circulate the fluid [1]. LHPs are being investigated for use as energy-saving cooling devices in electronic equipment, such as laptops. Future applications for LHPs could include smart houses and automobiles, which will need effective ways to use heat gained from the sun during daylight hours and exhaust heat from the engine. To realize such effective methodologies, heat must be transported over distances from a few meters to about ten meters. In this paper, experimental results of long-distance LHPs one-way heat-transport distances from evaporator to condenser of 2m, 4m, and 10m, have been reported.

The LHPs were designed based on a mathematical model [2]. Table 1 shows the geometric characteristics of the three LHPs with one-way heat-transport distances of 2 m, 4 m, and 10 m, respectively. Hereafter, these LHPs are referred to as 2m-LHP, 4m-LHP, and 10m-LHP. The photographs of the LHPs, the evaporator, and the wick are shown in Fig. 1. The LHP is composed of an evaporator, a vapor line, a condenser, a liquid line, and a compensation chamber (CC). A wick which is made of a PTFE porous material is enclosed in the evaporator. The advantage of the plastic wick is that it can reduce conductive heat leak from the evaporator to the CC because of its low thermal conductivity, which results in a lower loop-operating temperature. The three LHPs have the same evaporator and condenser. The condenser was cooled by natural air. Ethanol was used as the working fluid. Two aluminum heater blocks were attached to the evaporator to simulate instrument mass. To reduce heat losses, the LHPs, except for the condenser, were covered with thermal insulation. Temperatures in the LHPs were measured by T-type thermocouples.

Table 1: Specification of LHPs

Evaporator (SUS304)		Vapor Line(SUS304)	
Length[mm]	160	Length[m]	2, 4, 10
O.D.[mm]	21	O.D.[mm]	6.4
I.D.[mm]	19	I.D.[mm]	4.6
Wick(PTFE)		Liquid Line(SUS304)	
Length[mm]	150	Length[m]	2, 4, 10
O.D.[mm]	19	O.D.[mm]	3.2
I.D.[mm]	13	I.D.[mm]	1.8
Porosity	0.34	Condenser(SUS304)	
Pore size [μm]	1.2	Length[m]	3
CC(SUS304)		O.D.[mm]	6.4
Length[mm]	75	I.D.[mm]	4.6
O.D.[mm]	50	Working Fluid	
I.D.[mm]	44	Inventory[mL]	125, 260, 283
Additional CC		Material	Ethanol
Size[cc]	150		

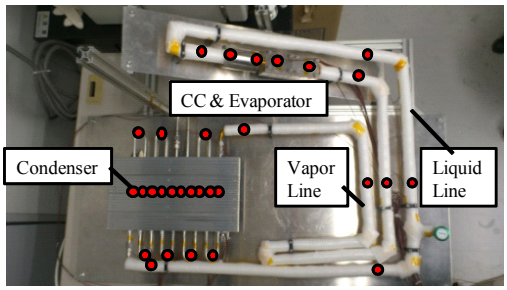

(a) 2m-LHP

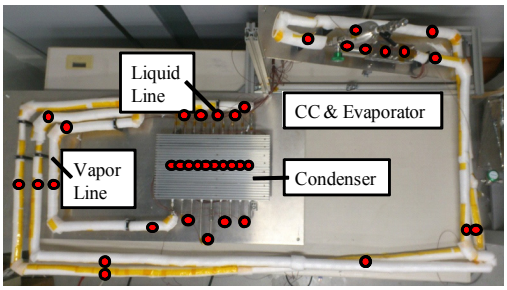

(b) 4m LHP

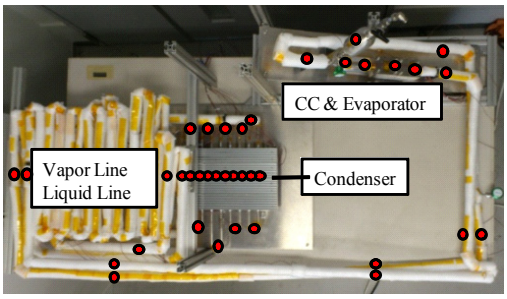

(c) 10m-LHP

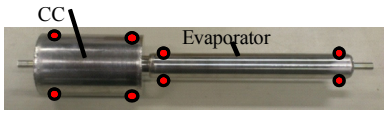

(d) CC & Evaporator

(e) PTFE Porous Wick

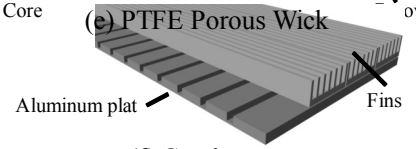

(f) Condenser

Figure 1: Photos of LHPs

Experiments were conducted on the 2m-LHP, 4m-LHP, and 10m-LHP at the heat-load increments of 20 W, starting from 40 W. The maximum heat load of the three LHPs was 160 W. In this case, the heat flux was 3.33 W/cm^2. Figure 2 compares the temperatures at the evaporator, CC, and the

outlet of the liquid line as the functions of the applied load for each LHP. The overall evaporator and CC temperatures generally decrease in the order 2m-LHP, 4m-LHP, and 10m-LHP. However, at high heat loads, the evaporator temperatures of 4m-LHP were lower than those of 10m-LHP. There are two possible reasons for this. First, the heat loss from the vapor and liquid lines through the thermal insulation increased as the heat-transport distance was extended. Therefore, the temperature of the outlet in the liquid line (Tll-out) decreased, and the CC temperature of the 10m-LHP was the lowest of the three LHPs. Second, the total pressure loss increases as the transport distance increases. Therefore, the temperature difference between the evaporator and the CC in the 10m-LHP was the highest of the three LHPs.

Figure 3 shows the thermal resistances in the three LHPs, where thermal resistance is defined by

$$R_{LHP} = \frac{\overline{T}_{ev} - \overline{T}_{con}}{Q_{load}} \qquad (1)$$

and $\overline{T}_{ev}$ and $\overline{T}_{con}$ are the average temperatures of the evaporator and condenser, respectively. The values of $\overline{T}_{con}$ of 2m-LHP, 4m-LHP, and 10m-LHP at 160 W were 80.4 °C, 73.0 °C, and 64.7 °C, respectively, because the heat loss from the vapor and liquid line to ambience increased as heat transport distance was extended. The values of $\overline{T}_{ev}$ of 2m-LHP, 4m-LHP, and 10m-LHP were 91.4 °C, 81.9 °C, and 85.3 °C, respectively. The reason that the evaporator temperature of 10m-LHP was higher than that of 4m-LHP is as mentioned above. Therefore, the thermal resistances of 2m-LHP, 4m-LHP, and 10m-LHP at maximum heat load were 0.073 K/W, 0.063 K/W, and 0.13 K/W, respectively. Figure 3 also shows the magnitudes of the two-phase regions in the condenser for the three LHPs. The two-phase region (L2f) was measured as the ratio of the length of the entire condenser to the length where the temperature did not change much. The figure shows that 10m-LHP had the highest thermal resistance and the lowest two-phase region of the three LHPs. This was because heat loss from the vapor line through the thermal insulation increased when the heat-transport distance increased. However, at the maximum heat load, the thermal resistance in 4m-LHP was lower than that in the 2m-LHP and the two-phase region of the 4m-LHP was higher. This was because, as shown in Fig. 2, the evaporator temperature in the 4m-LHP was lower than that in the 2m-LHP because the CC temperature was lower. If the evaporator temperature is low, the temperature difference between the vapor and ambience decreases; therefore, the thermal resistance decreases, and the two-phase region increases.

Figure 4 compares the calculated and measured temperature distributions for the 2m-LHP, 4m-LHP, and 10m-LHP operating at heat loads of 160 W. The calculated temperature distributions are almost in good agreement with the measured ones implying that this mathematical model could calculate the pressure distribution, temperature distribution, and the amount of the heat transportation in the LHP. However, the measured and calculated distributions for the liquid line temperatures differ for the 4m-LHP. This is because the mathematical model assumed that the fluid in the liquid line is always liquid; however, in the experiments for the 4m-LHP, the two-phase region at 160 W exceeded the capacity of the condenser.

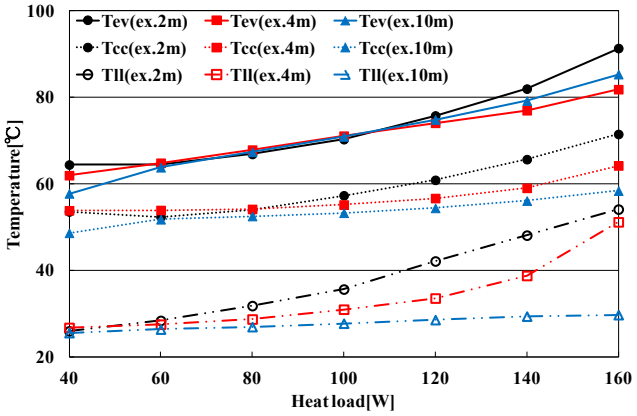

Figure 2: Effects of heat load on evaporator temperatures (Tev), CC temperatures (Tcc), and outlet liquid line temperatures (Tll-out) for the three LHPs.

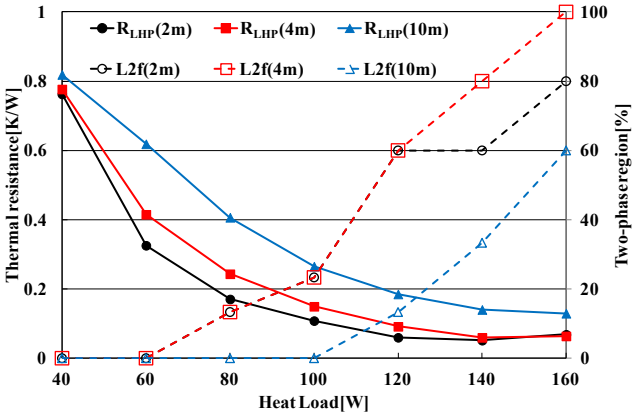

Figure 3: Effects of heat load on thermal resistance for the three LHPs.

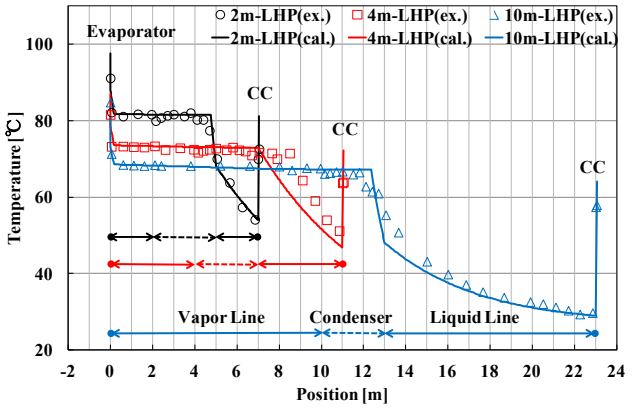

Figure 4: Comparisons of experimental (symbols) and computational (lines) temperature distributions for the three LHPs at a heat load of 160 W.

References

[1] J. Ku, Operating characteristics of loop heat pipes, International Conference on Environmental System, SAE Paper, 1999-01-2007 (1999).

[2] T. Kaya and T. Hoang, Mathematical modeling of loop heat pipes and experimental validation, Journal of thermophysics and heat transfer, 13, 3 314-320 (1999).

Ninth International Conference on
TWO-PHASE SYSTEMS FOR GROUND AND SPACE APPLICATIONS
Baltimore, Maryland, USA, September 22-26, 2014

Electrohydrodynamically Driven Two-Phase Heat Transport Devices for Space and Ground Applications

Jamal S. Yagoobi

Worcester Polytechnic Institute
Worcester, Massachusetts, USA
jyagoobi@wpi.edu

Electrohydrodynamic (EHD) pumping methods rely on the interaction between electric fields and the flow fields in a dielectric fluid via Coulomb force. There are three types of EHD pumps: conduction pumping, induction pumping, and ion-drag pumping. These methods differ in the manner of generating the non-zero net charge density that is required for a Coulomb force to exist [1]. Ion-drag pumping relies on the injection of ions into the liquid from sharp liquid/solid interfaces, while induction pumping uses an AC travelling wave to attract or repel charges induced in the liquid due to gradients or discontinuities of electric conductivity, for example due to temperature gradients [1]. Conduction pumping produces a non-zero charge density in "heterocharge layers" near the electrodes through bulk electric conduction through the liquid. As a result, the problems of ion-drag pumping (specifically, degradation of the electrical properties of the working fluid and potentially hazardous operation) and induction pumping (specifically, the need for a gradient in electric conductivity) can be avoided while still maintaining the ability to pump using the Coulomb force [2].

For a neutral species, *AB*, and its positive and negative ions, A^+ and B^-, there is reversible process of dissociation and recombination:

$$AB \leftrightarrow A^+ + B-$$

Under conditions of low electric field intensity, the dissociation and recombination rates are in dynamic equilibrium [3]. Any ions that are present in the fluid, for instance due to impurities, will be drawn along lines of constant electric field, attracted to the charges of opposite polarity on the electrode surface. This rearrangement of charges causes an electric double layer, with charges of one polarity on the solid electrode surface and charges of opposite polarity on the liquid side of the surface. This layer is further divisible into two sub-regions. The first region is a compact layer, typically about 0.5 nm thick, where a layer of ions is strongly attracted to the surface and immobilized as a result. The second region is the diffuse layer, where the ionic concentration gradually decreases from that of the compact layer to that of the liquid bulk and where ions remain mobile.

When the electric field exceeds a certain threshold value (on the order of 1 kV/cm, depending on the working fluid properties [4]), the rate of dissociation begins to exceed the rate of recombination, with the difference in rates further increasing with an increase in electric field intensity. Therefore, an additional layer forms, known as the heterocharge layer, in which the dissociation and recombination processes are not in equilibrium. Atten and Seyed-Yagoobi [2] describe these heterocharge layers as characteristic of dielectric liquids having sufficiently low electrical conductivity, below about 10^{-7} S/m; generally the case for non-polar or mildly-polar fluids. The charges in the heterocharge layer are attracted to the nearby electrode that is of opposite polarity, thereby causing a propensity for bulk fluid flow. The need for low electrical conductivity fluids relates to the Debye length, λ_D, which can be viewed as a typical length of diffusion of the ions during the relaxation time of the space charge, $\tau=\epsilon/\sigma_e$. If the electrical conductivity is too high, the heterocharge layers have a thickness on the order of λ_D and the electric field intensity in the heterocharge layers greatly exceeds that of in the bulk. By contrast, the Debye length in a low conductivity fluid will be much larger and the field in the heterocharge layer will be lower than the applied field in the liquid bulk. Therefore, the thickness of the heterocharge layers is dependent not on the diffusion process (which is now negligible), but on the drift of the ions [2].

Neutral species are continuously dissociating everywhere within the fluid; similarly, dissociated ions are continuously recombining. However, the rate at which these processes occur has a strong local dependence corresponding to the local variation of electric field intensity and concentration of positive, negative, and neutral species. Dissociation can only occur when there are neutral species present to dissociate. Similarly, recombination requires a pair of ions of opposite polarity. Overall, the dissociation and recombination rates are still at equilibrium, but the heterocharge layers can exist because of a local non-equilibrium. The attraction of charges to the electrodes occurs regardless of whether or not there is a net flow. An ion is continuously subject to many different forces including the Coulomb force and hydrodynamic phenomena such as fluid convection and local pressure gradients. Therefore, fluid circulation can occur near the electrodes due to the continued, impingement-like attraction of ions to the electrode and a subsequent hydrodynamic force that propels the ion away from the electrode. With proper asymmetric design of the electrode geometry, there can also be a production of net flow whereby the attraction of charges of one polarity to one electrode is not completely cancelled-out by the attraction of

the opposing charges to the other electrode (see Figure 1).

This presentation will illustrate the EHD conduction pumping mechanism and its resultant transport characteristics. Specifically, the heat and mass transport resulting from EHD conduction pumping of a dielectric fluid in macro-, meso-, and micro-scales in the presence and absence of phase change (liquid/vapor) will be described [e.g., 4 – 6]. Furthermore, the recent results of two-phase heat transport experiments that were conducted on board variable-gravity parabolic flights will be presented [e.g., 7]. As an example, Figure 2 illustrates the single phase liquid flow rate generated by a micro-scale heat transport device driven by EHD conduction pumping confirming the applicability of this technology in the absence of gravity [7].

From an application perspective, the EHD conduction pumping technology is expected to provide technological advances that will support NASA's various missions. EHD pumps are simple in design, light weight, non-mechanical, free of vibrations and noise, and they allow for effective active control of heat transfer and mass transport. EHD pumps require minimal electric power to operate. The resultant heat transport capacity is typically three orders of magnitude larger than the electric input power.

References

[1] Seyed-Yagoobi, J., Electrohydrodynamic Pumping of Dielectric Liquids, Journal of Electrostatics, vol. 63, no. 6–10, pp. 861-869 (2005).

[2] Atten, P. and Seyed-Yagoobi, J., Electrohydrodynamically Induced Dielectric Liquid Flow Through Pure Conduction in Point/Plane Geometry, IEEE Transactions on Dielectrics and Electrical Insulation, Vol. 10, No. 1, pp. 27–36 (2003).

[3] Jeong, S. I. and Seyed-Yagoobi, J., Experimental Study of Electrohydrodynamic Pumping through Conduction Phenomenon, Journal of Electrostatics, Vol. 56, No. 2, pp. 123–133 (2002).

[4] Pearson, M. R. and Seyed-Yagoobi, J., Advances in Electrohydrodynamic Conduction Pumping, IEEE Transactions on Dielectrics and Electrical Insulation, Vol. 16, No. 2, pp. 424-434 (2009).

[5] Pearson, M. R. and Seyed-Yagoobi, J., EHD Conduction Driven Single- and Two-Phase Flow in Micro-Channels with Heat Transfer, ASME Journal of Heat Transfer , Vol. 135, pp. 101701-1 to 10 (2013).

[6] Yazdani, M. and Seyed-Yagoobi, J., Electrically Induced Dielectric Liquid Film Flow Based on Electric Conduction Phenomenon, IEEE Transactions on Dielectrics and Electrical Insulation, Vol. 16, No. 3, pp. 768-777, (2009).

[7] Patel, V.K., Robinson, F., Seyed-Yagoobi, J. and Didion, J., Terrestrial and Micro-Gravity Experimental Study of Micro-Scale Heat Transport Device Driven by Electrohydrodynamic Conduction Pumping, IEEE Transactions on Industry Applications, Vol. 49, No. 6, pp. 2397 – 2401 (2013).

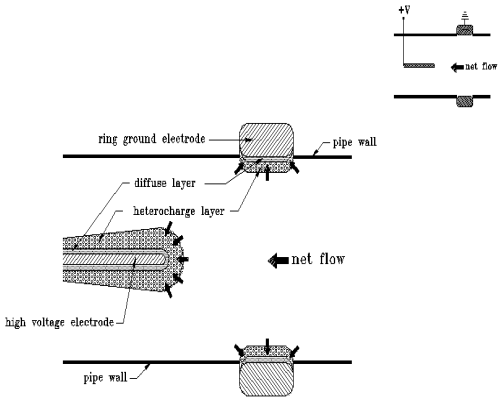

Figure 1. Illustration of EHD conduction pumping phenomenon

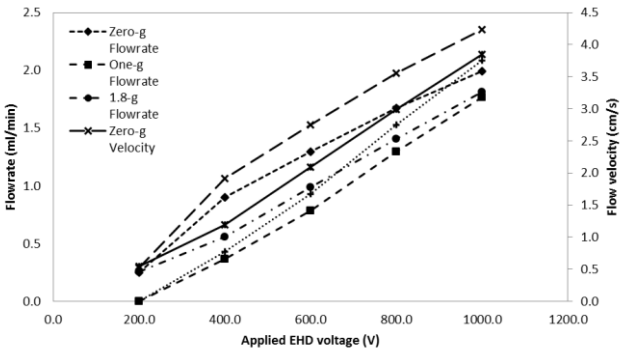

Figure 2. EHD pump flow rate and flow velocity vs. applied EHD voltage at different levels of gravity [7]

Condensation heat transfer and pressure drop of R32/R1234ze(E) mixture inside a single circular microchannel

Marco Azzolin, Stefano Bortolin, Davide Del Col

University of Padova, Dipartimento di Ingegneria Industriale
Via Venezia 1, 35131 Padova, Italy
Corresponding author: Davide Del Col - E-mail: davide.delcol@unipd.it

An experimental investigation of local heat transfer coefficient during condensation and frictional two-phase pressure drop for the R32/R1234ze(E) mixture at 46/54% mass composition in a 0.96 mm diameter microchannel is presented. Tests were conducted at different mass velocities, at a mean saturation temperature of 41°C. Experimental data were then compared against available correlations.

In the literature very limited data of condensation of mixtures in minichannels is available. Miyara et al. [1] investigated the heat transfer coefficient during condensation and evaporation of the R1234ze(E)/R32 mixture. Experiments were carried out for two different mass fractions 0.55/0.45 and 0.70/0.30, in a smooth horizontal tube with 4.35 mm internal diameter, at mass velocities ranging from 49 to 445 kg m^{-2} s^{-1}. They found that the condensation heat transfer coefficient of the blend is comparable with that of R410A. Wang et al. [2] presented condensation heat transfer data inside a horizontal smooth tube with an inner diameter of 4 mm and mass fluxes between 100 and 300 kg m^{-2} s^{-1}, for the R1234yf/R32 mixture, at two different compositions (0.52/0.48, 0.77/0.23 by mass). The test section is divided in five sub-sections and average heat transfer coefficients in each sub-section are determined.

Experimental data presented in this work were carried out in the test rig located at the Two Phase Heat Transfer Lab of the University of Padova. The experimental apparatus (Fig. 1) consists of a primary refrigerant loop where the sub-cooled refrigerant exiting the post-condenser is sent through a Coriolis-effect mass flow meter and then vaporized in a tube-in-tube heat exchanger. The superheated vapor can be sent through the test section for condensation heat transfer investigation or, in parallel, through the test section for pressure drop measurement. At the inlet of each test section, to achieve the desired saturation conditions, pre-conditioning sectors are used. The heat transfer test section is made from a copper rod having an internal hydraulic diameter of 0.96 mm with an inner surface roughness *Ra* equal to 1.3 µm. In this test section 28 thermocouples are installed: 15 in the cooling water and 13 embedded in the wall. The local heat transfer coefficients are measured from the saturation temperature, the local wall temperature measurements and the coolant temperature profile along the measuring channel. A detailed description of the test section and of the experimental apparatus is given in Matkovic et al. [3]. Pressure drop tests are performed under adiabatic two-phase flow in a dedicated test section, made from the same copper rod. The measuring sector includes two pressure ports connected to the copper channel.

Considering the mixture R32/R1234ze(E) very limited data on thermophysical properties are available. Akasaka [4] presented thermodynamic property models for this mixture and in the present work the mixture properties are calculated using REFPROP 9.1 with the model suggested by Akasaka [4]. At a mass composition of 46% for R32 and 54% for R1234ze(E), the temperature glide displayed at 1.75 MPa is about 8.2°C. The composition after the test runs was measured using a gas-chromatograph with an experimental uncertainty of ±0.001 by mass.

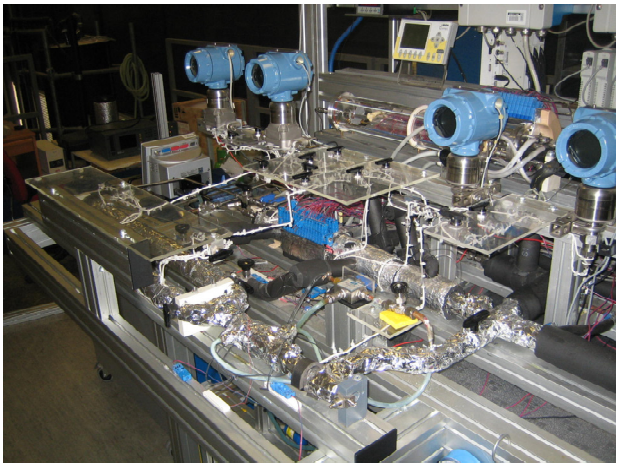

Figure 1: Experimental apparatus.

The experimental technique for the measurement of the heat transfer coefficient for pure fluids is reported in Matkovic et al. [3]. It is worth noting that for a refrigerant mixture, due to the temperature glide, the heat removed from the refrigerant blend includes both latent heat from phase change and sensible heat from cooling. As reported in Cavallini et al. [5] the isobaric change in enthalpy Δh_{cond} is:

$$\Delta h_{cond} = h_{lg}\Delta x + (1-x)\, c_{pl}\, \Delta T_{sat} + x\, c_{pg}\, \Delta T_{sat}$$

where the values of the differential latent heat h_{lg}, specific heat capacities of liquid c_{pl} and vapor c_{pg} depend on the saturation temperature and on the local liquid and vapor compositions. The saturation temperature T_{sat} is related to the vapor quality using:

$$T_{sat} = T_{dew} - \Delta T_{GL}\left(1 - f(x)\right)$$

where ΔT_{GL} is the temperature glide and $f(x)$ is an empirical function of the vapor quality that varies from 0 to 1. The condensation test runs are performed with mass velocity ranging from 150 to 800 kg m^{-2} s^{-1} at a mean saturation temperature of 41°C. Results show that the heat transfer coefficients for the mixture in the whole range of test

conditions are lower than those of the pure fluids: the condensation performance of pure R1234ze(E) is higher than that of the mixture by 14 % at 800 kg m^{-2} s^{-1}, by 21% at 400 kg m^{-2} s^{-1} and by 35% at 200 kg m^{-2} s^{-1}. The heat transfer penalization due to the additional mass transfer resistance is clear in Fig. 2, in which the heat transfer coefficient at two mass velocities and two vapor qualities for the pure fluids and the blend are reported. In the case of the mixture, when complete mixing in the liquid and in the vapor phase is reached and overall equilibrium is maintained, models for pure vapor condensation can be used coupled with a correction for the mass transfer resistance. So the Cavallini et al. [6] model to predict condensation heat transfer coefficient can be applied to mixtures using the Bell and Ghaly [7] and Silver correction [8]. The Cavallini et al. [6] model, with Silver-Bell-Ghaly correction, is able to predict the experimental data with an absolute deviation of about 9% and a standard deviation of 12%.

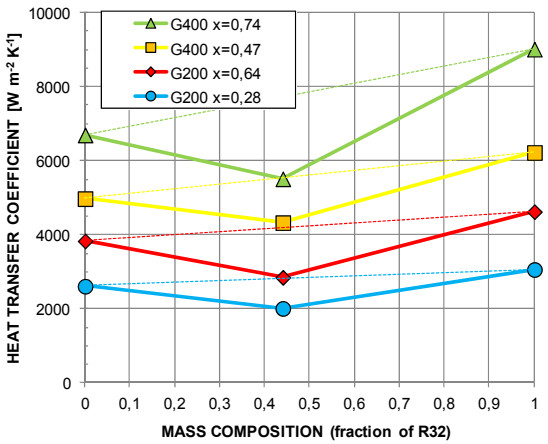

Figure 2: Experimental local heat transfer coefficient for the refrigerant mixture R32/R1234ze(E) and its pure components. Dashed lines refer to an ideal linear behavior between coefficients of the two pure fluids.

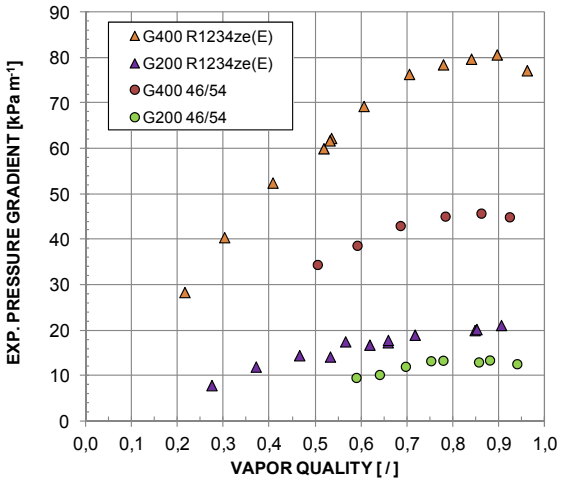

Figure 3: Experimental frictional pressure gradient versus vapor quality for the mixture R32/R1234ze(E) and the pure refrigerant R1234ze(E).

Adiabatic two-phase frictional pressure drop tests have been carried out in the dedicated test section at a pressure of about 1.78 MPa (41°C mean saturation temperature) and at 200 and 400 kg m^{-2} s^{-1} mass velocities. In Fig. 3 the experimental pressure gradient is reported and compared with that of pure R1234ze(E) taken in the same test section at a saturation temperature of about 40°C. For vapor quality between 1 and 0.5, when comparing the frictional pressure drop of the mixture to that of pure R1234ze(E) a drastic decrease is observed. The two-phase frictional pressure gradient of R1234ze(E) results higher by 75% at 400 kg m^{-2} s^{-1} and higher by 60% at 200 kg m^{-2} s^{-1} if compared to the 46/54 % mixture.

References

[1] Miyara, A., Anowar Hossain M.D., Afroz, H.M.M., Shagawa K., Condensation and evaporation heat transfer of R1234zE(E)/R32 mixture in a horizontal smooth tube, 4th IIR, Delft, (2013).

[2] Wang, L., Dang, C., Hihara, E., Experimental and Theoretical Study on Condensation Heat Transfer of Nonazeotropic Refrigerant Mixture R1234yf/R32 inside a Horizontal Smooth Tube, Proc. of Int. Ref. Air Cond. Conf., Purdue, (2012).

[3] Matkovic, M., Cavallini, A., Del Col, D., Rossetto, L., Experimental study on condensation heat transfer inside a single circular minichannel, Int. J. Heat Mass Transfer 52, pp. 2311-2323, (2009).

[4] Akasaka, R., Thermodynamic property models for the difluoromethane (R-32) + trans-1,3,3,3-tetrafluoropropene (R-1234ze(E)) and difluoromethane + 2,3,3,3-tetrafluoropropene (R-1234yf) mixtures, Fluid Phase Equilibria 358, pp.98-104, (2013).

[5] Cavallini, A., Censi, G., Del Col, D., Doretti, L., Rossetto, L., Zilio, C., Analysis and prediction of condensation heat transfer of the zeotropic mixture R-125/236ea, Proc. of IMECE'00, Orlando, Florida, (2000).

[6] Cavallini, A., Censi, G., Del Col, D., Doretti, L., Matkovic, M., Rossetto, L., Zilio, C., Condensation in Horizontal Smooth Tubes: A New Heat Transfer Model for Heat Exchanger Design, Heat Trans. Eng. 27 (8), pp.31-38, (2006)

[7] Bell K.J., Ghaly M.A., An approximate generalized design method for multicomponent / partial condenser, AIChE Symp. Ser. 69, pp. 72-79, (1973).

[8] Silver L., Gas cooling with aqueous condensation, Trans. Inst. Chem. Eng 25, pp. 30-42, (1947).

Acknowledgement

The support of ESA through the project ENCOM-2 is greatly acknowledged.

Condensation on Asymmetric Microstructures- Effect of Orientation, Microstructure Size and Gravity

Shashank Natesh[1], Vinod Narayanan[2*], Sushil Bhavnani[3]

[1, 2] Oregon State University, Corvallis, OR 97331, USA
[3] Auburn University, Auburn, AL 36849, USA

Advances in the field of space technology and the aerospace industry have resulted with an increased need of novel phase-change rejection techniques. Surface microstructures with repeated asymmetric topology have been employed previously for pumping the working fluid in a preferential direction in the boiling regime [1, 2]. A similar method of propelling the condensate is developed in this paper. Such microstructure topology could potentially be located in the inner walls of condensers and evaporators towards creating a pump-less and passive thermal management loop. Figure 1 shows a asymmetric ratchet with the liquid condensate motion. The hypothesis is that, because the advancing angle is to be maintained on both the steep and shallow slopes of the ratchet, the condensate rises at a higher rate along the steeper slope, thus causing a preferential direction of motion.

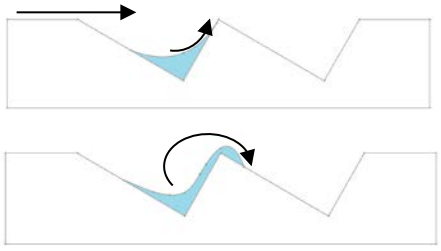

Figure 1: Motion of liquid film over an asymmetric ratchet. The arrows depict the direction of preferential motion of the condensate.

In this parametric CFD simulation study, a two-dimensional numerical model is developed to predict the growth of the liquid condensate and the associated heat transfer rate on an asymmetric ratchet. The asymmetry is introduced in the ratchet surface through two surfaces inclined at 30° and 60° to the horizontal respectively. In order to model the growth of the liquid condensate along the ratchet, is it necessary to capture the liquid-vapor interfacial effects occurring during the condensation process. The volume-of-fluid (VOF) method is used to track the liquid-vapor interface and the mass and energy exchange terms for the condensation process are deduced from the Hertz-Knudsen equation [3]. Surface tension acts as a volumetric source in the momentum equation. The mass and heat transfer from vapor to liquid phase only occurs across the liquid-vapor interface. A phase change model that allows accurate modeling of the vapor and liquid mass and energy exchange at the interface in addition to accurately predicting the preferential growth of the liquid condensate along the ratchet walls is developed. A code with user-defined functions is written to calculate all the source terms for the governing equations. The following equation for the mass condensation rate ($\dot{m}$") is applied across the liquid vapor interface:

$$\dot{m}" = \frac{2\sigma_c}{2 - \sigma_c}\left[\left(\frac{P_v}{(2\pi R T_v)^{1/2}}\right) - \left(\frac{P_{int}}{(2\pi R T_{int})^{1/2}}\right)\right]. \quad (1)$$

For condensation to occur, the temperature of the liquid-vapor interface, T_{int} (or the condensate surface facing the vapor) must be less than the saturation temperature of the vapor at pressure P_v. This temperature difference at the interface drives the condensation process and is given as

$$T_{sat}(P_v) - T_{int} = \frac{\dot{m}" \, h_{lv}}{\left[\frac{2\sigma_c}{2 - \sigma_c}\left(\frac{1}{2\pi R}\right)^{1/2}\left(\frac{\rho_v {h_{lv}}^2}{T_{sat}^{3/2}}\right)\right]}, \quad (2)$$

In Eq. 2, ρ_v, h_{lv} and T_{sat} are the vapor density, latent heat of condensation of the fluid and the saturation temperature at the vapor pressure respectively. The entire mathematical formulation is mentioned in detail in the work by Hardt & Wondra [4]. One-dimensional Stefan problems, axisymmetric bubble growth in a superheated liquid and a laminar condensation process over a symmetric ratchet surface are solved as benchmark tests to validate the numerical phase change model. Asymmetric ratchets of two different pitch sizes, 80 μm and 2.4 mm, are considered for the numerical simulations with FC-72 as the working fluid. A hydrophilic ratchet surface-fluid combination is assumed for all the simulations (contact angle = 10°). The 2.4 mm pitch ratchet geometry is further compared under two different orientations, viz., right- side-up (RSU) and up-side-down (USD), as shown in Fig. 2, to delineate the effects of gravitational force on the condensate growth. The effect of the size of the ratchet on the condensate growth is also explained.

Figure 2: Ratchet configurations with gravity acting downwards: right side up (left) and upside down (right).

Using the periodicity of the ratchet topology, a periodic boundary condition is imposed at the crests of the ratchet. Figure 3 shows the computational domain with the relevant boundary conditions. A small liquid droplet of radius equal to 1/20 of the pitch of the ratchet is placed at the trough of the ratchet to initiate the condensation process. A precursor (natural convection) solution is obtained for each case before introducing this droplet embryo.

Results from the 80μm pitch ratchet show a preferential motion of condensate along the ratchet. Temperature contours (in K), shown in Fig. 4, show the evolution in temperature along both surfaces of the ratchet. The thinning of the interface along both walls is apparent. Velocity vectors are depicted in Fig. 5 to understand this preferential motion and growth of the liquid condensate. It is seen that the mass influx of the vapor phase is large at the steeper wall accompanied by a strong inflow of vapor perpendicular to the liquid-vapor interface. The time-evolution of the interface position on each wall normalized by the length of the wall is a measure of the interface velocity at that wall and is plotted in Fig. 6. The condensate film grows quickly along the steeper wall and initiates a preferable growth along the ratchet. The 2.4 mm pitch ratchet show similar results for the condensate growth and heat transfer proving that scaling the ratchet does not inhibit its ability to move the fluid in a preferential direction. Figure 7 shows the contours of volume fraction of liquid at four time instants during the growth process. The liquid condensate has first propelled to the crest of the steeper wall showing a favorable motion of liquid films over larger ratchets. The gravitational effects are also studied in the 2.4 mm pitch ratchet and results show similar fluid behavior for the RSU and USD ratchets. Figure 8 shows the plot of interface position vs. time for both the RSU and USD ratchets. Despite slight changes in growth rates on the faces, preferable condensate rise is observed for both orientations.

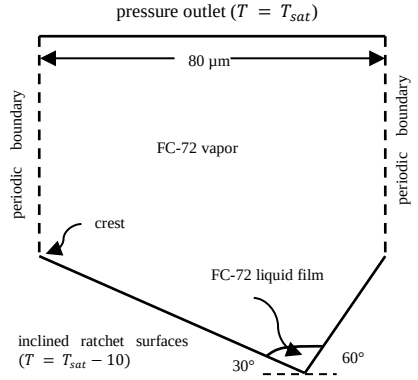

Figure 3: Computational domain showing pertinent boundary conditions for the ratchet problem.

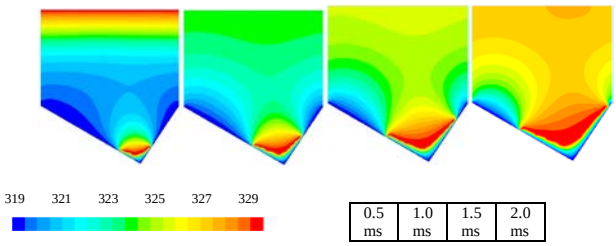

Figure 4: Evolution of fluid temperature in the domain.

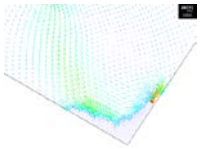

Figure 5: Velocity vector plot to depict the large vapor inflow on the steeper ridge of the ratchet.

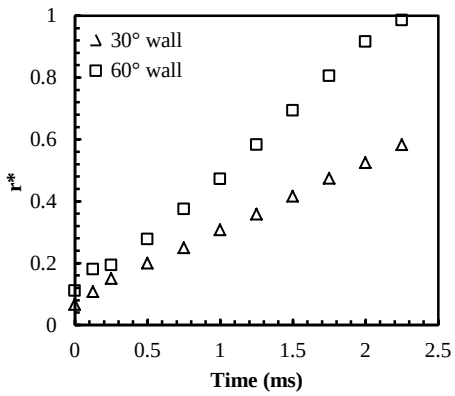

Figure 6: Rate of interface motion along the ratchet surfaces.

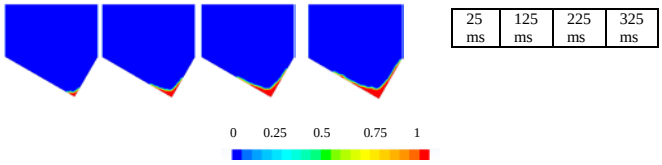

Figure 7: Contours of liquid volume fraction showing preferential motion of the liquid film over the right-side-up 2.4 mm pitch ratchet.

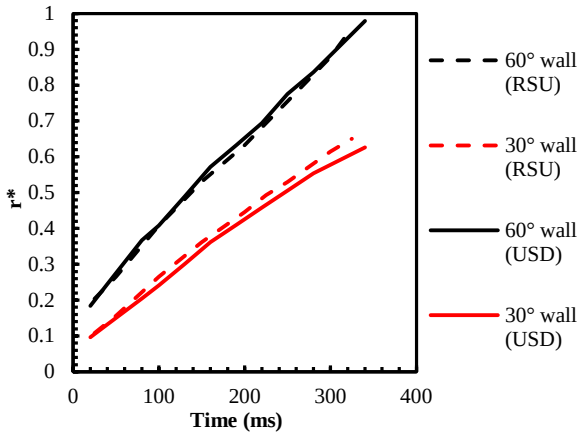

Figure 8: Plot of r* vs. time for RSU and USD ratchets.

References

[1] H. Linke, B. J. Alemán, L. D. Melling, M. J. Taormina, M. J. Francis, C. C. Dow-Hygelund, V. Narayanan, R. P. Taylor, and A. Stout. Self-propelled Leidenfrost droplets. *Physical Review Letters*, 96:154502 (2006).

[2] F. Kapsenberg, L. Strid, N. Thiagarajan, V. Narayanan, S. H. Bhavnani. On the Lateral Fluid Motion during Pool Boiling via Preferentially Located Cavities. *Aplied Physics Letters*, Vol. 104, 154105 (2014).

[3] V. P. Carey. *Liquid-Vapor Phase-Change Phenomena*. Taylor and Francis, second edition, (2007).

[4] S. Hardt and F. Wondra. Evaporation model for interfacial flows based on a continuum-field representation of the source terms. *Journal of Computational Physics*, 227:5871–5895, (2008).

Effect of Heterogeneous Wettability on Droplet Dynamic and Condensation Process

Felipe M. MANCIO REIS[1, 2], Pascal LAVIEILLE[1, 2], Marc MISCEVIC[1, 2] *

[1] Université de Toulouse, UPS, INPT, LAPLACE (Laboratoire Plasma et Conversion d'Energie), 118 route Narbonne, F-31062
[2] CNRS, LAPLACE, F-31062 Toulouse, France
* Corresponding author: marc.miscevic@laplace.univ-tlse.fr

It is considered that two-phase systems are among the most efficient systems to exchange large heat fluxes. These systems are based on the latent heat associated to a change of state of matter, i.e. a phase transition such as the boiling of a liquid, the evaporation of a droplet, or the condensation of a vapor. Even if two-phase systems are effective, their control under microgravity conditions is not yet completed, as the gravity forces do not allow the evacuation of the dispersed phase anymore. The present work deals with the use of surface tension forces induced by heterogeneous wettability to solve this problem. It is considered that a heterogeneous wettability property of a solid surface enables the mechanical non-equilibrium of the embryos forming on the wall. Dynamic contact angle of a droplet on a tilted surface (with an angle α compared to the horizontal) with a wettability gradient have been widely studied in the literature from both experimental and theoretical point of views [1-7]. The most common approach is based on hydrodynamic theory consisting in the balance between the driving force (F_θ) and the viscous force (F_μ). The driving force is directly related to the wettability gradient and gravity in the case of ($\alpha < 0$), and the viscous force corresponds to the integral of the viscous stress over the base of the droplet. Due to the singularity of viscous dissipation near the contact line, there are several studies regarding this viscous force, Subramanian et al. [4] proposed the viscous force model chosen in this study.

The Young equation corresponds to an equilibrated force balance on a static wedge of an interface. If an external action modifies the geometry of the problem, a new contact angle appears, i.e. the dynamic contact angle. The sum of the vectors will be perturbed and, consequently unbalanced. A new force exerts by the interface to compensate this situation, thus the droplet shrinks or spreads. If we assume that the forces are always unbalanced, a wetting force arises on the triple line causing the continuous motion of the liquid. Nevertheless, the contact angle hysteresis that is related to the roughness and the chemical heterogeneities on the surface, prevent the motion. The contact line pinning, i.e. contact angle hysteresis, has prove to be a major experimental problem, that's why a hydrodynamic model has been developed in order to describe the motion of a droplet on a heterogeneous surface. The aim of the model presented in this paper is to establish the velocity of the center of mass of the droplet taking into account the contact angle hysteresis. The model allows us to know the setting in motion conditions. Four hypotheses are made in this model:
- the droplet maintains its spherical cap shape during the movement, i.e. the dynamic contact angle is the same everywhere in the periphery of the droplet,
- the volume of the droplet remains constant,
- the interface is always in its most stable form, i.e. minimum of surface energy,
- the inertia term is neglected.

Finally, the momentum balance projected on the x-axis, tangent to the solid wall is:

$$F_\theta(\theta(x_G,t)) + F_\mu(\theta(x_G,t)) - mg\sin\alpha = 0. \qquad (1)$$

The driving force due to the surface tension gradient is well known in the literature [1-7]:

$$F_\theta(\theta(x_G,t)) = \gamma_{lv} R(x_G,t) \int_0^{2\pi} \left(\cos\theta_s(x) - \cos\theta(x_G,t)\right)\cos\phi\, d\phi, \qquad (2)$$

with $x = x_G + R(x_G, t)\cos\phi$ and where γ_{lv} is the vapor-liquid surface tension, θ_s is the static contact angle, θ is the real contact angle, ϕ is the azimuthal angle and $R(x_G, t)$ is the footprint radius of the droplet at the position of the center of mass x_G. Based on an analogy to droplet on an inclined surface, we established an expression of the driving force that explicitly takes into account the contact angle hysteresis:

$$F_\theta(\theta(x_G,t)) = \frac{\pi\gamma_{lv} R(x_G,t)}{2} \left[\cos\theta_a\left(x_G + R(x_G,t)\right) - \cos\theta_r\left(x_G - R(x_G,t)\right)\right]. \qquad (3)$$

This model assumes a linear cosine between the advancing contact angle at the front of the droplet and the receding contact angle at the rear of the droplet (figure 1).

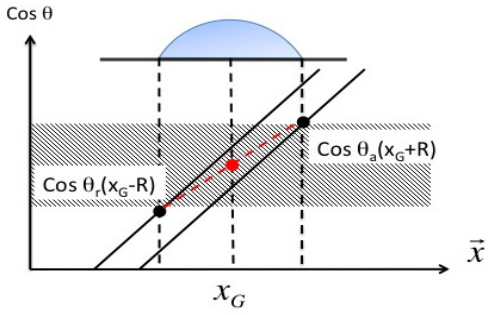

Figure 1: Driving force outline on the periphery of the liquid droplet.

The results obtained have been first compared to experimental data from Moumen et al. [5]. They prepared three different wettability gradient intensities labeled "weak", "intermediate" and "sharp". For convenience in calculating the theoretical forces involved, we fitted the data to a sigmoidal, logistic, four-parameter function. Because Moumen et al. [5] did not specify the CAH of their surface, we chose to determine it by an inverse method. We use a constrained least-square optimization method in which the adjustable parameter is the CAH and the studied parameter is the velocity of the droplet. Figure 2 shows the comparison

between measured and predicted velocities for a 500nL volume droplet placed on the intermediate gradient. The CAH calculated to adjust the experimental data varies between 5º and 7º. This is in agreement with typical values available in the literature [7]. It also appears that the velocity is much sensitive to CAH in the acceleration phase of the trajectory. The inset chart corresponds to the footprint radius plotted against the position. The droplet moves from the hydrophobic to the hydrophilic parts of the surface. Because of the conserved quantify hypothesis of the model, the footprint radius increases with position. To our knowledge, this model taking into account CAH is the first one that shows a so good agreement with the experimental data. This agreement suggests that the hypothesis that the contact angle hysteresis reduces the driving force is consistent in order to explain the behavior of the drops on the gradient surface. The model can then be used to analyze the mainly governing parameters of the motion.

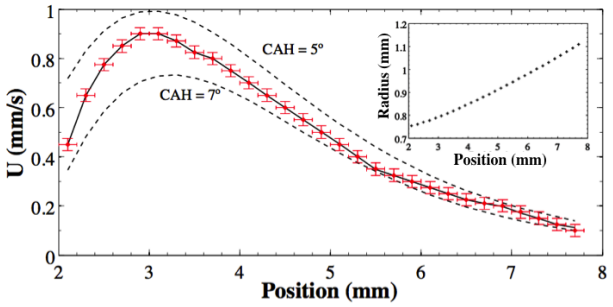

Figure 2: Comparison between measured and predicted velocities for a droplet which volume is 500nL placed on a wettability gradient. The filled diamonds correspond to the experimental data extracted from Moumen et al. [5], the dashed line curves represent the present model with a constant CAH while the solid line stands for the same model matching the experimental and predictive velocities.

Simultaneously with the theoretical approach an experimental setup is developed. Two different ways are explored to obtain heterogeneous wettability surfaces. The first one consists in a chemical deposition, i.e. silanization [3,5,6,7]. This surface treatment allows a silicon wafer or glass surface to react with vapors of a volatile R-$SiCl_3$ by using a diffusion-controlled process. As the silane droplet (~ 2 µL) evaporates and diffuses in the vapor phase, it generates a concentration gradient, and so a wettability gradient. The second way explored consists in plasma discharge process. The processing of samples is based on a Plasma-Enhanced Chemical Vapor Deposition (PECVD) using the Matrix Distributed Electron Cyclotron Resonance (MDECR) reactor. In a first step, the sample is completely rendered hydrophobic with a layer of hexamethyldisiloxane (HMDSO) and then using a movable mask, the surface is oxidized with an Argon-Oxygen mixture (ArO_2). The heterogeneous wettability is due to the exposure time: the more the surface is exposed to the gas and the more it gets hydrophilic. In order to understand the implications for passively enhancing heat transfer of heterogeneous wettability effect, a thermostated chamber was built. When a wettability gradient is designed into the substrate, in vapor condensation, the droplets nucleate and grow by both condensation and coalescence with the surrounding droplets and then move towards the more wettable parts (figure 3).

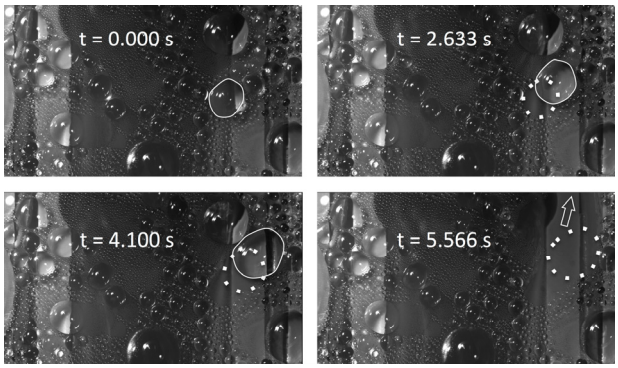

Figure 3: Water vapor condensation on a wettability gradient surface. The solid line shows the droplet at the time t and the dot line shows the droplet at the previous time. In the latter time (t=5.566s), the droplet is driven outside the scope of the camera.

Effectiveness of such treatment in two-phase systems has been proven when noticing that the droplet condensation persists in the center of the sample while a film is developed around the wettability gradient. The first results obtained in vapor condensation are promising in order to passively enhancing heat transfer. It is planned to conduct boiling experiments to verify the effectiveness of such a heterogeneous surface in both two-phase systems.

Acknowledgements
This work is funded by the European Space Agency Microgravity Application Program “MANBO” (Multiscale Analyses Boiling).

References

[1] P.G. de Gennes, Wetting: Statics and dynamics. Rev. Mod. Phys., Vol. 57, 827-863 (1985)

[2] F. Brochard, Motions of droplets on solid surfaces induced by chemical or thermal gradients. Langmuir, Vol. 5, 432-438 (1989)

[3] M.K. Chaudhury and G.M. Whitesides, How to make water run uphill, Science, Vol. 256, 1539-1541 (1992)

[4] R.S. Subramanian, N. Moumen and J.B. McLaughlin, Motion of a drop on a solid surface due to wettability gradient, Langmuir, Vol. 21, 11844-11849 (2005)

[5] N. Moumen, R.S. Subramanian and J.B. McLaughlin, Experiments on the motion of drops on a horizontal solid surface due to wettability gradient, Langmuir, Vol. 22, 2682-2690 (2006)

[6] S. Daniel, M.K. Chaudhury and J.C. Chen, Fast drop movements resulting from the phase change on a gradient surface, Science, Vol. 291, 633-636 (2001)

[7] S. Daniel and M.K. Chaudhury, Rectified motion of liquid drops on a gradient surfaces induced by vibration, Langmuir, Vol. 18, 3404-3407 (2002)

EXPERMENTAL INVESTIGATION OF A TRANSPARENT SINTERED HEAT PIPE

Cosimo Buffone
Microgravity Research Center, Université Libre de Bruxelles
Avenue F. D. Roosevelt 50, 1050 Bruxelles, Belgium
cbuffone@ulb.ac.be

A heat pipe is an evaporation–condensation device in which the latent heat of vaporization is exploited to transport heat over long distances. The two-phase heat transfer inside the heat pipe results in small temperature difference and also means that small quantities of working fluid are employed. The heat transport is realized by means of evaporating a liquid in the evaporator, where heat is given to the heat pipe, and subsequently condensing the vapour in the condenser, where heat is removed from the heat pipe. The circulation of the working fluid is maintained by the capillary action which is developed inside the wick structure that is the main component of a heat pipe [1]. There are three main different types of wick structures, namely: grooved, mesh and sintered. Sintered wicks are more performing and are usually employed when large transfer distances and/or gravity forces have to be overcome.

In this experimental study we report on thermal tests of a transparent sintered heat pipe properly designed for internal flow visualization. The main novelty is the positioning of the porous wick structure in the core of a borosilicate glass tube in order to visualize the internal flow. The test cell layout is shown in Figure 1. The dimensions of the transparent heat pipes are:

- Evaporator length 50mm;
- Condenser length 100mm;
- Adiabatic length 150mm;
- Wick diameter 30mm;
- Borosilicate pipe: ID 40mm and OD 50mm.

The evaporator section is made by inserting a cartridge heater with a maximum power of 175W inside a hole in one end of the wick structure while the condenser is made by inserting a brass cylinder inside the opposite end of the wick structure; the brass cylinder has two channels making a U-turn where cooling water is circulated. The cooling water comes from a thermostatic bath where the temperature can be varied between 5 and 40°C. Also the cooling water flow rate from the bath can be varied by a needle valve; and the flow rate measured by a geared flow meter. The outer vessel is made of borosilicate glass pipe to allow visualization inside the heat pipe. The borosilicate glass pipe is covered with ITO (Indium Tin Oxide) coating to avoid condensation on its inner surface with an electrical resistance of around 14.5 Ohms. The ITO and associated bus bars for electrical connection are deposited on the outside of the transparent glass tube.

One end cap of the Heat Pipe has two additional holes in its shoulders which allow connecting the vacuum pump in one and the other to connect a pressure gauge checking that a specified pressure is achieved with the vacuum pump before the Heat Pipe is charged with the working liquid. The opposite end cap has one opening to allow charging the Heat Pipe with the right amount of working fluid.

The Heat Pipe is instrumented with thermistors to measure the temperature in different locations. We have nine thermistors on top of the wick: three in correspondence of the evaporator; three in correspondence of the condenser; and, three on the adiabatic sector. The thermistors are positioned in a helix arrangement in order to spot any important circumferential variation of temperature. The thermal sensors are connected to an Agilent data logger which records the readings for subsequent post processing.

The working fluids are ethanol, acetone and water which are chemically compatible with the nickel wick structure.

During the tests we have varied several parameters. First we varied the amount of working fluid from 50%, 75%, 100%, 125% and 150% of the optimal value which correspond to the amount of liquid necessary to saturate the wick at the maximum heating load of 150W and condenser temperature of 5°C. Secondly we varied the heating load from a minimum of 30W to a maximum of 150W with step increase of 20W. Then we varied the condenser temperature from 5°C up to 40°C with step increase of 5°C. We also varied the cooling water flow rate for a corresponding Reynolds number from around 435 up to 1,475. The last important parameter that we varied is the inclination of heat pipe with respect to the gravity vector; to this end we constructed a tilting mechanism which allows pivoting the Heat Pipe at its center and having the evaporator above or below the condenser. We investigated inclination of -90°, -45°, 0, 45°, 90° where the first two inclinations correspond to evaporator above the condenser (Heat Pipe working against gravity), 0 correspond to Heat Pipe horizontal and the last two inclinations correspond to evaporator below the condenser (Heat Pipe gravity aided).

The porous wick is made of nickel sintered powder which is compacted and sintered inside a ceramic tube in a high temperature furnace with controlled atmosphere. After cooling the ceramic tube is carefully removed by mechanical means. The nickel wick structure has the following measured properties:

- Density 8,9 g/cm$^{3;}$
- Weight 687,4 g;
- Porosity 59,8 %;
- Mean hydraulic pore diameter 8,1 µm;
- Hydraulic permeability 1.1e-12 m^2.

Flow visualization inside Heat Pipes is rarely reported in the literature. There are a few recent studies which address this problem [2-3]. What we have done is to use two cameras one above the evaporator and one above the condenser, in order to have simultaneous images at the two ends of the Heat Pipe. The two CCD cameras have 752x480 pixels and a spatial resolution of at least 132µm.

We report on Figure 2 the results of the thermal resistance for three different cooling water flow rate (Reynolds numbers) for a heating load of 30W for all the Heat Pipe inclinations considered. The cooling water Reynolds numbers are between laminar and transitional. The thermal resistance is calculated with the following formula:

$$R = (T_e - T_c) / Q$$

where R is the thermal resistance, T_e and T_c are average (between the three thermocouple readings) evaporator and condenser temperature of the Heat Pipe, and Q is the heat load applied. As can be seen from Figure 2 the difference in thermal resistance for all Heat Pipe orientation is maximum 0.36 °C/W (the extreme cases being the gravity assisted and the against gravity positions). From Figure 2 it is also clear that the difference in thermal resistance decreases slightly with increasing of Reynolds number (Figure 2) which is probably due to the transitional regime at higher Reynolds. The estimated error with 0.2°C maximum error for the thermistors and 2.5W error for the power supply in calculation of thermal resistance, gives an overall error of around 8%.

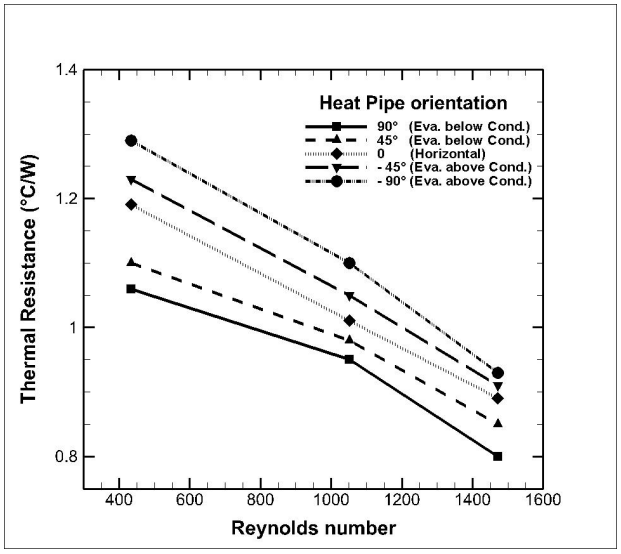

Figure 2: Heat Pipe thermal resistance vs cooling water flow rate Reynolds number.

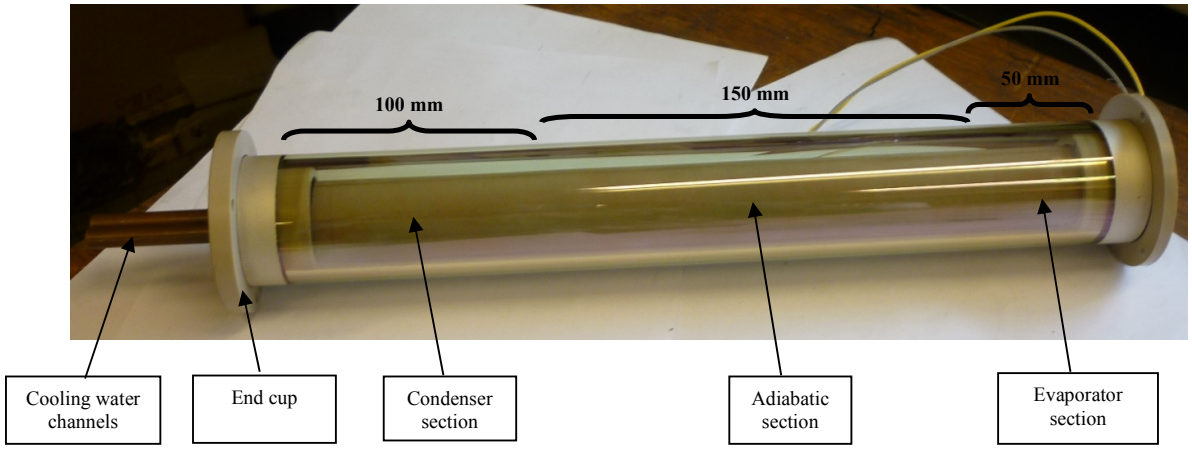

Figure 1: Transparent Heat Pipe Test Cell.

Acknowledgment

The author would like to thank the European Space Agency and Belgian Federal Science Policy Office for financial support.

References

[1] D. Reay and P. Kew, Heat Pipes: Theory, Design and Applications, 5th Edition, Elsevier, London, 2006.

[2] V. Ayel, C. Romestant, Y. Bertin, V. Manno, S. Filippeschi, Visualisation of flow patterns in flat plate pulsating heat pipe: influence of hydraulic behaviour on thermal performances, 17th International Heat Pipe Conference, Kanpur, India, October 13-17 (2013).

[3] M. Rao, F. Lefevre, S. Khandekar and J. Bonjour, Understanding transport mechanism of a self-sustained thermally driven oscillating two-phase system in a capillary tube, Int. J. Heat and Mass Transfer 65, 451-459 (2013).

Ground results with self-rewetting fluids in SELENE space experiment

W. Tzevelecos, S. Van Vaerenbergh

Microgravity Research Center (MRC), Université libre de Bruxelles (ULB)
Avenue F. D. Roosevelt 50, 1050 Brussels, Belgium
wtzevele@ulb.ac.be, svanvaer@ulb.ac.be

SELENE (SELf-rewetting fluids for thermal ENErgy management) is a microgravity experiment which is under development [1] to be integrated in Thermal platform 1 hardware and that will fly on board the ISS (International Space Station) inside the FSL (Fluid Science Laboratory) in the Columbus space laboratory.

Self-rewetting fluids are binary mixtures which have been already studied in standard Heat Pipes [2] and Pulsed Heat Pipes [3] and they result in an enhancing of the heat transfer performances. Thanks to the coupling of the capillary and inverse Marangoni effects the liquid is pumped to the warmest region of the heat transfer device in such a way to supply additional liquid to the evaporator and so to move the dry-out limit point and so increasing the maximum exchanged power respect to a standard Heat Pipe. Vapour from the evaporator is then driven towards the condenser for pressure drop, it condenses and the loop closes.

Heat transfer devices are widely used in several fields as micro-processor cooling devices, thermal regulator for buildings and structures, coolers for airplane engines and spacecraft reactors. To improve the efficiency of this kind of device means faster micro-processors, reduction of heat losses and more efficient and lighter cooling systems.

Inverse Marangoni effect consists in a non-linear dependence of surface tension with both temperature and concentration. Single component fluids have a negative variation of surface tension with temperature. The so called positive and negative mixtures have same dependence of single component fluids with temperature but opposed between them with concentration. Finally there are self-rewetting fluids which show a variation of this trend from specific temperatures and concentrations. In other words the self-rewetting fluids have the behaviour to change the surface tension trend with temperature and concentration in specified conditions.

The physics inside Heat Pipes using self-rewetting fluids is still not clear and several studies and experiments have been carried on in drop tower [4] and parabolic flight campaigns [5] to understand better this behaviour and its enhancing role in heat exchange devices.

SELENE proposes an additional piece of the puzzle allowing investigation of self-rewetting fluids in a mono-Grooved Heat Pipe (GHP) designed for space applications in which the driving force is surface tension and self-rewetting dynamics can be better understand [6][7].

Ground experiments are necessary before space experiments not only to test the breadboard design and the functionality of the experiment, but also to retrieve ground results which are fundamental to understand the effect of buoyancy, for instance in the evaporator of SELENE when boiling occurrence is studied. Ground experiments are also useful to test new diagnostic devices and filling procedures to allow changes of studied liquids which are not easy tasks in microgravity environment.

In this paper we will show the design of SELENE breadboard for ground experiments and we will describe the setup and the performed experimental procedure.

SELENE breadboard design allows groove changes and direct visualization from a top window installed on the cell as showed in figure 1c. The groove length is 180 mm with trapezoidal section with bottom and top base of 1 mm and 5 mm and 4.5 mm of depth. The breadboard is sealed using Viton seals between the groove and the case part and between the case and the glass on the top. Two entries allow liquid injection with a syringe and the air extraction with vacuum pump. The temperature of the window made of tempered glass of 3 mm thick is controlled to avoid condensation on the glass with water loop using a thermal conductive pad to put in contact the window with the heaters (figure 1c). Even the temperature of the SELENE case is controlled with water loop to compensate heat losses.

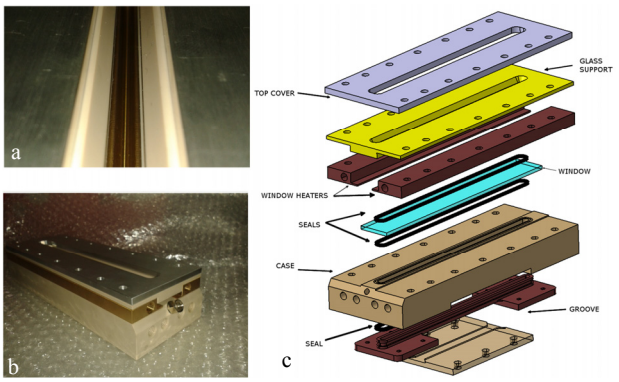

Figure 1: SELENE concept design: a) the groove seen from the window on the top; b) the manufactured SELENE breadboard; c) exploded CAD view.

Along the groove four temperature probes are in contact with the groove, one at the evaporator, one at the condenser and two at the limits of the adiabatic zone (figure 2). The input power was controlled with a 200W Peltier cooled with a thermal bath and heat was extracted at the condenser using an additional water loop.

Measuring the water temperature before and after the cooling water loop at the condenser (thermal sensors T5 and T6 in figure 2), and the water flux (F1 in figure 2), it's possible to calculate the exchanged heat which corresponds to the latent heat of the condensed vapor.

From the exchanged heat at the condenser and knowing the temperature difference between the evaporator and the condenser taking into account the heat losses, it is

calculated the thermal resistance which is the main parameter to classify the efficiency of a heat exchanger.

Thermal resistance of self-rewetting fluids in several standard conditions has been already investigated and it is less than Heat Pipes working pure fluids.

Before each experiment, the breadboard was evacuated at 10mbar using a vacuum line as showed in figure 2 and then, closed the valve V1, the SELENE breadboard was filled using a calibrated syringe L1 with a certain amount of liquid under investigation. When the valve V2 is opened the liquid is sucked rapidly in the breadboard. To avoid condensation on the wall of the breadboard, the cell is heated before the filling procedure and the liquid is injected directly inside the groove using a syringe needle already fixed to the connector where liquid is injected. The filling lines needs to be heated to avoid condensation inside the tube however. Then the valve V2 can be closed and the experiment can start.

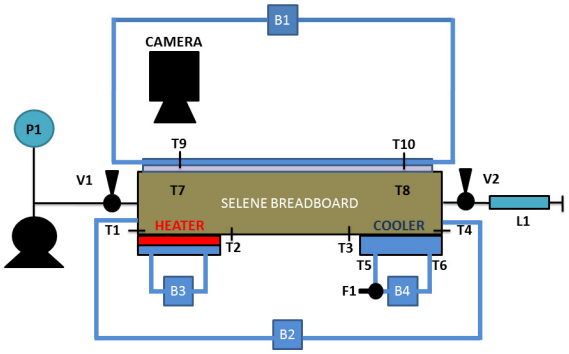

Figure 2: Scheme of the setup built for SELENE ground tests: 1) the valve V1 is open and V2 closed to evacuate the SELENE breadboard until the desired pressure measured by the barometer P1; 2) the valve V1 is closed and the breadboard pre-heated with the thermal bath B2; 3) the prepared liquid is sucked from the filling line when valve V2 is open; 4) once the valve V2 is closed the experiment can start; 5) the water loop of the thermal bath B1 avoid condensation on the visualization window, B3 supply water cooling loop to the peltier working as heater and finally the thermal bath B4 extract the latent heat from the condenser knowing the temperatures T5 and T6 and the water flux measured by the flowmeter in F1.

Between all available self-rewetting fluids, we chose n-Butanol in water solutions because of their strong surface tension trend with temperature and concentration; several concentration of n-Butanol in water solution have been studied to investigate also the impact of different concentration in the fluids. We also used deionized pure water as reference working fluids to compare the performances of the self-rewetting fluids in SELENE breadboard.

Future experiments on the SELENE space experiment will allow the concentration and pressure measurements along the cell in both the vapor and liquid regions and the use of diagnostics as thermography and direct optical visualization of the meniscus shape.

References

[1] R. Savino, A. Cecere, S. Van Vaerenbergh, Y. Abe, G. Pizzirusso, W. Tzevelecos, M. Mojahed, Q. Galand, Some experimental progresses in the study of the self-rewetting fluids for SELENE experiment to be carries in the Thermal Platform 1 hardware, Acta Astronautica 89 179–188, (2013).

[2] R. Savino, N. di Francescantonio, R. Fortezza, Y. Abe, Heat pipes with binary mixtures and inverse Marangoni effects for microgravity applications, Acta Astronautica 61 16 – 26 (2007).

[3] Yanxin Hu, Tengqing Liu, Xuanyou Li, Shuangfeng Wanga, Heat transfer enhancement of micro oscillating heat pipes with self-rewetting fluid, International Journal of Heat and Mass Transfer 70 496-503 (2014).

[4] Y. Abe, A. Iwasaki, K. Tanaka, Microgravity Experiments on Phase Change of Self-Rewetting Fluids, New York Academy of Science 1027 269-285 (2004).

[5] R. Savino, Y. Abe, R. Fortezza, Comparative study of heat pipes with different working fluids under normal gravity and microgravity conditions, Acta Astronautica 63 24 – 34 (2008).

[6] R. Savino, A. Cecere, R. Di Paola, Y. Abe, D. Castagnolo, R. Fortezza, Marangoni heat pipe: An experiment on board MIOsat Italian microsatellite, Acta Astronautica 65 1582–1592 (2009).

[7] R. Savino, R. Di Paola, A. Cecere, R. Fortezza, Self-rewetting heat transfer fluids and nanobrines for space heat pipes, Acta Astronautica 67 1030–1037 (2010).

The Constrained Vapor Bubble heat pipe experiment: A model to predict the thickness of the flat film in the Marangoni flow dominated region

Akshay Kundan, Joel L. Plawsky and Peter C. Wayner, Jr.

Department of Chemical Engineering, Rensselear Polytechnic Institute
Troy, New York, United States
kundaa@rpi.edu

The Constrained Vapor Bubble (CVB) is a wickless, grooved heat pipe and is the first, full- scale fluids experiment flown on the U.S. module of the International Space Station (ISS). The CVB system consists of a relatively simple setup – a quartz cuvette with sharp corners partially filled with either pentane or an ideal mixture of pentane and isohexane as the working fluids. Along with temperature and pressure measurements, the two-dimensional thickness profile of the menisci formed at the corners of the quartz cuvette was determined using a Light Microscopy Module (LMM). Even with the large, millimeter dimensions of the CVB, interfacial forces dominate in these exceedingly small Bond Number systems. The experiments were carried out for 30mm CVB model at power inputs of 2.2, 2.4, 2.6, 2.8, 3.0 and 3.125 W respectively. The composite image of the experimental visuals is shown in Fig 1.

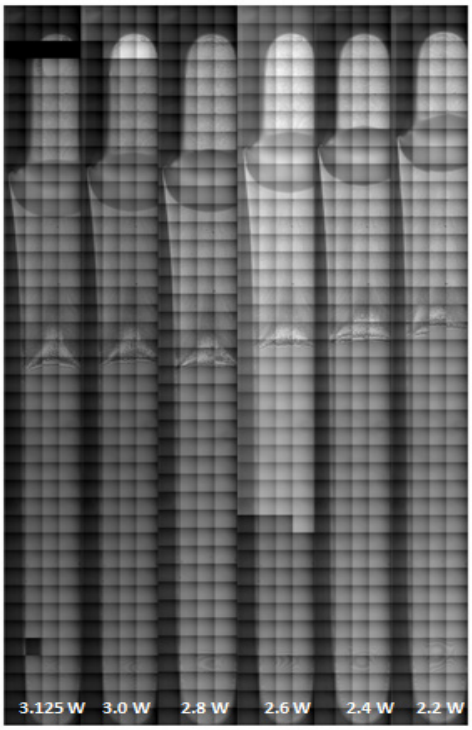

Figure 1: Composite images of the 30mm CVB run for high power heat inputs with pentane as the working fluid.

The temperature and temperature gradient profile along the length of the CVB for wet run (pentane as the working fluid) and dry run is shown in Fig 2. At the heated end of the CVB, due to high temperature gradient, we observe Marangoni flow. This region from the heated end to the central drop is defined as 'Marangoni dominated region'. The region below the central drop has comparatively less temperature drop compared to the one near the heater end. The fluid mechanics in this region is dominated by capillary pumping from the liquid pool and is termed as 'Capillary pumping dominated region'.

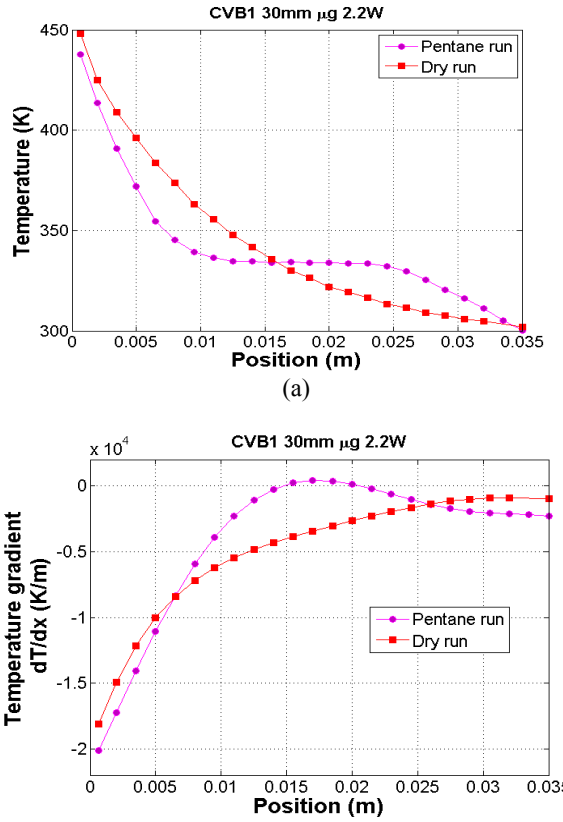

Figure 2: (a) Temperature position profile (b) Temperature gradient profile for pentane run and dry run along the length of the CVB for 30 mm at 2.2 W power input in μg,

In this paper we have found a simple analysis based on interfacial phenomena using only measurements from the ISS experiments that lead us to predicting the equation for the thickness of the film in the heated end of the CVB. The average pressure gradient for flow in the film is due to the measured capillary pressure at the two ends of the liquid film. The boundary conditions are 'no slip' condition at the wall interface and vapor interfacial shear stress at the liquid-vapor interface due to the Marangoni stress, which is due to the high temperature gradient. The analysis can predict the liquid film thickness which can be measured experimentally from Fig. 1.

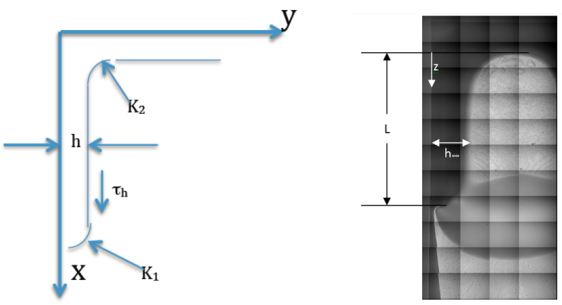

Figure 3: Marangoni dominated region

The model has been derived from the equation of motion for one dimensional (v_x) fluid flow in microgravity. The assumptions are that the flow is 1D and in a steady state with no acceleration ($dv_x/dx = 0$) in the x direction. Also, it is assumed that the pressure stress gradient due to cohesion self adjusts to a constant value over a distance L. Applying the boundary conditions mentioned above and the presence of a recirculation cell in the flat part of the film yields Eqn 1 and Eqn 2 to determine the velocity in the x direction and to predict the thickness of the flat film respectively.

$$v_x = \frac{\Delta P_l}{\mu L}\left(\frac{y^2}{2} - hy\right) + \frac{\tau_h}{\mu} y \qquad \text{Eq. (1)}$$

$$h = \frac{1.5\, L\, \tau_h}{\gamma\,(K_2 - K_1)} \qquad \text{Eq. (2)}$$

Fig 4 shows the predicted film thickness of the flat film with the experimentally obtained values. Fig 4a is obtained using the surface tension calculated at the vapor temperature. Improving on the model and using the surface tension of the liquid temperature in the Marangoni dominated region, Fig 4b is obtained. It is more reliable as the actual surface tension of the liquid is taken into consideration.. Near the central drop, we have two opposing radii of curvature and it cancels each other. Near the heater end, both the radius of curvature are sucking the fluid, so $K_2 = 2/r_2$.

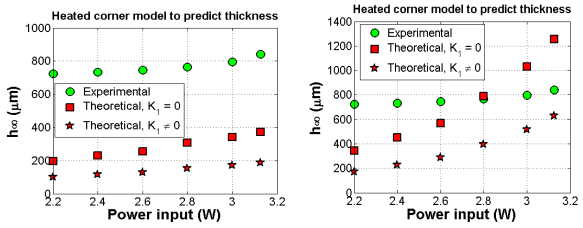

(a) (b)

Figure 4: The predicted film thickness using the model and the experimental values for different power input to the 30 mm CVB in microgravity. Assuming $K_1 = -1/r_1$ and $K_2 = 2/r_2$ where r is a positive radius of curvature obtained by fitting a circle to the liquid vapor interface curve at the central drop and at heated end respectively. Improving the model by assuming $K_1 = 0$ since K_1 has two opposing radii of curvature. The theoretical thickness calculated using (a) surface tension calculated at the vapor temperature (b) surface tension calculated at the liquid temperature at the heated end.

The profile of the fluid flow along the film is shown in Fig 5. The figure clearly indicates the presence of a recirculation cell along the thickness of the film.

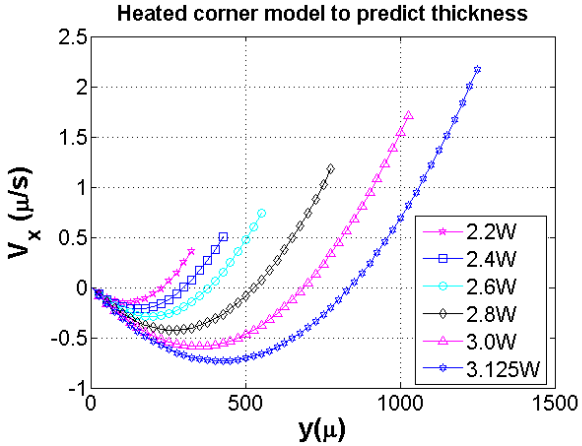

Figure 5: The velocity along the flat film profile indicative of the presence of a recirculation cell as the net area under the curve turns out to be zero.

The heated end is extremely complex since it includes three- dimensional variations in radiation, conduction, evaporation, condensation, fluid flow and interfacial forces. The data assuming $K_1=0$ (Fig 4b) confirms the model and assumptions. Using this model with the given assumptions, we were able to model the gist of these complex processes with a simple analysis..

References

[1] Panchamgam, S.S., Chatterjee, A., Plawsky, J.L., Wayner, P.C., Jr., Comprehensive experimental and theoretical study of fluid flow and heat transfer in a microscopic evaporating meniscus in a miniature heat exchanger, Int. J. Heat Mass Transfer, 51, pp. 5368–5379 (2008).

[2] Chatterjee, A., Wayner, P.C., Jr., Plawsky, J.L., Chao, D.F., Sicker, R.J., Lorik, T., Chestney, L., Eustace, J., Margie, R., and Zoldak, J., The Constrained Vapor Bubble Fin Heat Pipe in Microgravity, ACS Ind. Eng. Chem. Res., 50, pp. 8917-8926 (2011).

[3] Chatterjee, A., The Constrained Vapor Bubble Heat Pipe – on Earth and in Space, Ph.D. thesis, Rensselaer Polytechnic Institute, (2010)

[4] Fanton, X., Cazabat, A.M., Quere, D., Thickness and Shape of Films Driven by a Marangoni Flow, Langmuir, 12, pp. 5875-5880 (1996)

[5] Carles, P., and Cazabat, A.M., The Thickness of Surface-Tension-Gradient-Driven Spreading Films, J. Colloid Interface Sci, 157, pp. 196-201 (1993)

[6] Ludviksson, V., and Lightfoot, E.N., The Dynamics of Thin Liquid Films in the presence of Surface-Tension Gradients, AIChE, 17 (5), pp. 1166-1173 (1971)

CLOSED LOOP PULSATING HEAT PIPE: GROUND AND MICROGRAVITY EXPERIMENTS

M. Mameli[1*], L. Marelli[2], M. Manzoni[1], L. Araneo[2], S. Filippeschi[3], M. Marengo[1,4]

[1]Università di Bergamo, Viale Marconi 5, 24044 Dalmine (BG), Italy
[2]Politecnico di Milano, Dipartimento di Energia Via Lambruschini 4A, 20158 Milano, Italy
[3]Università di Pisa, DESTEC, Largo Lazzarino 2, 56122 Pisa, Italy
[4] School of Computing, Engineering and Mathematics, University of Brighton, Brighton BN2 4GJ, UK
[*]Corresponding author: mauro.mameli@unibg.it

1 INTRODUCTION

The Pulsating Heat Pipe (PHP) is a thermally driven two-phase passive device mainly based on the interplay between phase change phenomena (film evaporation, flow boiling, film condensation) and capillary forces. Because of its low cost and its potential capability to operate without gravity, it is one of the most novel, promising devices for the thermal control of electronic equipment for ground and space applications [1,2]. Thanks to the capillary dimension of the internal diameter (usually between 1 and 2mm) gravity is not essential to the PHP operation but affects its thermal performances.

This paper presents both ground test data and the results obtained during the 59th parabolic flight campaign organized by ESA in October 2013, complementary to those collected during the 58th parabolic flight campaign performed in May 2013 [3,4]. In particular the same Closed Loop PHP, made of a copper tube (I.D. 1.1mm, O.D. 2mm), bent into 16 turns and filled with FC-72, has been tested with a different volumetric filling ratio: 70%, while in the previous campaign the PHP has been filled 50%. The device is investigated in the vertical bottom heated configuration and results confirm that, during a parabolic flight, the PHP operation is strongly affected by the gravity field variation: hyper-gravity (1.8g) slightly assists the flow motion while during microgravity the PHP undergoes sudden temperature increase in the evaporator zone. The second hyper-gravity period is able to bring the PHP back to the previous thermal regime.

2 EXPERIMENTAL FACILITY

Figure 1 shows the main dimensions of the PHP with only the heater and thermocouples. The present PHP is equipped with a wire electrical heater (Thermocoax® Single core 1Nc Ac) wrapped 20 times around each evaporator U-turn in order to cover an evaporator length of about 6 mm and connected to a power supply (GWInstek® 3610A). Thermal characterization is provided by means of twelve "T" type thermocouples (wire diameter 0.127mm) located both in the evaporator and condenser zone (Figure 1). Furthermore the local fluid pressure fluctuations are recorded by means of a pressure transducer (Kulite®, ETL/T 312, 1.2bar A) plugged in the condenser section. The PHP is evacuated by means of a ultra-high vacuum system (Varian® DS42 and TV81-T), filled with degassed FC-72 (FR=70%) and finally sealed. The condenser section is embedded into an aluminum heat sink (Figure 2) which is cooled by means of four air fans. The CLPHP test cell as well as the cooling fan system, are mounted on a tilting structure in order to test it at different inclination angles. Thermocouples and the pressure transducer are connected to a data acquisition system (NI-CRio) and signals are recorded at 16Hz.

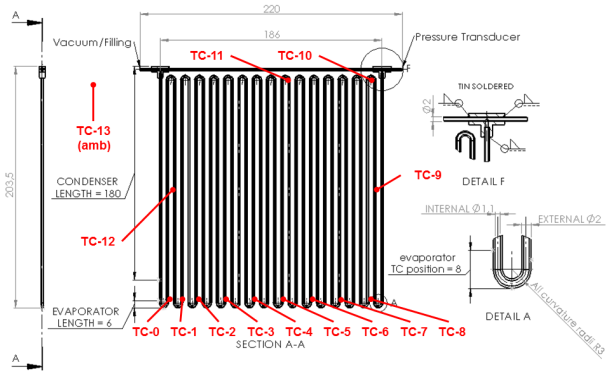

Figure 1: CLPHP test cell geometrical dimensions.

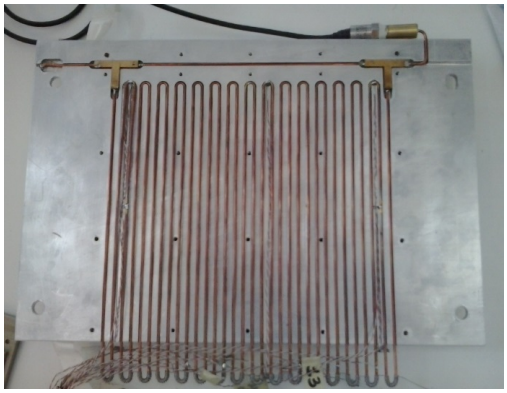

Figure 2: heat sink embedded PHP with pressure sensor and thermocouples.

3 RESULTS

Results are presented mainly in terms of temperature and pressure time evolutions. The tube wall temperature trends, both in the evaporator zone (reddish colors), condenser zone (bluish colors), and environment (green), are shown together with the heat input level on the secondary y-axis. Separately the local fluid pressure in the condenser together with the heat input level on the secondary y-axis. In case of flight test, the gravity acceleration is reported directly over the plot line.

3.1 Ground Tests

The complete thermal characterization in vertical and horizontal position has been performed ranging from 10W to 100W heating power with steps of 10W. Each step is kept for at least twenty minutes in order to reach the pseudo-steady state (all temperature signals shows an average component which is time constant). Figure 3 shows the PHP thermal behavior during the Vertical operation.

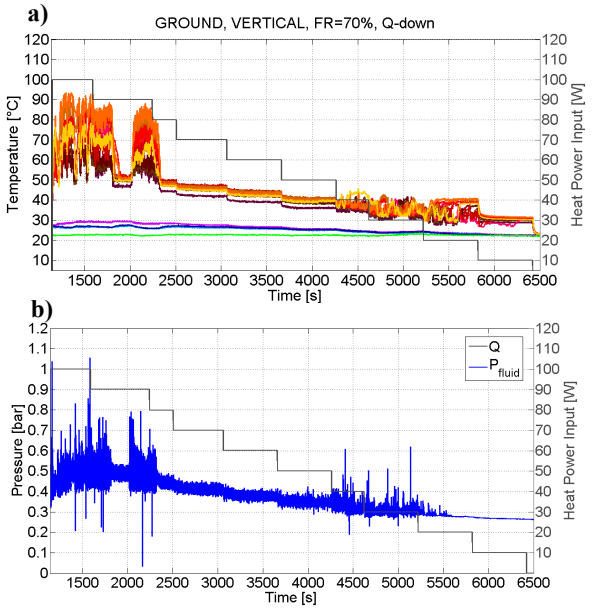

Figure 3: Vertical PHP on ground with different thermal loads: a) wall temperatures, b) local fluid pressure in the condenser.

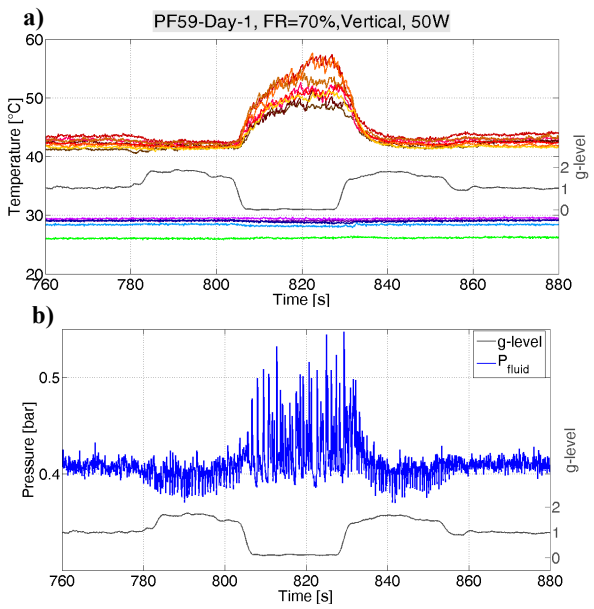

Figure 4: Vertical PHP during a parabolic maneuver: a) wall temperatures, b) local fluid pressure in the condenser.

Besides being more stable and efficient than the horizontal operation, the vertical PHP shows an interesting feature at high heat input levels (80W to 100W): some channels undergo a sudden thermal instability probably due to fluid motion dampening or local dry-out [5]. During this crisis the temperature distribution spreads op to 40°C while when the device works in a stable condition (from 80W to 50W) the evaporator temperature range is always narrower (less than 10°C). Between 40W and 20W the device undergoes a start-stop condition and does not operate at all at 10W.

3.2 Parabolic Flight Campaign

The same PHP is then tested during the 59th ESA Parabolic Flight (PF) campaign with a variable gravity regime (from 1.8 down to 10^{-2} g, 31 parables). As shown in figure 4, during a parabolic flight maneuver (1g, 1.8g, 0g, 1.8g, 1g), the vertical operation is affected by the gravity field variation as follows:

- hyper-gravity assists the flow motion, the heat transfer is slightly enhanced, thus a small decrease of the evaporator temperatures is appreciable.
- during microgravity the gravity force component is not present anymore and the PHP undergoes sudden temperature increase in the evaporator zone.
- during the microgravity period the pressure fluctuations are higher in amplitude but occur with lower frequency (Fig. 4b) similarly to the horizontal position on ground.
- the second hyper-gravity period is able to bring the PHP back to the previous thermal regime.

4 CONCLUSIONS

A Closed Loop Pulsating Heat Pipe filled with FC-72, has been investigated both on ground and in micro/hypergravity conditions during the 59th ESA campaign with 70% volumetric filling ratio. Ground tests are performed on ground at different heat input levels, and different orientations (Vertical, Horizontal). Results confirmed that despite the capillary inner diameter, the PHP thermal-hydraulic behavior is strongly affected by the orientation and by the gravity level. In particular:

- the vertical operation is more stable and efficient while the horizontal mode is characterized by an impulse driven flow with apparently lower oscillation frequency.
- a repeatable thermal instability is detected at high heat input levels for the vertical operation due to partial dry-outs.
- In case of perfectly planar geometry the horizontal operation on ground seems to be the most similar to the micro-gravity operation.

AKNOWLEDGEMENTS

The present work was carried out in the framework of the project PRIN2009 - MIUR. The authors acknowledge the financial support of the European Space Agency through MAP ENCOM project. A thanks is due to NOVESPACE team, V. Pletser, O. Minster and B. Toth for their interest and support.

REFERENCES

1. Akachi H., Structure of a heat pipe. *US Patent 4,921,041.* (1990).
2. Maydanik Y., Dmitrin V.I.,. Pastukhov V.G, Compact cooler for electronics on the basis of a pulsating heat pipe. Applied Thermal Engineering, vol. 29, 3511–3517 (2009).
3. Araneo L., Filippeschi S., Mameli M., Marelli L., Testa R., Manno V., Marengo M. Thermo-Hydraulics Characterization Of A Pulsating Heat Pipe in a Variable Gravity Regime 8th International Topical Team Workshop on Two-Phase Systems For Ground And Space Applications. Bremen, Germany, September 16-19, 2013.
4. Mameli M., Araneo L., Filippeschi S., Marelli L., Testa R., Marengo M., Thermal Response of a Closed Loop Pulsating Heat Pipe under Varying Gravity Field, accepted for publication on the Int. J. of Thermal Sciences, DOI: 10.1016/j.ijthermalsci.2014.01.023.
5. Mameli M., Manno V., Filippeschi S., M. Marengo, 2013, Effect of Gravity on the Thermal Instability Of a Closed Loop Pulsating Heat Pipe, 8th World Conference on Experimental Heat Transfer, Fluid Mechanics, and Thermodynamics June 16-20, 2013, Lisbon, Portugal.

Ninth International Conference on
TWO-PHASE SYSTEMS FOR GROUND AND SPACE APPLICATIONS
Baltimore, Maryland, USA, September 22-26, 2014

Two Phase Titanium water heat pipe for Space Rated Stirling Power Conversion

Marc Gibson, Jim Sanzi, Max Briggs

NASA Glenn Research Center
Cleveland, OH 44135
marc.a.gibson@nasa.gov

NASA's planetary science and human exploration programs are developing long life nuclear power systems to address the growing electrical power requirements of future missions. Typically these power systems convert the nuclear heat to electricity using solid-state thermoelectric conversion. In the past decade, dynamic power conversion has made significant progress using free piston Stirling convertors, which have shown orders of magnitude improvements in thermal to electric power conversion efficiency. Higher efficiency has been a supportive driver for integrating Stirling technology into Radioisotope Power Systems (RPS) as it directly reduces the amount of Plutonium fuel (Pu238) used in RPS. The Advanced Stirling Radioisotope Generator (ASRG, figure 1) was developed to specifically address the fuel consumption of Pu238 as quantities are diminishing. The ASRG is designed to produce approximately 140We using two Advanced Stirling Convertors (ASC) and fueled by two PU238 fueled General Purpose Heat Source (GPHS) modules. This is a four-fold reduction in fuel compared to the Multi-mission Radioisotope Generator (MMRTG) which uses eight GPHS fuel modules.

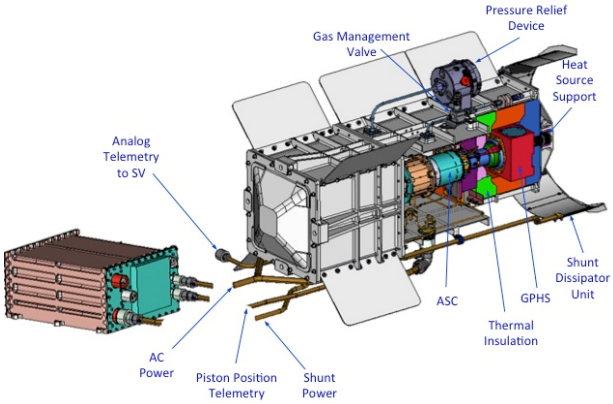

Figure 1: Advanced Stirling Radioisotope Generator (ASRG).

Each ASC under nominal operating conditions absorbs approximately 200Wt from one GPHS, converts the input heat into 70We using a linear alternator, and rejects 130Wt to space using the generator housing as a radiator. A conductive ring, commonly referred to as the Cold Side Adapter Flange (CSAF), is used to couple the "cold side" of the convertor to the radiator housing. The CSAF transfers heat radially from the convertor to the housing as well as provides structural support during thermal expansion and fuel loading of the assembly.

In late 2013, the reduced NASA RPS budget led to the termination of the ASRG flight development project. The RPS program is considering repurposing the Stirling development efforts to focus on a higher power Stirling Radioisotope Generator (SRG) that can affectively address 500+We flagship type missions. As the power level of SRG's increase, the heat transfer into and out of the convertors becomes increasingly difficult. An example of how this increased power level can affect generator design can quickly be found at the CSAF where the conductive area and radius needed to transfer the increased waste heat from the convertor to the heat rejection radiator creates significant mass penalties.

A new method of transferring heat from the convertor to the radiator housing using two phase heat pipe technology has been developed at the NASA Glenn research Center (GRC). This technology has been named the Radial Core Heat Spreader (RCHS) and uses a titanium structure and capillary wick with water as the working fluid. Figure 2 illustrates the current CSAF conduction technology versus the RCHS heat pipe technology.

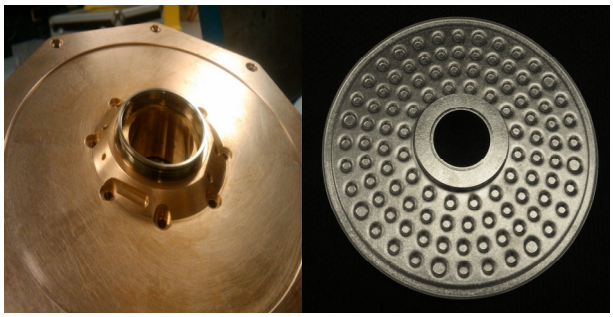

Figure 2: Left, Cold Side Adapter Flange (CSAF); Right, Radial Core Heat Spreader (RCHS)

Using water vapor as the thermal carrier in the heat pipe greatly reduces the mass of the assembly when compared to conduction methods as the cross sectional area is hollow vs. solid. With either system, heat is accepted at the inner radius of the unit from the Stirling convertor and transferred radially outward to the generator housing where it can be rejected to space. The two phase heat pipe cycle starts at the evaporator, located at the inner radius of the assembly, where the water is contained as a liquid in the sintered titanium capillary wick. Using the waste heat from the convertor, the water is vaporized and travels radially outward, through a short adiabatic section, to the condenser located at the outer most radius of the assembly. The condenser is conductively coupled to the generator housing that typically sees <10K sink temperatures in deep space. The water vapor loses its latent heat at the condenser wall and changes back into the liquid phase where the capillary wick absorbs the fluid and pumps it back to the evaporator to complete the cycle.

For purposes of addressing future higher power SRG's,

trade studies have been initialized to determine the appropriate breakpoint power level where two phase heat pipes replace conductive components in the heat rejection subsystem of the power generator. Variables in this study include mass, thermal performance, reliability, operating range, and Assembly Test and Launch Operations (ATLO) requirements. In a parallel effort, the RCHS heat pipe was designed and built to replace the CSAF as a direct physical comparison between the two components using the above mentioned design variables. Numerous prototypes of the RCHS where fabricated and underwent laboratory and zero gravity performance testing to address as many of the design requirements as could be affordably tested.

The first and foremost difficult requirement of the heat pipe cooled Stirling convertor for radioisotope power systems was the launch environment. The power system must actively cool the Pu238 GPHS fuel modules from the time of loading, just prior to launch, to the end of the mission. This requirement creates further challenges for the heat pipe as the capillary wick must pump the working fluid against hyper-gravity launch accelerations. These accelerations originate from typical vertical and longitudinal sources as well as rotational sources caused by the spin/despin and tipoff of the launch vehicle during ascent. If not designed correctly, these accelerations could easily stop the flow of fluid returning to the evaporator and cause a dryout condition that thermally stalls the heat pipe and overheats the convertor. Secondly, the orientation of the power system/heat pipe when assembled on the spacecraft is unknown and affects the directional vector of the acceleration forces that influence the fluid flow. Knowing this, it was determined that testing the RCHS in both the horizontal and vertical orientation should correctly address the best and worst case scenarios of all of the potential launch orientations and was incorporated into the test program.

For the RCHS to be a viable alternative it is necessary to mature it's Technology Readiness Level (TRL) to six. The relative environment for TRL6 would include thermal vacuum testing, reduced gravity testing, and launch vibrational qualification. Thermal vacuum testing will be completed at NASA GRC using vacuum facility seventeen that can produce space-like pressures of 1x10-7 Torr and 80K sink temperatures. Initial reduced gravity testing has been completed on a parabolic flight campaign with the Reduced Gravity Office (RGO), Flight Opportunities Program (FOP), and the Zero G Corporation. As a final proof of concept, the RCHS will be flown on a sounding rocket that will combine all relative environments for the first 10 minutes of a real mission. A 3 stage Peregrine rocket is expected to launch in February 2015 and will carry an experimental section with two RCHS assemblies (figure 3), one vertical and one horizontal, to 300km above the earth for approximately 6 minutes of microgravity. The RCHS requirements for the flight are to reject 130Wt throughout the launch and microgravity portions of the flight while maintaining the temperature of the simulated Stirling connection below 100C. Figure 3 illustrates the two RCHS assemblies in the Peregrine experimental section.

Information given in the presentation will document the current status of the RCHS heat pipe technology development.

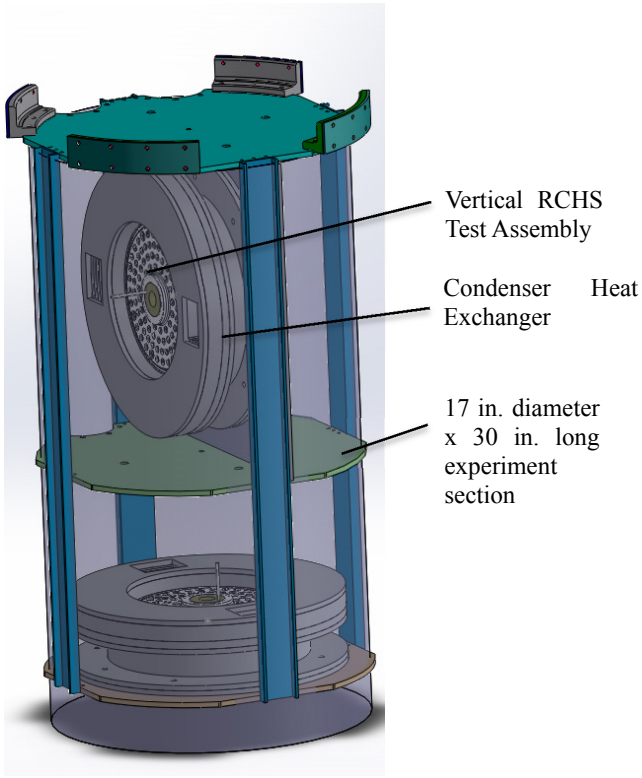

Figure 3: Radial Core Heat Spreader (RCHS) assembled in the vertical and horizontal orientation inside the Peregrine sounding rocket experiment section.

References

[1] Wong, W.A. et al, Pathfinding the Flight Advanced Stirling Convertor Design With the ASC-E3, NASA/TM-2014-217753

[2] Wood, J.G. et al, Continued Development of the Advanced Stirling Convertor (ASC),www.sunpowerinc.com /library/pdf/publications/Doc0104.pdf

[3] Chan, J., Wood, J.G., Schreiber, J.G., Development of Advanced Stirling Radioisotope Generator for Space Exploration, NASA/TM-2007-214806

[4] NASA Facts, Advanced Stirling Radioisotope Generator (ASRG), NF-2013-07-568-HG

Study on Internal Flow Characteristics of Multiple Evaporators Loop Heat Pipe (Visualization in Evaporators and Condenser under Microgravity)

Yuta Matsuda[1], Hosei Nagano[1], Shun Okazaki[2], Hiroyuki Ogawa[2] and Hiroki Nagai[3]

[1] Department of Aerospace Engineering, Nagoya University
[2] Japan Aerospace Exploration Agency
[3] Department of Aerospace Engineering, Tohoku University

[1] Building 2 of Engineering, Furo, Chikusa, Nagoya, Aichi, 464-8603, Japan
[2] 3-1-1 Yoshinodai, Chuo-ku, Sagamihara, Kanagawa, 252-5210, Japan
[3] 6-6, Aoba, Aramaki, Aoba-ku, Sendai 980-8579, Japan

matsuda@prop2.nuae.nagoya-u.ac.jp

1. Introduction

Loop heat pipe (LHP) is a heat transfer devices driven by capillary forces with high-effectiveness and performance, offering high-reliability in varying g-environments. Recently, multiple-evaporators LHP (MLHP) is under studies as a next-generation heat transfer technology since the MLHP supplies autonomous thermal control function. Visualization study of physical phenomena of LHP has been done until now [1-2], but visualization study under microgravity is not performed yet. In addition, visualization study of MLHP is not done. Therefore, the revealing internal flow characteristics of MLHP under microgravity and building a detailed mathematical model is intended in this study. In this paper, the internal visualization method was investigated and a new MLHP for visualization was designed, manufactured. The test was carried out under the microgravity by aircraft, and the vapor-liquid distribution inside the compensation chamber (CC) and the wick core of the evaporator is revealed. Furthermore, heat distribution on both sides heated was calculated by the observation.

2. Experimental apparatus

Figure 1 shows the scheme of the MLHP for visualization, and Table 1 shows the MLHP geometry characteristics. MLHP has two evaporators and CCs. Insertion opening is provided to each CC owing to observe the inside by borescope. It is possible to observe both of the CC side and the wick core side by rotating the borescope. The condenser is consisted by the transparent 1/8 inch tube made of PFA and the A15052 plate of 150×300mm. The condenser is also conduction cooled by insulator. Measurement of the temperature distribution is carried out by 34 T-type thermocouples. The pressure is measured by 4 pressure gauges.

3. Result and discussion

3.1. Vapor-liquid distribution in the evaporator and CC

Vapor-liquid distribution inside of the heated and non-heated evaporator and the CC is revealed by the microgravity experiment one side heat load. Figure 2 shows the internal observation of the evaporator of the heating side. Under 1G condition, the vapor phase is distributed the top of the core and the liquid phase is distributed the bottom of the core (Figure2 (a)). On the other hand, the vapor phase moves to the center of the core under 0G. In addition, bubbles due to heat leak are generated around the core (Figure2 (b)). After that, the bubbles grow so as to extend to the CC side (Figure2 (c) and (d)). Even if bubbles grow, bubbles and the inner wall of the core are not in contact. The liquid phase is also present between the inner wall and bubble (Figure2 (e) and (f)).

Table 1: MLHP geometry characteristics

Evaporator (SUS304)	O.D.	21mm	Vapor Line (SUS304)	O.D.	6.4mm
	Length	85mm		Length	350mm
CC (SUS304)	O.D.	50mm	Liquid Line (SUS304)	O.D.	3.2mm
	Length	75mm		Length	500mm
Wick (SUS304)	O.D.	19mm	Condenser (PFA)	O.D.	3.2mm
	Length	50mm		Length	1500mm
	Pore size	1.2μm	Working fluid	Material	Water
				Volume	180cc

Figure 1: Scheme of the MLHP

The bayonet tube inside the core is not encased in bubbles, and the liquid phase is present in the bayonet tube side (Figure2 (c) ~ (e)). Figure 3 shows the visualization result of the vapor-liquid distribution in the CC of the heated evaporator side. The vapor phase is distributed at the top of CC, the liquid phase is at the bottom of the CC under 1G. (Figure3 (a)). Meanwhile the vapor phase moves in the center of the core as a large bubble. After that, the bubbles draft around the bayonet tube. The bayonet tube is not incorporated into the bubbles, and the bubbles are not divided by the bayonet tube. The bubbles are located the rear of the CC (Figure3 (b)). Figure 4 shows the vapor-liquid distribution conceptual diagram of the heated evaporator and CC. In the heating side, the vapor-liquid distribution is in accordance with gravity. The vapor phase is the top of CC, the liquid phase is the bottom of the CC (Figure4 (a)). On the other hand, the effect of surface tension becomes dominant in microgravity. Because of this, the liquid stick to the wall and the bubbles gather in the center of the core.

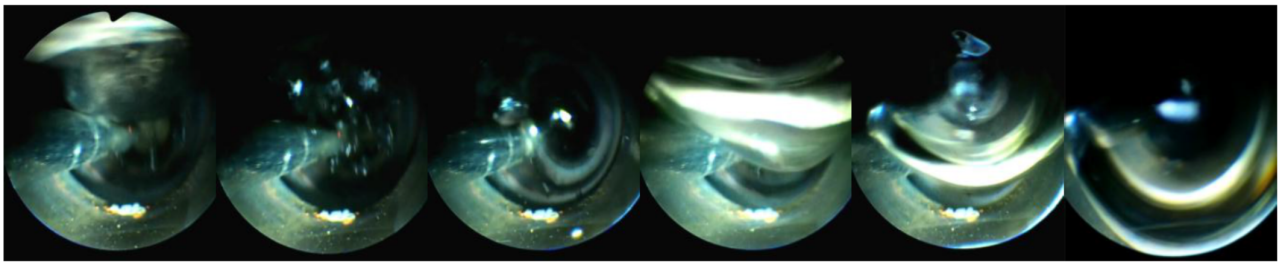

Figure 2: Inside of the evaporator (Heated side, 110W/0W)

In addition, the bubbles grow and move as to avoid the bayonet tube due to the surface tension. The bubbles in the wick core grow to the CC direction (Figure4 (b)).

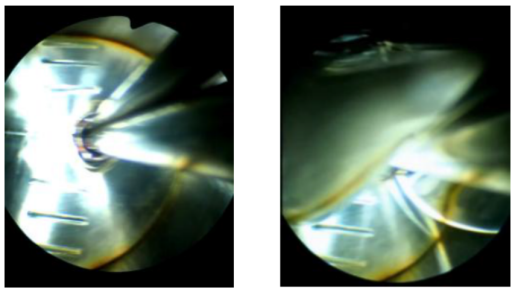

Figure 3: Inside of the CC (Heated side, 110W/0W)

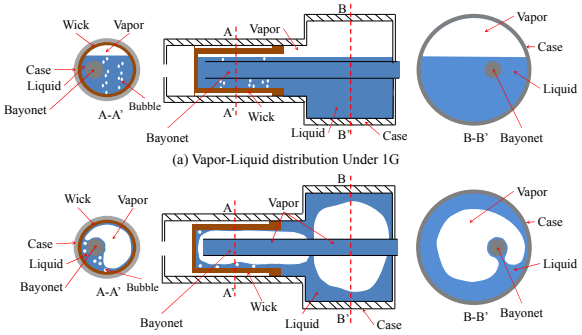

Figure 4: Vapor-liquid distribution (Heated side)

3.2. Heat distribution

The energy conservation equation of the evaporators is expressed as follow:

$$Q_{load}=Q_{amb}+Q_{vl}+Q_{con}+Q_{sub}+Q_{ll} \quad (1)$$

where, Q_{load}, Q_{amb}, Q_{vl}, Q_{con}, Q_{sub}, Q_{ll} are amount of the heat load, the heat loss from the evaporator and CC case to the ambient, the heat loss from the vapor line to the ambient, the heat radiation at the condenser, the sub-cooling at the condenser, and the heat loss from the liquid line to the ambient. In addition, heat leak from the evaporator to the CC is expressed as follow:

$$Q_{hl}=Q_{amb}+Q_{sub} \quad (2)$$

These are a function of mass flow rate ($\dot{m}$). Mass flow rate ($\dot{m}$) is calculated by estimating the flow rate of the working fluid entering the condenser from the video of high-speed camera. Figure 5 shows the heat distribution of the both sides 80W heat load test, and the one side heat load (110W/0W). $Q_{hl,1,2}$ on both sides 80W heat load is estimated 9.9W. This heat leak accounts for 12.2% of the total heat load. When this heat leak is calculated to the amount of evaporation in the core, this volume is estimated 6738mm^3/sec. This means that the bubble of its radius about 11.7mm is generated per unit time. This estimate is determined a reasonable amount by the video taken the core. Other hand, Q_{con} accounts for 87.5% of the total heat load.

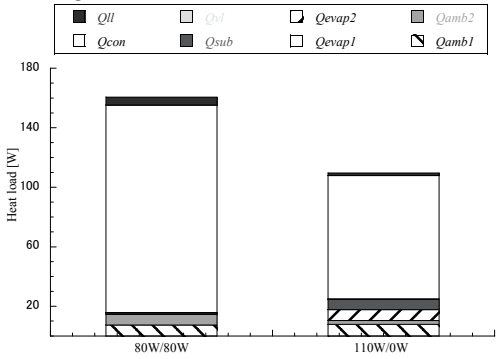

Figure 5: Heat distribution

Next, the evaporator (Evap.2) of non-heated side acts as the second condenser when the heat load is applied only one evaporator. The mass flow rate which has flowed into the non-heated side is estimated by the mass flow rate of the heated side evaporator (Evap.1) and the mass flow into the condenser. As a result, the mass flow ration of the condenser to the Evap.2 which acts as the second condenser is calculated $\dot{m}_{con}:\dot{m}_{evap.2}$=14.2:1. Figure 5 also shows the result of the heat distribution. The mass flow rate of the condenser side is dominated, and the vapor hardly flows to the non-heated evaporator side. Because the wick of the evaporator inside acts as a flow regulator, the vapor to flow to the core is blocked by the capillary forces.

4. Acknowledgement

This research is partially supported by Japan Aerospace Exploration Agency (JAXA), Japan Space Forum (JSF), and Diamond Air Service Inc. (DAS).

5. References

[1] J. M. Climbala, J. S. Brenizer, Jr, Study of loop heat pipe using neutron radiography, Applied Radiation and Isotope, 61, 701 (2004)

[2]B. P. d'Entremont, J. M. Ochterbeck, Investigation of loop heat pipe startup using liquid core visualization, Proc. Of the ASME Summer Heat Transfer Conference, 2, 387 (2008).

Ninth International Conference on
TWO-PHASE SYSTEMS FOR GROUND AND SPACE APPLICATIONS
Baltimore, Maryland, USA, September 22-26, 2014

2.5-D Modeling of Manifold-Microchannels in Thin Film Evaporation

Raphael Mandel, Serguei Dessiatoun, Michael Ohadi

Smart and Small Thermal Systems Laboratory
Department of Mechanical Engineering
University of Maryland, College Park
rmandel@umd.edu

ABSTRACT

A system of manifolds is utilized to divide long microchannels into an array of parallel, short, high aspect-ratio microchannels, resulting in more localized liquid feeding and reduced flow length, simultaneously allowing for enhanced heat transfer rate and reduced pressure drop. Although a previous model achieved relative success in predicting thermal performance of two-phase manifold microchannels, its simplifying assumptions limited its applicability to low mass fluxes, and it did not provide an accurate prediction of pressure drop. However, because sufficient agreement was achieved for thermal performance, the underlying thermal assumption—that all heat is transferred via steady-state, one-dimensional conduction through the thin liquid film—was transplanted into the more rigorous CFD-based model presented here, which should provide a more accurate prediction of pressure drop, flow distribution, and the resulting heat transfer at all mass flow rates. Due to the non-standard assumptions and model couplings, a custom numerical code was developed in-house. The governing 2-D Navier Stokes equations were discretized using the first-order upwind scheme and solved using the SIMPLEC algorithm. These equations were coupled to the Volume of Fluid (VOF) via the fluid mixture density, and the VOF equation was coupled to the wall temperature via two-phase heat and mass transfer. The custom code was then verified with numerous analytical tests and compared to the available experimental data. This model was then used to probe the physics by performing parametric studies on the effects of each of the variables on heat transfer and pressure drop.

1. INTRODUCTION

The continued demand for high performance electronic systems and the simultaneous trend of miniaturization continue to raise the dissipated power, heat flux, and heat densities to unprecedented levels. Meanwhile, the allowed temperature difference between the heat source and the sink has not changed, since high reliability must be maintained and thermal and mechanical stresses minimized. Accordingly, much smaller resistance between the heat source and the cooling medium—i.e. larger heat transfer coefficients—are needed.

One way to reduce the thermal resistance is by embedding microchannels as close as possible to the heat source, utilizing an innovative manifold-microchannel system. A manifold structure, containing alternating liquid feed channels and vapor outlet channels, is placed perpendicular to a microgrooved surface, as shown in **Error! Reference source not found.**. Saturated liquid enters the liquid inlet, where it is forced downward between the fins into the microchannel. The liquid is then heated and evaporated, and the resulting two-phase mixture flows upward through the vapor outlet.

Previous two-phase experimental testing on manifold microchannels has indicated the potential of manifold microchannels operating in two-phase mode. Heat fluxes as high as 1.2 kW/cm^2 and thermal conductances as high as 350 kW/m^2-K have been obtained at low outlet vapor qualities and moderate pressure drops [1]. However, there were discrepancies between the results and the available correlations in both the order of magnitude and the overall trends. These discrepancies indicate that additional physics not accounted for in the correlations are at play. Furthermore, visualization studies indicate the presence of many complicated phenomena, such as nucleate boiling, film evaporation, forced convection, flow distribution, partial dryout, fin efficiency, and two-phase cycling [1, 2]. A model is therefore needed to better understand the system and improve designs.

Although a 3-D Volume of Fluid (VOF) based CFD model could be employed—such as those available with commercial codes—such simulations are computationally expensive, due to the 3-D nature of the problem, the fine meshes required for resolution of the proper physics, and the resulting small time steps required for numerical stability. In addition, these models are often numerically unstable, difficult to converge, and sometimes provide only a brief transient solution. The simulation engineer is then left with the difficulty of coaxing the model to converge or analyzing the transient simulation data to assess thermal performance. Thus, an alternative method—one which is computationally inexpensive yet accurately models the most important physics—is desirable [3].

To obtain physically accurate results at drastically reduced simulation times, a "2.5-D" model was coded in house. Thus, the model approximates the fluid flow in the

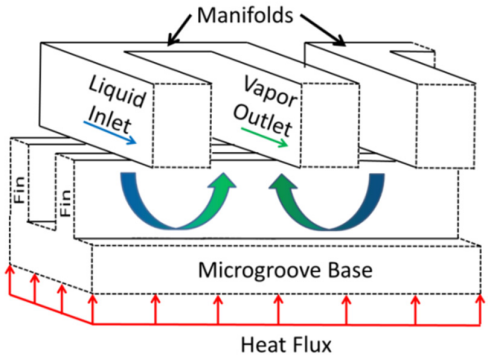

Fig. 1: Diagram of a two-phase, manifold-microchannel system. Saturated liquid is forced between fins into a microchannel, where it evaporates and escapes via the vapor outlet, as shown.

microchannel as being approximately 2-D, and utilizes a friction factor to simulate the effect the non-simulated third dimension would have on flow distribution. The 2.5-D model simplifies the 3-D domain into a series of parallel 2-D meshes, hence the coining of the term "2.5-D."

2. MODEL

Since simulating an array of manifold-microchannels is computationally expensive, a few simplifications to the solution domain are needed. If an even flow distribution from the manifolds can be assumed, the symmetric pattern of repeating inlets and outlets allows the solution domain to be reduced into a unit cell, containing half an inlet, a manifold, and half an outlet. A diagram of the unit cell appears in Fig. 2.

The following notable assumptions and simplifications were made in the model:

(1) The fluid flow is 2-D, steady-state, laminar, homogeneous, and hydrodynamically and thermally fully-developed

(2) A friction factor for steady-state, fully-developed, homogenous flow between two parallel plates can be used to account for pressure drop in the third, non-simulated dimension (z-coordinate)

(3) Liquid remains attached to the wall and forms a thin film with vapor passing through the center of the channel (no liquid droplet entrainment)

(4) Liquid film thickness is given via void fraction correlation

(5) Wall temperature distribution is 2-D (x- and y-coordinates)

3. RESULTS AND DISCUSSION

The model was then run for many different surfaces, manifolds, working fluids and operational conditions in order to study the physics and compare the model to the experimental results. In addition, a parametric study was conducted to determine the effect of each variable. Sample results are given in Fig. 3, indicating the effect of mass flux on the graph of wall heat transfer coefficient and pressure drop vs. outlet vapor quality.

From Fig. 3(a), it is clear that the predicted effect of mass flow rate from the model is significantly less than what was found in the experiment. We are currently developing a physics-based void fraction correlation which should account for the effect of mass flux on void fraction, and therefore, film thickness. Agreement between the experimental results and the model for pressure drop, however, is quantitatively closer and qualitatively accurate. Improvements to the pressure drop predictions are also underway and involve inclusion of a more accurate two-phase friction factor derived specifically for annular flow.

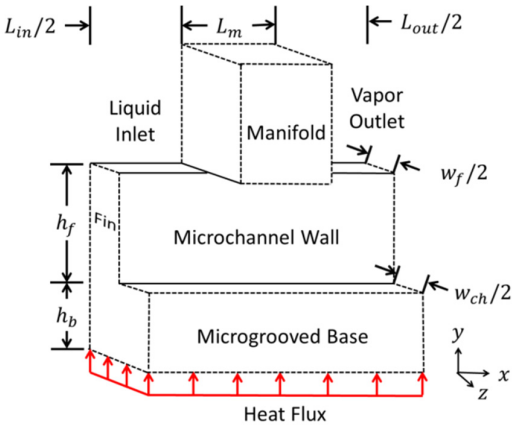

Fig. 2: Unit cell of manifold-microchannel.

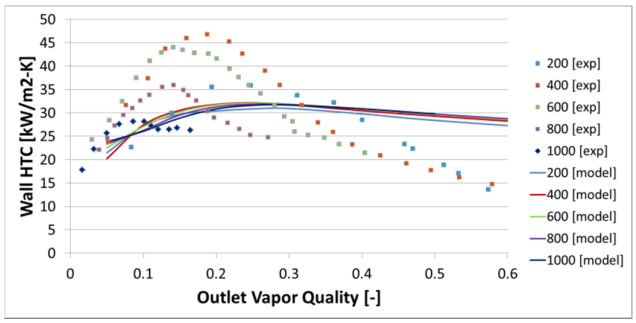

(a)

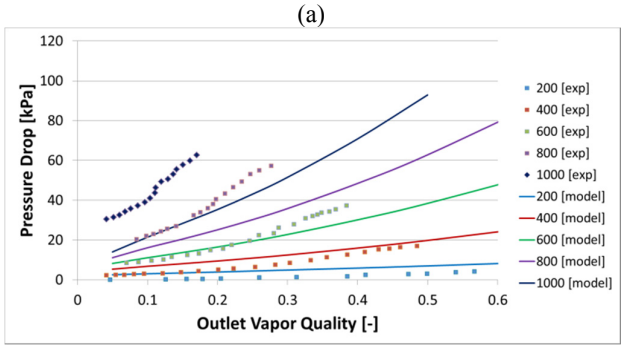

(b)

Fig. 3: Sample results from model (a) average wall heat transfer coefficient vs. outlet vapor quality for various mass fluxes and (b) pressure drop vs. outlet vapor quality for various microchannel mass fluxes. Units for mass flux are in kg/m^2-s. Experimental data taken from [1].

4. CONCLUSION

A novel "2.5-D" model was formulated to simulate the performance of a two-phase manifold-microchannel undergoing thin film evaporation. Although simplifications to the governing physics were made, the resulting model provided good insight into the governing physics and provides useful trends for wall heat transfer coefficient and pressure drop to allow for meaningful optimization. Comparison with the experimental results indicate a substantial agreement of the trends, thus suggesting the model can be improved to accurately predict the key characteristics of flow and heat transfer for the problem at hand.

References

[1] Cetegen, E., "Force Fed Microchannel High Heat Flux Cooling Utilizing Microgrooved Surfaces," Ph.D., University of Maryland, College Park (2010).

[2] Ohadi, M. M., Choo, K., Dessiatoun, S., and Cetegen, E., Next Generation Microchannel Heat Exchangers, Springer Publishing Co., (2012).

[3] Mandel, R., Shooshtari, A., Dessiatoun, S., and Ohadi, M., "Streamline Modeling of Manifold Microchannels in Thin Film Evaporation," ASME 2013 Summer Heat Transfer Conference, ASME, Minneapolis, MN (2013).

Heater Size Influence on Evaporation and Deformations of Liquid Film Sheared by Gas in a Microchannel

Yu. O. Kabova[1], V.V. Kuznetsov[2], O. A. Kabov[1,3]

[1] Institute of Thermophysics, pr. Lavrentyev 1, Novosibirsk, 630090 Russia, kabova@itp.nsc.ru, kabov@itp.nsc.ru
[2] Lavrentyev Institute of Hydrodynamics, pr. Lavrentyev 15, Novosibirsk, 630090 Russia, kuznetsov@hydro.nsc.ru
[3]Tomsk Polytechnic University, Lenin av., 30, Tomsk, 634050 Russia

Many engineering processes and laboratory experiments include liquid film heating by an intensive local heat source on a substrate. For instance, this situation occurs at cooling of microelectronic equipment, thin liquid films sheared by stratified or annular gas/vapor flow are a promising candidate for the thermal management of advanced semiconductor devices in earth and space applications [1]. Thermocapillary convection, boiling, evaporation, etc. are as well studied at local heating [2, 3]. Broad application of thin liquid films at local heating requires a fundamental understanding of the underlying hydrodynamic and thermal behavior of two-phase flow and evaporative heat transfer. In this paper we will analyze the influence of local heater shape and size on the thin film deformations and evaporation on the free interface.

We consider a system of thin film of incompressible viscous liquid in contact with a gas moving in *x*-direction in a flat microchannel of given height. On the bottom wall of the channel a local heater is located and the heater upper edge is located at the origin of coordinate system. The system is assumed to be unbounded in streamwise *(x)* and spanwise *(y)* directions. The acceleration of gravity is opposite to *z* direction. The free interface is assumed to be immiscible and deformable. The motions of the liquid film and gas are governed by the Navier-Stokes, continuity and energy equations in liquid and gas phases and diffusion equation in the gas phase. Convection heat transfer in the liquid and the gas phases as well as temperature dependence of surface tension and liquid viscosity are taken into account. We assume that the upper wall is adiabatic and impermeable. At the bottom wall no slip condition and thermal boundary conditions (prescribed temperature at the heater) are satisfied. The initial parameters such as initial film thickness, tangential stresses, the pressure drop, and velocity fields in the liquid and gas phases were found out as the exact solution of the problem of isothermal laminar co-current flow in the channel with straight streamlines. At the free gas-liquid interface the condition of continuity of the tangential component of the velocity vector (no-slip condition of two viscous media), the mass conservation for the liquid media and mutual mass conservation conditions, the dynamic condition with the term expressing the mechanical effect of the evaporated matter on the liquid and the thermal boundary condition, taking into account the energy spending on the phase transition as well as conditions of local thermodynamic equilibrium are posed. Numerical solution of the problem is implemented by the finite difference method using the grid approximation. The alternating directions implicit (ADI) method is used to solve the system of grid equations with boundary conditions [4].

Calculations have been performed for the constant channel height H_C=*250 μm*. The fluid is water and the gas is nitrogen. The liquid and the gas Reynolds numbers are equal correspondingly *Re=5 (H_0=86.3μm)* and Re_g=*15*. The initial temperature is equal to *20°C*. The heating area is constant in all calculations and is equal to *1 cm²*, temperature difference between the heating area and the substrate is equal to *1.0°C*. Present calculations have been made for small temperature difference between the heating area and the substrate because of fast film rupture on the long in streamwise direction heaters with the small width. As shown in [5] for such heaters the film rapture takes place at heat fluxes much smaller than for the square heaters.

Calculations show that heating area form has an important effect on the film evaporation, gas-liquid interface deformations and pattern. Fig.1 shows the gas-liquid interface position at different form of the heater, but heating area is remain constant. For the stretched in a spanwise direction heater the middle stream between two main lateral waves exists. While narrowing the heater the middle stream disappear and position of minimum film thickness moves from the edges of the heater to one point in the middle of the heater, see Figs. 1 and 2.

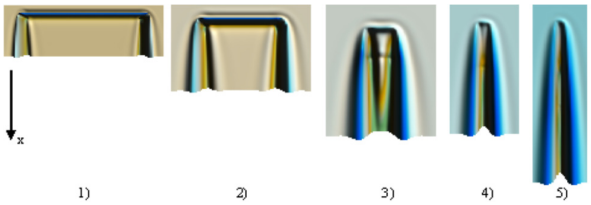

Figure 1: Thermocapillary deformations of the gas-liquid interface (top view). 1) *0.1x10.0 cm²* 2) *0.25x4.0 cm²* 3) *1.0x1.0 cm²* 4) *2.0x0.5 cm²* 5) *4.0x0.25 cm²*.

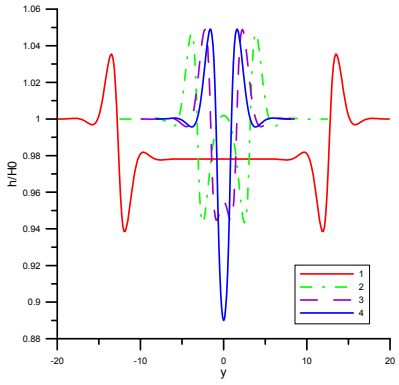

Figure 2: Gas-liquid interface position across the channel at *x=0.3 cm*. 1) *0.25x4.0 cm²*; 2) *1.0x1.0 cm²*; 3) *2.0x0.5 cm²*; 4) *4.0x0.25 cm²*.

Position of the liquid bump which appears on the upper edge of the heater remains constant irrespective of the heater form, see Fig. 3. In Fig. 4 one can see that maximum film thickness has minor dependence from the heater form unlike the minimum film thickness which decreases significantly with changing the heater form from stretched in spanwise direction to stretched in streamwise direction. And this dependence is strongly nonlinear. The reason of this could be significant increasing of the maximum temperature at the gas-liquid interface for the stretched in streamwise direction heaters, Fig. 5.

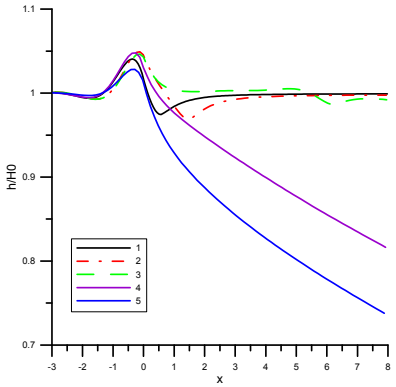

Figure 3: Gas-liquid interface position along the channel at *y=0* (liquid bump). 1) *0.1x10.0 cm²*; 2) *0.25x4.0 cm²*; 3) *1.0x1.0 cm²*; 4) *2.0x0.5 cm²*; 5) *4.0x0.25 cm²*.

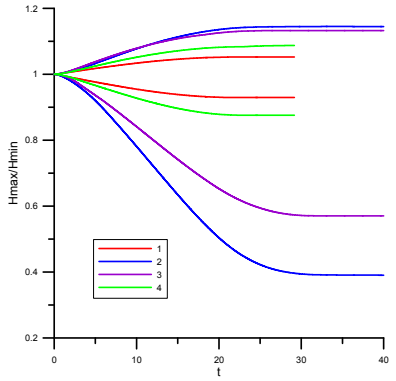

Figure 4: Maximum and minimum film thicknesses versus time. 1) *0.25x4.0 cm²*; 2) *4.0x0.25 cm²*; 3) *2.0x0.5 cm²*; 4) *1.0x1.0 cm²*.

Form of the heating area strongly affects the evaporation intensity, Fig. 5 (a). Here ***J*** is a nondimensional evaporation, it is calculated by the following formula: $\mathbf{J_{total}} = \int_{\Omega} \frac{1}{h(x,y)} \frac{\partial C}{\partial \xi}\Big|_{\xi=1} dxdy$, where Ω is the all area of calculations. At low heating intensity, evaporation is more significant for the heaters stretched in the spanwise direction when length of the heater is much smaller than its width. For the long in *x*-direction heaters, when the length of the heater is much bigger than its width, evaporation starts slowly because the heater width is rather small but then it start to grow due to enlarge the heating area and sufficient heat dissipation to the *y*-direction (compare lines 4 and 5, Fig. 5(a)). Figs. 5(b) and 6 shows temperature at the gas-liquid interface. The temperature is maximal for the long in *x*-direction heaters with the small width.

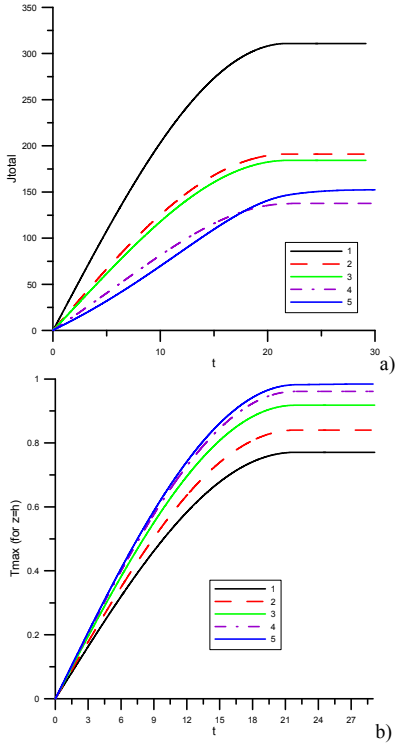

Figure 5: Total amount of matter evaporated from the gas-liquid interface (a) and maximum temperature for *z=h* (b) versus time. 1) *0.1x10.0 cm²*; 2) *0.25x4.0 cm²*; 3) *1.0x1.0 cm²*; 4) *2.0x0.5 cm²*; 5) *4.0x0.25 cm²*.

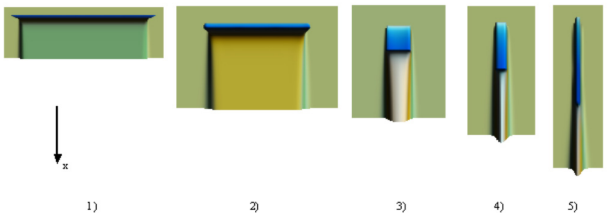

Figure 6: Temperature at the gas-liquid interface (top view). 1) *0.1x10.0 cm²* 2) *0.25x4.0 cm²* 3) *1.0x1.0 cm²* 4) *2.0x0.5 cm²* 5) *4.0x0.25 cm²*.

References

[1] Kabov, O.A., Interfacial Thermal Fluid Phenomena in Thin Liquid Films, Intern. J. of Emerging Multidisciplinary Fluid Sciences, 2 (2), p. 87-120, (2010).
[2] Nepomnyaschy, A. A., Velarde, M. G., and Colinet, P., Interfacial Phenomena and Convection, Chapman & Hall/CRC Press, London/ Boca Raton, (2002).
[3] Houshmand, F., Peles, Y., Convective heat transfer to shear-driven liquid film flow in a microchannel, Int. Journal of Heat and Mass Transfer, 64, p. 42–52, (2013).
[4] Kabova, Yu., Kuznetsov, V.V., Kabov, O., Gambaryan – Roisman, T., Stephan, P., Evaporation of a thin viscous liquid film sheared by gas in a microchannel, Int. J. Heat and Mass Transfer, 68, p. 527-541, (2014).
[5] Kabov, O.A., Heat Transfer from a small heater to a falling liquid film, Heat Transfer Research, 27(1), p. 221-226 (1996).

Modeling Shock Wave Propagation in Bubbly Media

Anil Kapahi, Chao-Tsung Hsiao, and Georges L. Chahine

DYNAFLOW, INC.
10621-J Iron Bridge Road, Jessup, MD 20794
Emails: anil@dynaflow-inc.com; ctsung@dynaflow-inc.com;
glchahine@dynaflow-inc.com

Understanding the propagation of acoustic pressures or shock waves through a bubbly medium is critical in various application areas such as bubble size distribution measurements [1], shock waves and cavitation mitigation [2], cavitation erosion [3], shock wave lithotripsy [4] and initiation of explosives [5].

Here, we present a compressible Eulerian multi-phase multi-material flow solver with three modeling approaches to examine shock wave propagation in a bubbly medium [6]. The compressible solver is based on fixed Cartesian grid and solves the conservation of mass, momentum, and energy using a fully conservative higher order MUSCL scheme [7]. The governing equations describe a set of hyperbolic conservation laws. Cast in Cartesian coordinates, the governing equations for conservation of mass, momentum, and energy take the following form:

$$\begin{aligned} &\frac{\partial \rho}{\partial t} + \nabla.(\rho \boldsymbol{V}) = 0, \\ &\frac{\partial \rho \boldsymbol{V}}{\partial t} + \nabla.(\rho \boldsymbol{V}\boldsymbol{V} + P\boldsymbol{I}) = 0, \\ &\frac{\partial \rho E}{\partial t} + \nabla.((\rho E\boldsymbol{V} + P\boldsymbol{I})\boldsymbol{V}) = 0, \end{aligned} \qquad (1)$$

where $\boldsymbol{V}$ is the material velocity, ρ is its density, E is its specific total energy, and P is the pressure. The system is closed by using an equation of state which defines the pressure as a function of the specific internal energy and the density.

The embedded interfaces are handled using a mixed-cell approach [7]. The method is capable of resolving and capturing non-linear wave fronts such as shock and rarefaction waves and contact discontinuities. In a first approach the multi-material solver is used directly without any modeling assumptions and resolves the gas water interfaces by fully discretizing each of the multiple bubbles. In a second approach a discrete singularity method (DSM) is used to describe the bubbles dynamics and their influence on the medium as resolved singularities [8].

In this setting, the bubbles are treated as spherical entities in a Lagrangian manner and follow a modified Rayleigh-Plesset-Keller-Herring equation and an equation of motion for bubble translation. This model coupled with the compressible Eulerian solver can handle a large number of bubbles. The third approach uses a homogeneous equivalent medium approach to describe the two phase bubbly mixture. This uses directly the compressible Eulerian solver in a medium with evolving void fraction starting with a prescribed initial void fraction distribution.

Figure 1 illustrates the time evolution of the pressure contours from the multi-material simulation of the shock wave propagating through a bubbly medium. When the shock wave encounters the array of bubbles it behaves very differently than a shock wave travelling in pure water. The presence of the bubbles attenuates significantly the wave. On the other hand, the collapses of the bubbles compressed by the shock wave cause local distortion and pressure spikes in the bubble region. Figure 2 shows a comparison of the pressure time history monitored downstream of the bubble column for different void fractions of bubble column. It is seen that the pressures decay much faster as the void fraction increased since bubbles absorb energy from the pressure waves.

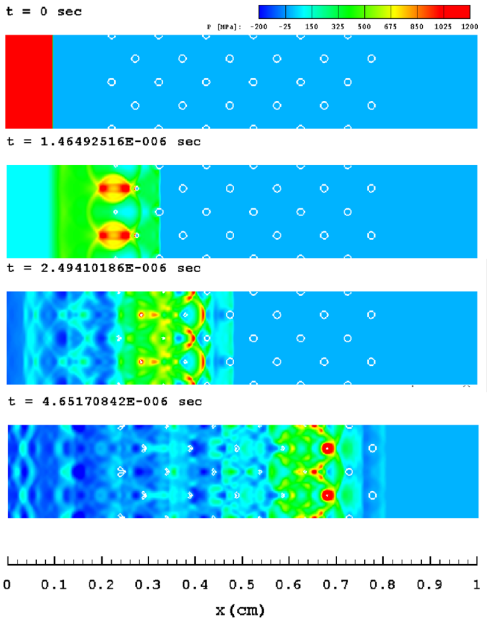

Figure 1: Time evolution of the pressure contours from the direct numerical simulation of the shock wave propagating through a bubbly medium.

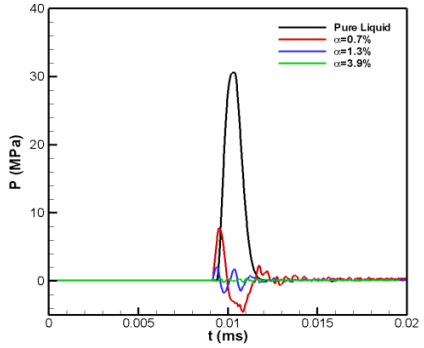

Figure 2: Comparison of the pressure time history monitored downstream of the bubble column for different void fractions of bubble column.

Though this approach completely captures the bubble dynamics and wave structure, it is limited by the numbers of bubbles that can reasonably be discretized. Moreover, this method requires a good resolution for embedded bubbles leading to large computation times making it challenging for real applications with large number of bubbles.

The second approach is to use the homogeneous model to solve the same problem. This method prescribes an initial void fraction (ratio of all bubble volumes to the total volume of the layer) corresponding to the bubble column region shown in Figure 1. Figure 3 shows the high pressure wave gets attenuated after traveling through the bubble column region due to the presence of air/water mixture. Although the homogenous mixture model can simulate pressure wave propagation and attenuation in the bubbly media, it cannot capture all features of the rich internal structure of the bubbly medium with the detailed pressure wave behavior.

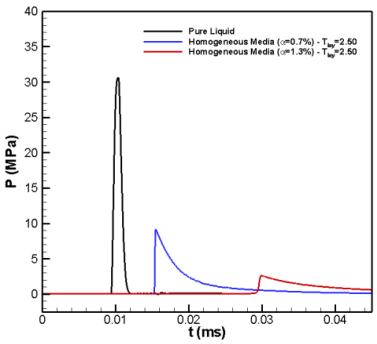

Figure 3: Comparison of the pressure time history monitored downstream of the bubble column for different void fractions of bubble column using homogeneous model.

In order to model many micron sized bubble without the cost of the full simulation, the DSM approach can be used. This approach defines bubbles as Lagrangian particles and can capture features like wave scattering and attenuation important for problems of interest to this work. Figure 4 shows the time evolution of the pressure contours from the DSM simulation of the shock wave propagating through a four-layer bubble column. It is seen that both pressure wave scattering and attenuation are observed although the bubbles change size but remain spherical during the dynamics.

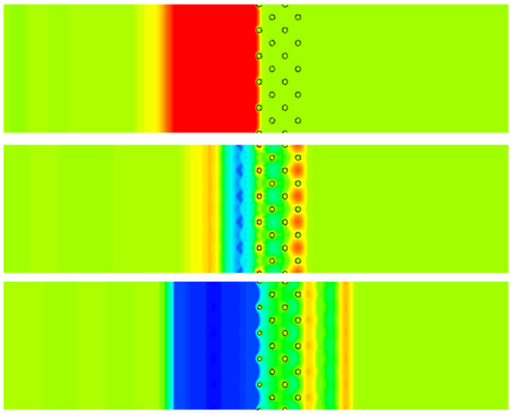

Figure 4: Time evolution of the pressure contours from the DSM simulation of the shock wave propagating through a four-layer bubble column.

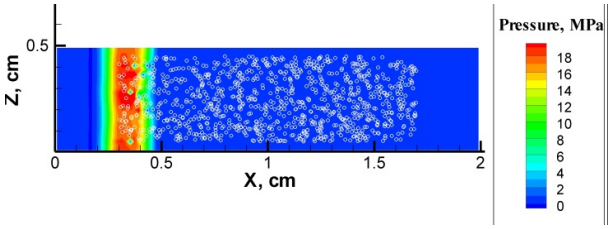

Figure 5: Attenuation and propagation of a shock wave of strength 35 MPa in the presence of thousands of bubbles using DSM approach.

The computational cost associated with DSM approach is much lower than the other methods making it suitable for applications involving large number of bubble as shown in Figure 5, which considers 1000 bubbles.

These three approaches will be further examined under various conditions. The key differences between the approaches will be presented by observing pressure amplitude and phasing in the computational domain including within the bubbly mixture.

Acknowledgments

We are grateful for DOE support under SBIR Phase II DE-SC0006443.

References

[1] Wu, X. and G.L. Chahine, Development of an acoustic instrument for bubble size distribution measurement. Journal of Hydrodynamics, Ser. B,. 22(5, Supplement 1): p. 330-336, 2010.

[2] Chahine, G.L., Hsiao, C.-T., Jayaprakash A., Raju R.,, Development of a Numerical Design Tool for Spallation Neutron Source Cavitation Mitigation. DYNAFLOW Technical Report 2M8015-DOE-Shock-2, 2012.

[3] Chahine, G.L. Modeling of Cavitation Dynamics and Interaction with Material, Chap. 6 in *Advanced Experimental and Numerical Techniques for Cavitation Erosion Prediction* Editors Kim, K.H., Chahine, G.L., Franc, J.P., & Karimi, A., , Springer. 2014

[4] Field, J., The physics of liquid impact, shock wave interactions with cavities, and the implications to shock wave lithotripsy. Physics in medicine and biology, 36(11): p. 1475, 1991.

[5] Field, J., Hot spot ignition mechanisms for explosives. Accounts of Chemical Research, 25(11): p. 489-496, 1992.

[6] Kapahi, A., C.-T. Hsiao, and G.L. Chahine., A multi-material flow solver for high speed compressible flow applications. To appear in Computers & Fluids, 2014.

[7] Colella, P., A direct Eulerian MUSCL scheme for gas dynamics. SIAM Journal on Scientific and Statistical Computing, 6(1): p. 104-117, 1985.

[8] Raju, R., S. Singh, C-T. Hsiao and G.L. Chahine., Study of Pressure Wave Propagation in a Two-Phase Bubbly Mixture. Journal of Fluids Engineering, 133(12):p.121302-1-121302-12, 2011.

Ninth International Conference on
TWO-PHASE SYSTEMS FOR GROUND AND SPACE APPLICATIONS
Baltimore, Maryland, USA, September 22-26, 2014

A Microgravity Two-Phase Flow Separator Experiment in Development for Flight on ISS

Lauren M. Sharp, Enrique Ramé, Kelly M. Gilkey,
Jay Owens, Nang T. Pham, Philip A. Stehno

NASA Glenn Research Center
21000 Brookpark Rd. Cleveland, OH 44135
lauren.m.sharp@nasa.gov

Dr. Yashiro Kamotani, Dr. Jaikrishnan Kadambi, Ming-Fang Kang

Case Western Reserve University
10900 Euclid Avenue
Glennan Building 418
Cleveland, OH 44106

Dr. Georges L. Chahine, Dr. Xiongjun Wu

DYNAFLOW, INC.
Research & Development in Applied Sciences
10621-J Iron Bridge Road
Jessup, MD 20794

Phase separation of two-phase flow in a microgravity environment is an on-going challenge. On earth, gas bubbles dispersed in a liquid can be easily separated using gravity-induced buoyancy. However, buoyancy is negligible in microgravity and the two phases have no desire to separate. External forces, such as surface tension, viscous forces, and inertial forces, must be utilized to separate bubbles from liquids. Achieving reliable and effective phase separation is crucial if more efficient, compact two-phase systems are going to be adopted for life support and thermal control in space.

The cyclonic separator is a type of two-phase flow separation device that utilizes the inertia of rotational flows for gas-liquid separation. Phase separation occurs as the tangentially injected flow mixture is swirled around the chamber, causing the gas to accumulate along the axis of the vortex as the denser liquid is forced to the walls [1]. Cyclonic separators are passive and therefore desirable as they exploit only the inertia of the incoming flow to accomplish this task. This passive phase separation technology is attractive in that fewer moving parts lends to greater reliability and lower power requirements. The advantages of passive phase separation technology outweigh its single-phase counterparts and motivate the Two-Phase Flow Separator Experiment (TPFSE) for flight on the International Space Station (ISS).

The main objective of TPFSE is to facilitate the maturation of passive cyclonic separation technology through the combination of experiments, computations, and analyses. These mutually reinforcing approaches are being employed in order to quantitatively assess and delimit the range of operability of a new separator design concept with respect to both transient and steady-state behavior at a device and system level – features that have yet to be completely explored in any such device.

Two cyclonic phase separators are the object of this project, one designed by Case Western Reserve University (CWRU), appropriate for moderate gas volume fractions [2], and one designed by DYNAFLOW, INC. which can separate gas volume fractions down to the order of 0.001 [3-4].

A recent campaign on the reduced gravity aircraft provided the opportunity to test the functionality of these two-phase flow separators. During these flights, the airplane flies parabolic "free fall" trajectories that offer approximately 20 seconds of a low-gravity environment, followed by approximately 40 seconds of climb during which one experiences close to 2 g of effective gravity. The rig used in this campaign is a flow loop system that allows for the metering of liquid-gas mixtures into an instrumented phase separator test section. In Figure 1, the CWRU phase separator is pictured (left) installed in the TPFSE aircraft rig. The DYNASWIRL® phase separator designed by DYNAFLOW, INC. is pictured on the right. Both phase separators are mounted inside a secondary containment box as a preventative measure against leaks from the test chamber.

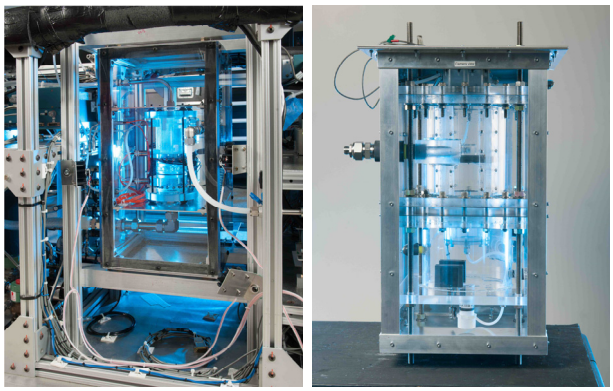

Figure 1: The test sections, CWRU on the left and DYNAFLOW, INC. on the right, are pictured installed in a secondary containment fixture. (Courtesy: NASA)

The two separator test sections possess tomographic, pressure, and high-speed video diagnostics. The flow loop on the rig was designed such that the test sections could be interchanged while sharing a common flow loop, gas and liquid supplies, controls, instrumentation, and diagnostic equipment. The gas for this aircraft experiment is breathing air, supplied by a commercial cylinder, and controlled via mass flow controllers. The test liquid is water, which is stored in a cylindrical supply tank that also contains a piston. The water is made motive by applying an appropriately regulated pressure from the compressed gas source to the top of the piston. The desired liquid flow rate is set manually using a needle valve and liquid is forced out of the liquid supply tank as the piston moves downward. The water and gas are brought together in a mixer and then directed to the test section through a two-phase flow development pipe. The two-phase flow enters the test section tangentially to

establish a circulatory swirling flow. As the two-phase mixture rotates around the test section, the rotational acceleration segregates the gas to a central core, leaving gas-free liquid near the test section wall. High speed video cameras and a standard definition camera record the behavior of the flow inside the test chamber. Figure 2 (CWRU) and Figure 3 (DYNAFLOW, INC.) illustrate the two-phase flow pattern as it occurs in low-gravity aboard the parabolic aircraft.

After separation occurs in the test chamber, the respective gas and liquid outlets are brought together in a collection tank. The gas is exhausted to the aircraft cabin through a backpressure regulator while the liquid remains in the tank to be re-circulated by a gear pump back into the supply tank. The design of the collection tank takes advantage of gravity during the high-g period between tests, when the liquid drops to the bottom and is then pumped back into the supply tank. Pressure, temperature, and flow rate data are recorded while varying gas and liquid flow rates to evaluate the functionality of the two-phase separators and their effectiveness at separating the gas and liquid phases.

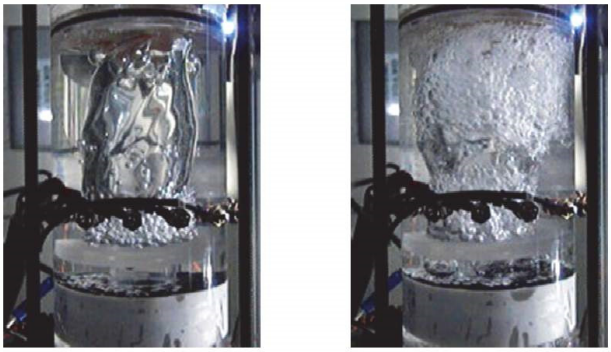

Figure 2: Images from the CWRU unit. Typical separator gas core for (a) liquid-only injection and for (b) two-phase injection as visualized by images extracted from high speed video. The test section diameter is approximately 7.6 cm.

Figure 3: Zoomed-in view of the separation action in the DYNASWIRL® phase separator during the low-g period of a parabolic aircraft flight. The horizontal scale of the field of view corresponds to approximately 10 cm.

While the TPFSE experiments performed on the parabolic aircraft rig facilitates the study of two-phase flow in low-gravity, the design of the rig itself relies on gravity for operating the collection tank. Thus, the aircraft rig flow concept cannot be used aboard the ISS. The next step for the project is to develop a breadboard flow loop for these two-phase separators that does not depend on periods of high-g to function, as a precursor to designing the flight hardware for the ISS.

The breadboard model will be used to develop and validate the hardware, flow-loop design, instrumentation, data acquisition and diagnostic techniques to be used on ISS. In an important departure from the aircraft rig flow loop, the breadboard model will consist of a closed flow loop where the liquid is continuously re-circulated through the system. The breadboard model will differ from the aircraft rig in other respects as well: the components must conform to stricter size and power limits consistent with the facilities aboard the ISS; they must be able to withstand radiation (a unique requirement of space hardware); and a secondary phase separator of proven microgravity performance will be located downstream of the test separators to ensure liquid only and gas only streams are re-circulated through the flow loop. Additional void fraction diagnostics will be introduced to evaluate the effectiveness of the phase separators. Further, high-speed video will be installed to obtain data of gas core-liquid interfacial dynamics during transient and steady operation, and an acoustic [5] will detect very small bubbles at void fractions as low as 0.001 in the liquid exit stream of the DYNASWIRL® phase separator. These diagnostics will serve to benchmark computational fluid dynamics calculations under way in the respective labs of the investigators.

In this talk, we will discuss preliminary results of the reduced gravity aircraft campaign and details of the breadboard model.

References

[1] L.M. Milne-Thompson, "Theoretical hydrodynamics", Dover, Ch. 13, 1968.

[2] Hoyt, N. C., M.-F. Kang, K.-L. Lee, Kharraz, A., Kadambi, J., and Kamotani, Y., “Study of Steady and Dynamic Behavior of Gas Core of Passive Cyclonic Separator for Space Applications”, Microgravity Science and Technology, Vol. 25, No. 3, 2013.

[3] G. L. Chahine and K. M. Kalumuck, "Swirling Fluid Jet Cavitation Method and System for Efficient Decontamination of Liquids", US Patent, 6,221,260, April 24, 2001.

[4] X. Wu, G. Loraine, G. L. Chahine, "Reduced Gravity Tests of a DYNASWIRL® Phase Separator for Space Applications", 28th Annual Meeting of American Society of Gravitational and Space Research, New Orleans, LA, Nov. 28, 2012.

[5] X., Wu, G. L. Chahine, “Development of an acoustic instrument for bubble size distribution measurement,” Journal of Hydrodynamics, Ser. B, Volume 22, Issue 5, Supplement 1, Pages 330-336, October 2010.

Void Fraction Characteristics and Flow Patterns of One Component Gas-Liquid Two-Phase Flow

Taisaku Gomyo[1*], Hithoshi Asano[1], Osamu Kawanami[2], Koichi Suzuki[3], Ryoji Imai[4],
Takashi Kurimoto[5], Satoshi Matsumoto[5], Yasuhisa Shinmoto[6], Tomoki Hirokawa[6], and Haruhiko Ohta[6]

[1] Dept. of Mech. Eng., Kobe University, 1-1 Rokkodai, Nada, Kobe, 657-8501, Japan
128t327t@stu.kobe-u.ac.jp
[2] Dept. of Mech. and System Eng., University of Hyogo, 2167 Shosha, Himeji, Hyogo, 671-2280, Japan
[3] Dept. Mech. Eng., Tokyo University Science-Yamaguchi, 1-1-1 Daigaku-Dori, Sanyo-Onoda, Yamaguchi, 756-0884, Japan
[4] Dept. of Mechanical, Aerospace and Material Eng., Muroran Institute of Technology, 27-1 Mizumoto-cho, Muroran, 050-8585, Japan
[5]Japan Aerospace Exploration Agency, 2-1-1 Sengen, Tsukuba, Ibaraki, 305-8505 Japan
[6] Dept. Aeronautics and Astronautics, Kyushu Univ., 744 Motooka, Nishi-ku, Fukuoka, 819-0395, Japan

Introduction

Recently, two-phase flow loop system has been attracting as a cooling and temperature control system for an increase in heat flux from electric or power device for space structures. Experiments at Japanese Experimental Module "KIBO" in International Space Station (ISS) are planned to clarify the effect of gravity on boiling flow characteristics [1]. One of the subjects is a detailed observation of the interface structure at the downstream of heating section. In this experiment, 3D observations will be performed by the method of stereoscopic photography using a high speed camera. In this paper, void fractions measured from images were compared to those by a capacitance method to evaluate the accuracy. Characteristics of the local void fraction fluctuations for each flow pattern are discussed.

Experimental setup and measurement method

Vertical upward two-phase flows of FC-72 were examined. The main component of FC-72 is n-perfluorohexane which is used in ISS experiment. The inlet conditions of refrigerant were set by an electric heater, and then two-phase flows were supplied to the test section with the inner diameter of 4 mm at 416 mm downstream of the heating section. The diameter is the same as that in ISS experiment. In the test section, a capacitance censor was installed. The detail of the capacitance censor is shown in **Fig. 1**.

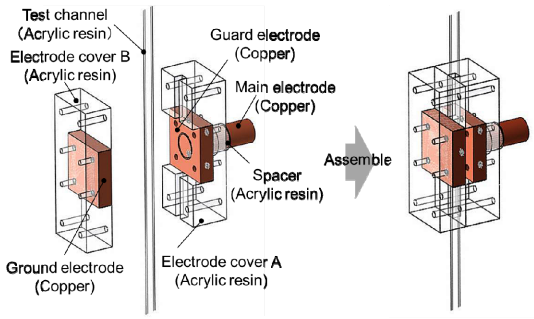

Figure 1: Schematic of capacitance sensor.

A parallel plate type was selected to visualize flow behaviors simultaneously. Flow behaviors were observed from the side by a high speed camera. The capacitance censor was calibrated using Teflon-rods as a simulant object of the liquid. Average void fraction can be measured by the following equation in Eq. (1) from the measured capacitance of two-phase flow, C.

$$\alpha_{capa} = 1-(C-C_0)/(C_1-C_0) \quad (1)$$

where C_0 and C_1 are the capacitance of vapor and liquid single-phase flow, respectively. The capacitance was measured with sampling frequency of 1 kHz, and the others parameters were measured with 100 Hz. Experiments were carried out for the mass flux, G, of 30 to 530 kg/(m^{2}s), the thermal equilibrium quality, x_{eq}, of -0.15 to 1.0, and tank pressure, P, for 0.1~0.13 MPa. Flow behaviors were observed by high speed camera with 1000 fps and exposure time of 100 μs.

Experimental results

Flow patterns observed in the test section were classified into bubble, slug, churn, semi-annular and annular flows. The difference between churn and semi-annular flows were defined by the presence or absence of intermittent liquid reverse flow in liquid film. **Figure 2** shows a flow pattern map obtained from the flow observation results. Broken lines are transition boundaries proposed by Mishima-Ishii [2]. Experimental data was well agreed with the Mishima-Ishii's flow pattern map.

The typical void fraction fluctuations for slug and annular flows are shown in **Fig. 3** with those observation images in **Figs. 4**. Dashed lines in **Figs. 4** show the capacitance sensing area. It cloud be seen the output of the capacitance censor fluctuated in response to low behaviors.

Void fraction was measured from images by some image processing in the following procedure. Firstly, background was eliminated by a subtraction image of the liquid single-phase flow. Secondly, a Gaussian filter was applied to the target images to enhance the contrast. Finally, the images were binarized at a suitable threshold to obtain

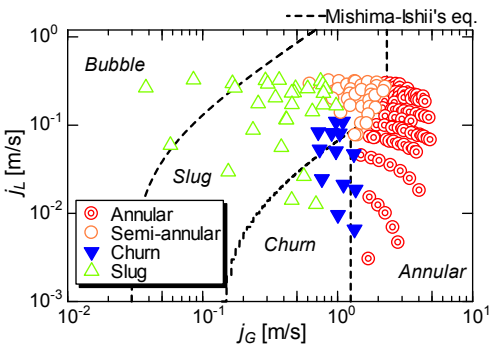

Figure 2: Flow pattern map.

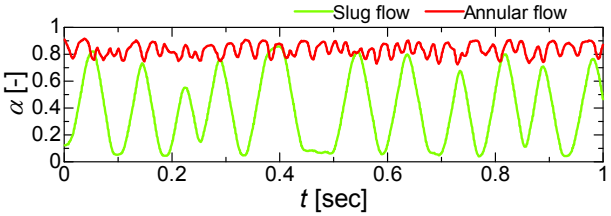

Figure 3: Example void fraction fluctuations of slug flow and annular flow.

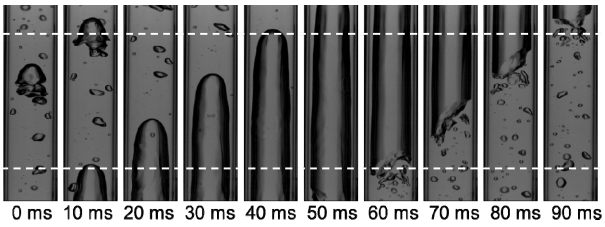

(a) Slug flow

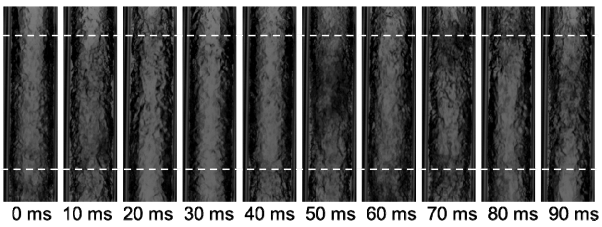

(b) Annular flow

Figure 4: Typical flow behavior, slug flow and annular flow.

the interface. Volumetric average void fraction in the imaging area was calculated by Eq. (2).

$$\alpha = \sum \Delta\alpha_{img} = \sum \left(\Delta D_g / D\right)^2 \qquad (2)$$

where D_g and D are the local diameter of gas phase and channel diameter, respectively. The pixel size in the image was about 16 μm/pixel.

Figure 5 shows a comparison of void fraction fluctuation for a slug flow between the capacitance method and imaging method. Measured results by two method by two methods agreed well. **Figure 6** shows the comparison of measured results of time average void fractions between by the capacitance method, $\alpha_{ave,capa}$, and the imaging method, $\alpha_{ave,img}$. For annular, semi-annular, churn flows which void fraction fluctuations were small, the values of $\alpha_{ave,\ img}$ were agreed with $\alpha_{ave,\ capa}$ within ±10 %. On the other hand, for intermittent flows like bubble, and slug flows, the values of $\alpha_{ave,\ img}$ were agreed with $\alpha_{ave,\ capa}$ within ±20 %. The reason on the decrease of accuracy might be on a lack of the data number in the imaging method.

To evaluate the possibility of flow pattern determination based on void fraction fluctuations, the mean square deviations in the probability distribution of void fraction were calculated, and were plotted against time average void fraction in each measurement, $\alpha_{ave,img}$ and $\alpha_{ave,capa}$. **Figure 7(a)** was obtained from output of the capacitance probe for 10 s with 1 kHz sampling. On the other hand, **Figure 7(b)** was obtained by imaging method. The imaging period and frames for each case were limited to about 0.4 s and 400 frames. It could be seen that characteristics for each flow pattern could be shown in such analysis on void fraction fluctuations in spite of the low number of data in imaging method.

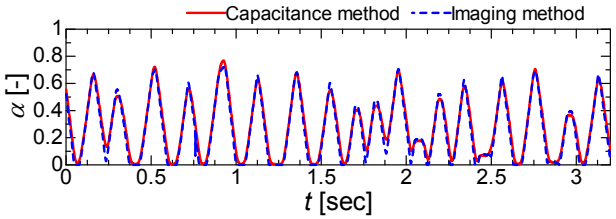

Figure 5: Comparison of measured void fraction luctuations between capacitance and imaging method.

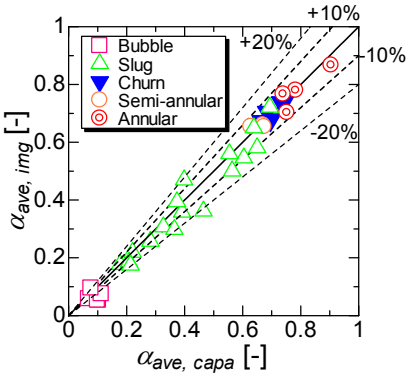

Figure 6: Comparison of time average void fractions by two different measuring method.

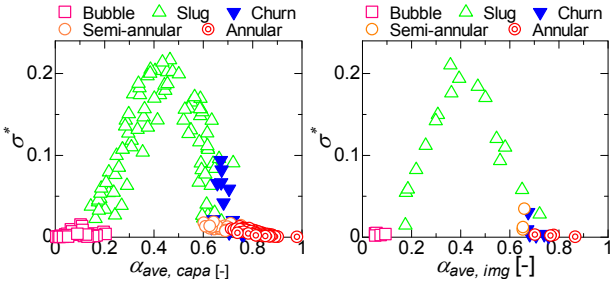

(a) Capacitance method **(b)** Imaging method

Figure 7: Mean square deviations in probability distribution of void fraction against time average void fraction.

References

[1] K., Fujii, M., Komasaki, T., Kurimoto, H., Kawasaki, K., Sawada, K., Suzuki, H., Asano, O., Kawanami, R., Imai, Y., Shinmoto and H., Ohta, Recent Progress in JAXA Project of Boiling Two-Phase Flow Experiment onboard ISS, Journal of Physical Science and Application, Vol. 2(4),pp. 71-79 (2012).

[2] K., Mishima and M., Ishii, Flow Regime Transition Criteria for Upward Two-phase Flow in Vertical Tubes, Int J. Heat Mass Transfer, Vol. 27, pp. 723-737 (1984).

Experimental Study on Bubble Dynamics of Gas-Liquid Two-Phase Flow in Capillary Vertical Tubes

Bo Xu[1], Wenguang Nan[2], Yueshe Wang[2], Gang Huang[1], Zhiqiang Wu[1]

[1] National Key Laboratory of Human Factors Engineering, China Astronaut Research and Training Center
No.26, Beiqing Road, Beijing, 100094, P.R. China
[2] State Key Laboratory of Multiphase Flow in Power Engineering, Xi'an Jiaotong University
No.28, Xianning West Road, Xi'an, 710049, P.R. China
*tsuiboo@sina.com

Air plug induced by bubbles accumulated is an important problem in the pump of Oxygen Generation System. Thus, it is necessary to accurately monitor the bubble volume in the induction pipe of the pump. Though a bubble sensor based on the Beer–Lambert law has been developed, its precision is greatly affected by the bubble dynamic, due to the complex reflection and refraction of the infrared rays on the bubble surface. For the purpose of calibration and further optimization of the bubble sensor, it is essential to study the bubble dynamic in vertical upward gas-liquid flow in the capillary tubes. Though much work has been carried out on the bubble dynamic in gas-liquid two phase flows in micro or macro tubes, quite few papers focus on the bubble dynamic in gas-liquid flow in the capillary tubes with inner diameters in millimeter-scale [1,2]. In a capillary tube, the effect of surface tension is remarkable, but not as important as that in a micro-tube. Therefore, it is pre-established that the bubble dynamic in gas-liquid flow in a capillary tube is different from that in a usual large tube or a micro-tube.

Figure 1 presents the typical flow patterns, including bubble-train flow (BT), bubble-slug flow (BS), slug flow(S) and chain-slug flow (CS):

(a) Bubble-train flow. This flow pattern could be found in most experimental conditions. The shape and size of bubbles varied with the gas and liquid superficial velocities correspondingly. And the bubbles migrated one by one like a train, without coalescence.

(b) Slug flow. This flow pattern was observed when the liquid superficial velocity was low while the gas superficial velocity was lower than the liquid superficial velocity. Two adjacent gas slugs were completely separated by the liquid slugs in the flow direction. Most cross-sections of the tube were occupied by gas slugs which had a length much larger than the inner diameter of the tube. The gas slugs showed a hemi-spherically shaped nose and tail at quite low liquid and gas superficial velocities. In contrast, when the liquid and gas superficial velocities went up owing to the strong interaction between the gas slugs and liquid, the bodies of the gas slugs were distorted, and the tops and tails were flattened.

(c) Bubble-slug flow. It was a transitional flow pattern between the bubble-train flow and slug flow. The bubble length was just a little bigger than the inner diameter of the tube.

(d) Chained-slug flow. This flow pattern could be observed when the gas superficial velocity was high while the liquid superficial velocity was low. The slugs connected end to end but with apparent interfaces between each other. The number of the chained slugs was determined by the gas and liquid superficial velocities.

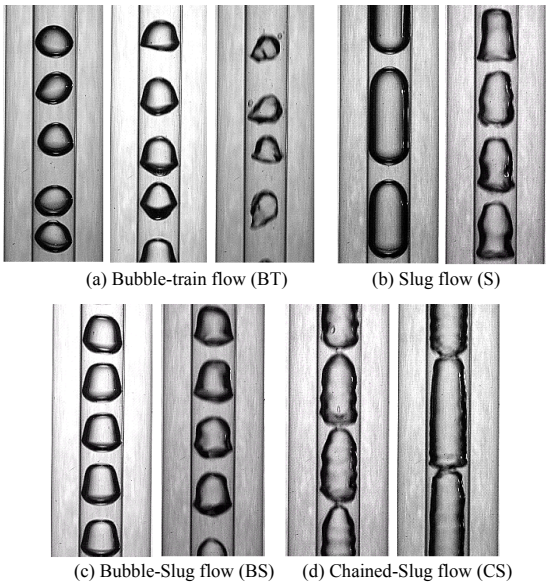

Figure 1: Typical images of flow pattern.

At low gas and liquid superficial velocities, bubbles formed and then detached in slow succession at the tip of the nozzle. As the shear force was much lower than the surface tension, the detachment of bubbles was mainly controlled by the differential pressure between the head and tail of the bubble. As a result, even though not perfectly spherical, the bubble shape was regular. Similarly, as the pressure around the bubbles was not homogeneous and imbalanced, the shape and radial position of the bubble varied with time. Images of the bubble shape and position at different time with an interval of 27ms were shown in Fig. 2. The detached bubbles travelled upward in a helical path without any major collision or coalescence. The rising velocities of well distributed bubbles were approximately constant. As gas and liquid superficial velocities went up, bubble forming at the nozzle tip was still in connection with the previous bubble. And their separation was mainly controlled by the shear force, unlike the separation mechanism at low gas and liquid superficial velocities. As a result, the shape of bubble altered spatially and temporally irregularly. Fig. 3(a) and Fig. 3(b) showed the bubble shape at different gas and liquid superficial velocities with a time interval of 3ms (time increased with sequence number 1, 2, 3…). The degree of irregularity increased as the gas and liquid superficial velocities accelerated.

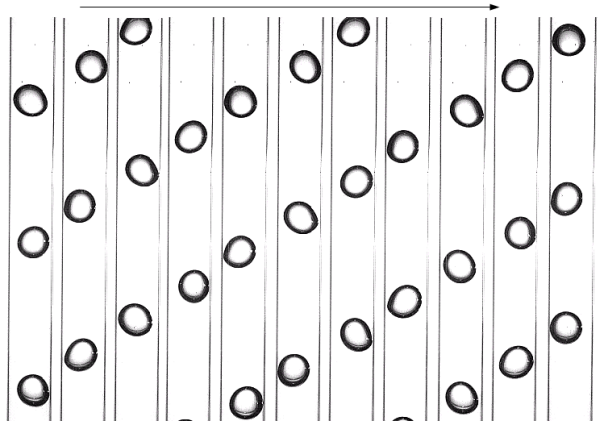

Figure 2: The shape and position of regular bubble.

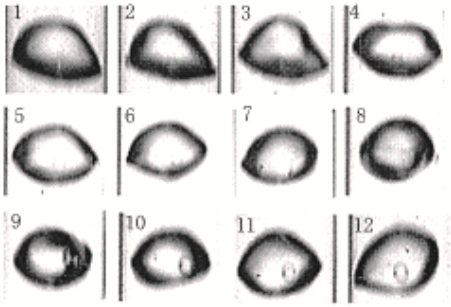

(a) U_{gs} =19.9 cm/s, U_{ls} =67.1 cm/s

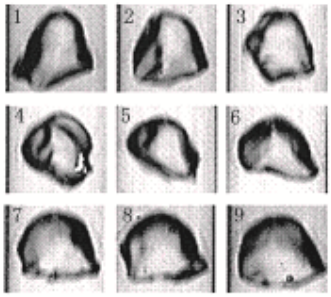

(b) U_{gs} =31.4cm/s, U_{ls} =134.6cm/s

Figure 3: The shape of irregular bubbles.

The reflection and refraction of infrared rays on every cross section were very complex, that two different irregular bubbles might have the same ratio of transmission and receiving, which were observed in the calibration. As a result, the bubble shape couldn't be simplified to prolate, oblate or other ideal shape, and this phenomenon should be taken into account in optimizing design of bubble sensor.

The bubble experienced a force balance among the drag force, buoyancy force, hydrostatic pressure, and the surface tension between the gas and the liquid. The hydrodynamic force (drag force, buoyancy force, and hydrostatic pressure) depended on the bubble's motion, and concurrently altered that motion. These nonlinear interactions were responsible for the path instability of the bubble. When the bubble moved near the tube wall, its surface pushed the water away from the wall. This moving mass of fluid added a strong inertia to the dynamics of the bubble due to the large density ratio between the liquid and the gas inside the bubble. Meanwhile, the inhomogeneity of hydrostatic pressure around the bubble increased. As a result, the bubble migrated slower in the radial direction until it nearly contacted the wall when the bubble was supposed to be pushed away from the wall. Then the bubble drifted with a zigzag trajectory. Fig. 4(a) and Fig. 4(b) showed the trajectory of a single bubble with a zigzag motion, which was also certificated by Maldonado et al.[3] and Salari et al.[4]. In Fig. 4(a), the trajectory was characterized by a point on the left boundary of the bubble, instead of the center of the bubble. In Fig. 4(b), the two lines, on either side of the bubble, were the projection of the tube wall. Of course, time and distance of periodicity were mainly dominated by the vertical velocity of the bubble. However, as shown in Fig. 4(c), the 'wall-climbing' straight trajectory, which was observed when the bubble has an antenna, was quite different from the zigzag motion. The antenna was almost continuously bonded to the wall within the observation limit. Obviously, the antenna was responsible for this strange phenomenon. The existence of antenna may change the distribution of pressure around the bubble, and then altered the motion of the bubble.

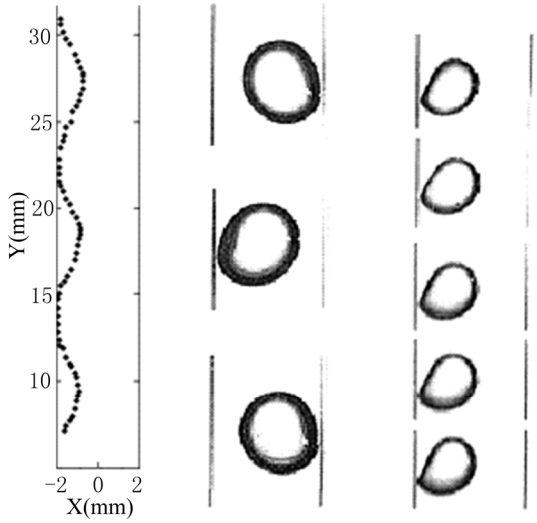

Figure 4: Bubble trajectory.

References

[1] Yang, Z. C., Bi, Q. C., Liu, B., Nitrogen/non-Newtonian fluid two-phase upward flow in non-circular microchannels, International Journal of Multiphase Flow, 36(1), 60-70(2010).

[2] Eskin, D., F. Mostowfi, A model of a bubble train flow accompanied with mass transfer through a long microchannel. International Journal of Heat and Fluid Flow, 33(1), 147-155(2012).

[3] M. Maldonado, J.J. Quinn, C.O. Gomez, J.A. Finch, An experimental study examining the relationship between bubble shape and rise velocity, Chemical Engineering Science, 98, 7-11 (2013).

[3] Salari, A, M. Shafii, S. Shirani, An Experimental Review on Microbubble Generation to be Used in Echo-Particle Image Velocimetry Method to Determine the Pipe Flow Velocity. Journal of fluids engineering, 135(3), (2013

Notes

April 26-30, 2015 Boulder, CO

9th International Conference on Boiling and Condensation Heat Transfer

Conference Chair
Jungho Kim, U. of Maryland

Conference Co-Chairs
J. Buongiorno, MIT
V. Carey, UC Berkeley
C. Colin, U. of Toulouse
Y. Takata, Kyushu U.
R. Yang, CU Boulder

Int. Scientific Committee
D. Attinger, Iowa State U.
D. Banerjee, TAMU
J. Barbosa, U. Santa Catarina
S. Bhavnani, Auburn U.
G. Celata, ENEA
C.H. Chen, Duke U.
P. Di Marco, U. of Pisa
S. Garimella, Georgia Tech
H. Kim, Kyung Hee U.
J. Klausner, U. of Florida
T. Kunugi, Kyoto U.
M. McCarthy, Drexel U.
J. Meyer, U. of Pretoria
V. Narayanan, Oregon State U.
H. Ohta, Kyushu U.
Y. Peles, RPI
J. Plawsky, RPI
W. Qu, U. of Hawaii
G. Ribatski, U. of Sao Paulo
K. Sefiane, U. of Edinburgh
H. Soliman, U. of Manitoba
P. Stephan, TU Darmstadt
J. Thome, EPFL
G. Tryggvason, U. Notre Dame
I. Ueno, Tokyo U. of Science
E. Wang, MIT
J.F. Zhao, Chinese Acad. Sci.

Announcement

Plan to join us in beautiful Boulder, Colorado for the 9th conference of this series, the premier forum to discuss and disseminate the latest developments in boiling and condensation heat transfer. Previous conferences have been held in Santa Barbara, Banff, Irsee, Alyeska, Jamaica, Spoleto, Florianopolis, and Lausanne. Papers related to all aspects of pool and flow boiling, and condensation heat transfer are invited. Specific topics could include:

- Nucleation
- Bubble heat transport
- Critical heat flux mechanisms and modeling
- Surface modification and morphology effects
- Boiling in microchannels and on the microscale
- Flow boiling within complex geometries
- Numerical modeling and analysis of boiling and condensation
- Experimental techniques
- Convective condensation
- Droplet evaporation and condensation
- Spray and jet cooling
- Boiling of mixtures

All authors are required to submit 1-2 page extended abstracts. Authors will then be given the option of submitting full papers to be presented in oral sessions. Those submitting abstracts only will be assigned to oral sessions as space permits or to a poster session (with a short oral presentation).

Schedule

Abstracts submission: July 31–October 15, 2014
Notification of abstract acceptance: November 15, 2014
Draft papers due: December 15, 2014
Notification of draft paper acceptance: January 15, 2015
Final papers due: February 15, 2015
Conference dates: April 26-30, 2015

For Further Information

Contact J. Kim, UMD, kimjh@umd.edu, (+1) 301-405-5437
Web site: boiling2015.umd.edu

UNIVERSITY OF MARYLAND 1856 THE DEPARTMENT OF MECHANICAL ENGINEERING

Boulder

PROGRAM OVERVIEW

Time	Monday	Tuesday	Wednesday	Thursday	Friday
Morning		Registration	Registration	Registration	
		Technical Sessions	Technical Sessions	Technical Sessions	ITT Meeting (by invitation only)
		Coffee Break	Coffee Break	Coffee Break	
		Technical Sessions	Technical Sessions	Technical Sessions	
Lunch	Registration	Lunch Break	Lunch Break	Lunch Break	
Afternoon	Technical Sessions	Technical Sessions	Technical Sessions	Technical Sessions	
	Coffee Break	Coffee Break	Coffee Break	Coffee Break	
	Technical Sessions	Technical Sessions	Technical Sessions	Technical Sessions	
Evening	Welcome Reception NASA Special Session on fluidsLAB	Scientific Committee Meeting (by invitation only)	Conference Banquet		